

**SIMULATION OF A SIX WHEELED
MARTIAN ROVER CALLED
THE ROCKER BOGIE**

A Thesis

Presented in Partial Fulfillment of the Requirements for
the degree Master of Science in the
Graduate School of The Ohio State University

by

Jeffrey E. Chottiner

* * * * *

The Ohio State University

1992

Master's Examination Committee:

Dr. Kenneth J. Waldron

Dr. Gary L. Kinzel

Approved by



Advisor
Department of Mechanical Engineering

To my grandparents
Abe and Lillian Chottiner

ACKNOWLEDGMENTS

First, I would like to thank Dr. Kenneth J. Waldron for the opportunity to work with him and for his guidance throughout my research. I would also like to express gratitude to Dr. Kennedy and the people at OAI (Ohio Aerospace Institute) for the generous fellowship and the privilege of working at JPL (Jet Propulsion Laboratory). Many thanks to Roger J. Bedard Jr. and his secretary Beverly Mendoza for bringing me to JPL and for their concern for my welfare once I was there. Donald Bickler's and Randel Lindemann's support at JPL, and their attempt to answer my perplexing questions pertaining to my research, is much appreciated. On a lighter note, I would like to thank Jennifer Dubin for her companionship and for her understanding of my work load. Finally, and most importantly, I would like to thank my parents who have stressed the importance of education, and who are always there when I need them.

VITA

October 22, 1967	Born - Syracuse, New York.
1988-1990	Coop Student, United Technologies Carrier, Syracuse, New York.
1986-1990	B.S., Syracuse University, Syracuse, New York.
Summer 1991	Consulting Engineer, Jet Propulsion Laboratory, Pasadena, California.

FIELDS OF STUDY

Major Field: Mechanical Engineering

Specialization: kinematics, dynamics, mechanics, design, and control.

TABLE OF CONTENTS

	PAGE
DEDICATION	ii
ACKNOWLEDGMENTS	iii
VITA	iv
LIST OF TABLES	vii
LIST OF PLATES	viii
LIST OF FIGURES	ix
LIST OF VARIABLES	xiii
CHAPTER	
I. INTRODUCTION	1
Section 1.1 - Objective	1
Section 1.2 - Mars	3
Section 1.3 - Rover designs	11
Section 1.4 - Rocker Bogie	25
II. KINEMATICS	34
Section 2.1 - The terrain map	34
Section 2.2 - Steering	47
Section 2.3 - Wheel positions	59

CHAPTER	PAGE
III. DYNAMICS	74
Section 3.1 - Initial parameters	74
Section 3.2 - z-direction dynamics	91
Section 3.3 - xy plane dynamics	102
IV. MOVING FORWARD	121
Section 4.1 - New contact forces	121
Section 4.2 - The vehicle's new position	131
Section 4.3 - Program simplifications	148
Section 4.4 - Path planning	160
V. RESULTS	169
Section 5.1 - Input and output	169
Section 5.2 - Performance	184
Section 5.3 - Conclusions	221
BIBLIOGRAPHY	227
 APPENDICES	
A. Assumptions	229
B. Total vehicle moment of inertia	233
C. Running the program	244

LIST OF TABLES

Table		Page
4.1	Vehicle parameters	154
4.2	Comparing dynamic and 'quasi-static'	155
5.1	Input file Mars.dat	169
5.2	Input	184
5.3	New design	221
5.4	Climbing comparison	224
5.5	Efficiency comparison	225
5.6	Average power comparison	226

LIST OF PLATES

Plate		Page
I	Rocker Bogie prototype	26
II	Rocker Bogie without body	27

LIST OF FIGURES

Figure	Page	
1.1	Mars as seen by Viking I	4
1.2	Mars as seen by Viking II	5
1.3	Mars	6
1.4	Walking Beam	12
1.5	Body translating	13
1.6	Beam translating	14
1.7	Two modes of operation	16
1.8	FMC rover	17
1.9	Surmounting a step	18
1.10	Roll over recovery	19
1.11	Steering method two	20
1.12	Steering method three	21
1.13	Ambler	24
1.14	Effect of differential on body	28
1.15	Front view illustrating roll	30
1.16	Steering - top view	31
1.17	Schematic of mechanical stops	32
2.1	Top view of terrain map	35
2.2	Steering of wheel one	40
2.3	Contact angle	41
2.4	Contact angle variation	42
2.5	Impossible contact	44
2.6	Top view of wheel one	45
2.7	Ackerman steer for 2-D	47
2.8	Rocker Bogie model	50
2.9	Left side view	50

Figure		Page
2.8	Rocker Bogie model	50
2.9	Left side view	50
2.10	Ackerman steer for 3-D	52
2.11	Three different Ackerman axis cases	54
2.12	Side and top view of rocker	59
2.13	Illustration of last term in Eqn. 2.24	61
2.14	Guessing θ_{12}	62
2.15	Finding position of wheel three	64
2.16	Guessing θ_L	66
2.17	Beam to body joint offset	68
2.18	Beam to body joint offset	70
2.19	Finding initial positions of wheels	72
3.1	Rocker parameters	75
3.2	Beam parameters	76
3.3	Moment of inertia of the body	78
3.4	Determining static beam pivot forces	79
3.5	Determining initial contact force	80
3.6	Determining initial contact forces	81
3.7	Determining tractive force	82
3.8	Controlling tractive force	84
3.9	Tire map	91
3.10	Determining slip angle for wheel six	92
3.11	Lateral force due to roll	94
3.12	Force couple system	98
3.13	Freebody diagram of the left rocker	102
3.14	Rocker's acceleration due to vehicle's cg motion	105
3.15	Beam freebody diagram	111
3.16	Beam's acceleration due to vehicle's cg motion	113
3.17	Freebody diagram of the body	115
4.1	Nomenclature	122
4.2	Uniform acceleration assumption	123
4.3	Determining contact force	128
4.4	Finding equivalent contact force	129
4.5	Rocker moving forward	131
4.6	Adjusting rocker angle	133

Figure	Page	
4.3	Determining contact force	128
4.4	Finding equivalent contact force	129
4.5	Rocker moving forward	131
4.6	Adjusting rocker angle	133
4.7	Possible oscillation problem	136
4.8	Adjusting beam angle	138
4.9	Flowchart for adjusting joints	144
4.10	Program flowchart	147
4.11	Freebody diagram of rocker	151
4.12	Freebody diagram of beam	151
4.13	Program flowchart - 'quasi-static'	153
4.14	Oscillation problem	158
4.15	Path planning	161
4.16	Finding X_i' , Z_i'	166
4.17	Example of path planner	168
5.1	Variation of time step with speed	173
5.2	Specified terrain	175
5.3	Program Output	177
5.4	Top view 1.5 seconds later	179
5.5	Surmounting hill, stops not contacted	180
5.6	Surmounting hill, stops are contacted	181
5.7	Recovery from instability	182
5.8	Specified terrain I	185
5.9	Rocky III unable to proceed	185
5.10	Efficiency vs. Hill Height of Rocky III	186
5.11	Instability case one	187
5.12	Instability case two	188
5.13	Hill Height and Efficiency vs. b	189
5.14	Hill Height and Efficiency vs. d_1	192
5.15	Disadvantage of mechanical stops	195
5.16	Rocky III unable to proceed	196
5.17	Specified terrain II	199
5.18	Rocky III unable to proceed	200
5.19	Change in rock climbing vs. b	201
5.20	Specified terrain III	204
5.21	Interference	205

Figure		Page
5.20	Specified terrain III	204
5.21	Interference	205
5.22	Specified terrain IV	206
5.23	Specified terrain V	207
5.24	Unable to cross crevasse	208
5.25	Failure of mechanical stops	209
5.26	Specified terrain VI	210
5.27	Vehicle yaw	212
5.28	Hill height for rollover vs. track	214
5.29	New design	221
B.1	Local frame at body center	234
B.2	Front view of rocker	236
B.3	Top view of rocker	237
B.4	Rotation about z-axis	241

LIST OF VARIABLES

Note:

- 1) When it states 'wheels one to six' in the variable list, it means the subscript changes depending on the wheel number (see Figure 1.16).
- 2) Often only wheel one variables are listed here.
- 3) Primed moments of inertia in Appendix B are those that have been moved with the parallel axis theorem and are not listed here.
- 4) Double primed moments of inertia in Appendix B are those that have been rotated to the vehicle's local frame and are not listed here.
- 5) WRT means with respect to.

a	Horz. distance from wheel one to the rocker pivot ($\theta_{12}=0$).
A_s	Area of square stock used in the rocker and beam.
A_x, A_y, A_z	Acceleration of vehicle along the local x, y, and z-axes.
a_{x12}, a_{y12}	Total linear accelerations seen by the left rocker's cg.
$\ddot{a}_{x12}, \ddot{a}_{y12}$	Linear accl. of left rocker due to rotation about O_{12} .
$\ddot{a}_{x12}, \ddot{a}_{y12}$	Linear accl. of left rocker due to rotation about O_L .
$\ddot{a}_{x12}, \ddot{a}_{y12}$	Linear accl. of left rocker due to rotation about O_B .
a_{xL}, a_{yL}	Total linear accelerations seen by the left beam's cg.
$\ddot{a}_{xL}, \ddot{a}_{yL}$	Linear accl. of left beam due to rotation about O_L .
$\ddot{a}_{xL}, \ddot{a}_{yL}$	Linear accl. of left beam due to rotation about O_B .
b	Horz. distance from wheel two to the rocker pivot ($\theta_{12}=0$).
C_a	Tractive force constant for acceleration.
C_d	Tractive force constant for deceleration.
c_g	Center of gravity.
C_h	Camera's horizon.
C_p	Proportion of tractive force to rear tires.
C_r	Camera's resolution.
C_t	Central tendency factor of the path planner.

D_1	Distance from wheel one to final destination point.
d_1	Horz. distance from rocker pivot to beam pivot ($\theta_L=0$).
D_2	Distance from vehicle's cg to (X_i, Y_i) chosen from path planner.
d_2	Horz. distance from beam pivot to wheel three ($\theta_L=0$).
D_3	Distance from vehicle's cg to the final destination point.
d_{R1}, d_{L1}	Distance from the both rear wheels to the z-axis in xz plane.
d_{R2}, d_{L2}	Distance from the z-axis to both middle wheels in xz plane.
d_{R3}, d_{L3}	Distance from the z-axis to both front wheels in xz plane.
e	Vert. distance from wheel center to body center ($\theta_{12}=\theta_L=0$).
E, F, G, H	Constants in the equation of a plane.
$E_1 \dots E_6$	Power of motors for wheels one to six.
$f_{b1} \dots f_{b6}$	Braking forces on wheels one to six.
$f_{c1} \dots f_{c6}$	Contact forces on wheels one to six.
$f_{cb1} \dots f_{cb6}$	Contact forces on back side of wheels one to six.
$f_{cf1} \dots f_{cf6}$	Contact forces on front side of wheels one to six.
f_d	Total dynamic tractive force of all wheels.
$f_{d1} \dots f_{d6}$	Dynamic tractive forces on wheels one to six.
$f_{f1} \dots f_{f6}$	Lateral forces of the wheels above that to overcome friction.
$f_{L1} \dots f_{L6}$	Lateral forces on wheels due to contact and tractive forces.
$f_{r1} \dots f_{r6}$	Resistive forces on wheels one to six.
f_s	Total static tractive force of all wheels.
$f_{s1} \dots f_{s6}$	Static tractive forces on wheels one to six.
$f_{st1} \dots f_{st6}$	Sticking forces in lateral direction for wheels one to six.
f_t	Total tractive force of all wheels.
$f_{\tau1} \dots f_{\tau6}$	Forces of force couple to replace τ_y for wheels one to six.
$f_{t1} \dots f_{t6}$	Tractive forces (static and dynamic) on wheels one to six.
$(f_{t1})_{max}$	Max. Tractive force for wheels one to six before tang. slip.
f_x, f_y	Components of contact forces in x and y-direction.
f_{x12}, f_{y12}	x and y-direction forces on left rocker pivot.
f_{x45}, f_{y45}	x and y-direction forces on right rocker pivot.
f'_{xL}, f'_{yL}	f_{xL} and f_{yL} of previous step.
f_{xL}, f_{yL}	x and y-direction forces on left beam pivot.
f_{xR}, f_{yR}	x and y-direction forces on right beam pivot.
$f_{z1} \dots f_{z6}$	Total lateral forces for wheels one to six $f_{\tau} + f_L$.
h	Height of body.
I_1	Moment of inertia of rocker at rocker's cg.
I_2	Moment of inertia of beam at beam's cg.
I_{12} or I_{z12}	Moment of inertia of left rocker about its z-axis.
I_{45} or I_{z45}	Moment of inertia of right rocker about its z-axis.

I_{ab}	Moment of inertia of link of length $a+b$ about its cg.
I_d	Moment of inertia of link of length $d_1 + d_2$ about its cg.
I_e	Moment of inertia of link of length e about its cg.
I_L or I_{zL}	Moment of inertia of left beam about its z-axis.
I_R or I_{zR}	Moment of inertia of right beam about its z-axis.
I_w	Moment of inertia of wheel about its cg.
I_x	I_x rotated by θ_B .
I_x, I_y, I_z	Moment of inertia of the body about the x, y, and z-axes.
I_{x12}, I_{y12}	Left rocker's x and y-axes inertia at pivot with ($\theta_{12} = 0$).
I_{x45}, I_{y45}	Right rocker's x and y-axes inertia at pivot with ($\theta_{45} = 0$).
I_{xab}, I_{yab}	Moment of inertia of length $a+b$ about x and y-axes at its cg.
I_{xB}, I_{yB}, I_{zB}	I_x, I_y, I_z used in Appendix B
I_{xd}, I_{yd}	Moment of inertia of length d_1+d_2 about x and y-axes at its cg.
I_{xe}, I_{ye}	Moment of inertia of member e about x and y-axes at its cg.
I_{xL}, I_{yL}	Left beam's x and y-axes inertia at pivot with ($\theta_L = 0$).
I_{xR}, I_{yR}	Right beam's x and y-axes inertia at pivot with ($\theta_R = 0$).
I_{xt}, I_{yt}, I_{zt}	Total moment of inertia about the local x, y, and z-axes.
I_{xw}, I_{yw}	Moment of inertia of wheel about its x and y-axes.
I_{xy12}	Product of inertia at pivot of left rocker with ($\theta_{12} = 0$).
I_{xy45}	Product of inertia at pivot of right rocker with ($\theta_{45} = 0$).
I_{xyL}	Product of inertia at pivot of left beam with ($\theta_L = 0$).
I_{xyR}	Product of inertia at pivot of right beam with ($\theta_R = 0$).
j	Number of joints.
$k_{e1} \dots k_{e6}$	Effective tire-ground stiffnesses for wheels one to six.
k_s	Stiffness of the soil.
k_w	Stiffness of the tire.
L	Length and width of square terrain.
l	Length of body.
$L_1 \dots L_6$	Lengths from the Ackerman axis to wheels one to six.
L_{12}	Distance from rocker pivot to rocker cg.
L_b	Length from body's cg to beam's cg.
L_L	Distance from the beam pivot to the beam cg.
L_p	Length from the beam pivot to the rocker cg.
L_r	Length from body's cg to rocker's cg.
M	Mobility or DOF of the linkage
m	Number of members.
m_{12}	Mass of rocker
M_{12}, M_{45}	Moment about left and right rocker pivot (0 unless mech. stop).

M_{12a}, M_{45a}	Moment about rocker pivots to create a desired ang. acccl.
M_{12c}, M_{45c}	Moment about rocker pivots in the new position.
m_{ab}	Mass of link of length $a+b$.
m_B	Mass of the body.
M_{Bxa}	Moment about body's x-axis to create a desired ang. acccl.
M_{Bxc}	Moment about body's x-axis in the new position.
m_d	Mass of link of length $d_1 + d_2$.
m_e	Mass of link of length e.
m_L	Mass of beam.
M_L, M_R	Moment about left and right beam pivot (due to body inertia).
M_{La}, M_{Ra}	Moment about beam pivots to create a desired ang. acccl.
M_{Lc}, M_{Rc}	Moment about beam pivots in the new positon.
m_t	Mass of the entire vehicle.
m_w	Mass of wheel.
M'_x, M'_y, M'_z	M_x, M_y, M_z rotated by θ_B .
M_x, M_y, M_z	Moment about vehicle's local x,y, and z-axes.
N	A particular time step. The Nth step.
O_{12}, O_{45}	Origin of the left and right rocker frame.
O_B	Origin of the local frame. At the body and vehicle cg.
O_L, O_R	Origin of the left and right beam frame.
$p_1 \dots p_6$	Specified terrain parameters (see Figure 5.2).
P_{ij}	Height of terrain at mesh coordinate (i,j).
P_{max}	Maximum relative height of terrain node.
q	Slope of force couple distribution to replace τ_y .
q_1	Slope of segment one of terrain at a given camera angle.
q_x, q_z	Slope of terrain along global X and Z-axes at a particular point.
R	Random number from -1.0 to 1.0.
r	Radius of the tire.
$R_1 \dots R_6$	Distances from vehicle's cg to cg of wheels one to six.
s	Width of hollow square stock used in rocker and beam.
S_d	Seed value for random number generator.
S_t	Total distance traveled in a time step by the vehicle's cg.
S_x, S_y, S_z	Displacement of vehicle along the local x,y, and z-axes for step.
S_{xG}, S_{yG}, S_{zG}	Total displacements measured in the global frame.
T	If 0 than random terrain, if 1 than specified terrain.
T_I	4×4 homogeneous transformation matrix.
T_{SL}	Soil for specified terrain (integer 1 is rock, other sand)
t	Seconds in the time step.
t_i	Real time before the graphics is updated.

t_s	Thickness of hollow square stock used in rocker and beam.
U	Unit mesh size of terrain or distance between adjacent nodes.
$u_1 \dots u_4$	Lengths used to analyze roll and yaw angular accelerations.
$v_1 \dots v_6$	Velocities of the center of the tires in the plane of the tires.
$v_1 \dots v_{10}$	Force vectors used in rocker and beam freebody diagrams.
$v_1 \dots v_6$	Velocities of wheel centers including lateral slip.
v_x, v_y, v_z	Velocity of vehicle along the local x, y, and z-axes for a step.
v'_x, v'_y, v'_z	v_x, v_y, v_z of previous step.
w	Width of body. Also considered to be the width of vehicle.
$w_1 \dots w_6$	Wheels one to six.
w_t	Width of the tire.
X, Y, Z	Position measured with global axis.
x, y, z	Position measured with local axis.
X_1, Y_1, Z_1	Initial global (X,Y,Z) position of wheel one to six.
X_{12}, Y_{12}, Z_{12}	Vector from vehicle's cg to left rocker pivot O_{12} .
X_{45}, Y_{45}, Z_{45}	Vector from vehicle's cg to right rocker pivot O_{45} .
X_a, Y_a, Z_a	Position of terrain in global (X,Y,Z) coordinates at point a.
x_{ab}, y_{ab}	Local axis at cg of member of length $a+b$.
$X_{\beta 1}, Y_{\beta 1}, Z_{\beta 1}$	Global position of a point on a tire circumference at angle β .
X_{c1}, Y_{c1}, Z_{c1}	Center of wheels one to six in global coordinates.
X_{cg}, Y_{cg}	Center of gravity of rocker or beam WRT a reference frame.
x_d, y_d	Local axis at cg of member of length d_1+d_2 .
x_e, y_e	Local axis at cg of member of length e.
X_{f1}, Y_{f1}, Z_{f1}	Final or destination global (X,Y,Z) position of wheel one to six.
X_i, Z_i	Intermediate destination point that wheel one aims for.
X_j, Z_j	Intermediate destination point used by path planner.
X_L, Y_L, Z_L	Global position of the left beam pivot (O_L).
X_p, Y_p, Z_p	Global position of left rocker's pivot (O_{12}).
X_R, Y_R	Global position of the right beam pivot on the beam.
X_R, Y_R, Z_R	Global position of the right beam pivot on body (O_R).
X_{r1}, Y_{r1}, Z_{r1}	Global coord. of terrain one camera resolution from (S_{x6}, S_{z6}).
x_w, y_w	Local axis at cg of wheel.
y_s	Wheel sinkage.
Z_{AK}	The distance along z-axis the Ackerman axis is from wheel one.
Z_L, Z_R	Half the width of the vehicle.

GREEK VARIABLES

α_{12}, α_{45}	Actual angular accl. of left and right rocker about its pivot.
α_{12nt}	Angular accl. of the rocker as if there was no terrain.

α_B	Angular accl. of body about the local z-axis.
α_L, α_R	Actual angular accl. of left and right beam about its pivot.
α_{Lnt}	Angular accl. of the beam as if there was no terrain.
$\alpha_x, \alpha_y, \alpha_B$	$\alpha_x, \alpha_y, \alpha_B$ rotated by θ_B .
$\alpha_x, \alpha_y, \alpha_B$	Roll, yaw, and pitch ang. accl. about local x,y, and z axes.
α_{xnt}	Roll angular accl. as if there was no terrain.
β	Angular position measured by an axis at cg of tire.
$\delta_1 \dots \delta_6$	Steering angle of wheels one to six measured from local x-axis.
Δa	Distance in x-dir. from O ₁₂ to wheel one's contact.
Δb	Distance in x-dir. from wheel two's contact to O ₁₂ .
Δe_1	Distance in y-dir. from wheel one's contact to O ₁₂ .
Δe_2	Distance in y-dir. from wheel two's contact to O ₁₂ .
ΔM_{12}	Difference between M _{12c} and M _{12a} .
ΔM_{Bx}	Difference between M _{Bxc} and M _{Bxa} .
ΔM_L	Difference between M _{Lc} and M _{La} .
$\Delta \theta_{12}$	The change in the left rocker angle θ_{12} .
$\Delta \theta_L$	The change in the left beam angle θ_L .
$\Delta \theta_x$	The change in the roll angle θ_x .
Δx	Change in the x-direction between two points.
$\Delta x_1, \Delta x_2, \Delta x_3$	Distance in x-dir. from wheel one, two and three to O _L .
Δy	Change in the y-direction between two points.
$\Delta y_1, \Delta y_2, \Delta y_3$	Distance in y-dir. from wheel one, two and three to O _L .
ΔY_{max}	Maximum compression of a tire.
$\Phi_1 \dots \Phi_6$	Steering angles of all the wheels measured WRT global X-axis.
$\Gamma_1 \dots \Gamma_6$	Torque of wheels one to six.
η	Efficiency.
ϑ_1, ϑ_2	Min. and max. view angles measured WRT global X-axis.
ϑ_a	Camera view angle in radians.
ϑ_f	Angle of line bisecting the camera view angle and global X-axis.
ϑ_i	Angle between lines (X _i , Z _i) to O _B and then to (X _{i'} , Z _{i'}).
ϑ_p	Angle of line from (X _i , Z _i) to O _B and global X-axis.
$\lambda_1 \dots \lambda_6$	Contact angles of wheels one to six.
$\lambda_{b1} \dots \lambda_{b6}$	Back contact angles of wheels one to six.
$\lambda_{f1} \dots \lambda_{f6}$	Front contact angles of wheels one to six.
$\mu_1 \dots \mu_6$	Coefficients of friction under wheels one to six.

θ_1, θ_2	Angles used to analyze the roll and yaw angular accelerations.
θ_{12}, θ_{45}	θ_{12} and θ_{45} of the previous step.
θ_{12}, θ_{45}	The left and right rocker pivot angles.
θ_B	Body angle WRT the local x-axis.
θ_g, ψ, γ	Intermediate angles used to determine the initial pivot angles.
θ_L, θ_R	θ_L and θ_R of the previous step.
θ_L, θ_R	The left and right beam pivot angles.
$\theta_{\min}, \theta_{\max}$	Min. and max. relative angle between the rocker and the beam.
θ_p	Angle between beam pivot to rocker's cg and x-axis.
θ_x, θ_y	Initial roll and yaw. Later roll and yaw WRT N-1 local frame.
θ_{xG}, θ_{yG}	Roll and yaw WRT the global frame.
ρ	Density of material used in the rocker and beam.
ΣF	Degrees of freedom of all the joints.
$\Sigma M_{O_{12}}$	Summing moments of left rocker about O_{12} .
τ_f	Torque about vehicle's local y-axis due to the $f_{f1} \dots f_{f6}$ forces.
τ_{st}	Torque about vehicle's local y-axis due to $f_{st1} \dots f_{st6}$ forces.
τ_x, τ_y, τ_z	Torque about vehicle's local x,y, and z-axes.
τ_y'	Total torque about vehicle's local y-axis $\tau_y' + \tau_y''$.
τ_y''	Torque about vehicle's local y-axis due to z-direction forces.
τ_y'''	Torque about vehicle's local y-axis due to xy plane forces.
Ω	Angular velocity about the Ackerman axis.
$\omega_1 \dots \omega_6$	Angular velocities about its center of wheels one to six.
ω_{12}, ω_{45}	ω_{12} and ω_{45} of previous step.
ω_{12}, ω_{45}	Angular velocity of the left and right rocker about its pivot.
ω_B	Angular velocity of body about the local z-axis.
ω_L, ω_R	ω_L and ω_R of previous step.
ω_L, ω_R	Angular velocity of the left and right beam about its pivot.
ω_x, ω_y	ω_x, ω_y of previous step.
ω_x, ω_y	Roll and yaw ang. velocity WRT the local frame.
ξ	Particular camera angle.
ξ_{12}	Angle of rocker's cg as measured from the rocker's y-axis.
ξ_L	Angle of beam's cg as measured from the beam's y-axis.
$\psi_1 \dots \psi_6$	Slip angle of wheel one to six.

CHAPTER I

INTRODUCTION

SECTION 1.1 - OBJECTIVE

The objective of this thesis is to determine how varying different parameters on a particular six wheeled robot, called the Rocker Bogie, will affect its performance. In other words, what happens to its power consumption and rock climbing characteristics as the tire size, the vehicle length, the vehicle width, etc... are changed. One can optimize the performance of the vehicle in this manner.

The performance will be determined by modeling the robot with a computer program and varying the parameters of the model. Although this robot can be modeled on existing dynamic software packages such as DADS and ADAMS, it would be difficult to iterate on different robot models and different terrains since both are time consuming to build. In addition, both software packages require a considerable amount of computer time. For these reasons, a simplified and specialized computer model makes sense.

The vehicle's objective is to transverse the martian surface, pick up rock samples, and do various scientific experiments in a semi-autonomous manner. Since it could take about 25 minutes to send a signal to Earth and back to Mars, the vehicle cannot be controlled entirely by Earth [3]. Hence, it is extremely important for this vehicle to be able to determine what terrain is safe for it to navigate. This indeed is perhaps an even more important objective of this project. If it fails to determine what terrain is safe for the robot to navigate, the mission could fail and billions of dollars could be lost.

A method for determining what terrain is safe for the vehicle to navigate, might be to first take a picture perhaps 10 meters ahead of the vehicle. Then, modeling the terrain with on board computers, a dynamic simulation, perhaps similar to the one developed in this thesis, could be run. The program should be able to determine if the vehicle will be able to navigate the terrain, if it will be stable, how long it will take, what the power consumption would be, and what the steering angles should be to reach the desired point. If it cannot navigate one particular route, it must be able to choose another. All of this requires a lot of fast calculations which ADAMS and DADS are unable to do in a reasonable time frame. Hence, for these reasons, a simplified code should and will be developed to model the robot.

Before going into the details of this computer program, the motivation behind sending a robot to Mars in the first place will be discussed. In addition, previously designed martian rovers will be mentioned to give a little history to the project and to compare the advantages and disadvantages of a walking machine and a wheeled vehicle.

SECTION 1.2 - MARS

Ever since the advent of the telescope, Mars, the fourth planet in the solar system, has been a fascination of man. Galileo was the first to observe Mars through a telescope in 1610 [1]. Since that time, Mars has been mapped by countless observers. No two of these mappings appear the same however. Martian topography seemed to change seasonally through the telescope. This discrepancy in observations was later explained by the Martian atmosphere. The early observers were essentially mapping light and dark regions since only the largest topographical features could be discerned. The light regions could be a desert, cloud cover, or frost; all of which will vary along with the atmosphere. Seasonal dust storms are another culprit of the variety of different sitings [1].

Therefore, if an early observer were to stare at Mars and perhaps use a little imagination, he could see just about anything. In 1877, an Italian astronomer by the name of Giovanni Schiaparelli, claimed he saw canals on Mars. Percival Lowell supposedly confirmed this and went farther to claim that they were made by an advanced civilization [1]. This was the beginning of the science fiction frenzy about the aliens on Mars.

The first close up views of Mars were taken by the Mariner 4, 6 and 7 spacecraft as they flew by. These probes disproved that there were any canals on Mars, and seemed to show that Mars was very similar to the moon. Then in 1971, Mariner 9 and several Soviet spacecraft orbited Mars and gave us a glimpse of the diverse and fascinating landscape known today. Most of what is known about Mars today is from the Mariner 9 probe and the next generation of space probes called the Viking probes [1].

In 1976, two Viking probes began to orbit Mars. Three years and 50,000 pictures later, Mars was mapped to 200 meter resolution. Detailed landscapes are known in only two areas of Mars where the two landers settled. These areas showed a relatively rocky terrain. Viking I saw copious sand dunes, a large 2 meter boulder, as well as smaller boulders. This is shown in Figure 1.1. Viking II, on the other hand, saw mostly a uniform field of boulders under 1 meter in size as is shown in Figure 1.2 [1].



Figure 1.1 - Mars as seen by Viking I

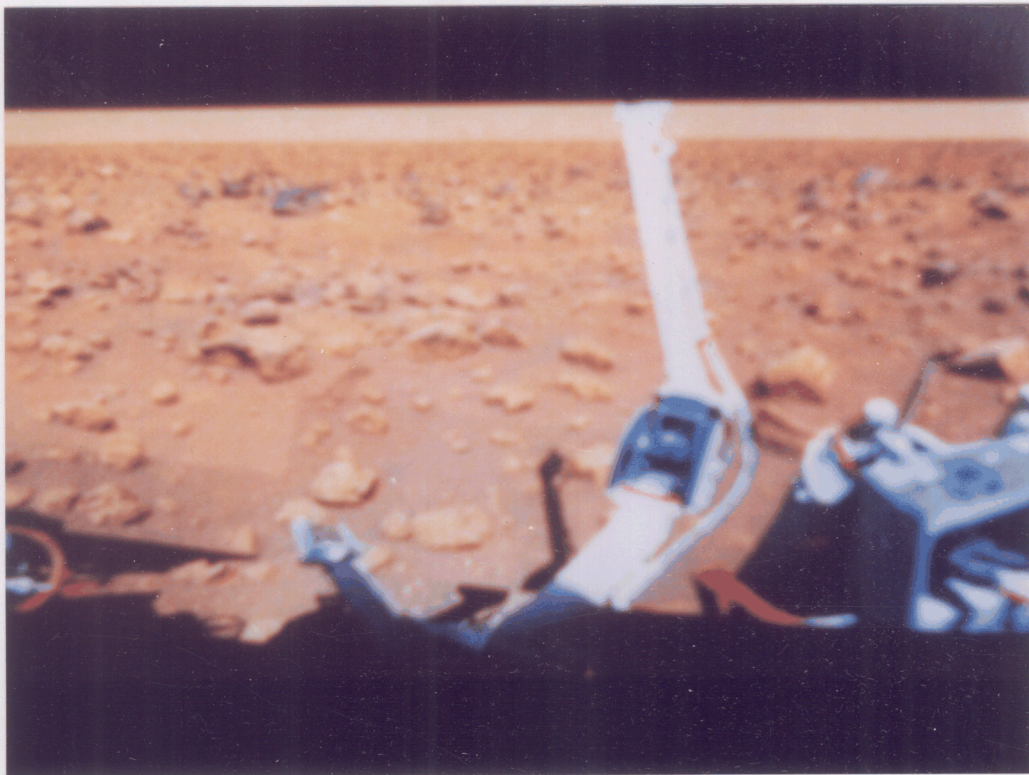


Figure 1.2 - Mars as seen by Viking II

Since only two areas of Mars are known in any detail, it is very difficult to assess what a robot would face. Mars, as seen in the 200 meter resolution photographs is extremely diverse. One can only conclude that the detailed landscape that the robot will transverse will also be diverse. This guesswork should be improved once the Mars Orbiter maps the planet in more detail in the near future.



Figure 1.3 - Mars

Mars has the largest mountains and canyons in the solar system. Thus, one might argue that Mars also has the roughest terrain known to mankind. A volcano by the name of Olympus Mons in the region of Tharsis is 15.5 miles high and 340 miles in diameter. This is approximately 10 times the size of any volcano seen on earth. It may still be active since its lava flows appear recent. Mars also sports a canyon which dwarfs the Grand Canyon in Arizona. This canyon on Mars is about 135 miles wide, 4000 miles

long, and up to 4 miles deep [1]. Both the canyon and one of the volcanoes (far right edge) can be readily seen in Figure 1.3 which is a superposition of several Viking orbiter photographs. Just as the Grand Canyon has told us much about the history of Earth, the canyons on Mars can tell us a lot about Mars. Of course, navigating a robot in such a rough terrain is far from easy. Thus the need for a robust, intelligent, and agile robot to explore Mars is apparent since the most scientifically interesting terrain is often synonymous with the roughest terrain.

One very puzzling feature of Mars is what appears to be huge dried out river beds. Some of these are up to 60 miles wide [1]. What could have possibly flowed in these riverbeds at one time is a mystery. This is one of the most important questions that a robot probe will have to answer. Perhaps, at one time, water flowed in these huge channels. Today, it is estimated that if it were to rain on Mars, it would only cover Mars with 4/10,000ths of an inch of water [1]. However, perhaps most of the water that flowed in the rivers is now trapped and frozen in the soil. A discovery like this by a robot probe would make terraforming Mars into a habitable planet for earth life more plausible. If not, then what happened to whatever once flowed in those dried out river beds? Thus, one can see the motivation for a preliminary scientific robot probe. If some of these questions can be answered, not only would it give direction for future missions, but man can discover what might await Earth in the future.

There are those that speculate that if, indeed, there was water running in those rivers, there could have also been life. After all, they argue, there is the vital ingredient of life or carbon in the form of carbon dioxide on Mars. In addition, there is an atmosphere. Albeit, it is a weak

atmosphere which has 1/100 th the pressure of earth's atmosphere [1]. The Viking probe seemed to dash all hopes for life since it discovered the oxidizing agent that gives Mars its red hue and kills off life known to man [1]. Perhaps there are other forms of life that could have existed or perhaps this oxidizing agent was not always on Mars. The questions and puzzles are endless and a robot probe could be the first step toward answering them.

If one were to make some general observations about Mars, one would see that the southern hemisphere is heavily scared by 4 billion year old impact craters. The terrain of the northern hemisphere, on the other hand, appears to be newer and to have been reshaped by volcanoes and wind. At the boundary between the two hemispheres is a scarp with a drop of several miles. The poles have extensive sand dunes and frozen carbon dioxide and may also contain some frozen water [1]. Even if they do not, they could contain evidence of the history of Mars and its climactic changes. Drilling could give clues as to whether there was more water at one time, what the atmosphere was composed of, and other climate facts.

In comparing Mars to Earth, it is seen that Mars is 1/2 the diameter and 1/10 th the mass. Due to the lower mass and a 1/4 lower density, Mars has a gravitation pull which is 3/8 ths that of earth [1]. Although a lower gravity might appear to make climbing rocks easier for a wheeled vehicle, it must be remembered that the vehicle also loses tractive pull or the ability for the vehicle to propel itself forward. Mars' year is 687 days and its day is 24 hours and 37 minutes [1]. Perhaps, as a promotional campaign to live on Mars one day might be the added attraction of sleeping an additional half hour ! The angle of inclination of Mars' axis is very similar to earth. Hence, it has analogous seasonal patterns.

Mars presents engineers with some very difficult problems with respect to a robot probe. Firstly, as already discussed, Mars is probably very rugged. In particular, the areas of scientific interest are usually extremely dangerous. If not dangerous, there may be bitter cold at areas of interest such as the poles. It is thought that temperatures at the poles can reach -220 °F [1]. At these temperatures, martensitic steels become brittle and fail in fatigue or impact [2]. Particularly devastating is thermal fatigue. The temperature as measured by the Viking probes can swing from -220 °F to a balmy 70 °F [1]. The thermal stresses that can result are obviously enormous. Polymers become hard and brittle as well. Kevlar and silicone seem to work well at low temperatures while oil and grease can tolerate only about -65 °F. Hence the robot needs either a solid lubricant such as teflon or molybdenum disulphide or a way to heat the lubricant [2]. Perhaps this can be done by using the heat dissipated by the RTG's (radioisotope thermoelectric generators).

Besides the high temperature gradient and rugged terrain, Mars radiation could cause computer difficulties. Since it takes 25 minutes to get a signal from Mars to Earth and back [3], the robot will be, by necessity, nearly autonomous. This requires extensive computer power which is the problem. Radiation hardened computers are only available with technologies which are otherwise obsolescent [3]. Hence, the robot would need to carry a heavy load of computers especially when taking into account radiation shielding. This could weigh down the vehicle and limit its cargo capacity.

One final problem that the inhospitable planet of Mars contains are the dust storms. Dust tends to be able to get into every joint which would, in turn, cause an abrasive wear and lead to failure. The Viking probes

measured these storms with winds of up to 40 mph [1]. That could be enough to blind the vehicle for days on end during a storm. The current plan is to send up several minirobots (about 1/2 meter in length and 5 kilograms) so that if a couple microrobots fail, the mission does not fail. For smaller robots, solar power becomes more attractive. This would extend the vehicle's life beyond a power consumption criterion as long as there was enough sun. The dust storms, however, not only block the sun, but could damage these collectors. For this reason, and since RTG units are still deemed more practical, RTG's are planned to be used.

Before proceeding to discuss some of the current designs and concepts for possible rovers, it can be seen that there is a lot to learn from a mission to Mars. Waiting to be discovered is the history of Mars, the composition of its soil, what flowed in the riverbeds, what can the poles tell us, and whether the planet can be terraformed for mankind. To answer these scientific questions, a robot probe must face a planet which presents engineers with many challenges. Mars is very rugged, has a large temperature gradient, low temperatures, dust storms, radiation, and it is a great distance from earth in terms of delivery and communications.

The first step in any engineering project is to understand the problem. This is difficult since Mars is only known to 200 meter resolution. Although this will improve with the planned Mars Observer mission, it will still not be the less than 1 meter resolution necessary to see what the rover will actually face. Therefore, one can only guess the local terrain features that the robot might face. As a result, there are no real concrete standards by which to evaluate different designs.

SECTION 1.3 - ROVER DESIGNS

Until recently, NASA was actively funding several contractors in a competition for a suitable robot to go to and transverse Mars. Due to budget constraints, the MRSR (Mars Rover Sample Return) program has been curtailed to include only the Ambler project at Carnegie Mellon University, and the rover project at JPL (the Jet Propulsion Laboratory) in Pasadena California. This is augmented by a handful of determined graduate students.

Although the exact details of the Martian landscape are unknown, NASA originally set a criteria that the vehicle or walker should be able to meet. It should be able to climb a 1 meter step, cross a 1 meter crevasse, and travel 100 to 200 kilometers in 300 days with an average speed of 0.14 m/sec [4]. Its mission would be to perform a variety of scientific experiments and collect soil samples which would be returned to the lander. Part of the lander would then leave the robot and lift off Mars to join the orbiter which would, in turn, head back to earth. With this in mind, two designs will be discussed in some detail. This is discussed to give a little background to the project, and to compare the advantages and disadvantages of a wheeled vehicle as compared to a walker.

The wheeled vehicle that will be focussed on is the FMC rover, while the focus for a walking machine will be the Walking Beam. The Walking Beam was sponsored by JPL. A preliminary design was done by Martin Marietta Corporation and Dr. Kenneth J. Waldron at Ohio State University, and a 1/4 scale prototype was built by Martin Marietta [2]. The FMC corporation did a preliminary design and study of the FMC rover, but no prototype was built [3]. Other robots such as the Ambler, and the WAAV will also be mentioned, but in less detail.

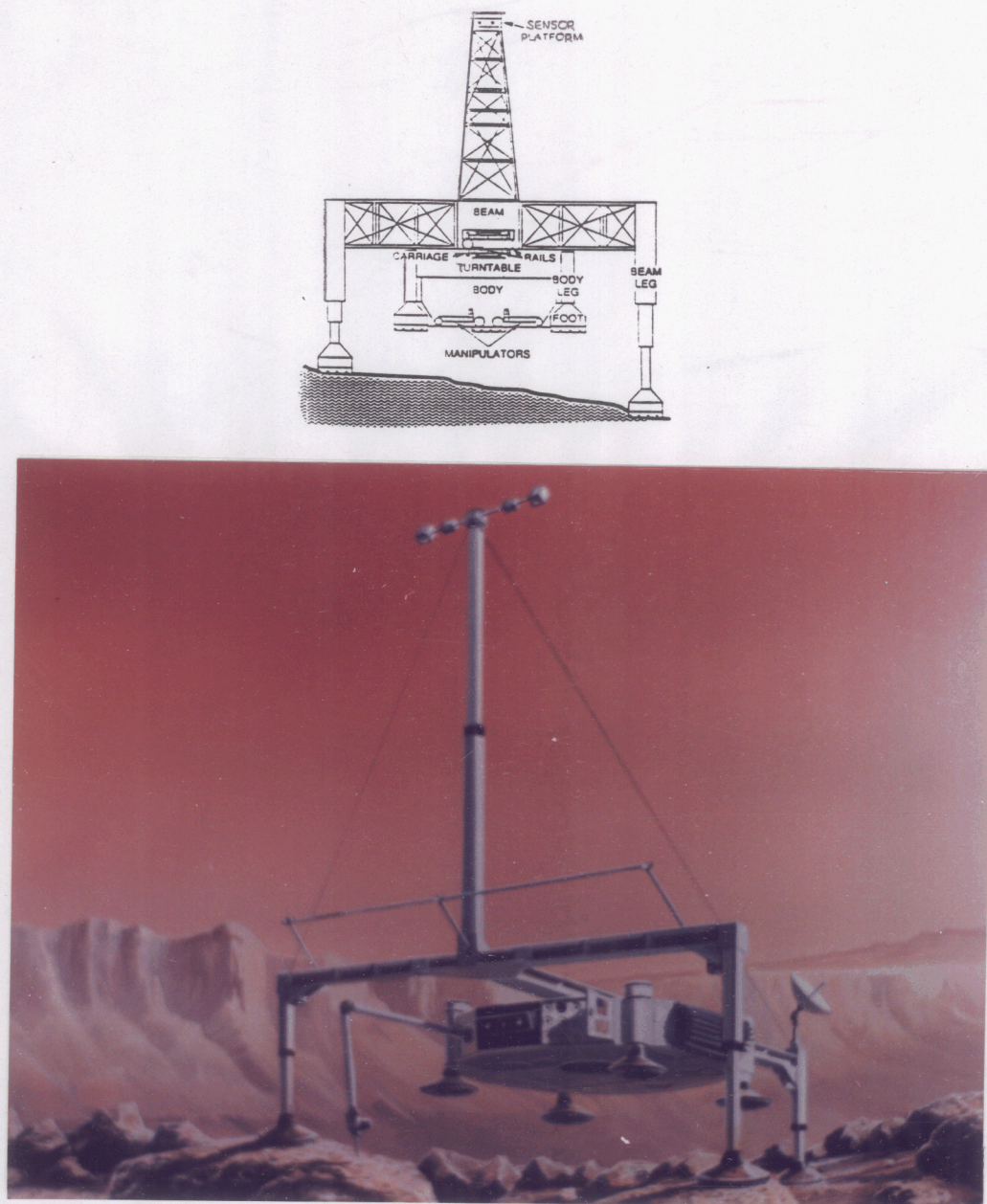


Figure 1.4 - Walking Beam

The Walking Beam, as shown in Figure 1.4, is composed of essentially two parts, the body and the beam. The beam is the outer support structure, which if one were to connect the legs with a straight line would form an equilateral triangle with sides 6 meters in length [2]. At the top of the

beam is contained the laser range finders and/or stereo cameras to be used to determine what is ahead. The smaller inner part is the body. The body is the heart of the Walking Beam and contains all the computers, scientific instruments, two sampling arms, articulated sensors, and the power supply. The power comes from RTG's. The body was originally a tripod (three legs) like the base, but it was decided to go to a quadruped body (four legs) after theoretical studies and the 1/4 scale prototype demonstrated that this greatly improved the stability of the vehicle [2]. Some of the following figures will show a tripod for the body, as it was originally designed.

Forward motion of the Walking Beam is accomplished by relative motion between the two parts (the body and beam). As is shown schematically in the top and side views of the Walking Beam in Figure 1.5, the body's legs are retracted (vertical motion), and it is moving along the rails of the beam (horizontal motion). It is actuated by means of a DC brushless motor, rollers, and a cable pulley system [2].

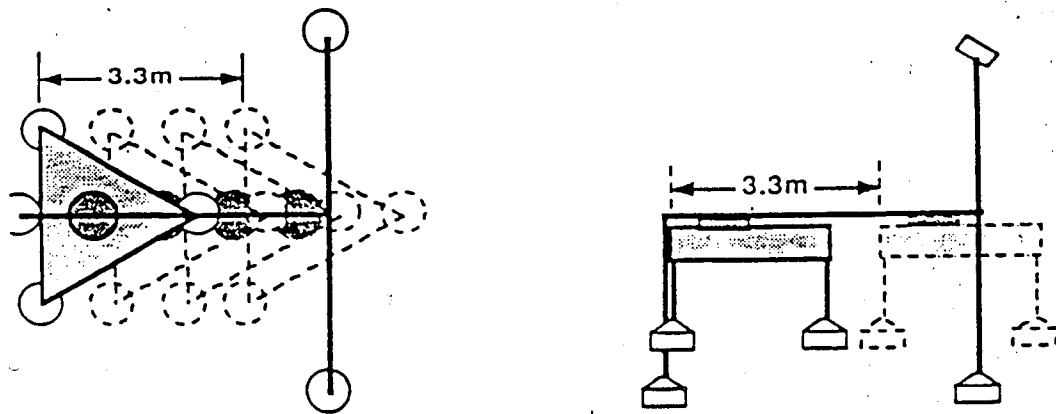


Figure 1.5 - Body translating

Once the body has reached the end of its motion (about 3.3 meters), the body legs extend to support the robot. The legs on the beam retract, and the beam moves on the same rail with respect to the body as is shown schematically in a top and side views in Figure 1.6.

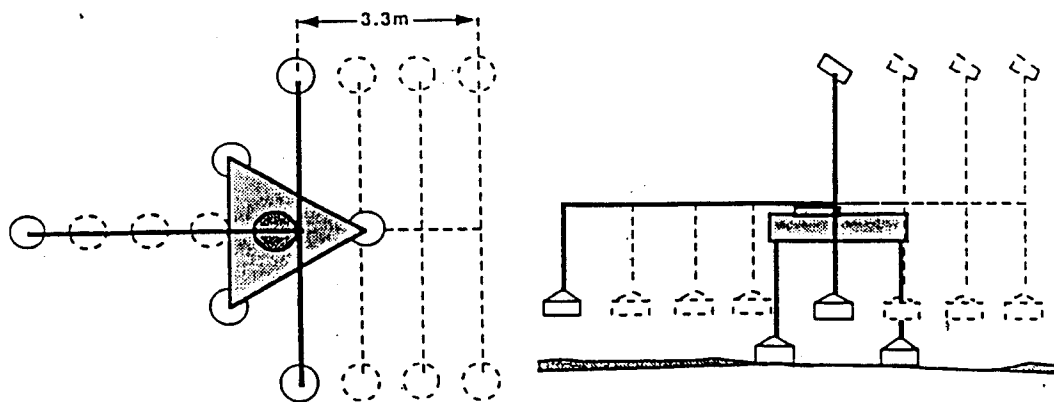


Figure 1.6 – Beam translating

This is a simple walking machine since the horizontal and vertical motions are decoupled. That is to say, the vertical motion, such as the body legs retracting, does not occur at the same time as the horizontal motion or the relative motion between the body and beam. This simplifies the equation of motion and the complexity of control. In the preliminary design, a full step of 3.3 meters takes about 2 minutes [2]. Hence, the vehicle travels at about 2.6 cm/sec or 820 km/year. It would take the Walking Beam three months to travel the required 200 km.

Much work was done on the stability of the Walking Beam. Dr. Waldron's graduate student, Samir Bhargava, looked at what type of slopes

the robot could navigate. Different factors such as the size of the vehicle, the height of the vehicle, the mass of the body with respect to the beam, and the travel distance along the rail all effect the stability of the Walking Beam [5].

The vehicle is turned by means of a turntable as shown in Figure 1.4. Again, using a cable pulley system, the body can be rotated on conical rollers with respect to the beam. A cable pulley system is used to avoid backlash as seen by gears as well as to reduce weight [2]. This turning motion can be coupled or can occur at the same time as the horizontal motion of the body on the rail. When the body then puts down its feet and the beam retracts its legs, the beam rotates through the same amount by means of the turntable, and the turn is complete. This enables the Walking Beam to turn in place and is one of its virtues.

In all, the Walking Beam has nine degrees of freedom. There are seven degrees of freedom in the three segment telescoping legs. Each of these legs are retracted and extended by a separate pretensioned cable pulley system and a DC brushless motor. The cables are driven positively for both extension and retraction by a redundant cable pulley set up. The other two degrees of freedom are the horizontal motion along the rail and the turning of the turntable [2].

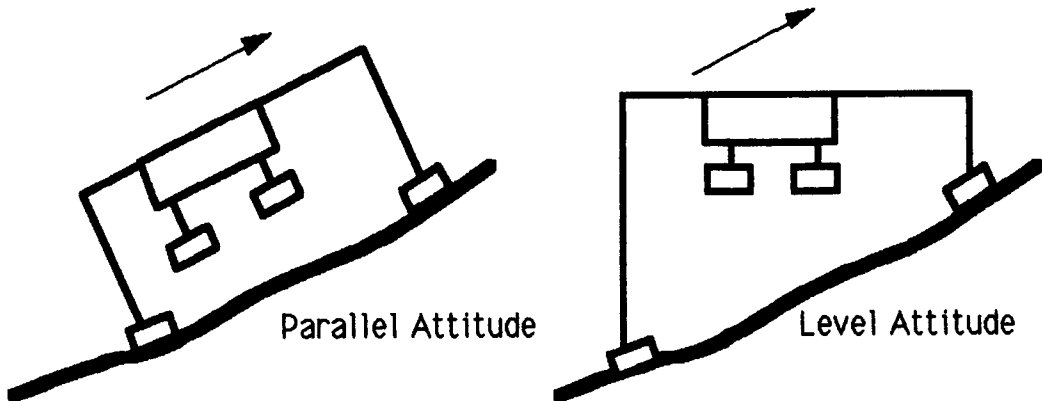


Figure 1.7 - Two modes of operation

As shown in Figure 1.7, the Walking Beam can operate using two attitude control strategies, the parallel attitude mode (parallel to the ground), or the level attitude mode (perpendicular to gravity), or using intermediate attitudes. Both strategies have their advantages and disadvantages. For the parallel attitude mode, the vehicle requires less leg length, which could save about 160 kg in weight. It can, in addition, climb steeper slopes. The disadvantage would be that the scientific instruments are not level, it is less stable, and the legs would see higher side loads. For the level attitude mode, more stability is obtained, lower, if any side loads result, and the scientific equipment in the body is level. However, it results in longer legs which add weight, and it cannot climb as steep a slope [2].

Another very different concept of a Mars robot is the FMC rover. FMC was awarded a contract in October 1987 by JPL to study the design of a rover. They chose to design a six wheeled vehicle as shown in Figure 1.8. The FMC rover is 4.52 meters long and 2.1 meters wide [3]. This makes it 1/3 the width of the Walking Beam and 1 meter shorter.

The FMC rover can be broken up into three segments. The front contains a robot arm, batteries, roll bar, SLV (Structured Light Vision), and

stereo cameras for mapping. The middle section has 6 to 7 cubic feet reserved for a science package as well as a retractable communications disk. Finally, the rear contains the RTG units for power as well as a roll bar [3].

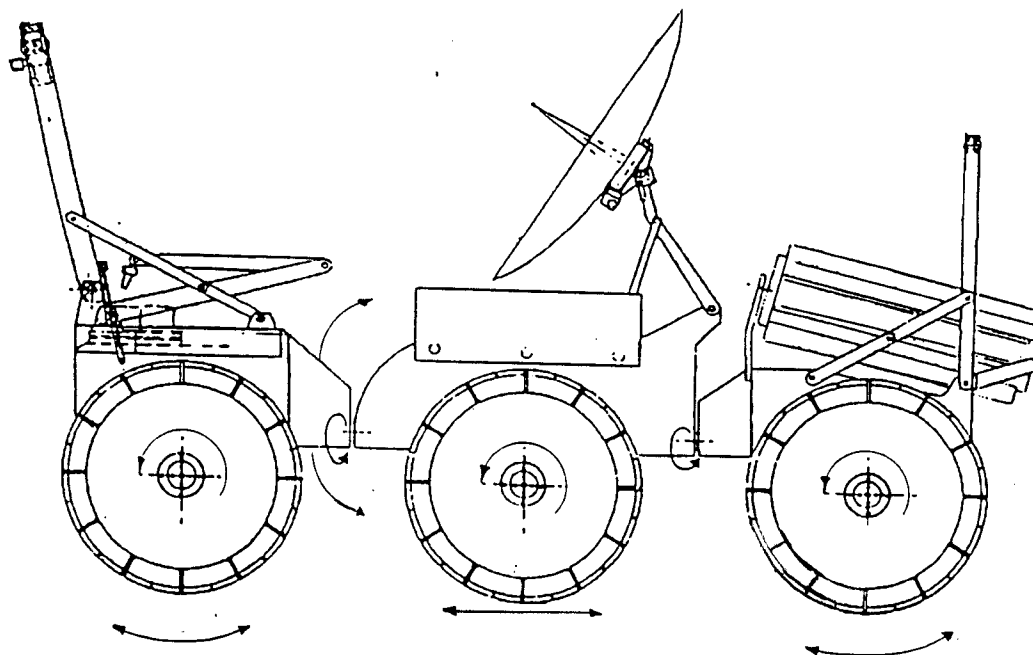


Figure 1.8 - FMC rover

The degrees of freedom of the vehicle are sketched on Figure 1.8. Each of the six wheels are independently driven by a motor concentric with the tire. This allows for some redundancy in case some of the wheel motors fail. The front can be pitched up and down by 55° with an actuator [3]. This is illustrated in Figure 1.9 as the vehicle surmounts a step. Once the front tire has cleared the step, the pitch motor is powered down to lift the second

wheel over the step with the third wheel to follow. In this manner, the vehicle can surmount a 1.3 meter step [3] while the Walking Beam can overcome a 1.7 meter step [2].

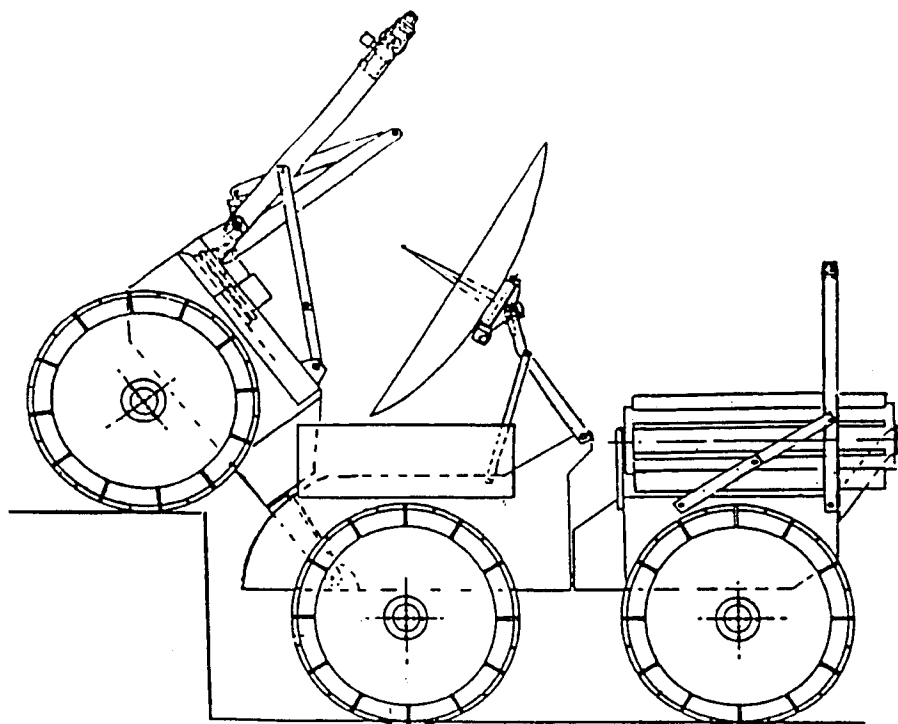


Figure 1.9 – Surmounting a step

Each segment of the vehicle can roll with respect to the other segment so as to maintain a constant force on each wheel on an uneven terrain. This minimizes slippage and energy consumption. The roll degree of freedom also allows the vehicle to upright itself in the event of a roll over. This is illustrated in Figure 1.10 where the vehicle is tipped over on to its left side. To overcome this, the middle module first rolls into an upright position. This is possible since the rover's middle axle is shorter than the front and rear axle. Next, the pitch axis is activated which puts the

front section in the air and the middle tires on the ground. The front can then be rolled upright into place. Next the middle axle moves backwards relative to the middle module (this is another degree of freedom). This increases the front lever arm and, hence, puts the front tires on the ground and the rear tires up in the air. Finally, the rear tires can be rolled upright, the pitch set to put all the wheels on the ground, and the vehicle is ready to go [3].

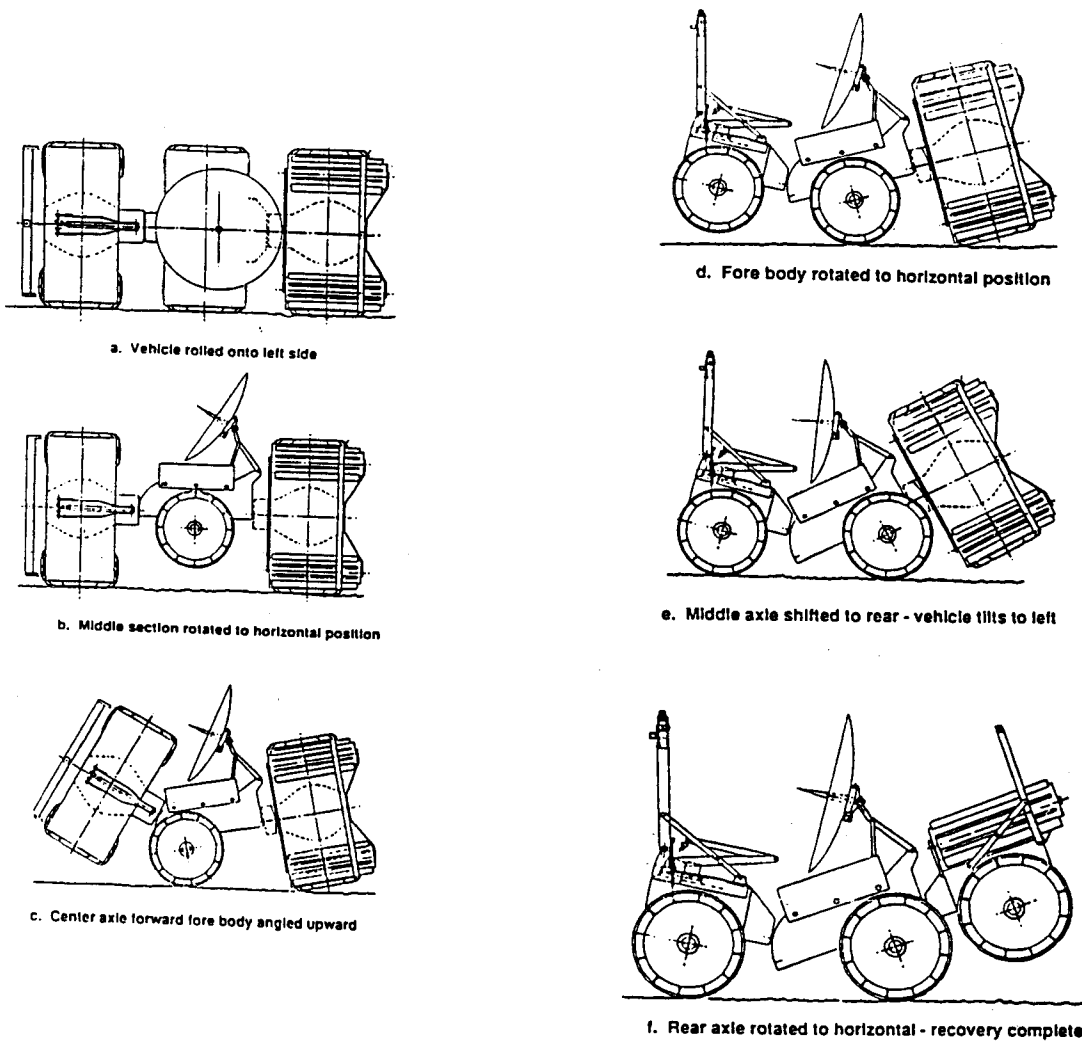


Figure 1.10 - Roll over recovery

The motion of the middle axle aids its crevasse crossing ability. First the middle axis is driven all the way forward to make the back a stable base. The front wheel is then driven to the other side of the crevasse where it checks the soil. If the front wheel sensors indicate that it is safe on the other side, the vehicle begins to drive over. Once the middle axle has crossed the crevasse, it begins to move backwards so as to make a stable base using the front four wheels [3].

The vehicle can be steered in a number of different ways. Normally it is turned by driving the wheels on one side of the vehicle faster than on the other side. This method consumes a lot of energy. Another redundant way of steering is to pivot the rear and front axles as shown in Figure 1.11. A final method of steering is shown in Figure 1.12. Here the vehicle balances on its center axle by shifting the middle axle to the center of gravity and activating the pitch axis. By driving one of the middle wheels forward and the other backwards, the vehicle can turn in place [3]. The redundant number of steering techniques is a virtue of the rover. If the vehicle cannot turn around it cannot get back to the lander and the mission has failed.

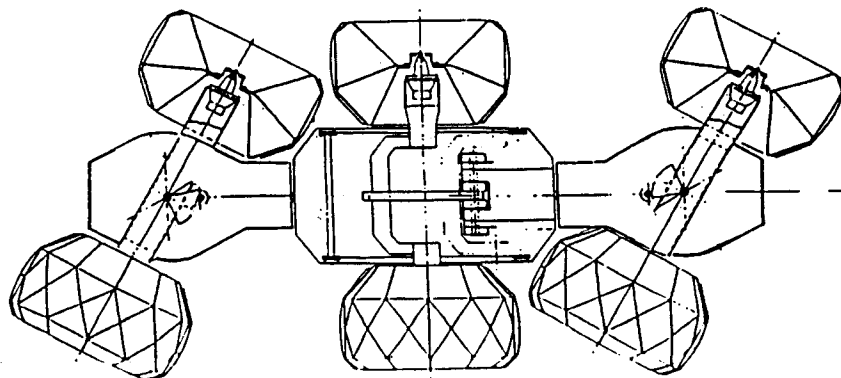


Figure 1.11 - Steering method two

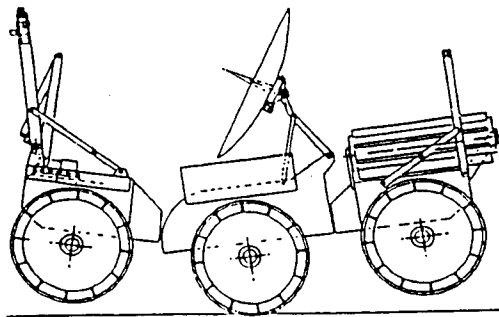


Figure 1.12 - Steering method three

In comparing the two robots, we see firstly, that unlike the FMC rover, the Walking Beam is able to keep the cameras and scientific equipment stationary and level for some time. This can be accomplished even as the vehicle is moving forward. The cameras are stationary when the beam legs are down and the body is moving while the scientific equipment is stationary when the body legs are down and the beam is moving. Both are level if it is operated in the level attitude mode. This facilitates the mapping of the surrounding terrain and the ability to conduct scientific experiments. The walker's navigation system is also perched higher up on a mast and can see farther than the one on the FMC rover. For the FMC rover, the scientific equipment would be subject to random motion at all times the vehicle is in motion and it would also see some vibration. This leads to difficulties in navigation since the cameras are moved up and down with the terrain. As a result, the wheeled rover has to be somewhat faster to accomodate a 'stop and look' strategy. In addition, the added vibrations,

which a walker does not experience, can add to vehicle and equipment failure due to fatigue and impact.

Some other advantages of the Walking Beam are that it can clear a 1.7 meter step and 3 meter crevasse [2] versus the 1 meter step and 1.3 meter crevasse transversible by the FMC rover [3]. As far as power consumption is concerned, there is often less soil work for a walking machine which cuts down on the walker's power consumption. It is also easier to seal the joints of the walker from dust as compared to the rotating joints of the rover [2]. Finally, the walker has nine degrees of freedom which is three less than the FMC rover.

It would seem from this analysis, that a wheeled vehicle would not be a good choice for the Mars mission. Nonetheless, the rover has many good points, too. The rover can move at least 3 times as fast as the Walking Beam which would normally allow it to cover more terrain. This could, however, be offset by its 'stop and look' strategy. Perhaps, since the walkers are better equipped to handle rougher terrains, a walker can be sent to the more challenging terrain. The wheeled vehicle can be used for the flatter terrain where it can cover more ground than the walker. The rover is also more compact, and therefore, transporting it to Mars would be less costly. Techniques have been devised to store the walker in a compact manner and unfold it once it gets to Mars. However, this adds one more thing that can go wrong. Already the failure to unfold the Galileo antenna has been witnessed. The rover, on the other hand, can simply drive off the lander already deployed. Thus, in light of the Galileo and other satellites that have failed in the deployment of solar panels, antennas etc..., the already deployed rover is perhaps its most significant advantage.

The FMC rover also has three redundant steering strategies as opposed to the one of the walker. As already mentioned, if the vehicle cannot steer, it cannot get back to the lander, and the mission has failed. In addition, the FMC rover has six wheels to propel it. If some of the wheel motors fail, the transmission can be put into neutral for those wheels, and the mission can proceed with a slightly degraded climbing ability. If this is not a viable solution, the wheel with the failed motor can be lifted clear of the ground. It is hard to say if the rover has a better survivability than the Walking Beam in this respect since the Walking Beam can operate on as few as three operating legs. Some other advantages of the FMC rover are that it is more compact and can therefore fit through narrower channels. It is stiffer, and hence, has a higher natural frequency, and it can recover from a rollover unlike the Walking Beam. To be fair, however, the rover is more likely to roll over than the Walking Beam.

As one can see both robots have advantages and disadvantages. It is hard to say which one could carry out the mission more effectively. Perhaps the answer is that it depends on what type of terrain the vehicle faces. Of course, the catch 22 is that the specifics of the terrain will not be known until the robot arrives.

There are many other designs of possible martian rovers. Carnegie Mellon University, has a full scale working prototype of a walker called the Ambler. Motion is attained by first retracting the rear legs in a telescoping manner in the vertical direction. These legs then move in an arc through the center of the walker to the front while the other four legs maintain a stable base. Once these legs extend and are place firmly on the ground, the body advances and the process is repeated [6]. This project is still being funded.

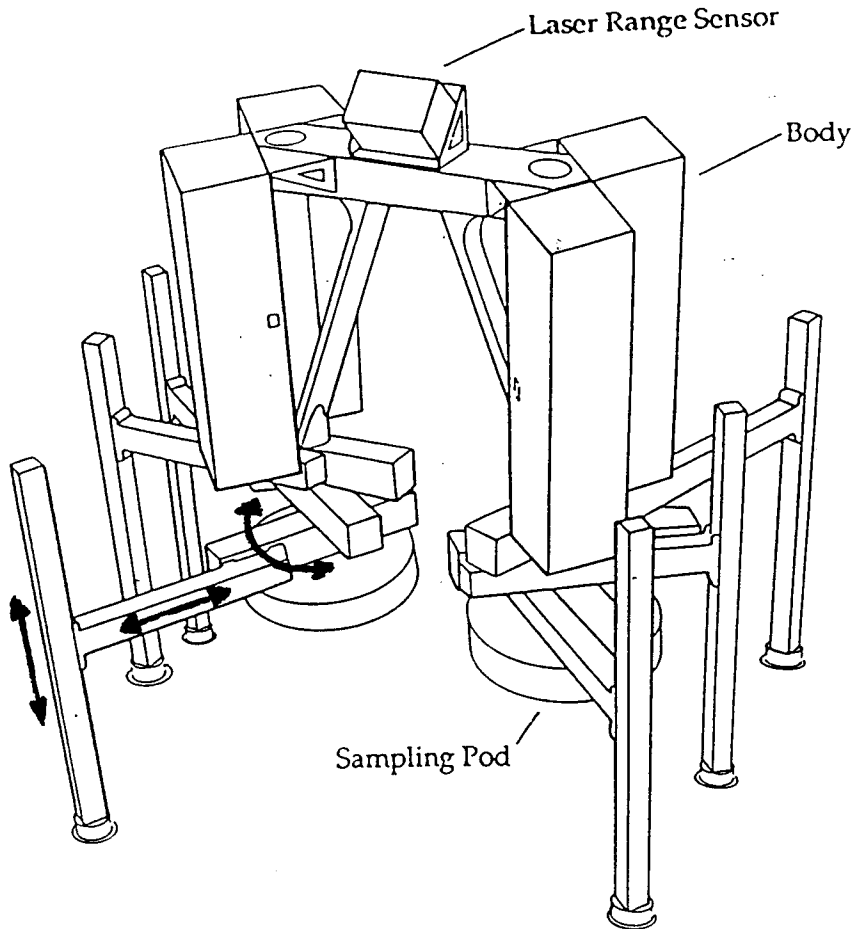


Figure 1.13 - Ambler

The WAAV was studied by Dr. Waldron's graduate students Siglagata Sreenivasan and Jason Yu. It is similar to the FMC rover except that the joints between each module have three degrees of freedom (roll, pitch, and yaw) and the middle axle remains stationary with respect to the middle module. A computer simulation package similar to the one to be developed for the Rocker Bogie in this thesis has been developed for the WAAV by Sidlagata Sreenivasan [7]. A scaled down model of the WAAV was designed by Jason Yu and is in the process of being assembled at Ohio State University for testing in the near future [8].

SECTION 1.4 - ROCKER BOGIE

The Jet Propulsion Laboratory is also working on a six wheeled vehicle called the Rocker Bogie or Rocky for short. The one thing that the Rocker Bogie, the FMC rover, and the WAAV all have in common is that they each have six wheels independently driven by motors concentric with the tire. However, as is shown in the third prototype photographs of Plate I, the Rocker Bogie diverges from there. In addition, since the time that the FMC rover has been designed, the design criteria of the vehicle have changed due to budget cuts.

NASA is now calling for minirovers (about 1/2 meters in length) that weigh under 5 kilograms. This would allow NASA to send up several, possibly four, of these robots and increase the probability of success of the mission. That is to say, if a couple of robots fail, the mission does not fail. The smaller vehicles would also greatly reduce the cost of the project since the delivery system could be scaled back. At the same time, due to the limited cargo space on the minirovers, the amount of scientific equipment and room for soil samples will be very limited. The rover will also not be able to travel the 200 km originally planned [4], and may only go a couple of kilometers. Finally, the rock climbing and crevasse crossing capability of the vehicle will also be greatly reduced. Just what the performance of these vehicles are is the objective of this thesis.

Unlike the FMC rover and the WAAV, which are both segmented into three modules, the Rocker Bogie has only one body. As is seen in Plate I, the body contains a computer, a manipulator for picking up rock and soil samples, a communications antenna, and a battery pod underneath the

Plate I - Rocker Bogie prototype

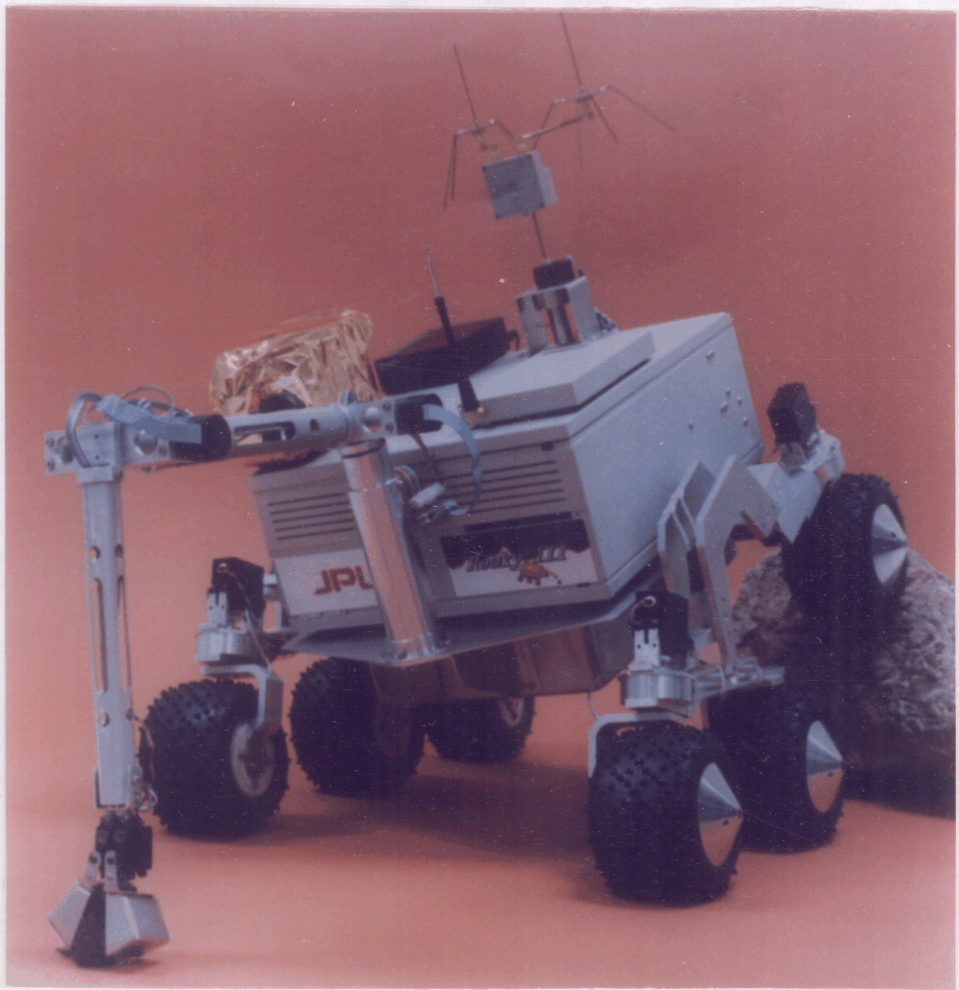


Plate II - Rocker Bogie without body



computer. The actual vehicle will probably carry RTG's instead of conventional batteries. Plate II is the same as Plate I, but with the body removed. As seen in Plate II, the body sits on a differential whose purpose is to maintain the body at the average of the two beam angles. This is illustrated in Figure 1.14. In this manner, the body remains more nearly parallel to the ground at all times. As is seen in Plate II and labeled in Figure 1.14, the beam is the piece which the differential shaft passes through and which connects the rear wheel to the bogie which carries the front two wheels. The connection between the beam and the differential shaft serves as a passive or unpowered hinge. The beam is, in turn,

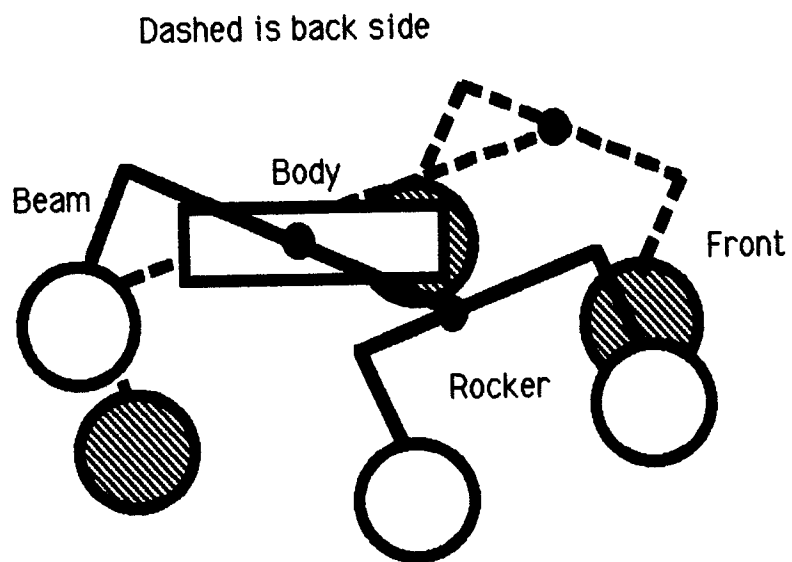


Figure 1.14 - Effect of Differential on body

connected to the rocker by means of another passive hinge. As labeled in Figure 1.14, the rocker is the piece which connects the two front wheels. One of the parameters to be varied on the model will be the positioning of these hinges. For example, how is the rock climbing ability of the Rocker Bogie affected as the rocker's passive hinge is moved farther back?

Instead of the straight axles on three body segments of the FMC rover and WAAV, the Rocker Bogie has one body with the wheels connected in a bogie arrangement. Donald Bickler at the Jet Propulsion Laboratory received the inspiration to build the vehicle when he read in Bekker's book Introduction to Terrain Vehicle Systems [9] that one particular vehicle arrangement had climbing characteristics almost as good as a bogie. "Well", said Don Bickler, "Why not just use a bogie"? That is indeed what he did. Old trains and trucks used to use a bogie in the reverse direction from that shown in Figure 1.14. In other words, the rocker was in the back and not the front. Manufacturers lost interest in this arrangement since it caused instability at high speeds particularly in braking maneuvers. The Rocker Bogie, however, will only travel at about 5 cm/sec. This speed is low enough not to be concerned with the instability of the bogie arrangement and to take advantage of its superior rock climbing characteristics.

Unlike both the WAAV and the FMC rover, the Rocker Bogie cannot have any part move about the roll axis with respect to another. The vehicle can only move in roll as a whole as illustrated in the front view of Figure 1.15. As a result, only the edges of the tires will contact the terrain in particular maneuvers. In addition, unlike its two cousins, it cannot maintain an equal normal force on each tire. That is a direct result of having no control on the passive hinges and of not having the ability to roll one segment of the

vehicle with respect to another. In the event of a rollover, the Rocker Bogie would not be able to recover like the FMC rover. Thus, one can see the extreme importance of being able to determine if the terrain is safe to navigate before actually attempting it.

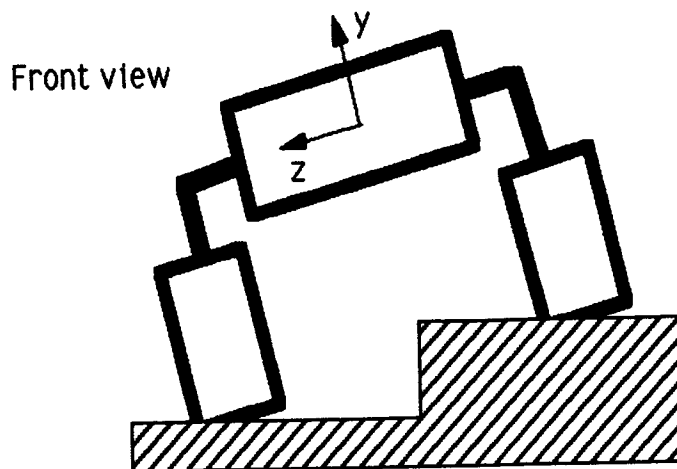


Figure 1.15 – Front view illustrating roll

Besides the rollover problem, it would seem, at first glance anyway, that the Rocker Bogie has a better survivability. This is due to the smaller number of powered or actuated parts than the FMC rover or the WAAV. This was accomplished by replacing active or powered joints with passive joints. In actuality, the Rocker Bogie has 10 powered joints or only two less than the FMC rover. The powered joints are the six wheels and the four steering actuators for the two front and two back wheels. Currently, the vehicle has four wheel steer as illustrated in the top view of Figure 1.16. JPL is considering six wheel steer to better enable it to turn about its own center

of gravity. If it was to have six wheel steer, then the number of actuators on the Rocker Bogie would be the same as on the FMC rover. It would seem then that the survivability has not improved at all, and in addition, some performance characteristics, such as recovery from rollover, have been lost.

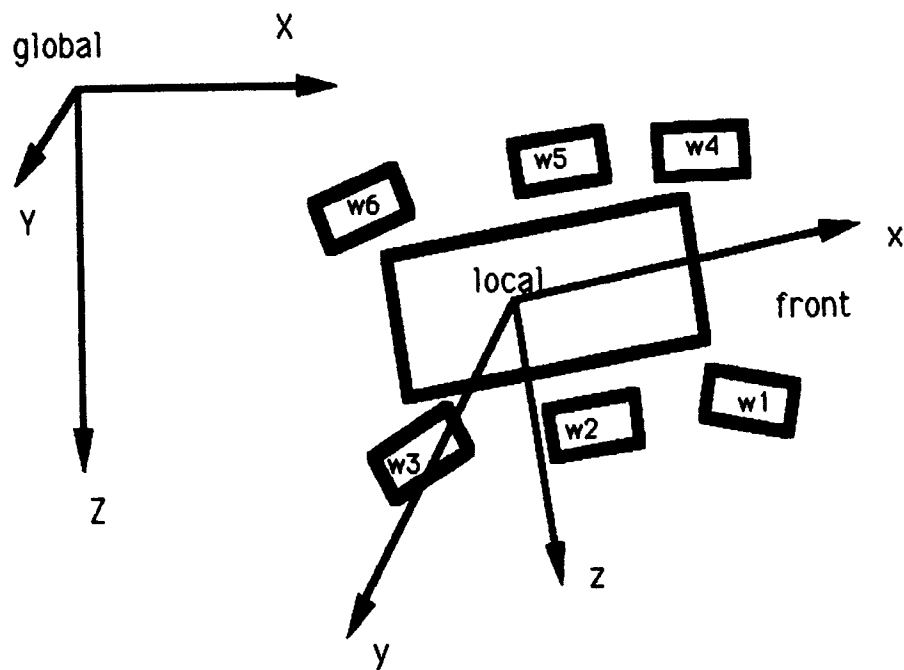


Figure 1.16 - Steering - top view

Nonetheless, the steering degrees of freedom are redundant since the vehicle has more than one way to steer. The vehicle can steer similar to a tractor by driving one side harder than the other. In addition, it can still steer similarly to a car if only two steering actuators are operating. It probably could even manage with some difficulty if only one steering actuator functioned. Hence, although the other wheeled vehicle's have a couple redundant means of steering, the Rocker Bogie has several. For these

reasons, and assuming rollover is effectively detected and prevented before it happens, the survivability of the Rocker Bogie is slightly better than the FMC rover and the WAAV.

In order to improve the vehicle's crevasse crossing abilities, mechanical stops have been added to limit the motion, or relative angular displacement, of the rocker with respect to the beam. These mechanical stops, as illustrated in Figure 1.17, are designed in the prototype to allow the middle wheel to drop one wheel radius in the event of a crevasse, and the front wheel to drop one wheel radius in the event of a downward step. These mechanical stops will be varied in the program to determine how they affect performance.

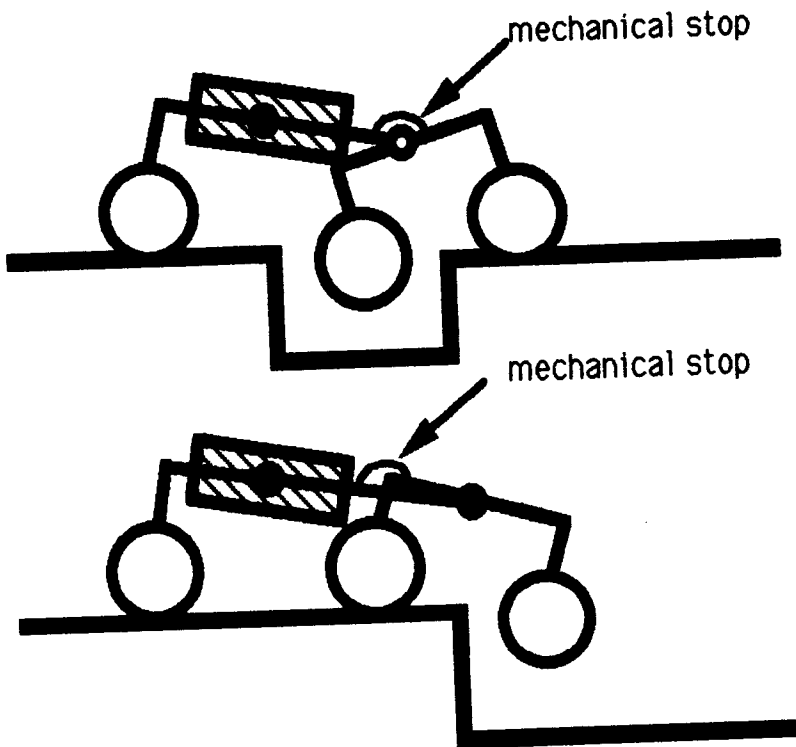


Figure 1.17 - Schematic of mechanical stops

The coordinate system to be used in this report, which is different from SAE standards, is illustrated in Figure 1.16. The global frame, which is indicated by capital XYZ, has the Y-axis parallel to gravity and the X and Z-axes perpendicular to gravity. The local frame, which is indicated by small xyz, is located at the center of gravity of the body and has its y-axis parallel to gravity plus or minus any vehicle roll. The local x-axis is in the direction of forward travel and perpendicular to gravity. Obviously, the local z-axis is perpendicular to the other two axes. Finally, as a formality, the mobility of the Rocker Bogie is analyzed below using the Kutzbach constraint Equation 1.1.

$$M=6(m-j-1) + \Sigma f \quad (1.1)$$

members

$m = 16$ --- 6 wheels, 2 rocker bogie sections, 2 beams
 4 steering devices, 1 module, 1 ground

joints

$j = 20$ --- 6 wheel-ground contacts, 6 axle-wheel joints
 2 rocker bogie pivots, 2 body joints, 4 steering joints

DOF of joints

$\Sigma f = 32$ --- 3 at each wheel contact = 18, 6 wheel joints, 4 turning pivots,
 2 rocker bogie pivots, 2 body joints

mobility - DOF of linkage

$M = 2$ --- actually $M = 1$ since the body and beam angles are dependent on
 one another through the differential.

CHAPTER II

KINEMATICS

SECTION 2.1 - THE TERRAIN MAP

The first problem tackled was, given the position of wheel one (see Figure 1.16), where are the positions of all the other tires and the angles of all the joints. Before this problem can be solved, the terrain map and the method of steering must be discussed.

The user 'specifies', through an input file, what type of terrain he wishes to run the vehicle over. The terrain is actually generated in a random manner, but the user still has control over some parameters. The user controls the size of the terrain plot (L), the unit mesh size (U), and the maximum relative peak size (P_{\max}). This is illustrated in the top view of the terrain in Figure 2.1. At each of the mesh crossings or nodes, the computer 'randomly' selects a relative peak size using Equation 2.1 where the variable R is a random number from -1.0 to 1.0 and i and j are the global X and Z coordinates for a particular node. It is actually a pseudo random process since the user can also specify the seed value for the random generator. If the seed is left the same, it will give the same terrain

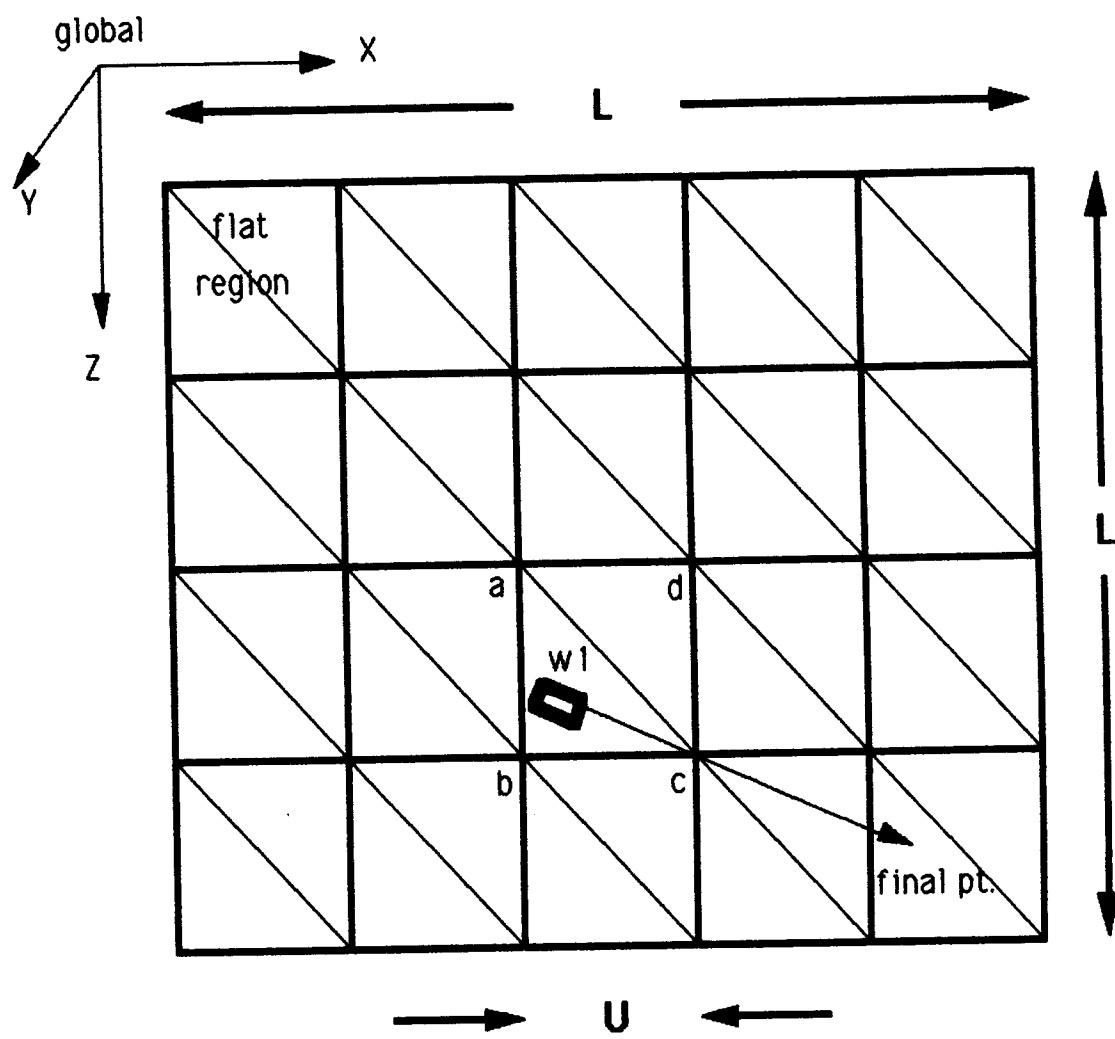


Figure 2.1 - Top view of terrain map

$$P_{ij} = \left| P_{\max} R + \frac{P_{i-1,j} + P_{i,j-1} + P_{i-1,j-1}}{3} \right| \quad (2.1)$$

for each run providing the variables L and U are kept the same. This is handy for comparing two different vehicles on the same terrain.

Equation 2.1 shows that the peak size, or the global Y coordinate at a particular node, is a random variable plus the average of three adjacent nodes. For example, in Figure 2.1, point c has a height equal to a random number, whose maximum absolute value is specified by the user, plus the average of the heights of points a,b, and d. Using this method, large inclines and declines result as opposed to a number of jagged peaks and valleys that occur if the average of the adjacent points are not added. In order to begin the process, the left and upper borders of the terrain are all set to 1.0 meter in height. In addition, all the mesh points that lie in a 3.0 meter by 3.0 meter square at the top left corner of the terrain, or at the origin of the global frame, are set to 1.0 meter in height. This allows the user to start on flat ground if desired.

By varying the unit mesh size and peak size, many different types of terrain can be realized. Increasing the maximum relative peak size (P_{max}) will obviously give steeper slopes. Decreasing the unit mesh size (U), on the other hand, will give a more jagged or faster varying terrain. If the unit mesh size is 1.0 meter and a 10.0 by 10.0 meter terrain is specified, there will be 121 (or 11^2) heights specified. If a more jagged terrain is desired, a 0.5 meter unit mesh size could be chosen which would give 441 (or 21^2) heights specified in the same terrain. By cutting the unit mesh size in half, a terrain that is about 4 times as jagged results. Making the unit mesh size too small and the terrain size too large will result in the computer crashing since there are too many random numbers to generate. In order to prevent this from happening, the proportion L/U is monitored. If this proportion

exceeds 300, the program warns the user to select a smaller terrain plot and/or a larger unit mesh size.

The terrain map also randomly sets 1/3 of the terrain as rock with a coefficient of friction of 0.8 and the other 2/3 as sand with a coefficient of friction of 0.3. The ratio of rock to sand on Mars was determined by taking thermal inertias using Viking's Infrared Thermal Mapper as discussed in the paper Preliminary Mars Surface Models by Henry J. Moore [10]. By defining a rock to be a surface that gives a thermal inertia of $30 \text{ kg-m}^2/\text{K}$ (a rock of about 0.1 meter on edge), it was determined that the modal value of the surface rock cover on Mars is 6% of the total surface area. In the worst case, or in particularly rough areas, rock covers 35% of the Martian surface [10]. Hence, the worst case scenario of 1/3 of the terrain covered by rock was used in the terrain model.

In order to determine whether a particular tire is on a rock or sand terrain, the first step is to determine which node the tire is closest to. The terrain under the tire takes on the terrain characteristics of that node. For example, wheel one as shown in Figure 2.1 is closest to point b. If mesh point b is assigned as sand, wheel one is defined to be on sand. As soon as wheel one passes the half way point between points b and c in its travel with direction shown on Figure 2.1, it will take on the terrain characteristics of point c.

Since there are only a set of discrete heights at each node in the XZ plane and a continuous terrain is required, it is necessary to linearly interpolate between the nodes. This is done by dividing the terrain into triangles as shown in Figure 2.1 and determining the equation of the three dimensional triangular plane that each tire rests on. For example, suppose

the user has specified the initial global X and Z coordinate position of wheel one (called X_1 , Z_1) in the input file as is shown in Figure 2.1. Since the tire does not in general rest on a node, the computer has to first determine which plane the tire lies in (plane abc for this case), and then it has to determine the height or global Y coordinate of wheel one (called Y_1). This is done by solving for the equation of the triangular plane using Equations 2.2 and 2.3. Using Equation 2.4 and the known X_1 and Z_1 coordinate, the tire height or Y_1 coordinate can then be solved. The equation of a plane is

$$EX + FY + GZ + H = 0 \quad (2.2)$$

Setting E=1 the following three equations for the vertices of the plane result:

$$\begin{aligned} X_a + FY_a + GZ_a + H &= 0 \\ X_b + FY_b + GZ_b + H &= 0 \\ X_c + FY_c + GZ_c + H &= 0 \end{aligned} \quad (2.3)$$

Since the positions (X,Y,Z) of points a,b, and c are known, the constants F,G, and H can be solved for simultaneously from these three equations. Using these values, the height of the tire to ground contact for wheel one is solved for from Equation 2.4.

$$Y_1 = \frac{-H - G Z_1 - X_1}{F} \quad (2.4)$$

where

$$F = \frac{-X_b Z_c + X_c Z_b + X_a Z_c - X_c Z_a - X_a Z_b + X_b Z_a}{Y_b Z_c - Y_c Z_b - Y_a Z_c + Y_c Z_a + Y_a Z_b - Y_b Z_a}$$

$$G = \frac{-X_c Y_b + X_b Y_c + X_c Y_a - X_a Y_c - X_b Y_a + X_a Y_b}{Y_b Z_c - Y_c Z_b - Y_a Z_c + Y_c Z_a + Y_a Z_b - Y_b Z_a}$$

$$H = \frac{-X_a Y_b Z_c + X_a Y_c Z_b + X_b Y_a Z_c - X_b Y_c Z_a - X_c Y_a Z_b + X_c Y_b Z_a}{Y_b Z_c - Y_c Z_b - Y_a Z_c + Y_c Z_a + Y_a Z_b - Y_b Z_a}$$

and X_1 and Z_1 are the position of wheel one in plane abc as given in the input file.

The user has not only specified the initial position of wheel one (X_1, Z_1) in the input file, but he has also set a final destination point for wheel one (X_{f1}, Z_{f1}) as well as the initial vehicle yaw angle (θ_y). The yaw angle, as shown in the top view of Figure 2.2, is the angle between the global X-axis and local x-axis. As is the case with most angles in this thesis, the right hand rule is used. In other words, counterclockwise motion corresponds to positive angles and clockwise motion corresponds to negative angles. Wheel one is pointed directly at the final destination point as seen in Figure 2.2. As the vehicle progresses, the steering angle of wheel one (δ_1) is updated to ensure it reaches the final destination. This is essentially a simple proportional controller. Alternatively, a more

sophisticated path planning scheme can be selected as explained later in Chapter IV Section 4.4.

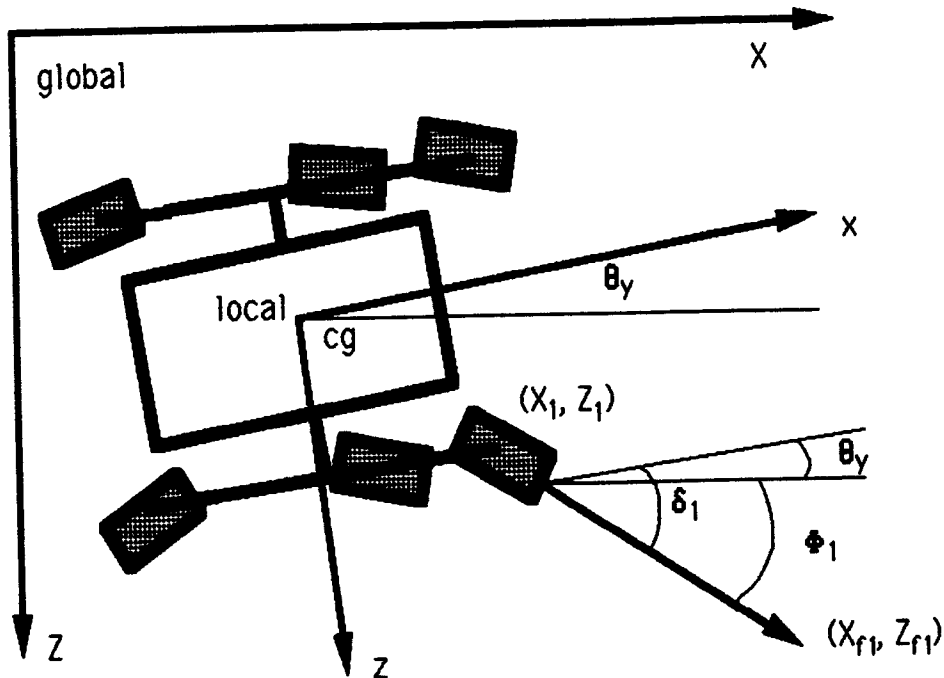


Figure 2.2 - Steering of wheel one

The steering angle (δ_1) as shown in Figure 2.2 is defined to be the angle between the plane of the tire and the local x-axis of the vehicle. To determine δ_1 , first Φ_1 , as is shown in Figure 2.2, is found using Equation 2.5.

$$\Phi_1 = -\text{ATAN} \left(\frac{Z_{f1} - Z_1}{X_{f1} - X_1} \right) \quad (2.5)$$

There is a negative sign in front of this expression since both the numerator and denominator are positive, while the angle is negative, as is shown in Figure 2.2. Since θ_y is known from the input file, the steering angle can be readily determined:

$$\delta_1 = \Phi_1 - \theta_y \quad (2.6)$$

Now, the height of wheel one's tire to ground contact (Y_1) as well as the steering angle (δ_1) are known. The heights of the other wheels' tire to ground contacts can be determined as is shown in Section 2.3, and the other wheels' steering angles can be found as is shown in Section 2.2.

First, there is more information needed about wheel one. The contact angle of wheel one (λ_1) needs to be determined. The contact angle is defined as the angle with which the tire-ground contact normal makes with a line parallel to gravity or alternatively to the local y-axis. This is illustrated in Figure 2.3. Notice that the contact angle is synonymous with the slope of the terrain it is contacting. Hence, a positive slope gives a positive contact angle while a negative slope gives a negative contact angle.

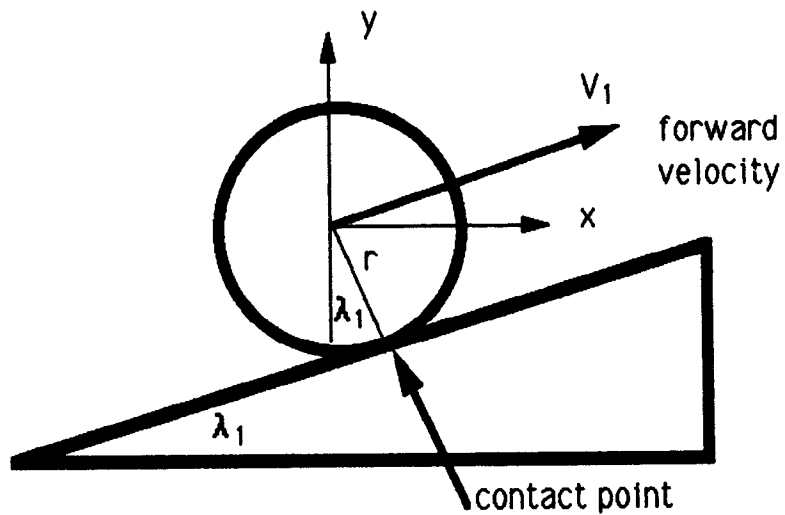


Figure 2.3 - Contact angle

Referring back to Figure 2.1, it is seen that if the tire is aligned parallel to line bc, then its contact angle is simply the slope of line bc which is defined as q_x . Similarly, if the tire is aligned parallel to line ab, then its contact angle is the slope of line ab or q_z . Since the terrain is linear, any steering angle between line ab and bc can be found by linearly interpolating.

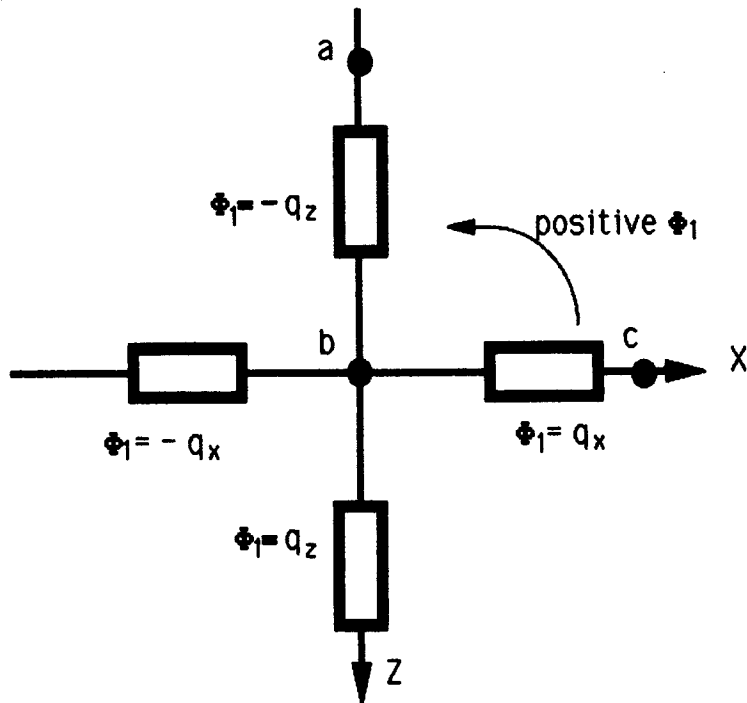


Figure 2.4 – Contact angle variation

As is shown in Figure 2.4, the contact angle changes sign as the tire rotates through 180° . This is because the contact angle is defined with the tire moving to the left as seen in Figure 2.3. If the tire is rotated by 180° , its contact point will not change, but the direction of travel changes by 180° . The contact is now in the rear of the tire instead of in the front, therefore, the contact angle changes sign.

The contact angles along the X and Z axis are as shown below.

$$q_x = \text{ATAN} \left(\frac{Y_c - Y_b}{U} \right) \quad q_z = \text{ATAN} \left(\frac{Y_b - Y_a}{U} \right) \quad (2.7)$$

Linearly interpolating with the angle Φ_1 as is shown in Figure 2.4 then results in Equations 2.8.

If $\pi/2 \geq \Phi_1 \geq 0$ then

$$\lambda_1 = q_x \left(1 - \frac{\Phi_1}{\pi/2} \right) - q_z \left(\frac{\Phi_1}{\pi/2} \right)$$

If $\pi \geq \Phi_1 > \pi/2$ then

$$\lambda_1 = -q_x \left(\frac{\Phi_1}{\pi/2} - 1 \right) - q_z \left(1 - \frac{\Phi_1 - \pi/2}{\pi/2} \right)$$

If $3\pi/2 \geq \Phi_1 > \pi$ then (2.8)

$$\lambda_1 = -q_x \left(1 - \frac{\Phi_p}{\pi/2} \right) + q_z \left(\frac{\Phi_p}{\pi/2} \right)$$

where $\Phi_p = \Phi_1 - \pi$

If $2\pi > \Phi_1 > 3\pi/2$ then

$$\lambda_1 = q_x \left(\frac{\Phi_p}{\pi/2} - 1 \right) + q_z \left(1 - \frac{\Phi_p - \pi/2}{\pi/2} \right)$$

The contact angle, steering angle, and height of the contact point of wheel one have been determined, but in the process, some things were neglected. First, both the terrain and the tire were assumed to be rigid for computation of the kinematics (see assumptions in Appendix A). These

deformations will be handled in a simplified manner for dynamics, however. For a real tire, one cannot talk about a contact point, but must instead deal with a contact patch. The assumption is that the contact point is at the centroid of the contact patch. In addition, it is assumed that the contact force at the contact point is the effective or resultant force of the distributive force at the tire patch. This force will be determined in Chapter III.

The width of the tire is also neglected in this analysis. If the width was included, the tire contacting on its edges as is shown in Figure 1.15 would have to be dealt with. The tire diameter, however, is not neglected. That is to say, if the user selects a point at a sharp corner, it may not be possible for the tire to contact there. This is illustrated in Figure 2.5.

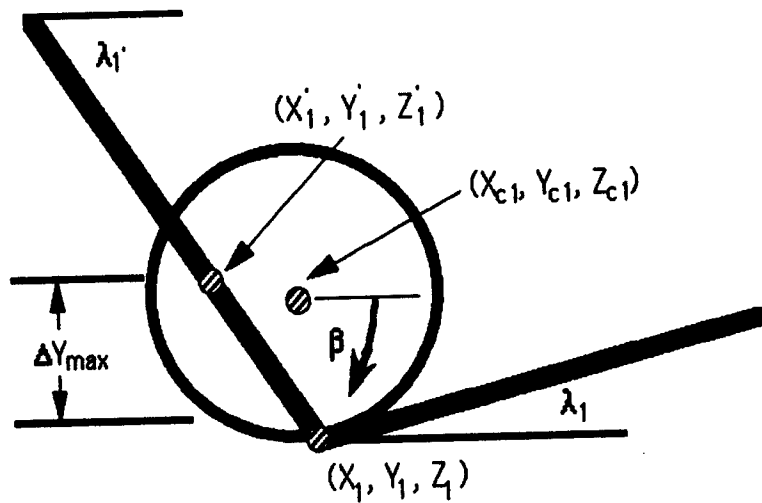


Figure 2.5 - Impossible contact

Due to the two dimensional shape of the tire, it would be impossible for it to contact at (X_1, Z_1) , particularly since it was assumed that neither

the terrain nor the tire can deform in this kinematic model. In order to rectify this, the tire is raised so that it only contacts at one point.

In order to do this, the center of the tire (X_{c1}, Y_{c1}, Z_{c1}) is solved for as if it was contacting at (X_1, Y_1, Z_1) as is shown in Equation 2.9. It is

$$X_{c1} = X_1 - r \sin(\lambda_1) \cos(\Phi_1)$$

$$Y_{c1} = Y_1 + r \sin(\lambda_1) \sin(\Phi_1) \quad (2.9)$$

$$Z_{c1} = Z_1 + r \cos(\lambda_1)$$

necessary to deal in global coordinates since the terrain map is in global coordinates. Thus, the tire orientation Φ_1 must be included as is shown in Figure 2.6.

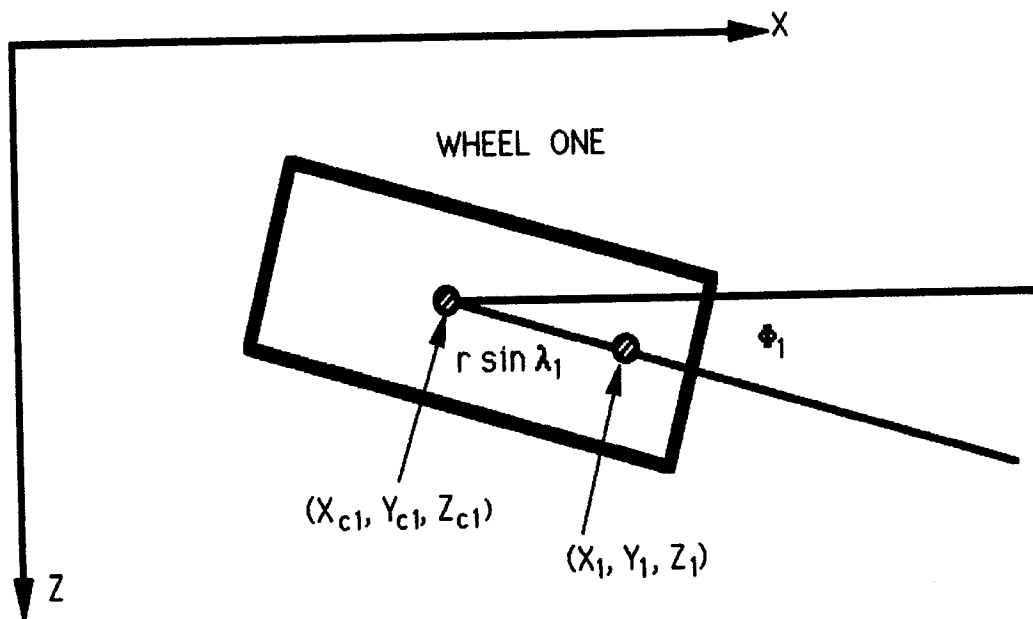


Figure 2.6 – Top view of wheel one

The bottom half of the wheel is then divided into 15 equally spaced points along its circumference. In other words, β , as seen in Figure 2.5 goes from 0 to π clockwise by $\pi/15$ radians. Each of these points on the tire circumference are calculated from Equation 2.10.

$$X_{\beta_1} = X_{c1} + r \cos(\beta) \cos(\Phi_1)$$

$$Y_{\beta_1} = Y_{c1} - r \sin(\beta) \quad (2.10)$$

$$Z_{\beta_1} = Z_{c1} + r \cos(\beta) \sin(\Phi_1)$$

The variable Y_{β_1} is the height of a perimeter point at a particular value of β on the tire, as if the tire was contacting at (X_1, Y_1, Z_1) as is shown on Figure 2.5. The terrain height can be obtained at a particular value of β by solving the equation of the plane using the previous methods. By comparing the height of Y_{β_1} and that of the terrain for the 15 points around the tire, the point at which the tire is most compressed, or at ΔY_{max} as is seen in Figure 2.5, is chosen as the actual contact point (X'_1, Y'_1, Z'_1) . Now that all the parameters of wheel one have been determined, the parameters of the remaining tires need to be found.

SECTION 2.2 - STEERING

The Ackerman point is the point about which the vehicle rotates if Ackerman type steering is used [11]. In other words, it is the center of the arc the centroid of the vehicle is on or the point from which the radius of curvature is measured. Figure 2.7 shows the application of Ackerman steering to a two-dimensional or flat terrain. Later, this will be extended to three-dimensional terrains in which the tires are not all on the same plane.

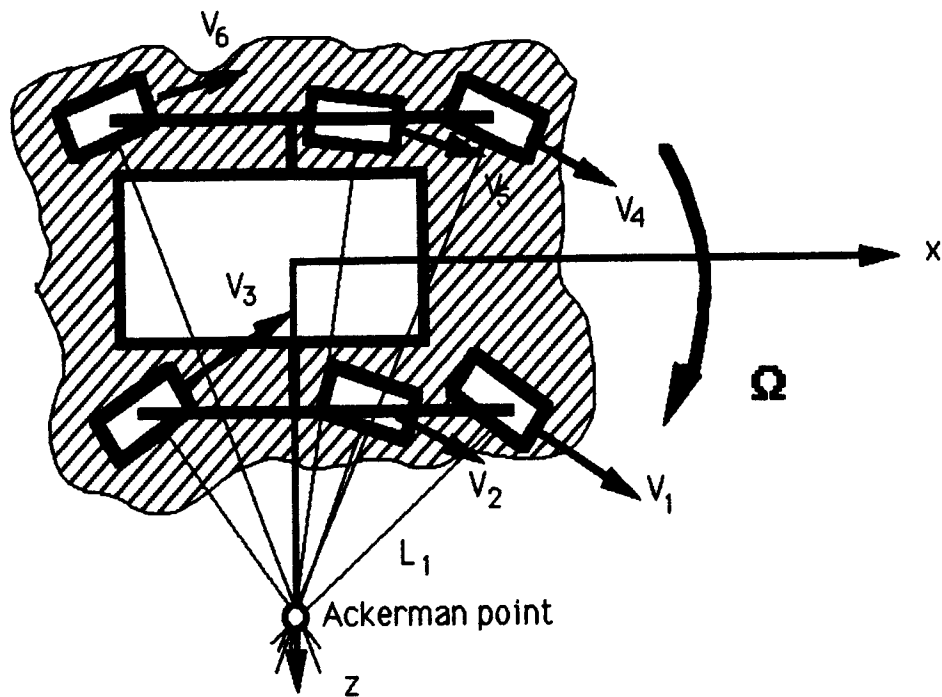


Figure 2.7 - Ackerman steer for 2-D

As is shown in Figure 2.7, the Ackerman point is chosen to lie along the local z-axis of the vehicle. There are actually an infinite number of points at which the Ackerman point can be placed for a six-wheel-steered

vehicle. Anywhere in the plane of the tire-ground contact is valid. If one set of tires could not be steered for example, the rear tires, the Ackerman point would be forced to remain somewhere along the axis joining the centers of the two rear tires. It was chosen to restrict the Ackerman point to remain on the local z-axis of the vehicle to simplify the analysis. In addition, this would allow the vehicle to rotate about its own center of gravity. That is, the Ackerman point can be chosen to coincide with the center of gravity of the vehicle.

Since the steering angle of wheel one (δ_1) has already been determined, the Ackerman point can be found by drawing the normal to the plane of wheel one. The Ackerman point is where this line intersects the local z-axis of the vehicle. By drawing all the other wheel normals to this point, as is shown in Figure 2.7, the remaining wheel steering angles can be determined. This is actually the steering configuration to minimize wheel slip in the lateral direction. In addition, since the angular velocity of the vehicle about the Ackerman point $\boldsymbol{\Omega}$ (where bold indicates a vector) is the same for each point on the body, one can also determine the forward velocity of each of the tires. As an example, the forward velocity of wheel one (\mathbf{V}_1) can be found as is shown in Equation 2.11.

$$\mathbf{V}_1 = \boldsymbol{\Omega} \times \mathbf{L}_1, \quad (2.11)$$

where \mathbf{L}_1 is the normal distance of wheel one from the Ackerman point as is drawn in Figure 2.7. From the forward velocity of wheel one, the angular rotational rate of wheel one (ω_1) can also be solved for assuming no tangential slip. This is done by using Equation 2.11 again, except \mathbf{L}_1 is

replace by the radius of the tire (r) and Ω becomes the angular rotational rate of wheel one (ω_1). The angular rotational rates of the other wheels can be calculated in a similar manner. This is useful in order to determine the power of a particular tire motor (E_1), like wheel one, if the torque (T_1) is also known as is seen in Equation 2.12.

$$E_1 = T_1 \omega_1 \quad (2.12)$$

In order to extend this analysis to three dimensions, some new parameters need to be defined. The local coordinate systems to be used in the three dimensional analysis are shown in the oblique view of Figure 2.8. Whenever a local coordinate system is referred to, it is intended to mean the local axes at the center of gravity of the vehicle (O_B) unless otherwise stated. Since the body accounts for the majority of the vehicle's weight, it is assumed that the center of gravity of the vehicle is synonymous with the centroid of the body (see Appendix A). In other words, the origin of the local axes remains at the centroid of the body at all times. This assumption greatly simplifies the analysis.

As is shown in Figure 2.8, all the passive joints also have a local coordinate system. These local coordinate systems will be referred to as the rocker's local frame (O_{12} or O_{45}) or the beam's local frame (O_L or O_R). The side view of the left side (named facing the front) is shown with variables defined in Figure 2.9. The side view of the right side will look similar, but it will have the rocker angle θ_{45} instead of θ_{12} and the beam angle θ_R instead of θ_L .

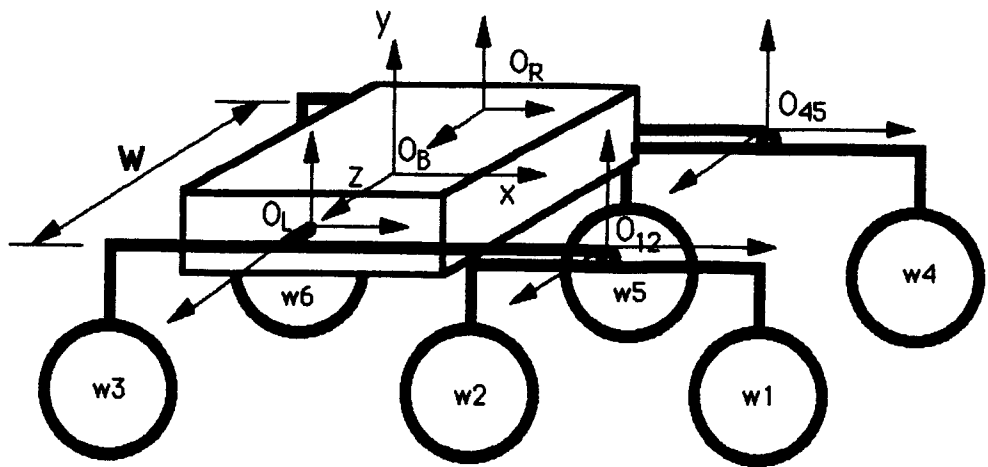


Figure 2.8 – Rocker Bogie model

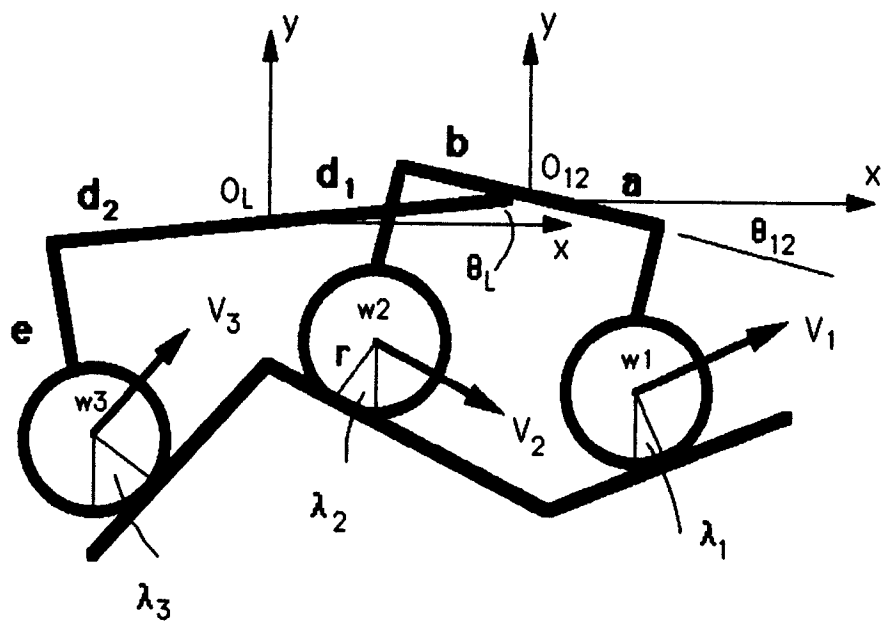


Figure 2.9 – Left side view

Extending the Ackerman steering principle to a three dimensional terrain, it is first noticed in Figure 2.9 that the contact points are not at the bottom of the tire or that the contact angle is not zero. Hence, the velocities are not perpendicular to gravity. In addition, the tires are not on the same plane. Therefore, the normals to the tires will never intersect at a point.

One way around this is to define what will be called an Ackerman axis, instead of a point. This axis is perpendicular to the local z-axis of the vehicle and parallel to the y-axis. Note that, since no part of the vehicle can roll with respect to another, all the local coordinate systems as defined in Figure 2.8 will have the same orientation. If Figure 2.10 is viewed looking straight down the local y-axis, the Ackerman axis is relatively easy to obtain and understand.

The Ackerman axis is obtained similarly to the Ackerman point by first drawing the normal to the plane of wheel one whose steering angle is already known. This normal as well as the other wheel normals, pass through the tire to ground contact instead of the center of the tire for the two dimensional terrain analysis. The axis which is perpendicular to the vehicle's local z-axis and intersects the normal of tire one is defined as the Ackerman axis. In order to determine the other wheel steering angles, the lengths as defined in the top view of Figure 2.10 need to be solved for in terms of the variables shown in Figure 2.9. This is shown in Equation 2.13.

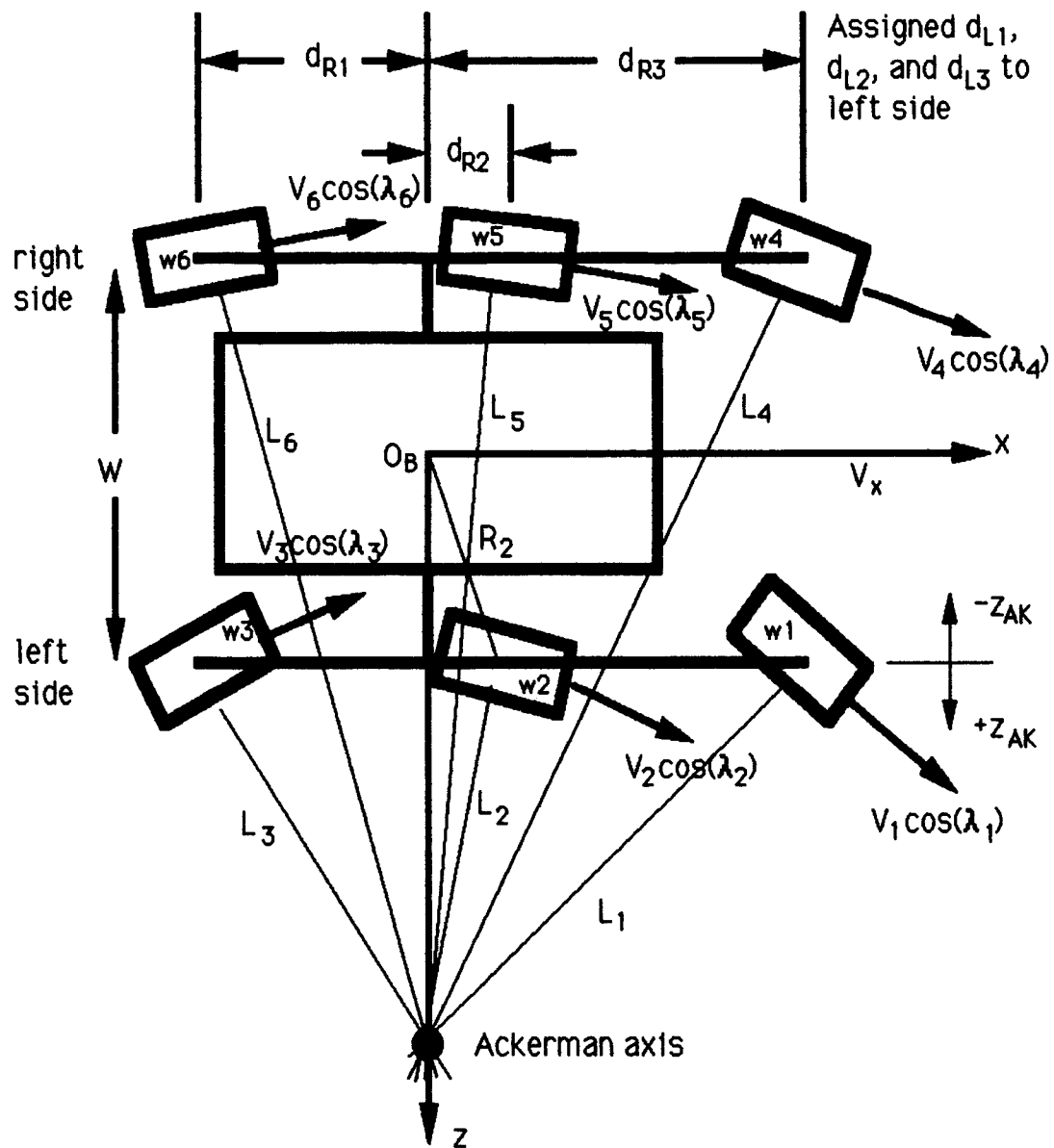


Figure 2.10 - Ackerman steer for 3-D

$$d_{R1} = d_2 \cos(\theta_R) - e \sin(\theta_R) - r \sin(\lambda_6)$$

$$d_{R2} = d_1 \cos(\theta_R) - b \cos(\theta_{45}) + e \sin(\theta_{45}) + r \sin(\lambda_5)$$

$$d_{R3} = d_1 \cos(\theta_r) + a \cos(\theta_{45}) + e \sin(\theta_{45}) + r \sin(\lambda_4)$$

Similarly, for the left side (2.13)

$$d_{L1} = d_2 \cos(\theta_L) - e \sin(\theta_L) - r \sin(\lambda_3)$$

$$d_{L2} = d_1 \cos(\theta_L) - b \cos(\theta_{12}) + e \sin(\theta_{12}) + r \sin(\lambda_2)$$

$$d_{L3} = d_1 \cos(\theta_L) + a \cos(\theta_{12}) + e \sin(\theta_{12}) + r \sin(\lambda_1)$$

Note that the vehicle's yaw and roll is not included here since this analysis deals with the local coordinate systems which yaw and roll together.

Tracking the position of wheels one and four for different locations of the Ackerman axis, the following three cases as shown in Figure 2.11 are seen.

For all three cases, z_{AK} , as defined in Figure 2.10, can be determined since δ_1 is already known. For case one of Figure 2.11, or when $\delta_1 < 0$

$$z_{AK} = d_{L3} \tan\left(\frac{\pi}{2} + \delta_1\right) \quad (2.14)$$

And for cases two and three or when $\delta_1 > 0$

$$z_{AK} = -d_{L3} \tan\left(\frac{\pi}{2} - \delta_1\right) \quad (2.15)$$

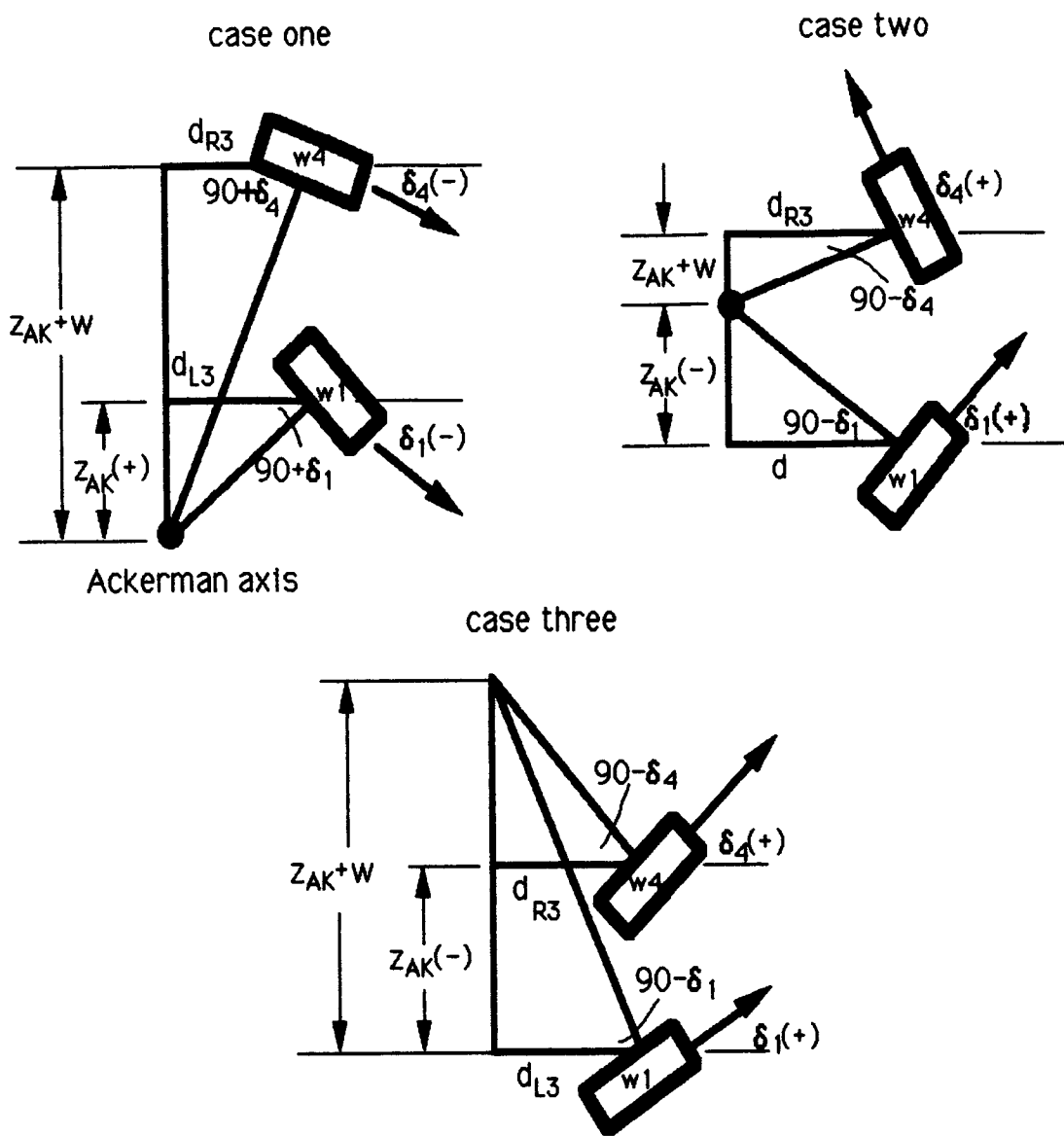


Figure 2.11 - Three different Ackerman axis cases

Now that the distance from wheel one along the local z-axis to the Ackerman axis (Z_{AK}) has been determined, one can determine the remaining wheel steering angles for quasi-Ackerman steering. For case one, as seen in Figure 2.11,

$$\delta_4 = \text{ATAN} \left(\frac{z_{AK} + w}{d_{R3}} \right) - \frac{\pi}{2}$$

similarly, (2.16)

$$\delta_2 = \text{ATAN} \left(\frac{z_{AK}}{d_{L2}} \right) - \frac{\pi}{2} \quad \delta_3 = -\text{ATAN} \left(\frac{z_{AK}}{d_{L1}} \right) + \frac{\pi}{2}$$

$$\delta_5 = \text{ATAN} \left(\frac{z_{AK} + w}{d_{R2}} \right) - \frac{\pi}{2} \quad \delta_6 = -\text{ATAN} \left(\frac{z_{AK} + w}{d_{R1}} \right) + \frac{\pi}{2}$$

and for cases two and three,

$$\delta_4 = \text{ATAN} \left(\frac{z_{AK} + w}{d_{R3}} \right) + \frac{\pi}{2}$$

similarly, (2.17)

$$\delta_2 = \text{ATAN} \left(\frac{z_{AK}}{d_{L3}} \right) + \frac{\pi}{2} \quad \delta_3 = - \left(\text{ATAN} \left(\frac{z_{AK}}{d_{L1}} \right) + \frac{\pi}{2} \right)$$

$$\delta_5 = \text{ATAN} \left(\frac{z_{AK} + w}{d_{R3}} \right) + \frac{\pi}{2} \quad \delta_6 = - \left(\text{ATAN} \left(\frac{z_{AK}}{d_{R1}} \right) + \frac{\pi}{2} \right)$$

Now that the steering angles of all the tires have been found, the rotational speeds of these tires can be solved for. In order to do this, there are some assumptions that need to be made.

The Ackerman axis is analogous to an instantaneous screw axis (ISA). An instantaneous screw axis is an axis such that there is pure rotation about the axis and pure translation along the axis. Assuming that the horizontal component of velocity is the component of the velocity which causes the pure rotation about the Ackerman axis, all the wheel velocities

can be solved for. The horizontal component of the velocity can be found by multiplying the total wheel velocity by the cosine of the contact angle as seen in Figure 2.10. This assumption of pure rotation about the Ackerman axis is only valid when the vehicle does not experience any significant lateral slip. Lateral slip will be considered in Chapter III when z-direction dynamics is dealt with.

The analogy between the Ackerman axis and an instantaneous screw axis breaks down when it is checked to see if there is pure translation along the axis. In order to have pure translation along the Ackerman axis each tire needs to have the same vertical velocity. This is clearly not the case, since the contact points vary on each tire according to the terrain. As a result, the vehicle will pitch and roll as well as translate in the vertical direction. Nonetheless, the passive hinges will 'absorb' some of this effect and make the above assumption reasonable for an approximation. With this in mind, the rotational rate of each tire can be solved for if the contact angles, the steering angles, and the center of gravity velocity are known.

The center of gravity velocity in the forward direction (V_x) can be found as shown in Chapter III. Using the idea that the Ackerman axis is similar to the ISA, it can be said that the angular velocity at any point on the vehicle is the same. This was done for the two dimension case as well, but about an Ackerman point instead of an axis. This angular speed about the Ackerman axis is equal to,

$$\Omega = \frac{V_x}{z_{AK} + \frac{W}{2}} \quad (2.18)$$

The velocity of wheel one can now be found as follows:,

$$\Omega = \frac{V_1 \cos(\lambda_1)}{L_1} \quad \text{or} \quad V_1 = \frac{\Omega L_1}{\cos(\lambda_1)} \quad (2.19)$$

Therefore the rotational speed of wheel one is,

$$\omega_1 = \frac{\Omega L_1}{r \cos(\lambda_1)} = \frac{V_x L_1}{(z_{AK} + W/2) r \cos(\lambda_1)} \quad (2.20)$$

where all the values on the right side are known and defined in Figures 2.9, 2.10, and 2.11. The angular rotational speeds of the other wheels can be determined in a similar manner.

$$\begin{aligned} \omega_2 &= \frac{V_x L_2}{(z_{AK} + W/2) r \cos(\lambda_2)} & \omega_3 &= \frac{V_x L_3}{(z_{AK} + W/2) r \cos(\lambda_3)} \\ \omega_4 &= \frac{V_x L_4}{(z_{AK} + W/2) r \cos(\lambda_4)} & \omega_5 &= \frac{V_x L_5}{(z_{AK} + W/2) r \cos(\lambda_5)} \\ \omega_6 &= \frac{V_x L_6}{(z_{AK} + W/2) r \cos(\lambda_6)} \end{aligned} \quad (2.21)$$

The acceleration of the vehicle in the z, or lateral, direction can also be determined as shown in Equation 2.22. This is again assuming that there is little or no lateral slipping.

$$A_z = \frac{V_x^2}{z_{AK} + W/2} \quad (2.22)$$

An alternative method of determining the steering angles using vector notation is to first determine Ω as is shown in Equation 2.18. Then, for wheel two, for example, the wheel velocity can be found as is shown in Equation 2.23.

$$\mathbf{V}_2 = \mathbf{V}_x + \boldsymbol{\Omega} \times \mathbf{R}_2 \quad (2.23)$$

The variable \mathbf{R}_2 is the vector in the local xz plane from the origin of the local frame to wheel two (Figure 2.10). Finding the direction of \mathbf{V}_2 will give the steering angle of wheel two for minimum slip. This analysis was done for each tire and confirmed the results of the original method.

Now that the steering angles of all the tires have been found, the positions of the other tires and their contact angles must be found. It should be realized that in order to determine the steering angles in the first place, the positions of all the wheels need to be known. Thus, this is an iterative process. In the program, all the steering angles are first determined as if the wheels were on a flat plane (2D analysis). Then, after the wheel positions have been determined (Section 2.3), the steering routine is repeated. Of course, adjusting the steering angles will also slightly vary the position of the tires. Therefore, their positioning is iterated once more. Since the correction to steering is not very coarse, the iterative process is terminated here after only two loops.

SECTION 2.3 - WHEEL POSITIONS

The first step in locating the other wheels is to find the position of wheel two. As is illustrated in the side and top view of the left rocker in Figure 2.12, θ_{12} and λ_2 are not known so they are both assumed to be zero for the first iteration.

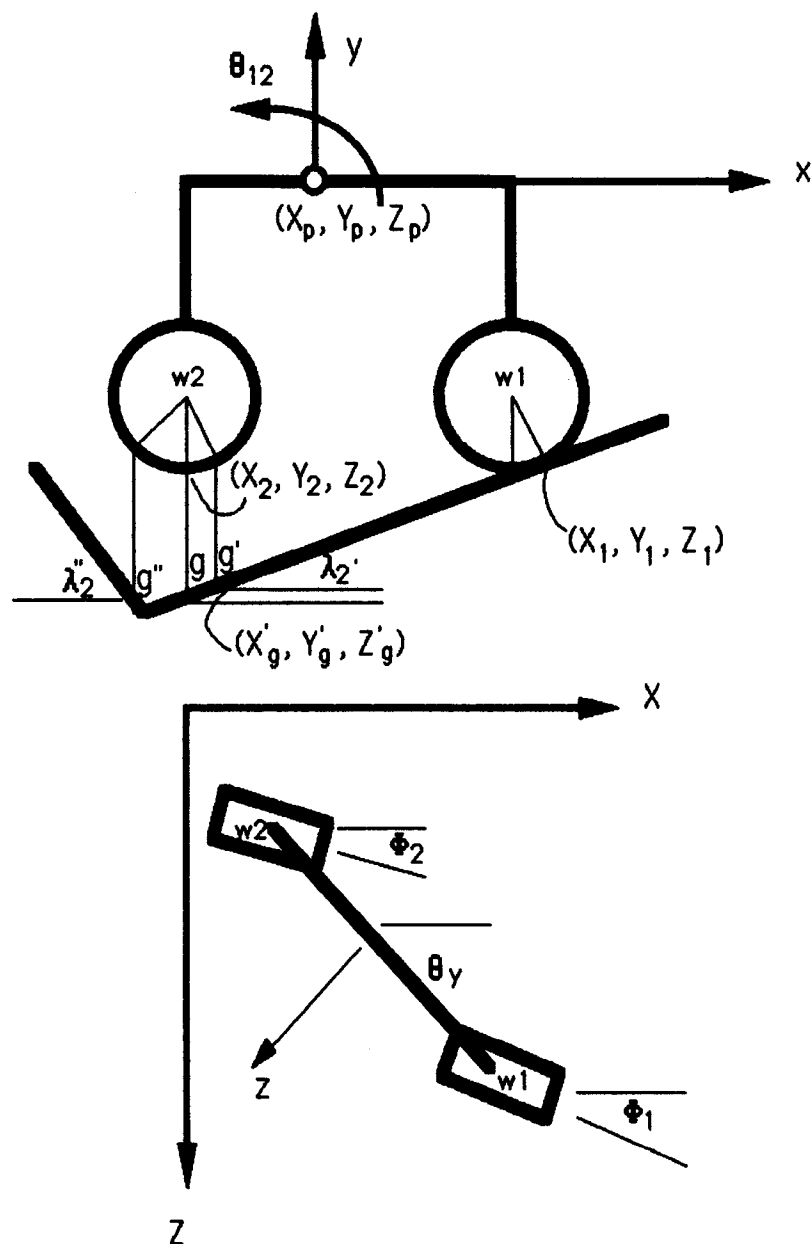


Figure 2.12 - Side and top view of rocker

Since the terrain is defined in global coordinates, the analysis must also be in global coordinates, where both the initial roll or rotation about the local x-axis (θ_x) and the yaw or rotation about the local y-axis (θ_y) are included. It is assumed that the vehicle is first yawed about the y-axis and then rolled about the x-axis. It makes a difference as to which order these rotations are considered. If the order of the rotations are reversed, a different vehicle orientation will result. The initial vehicle yaw (θ_y) has been specified in the input file, however, the roll (θ_x) is not known. Therefore, along with θ_{12} , and λ_2 , it is initially assumed that the roll is zero.

From the known position of wheel one, the position of wheel two (X_2 , Z_2) can be found using the above assumptions as is shown in Equation 2.24. This is point g as is shown in Figure 2.12.

$$\begin{aligned} X_2 &= X_1 + r \sin(\lambda_2) \cos(\Phi_2) - r \sin(\lambda_1) \cos(\Phi_1) - \\ &\quad (a+b) \cos(\theta_{12}) \cos(\theta_y) - \Delta Y \sin(\theta_x) \sin(\theta_y) \\ Z_2 &= Z_1 - r \sin(\lambda_2) \sin(\Phi_2) + r \sin(\lambda_1) \sin(\Phi_1) + \\ &\quad (a+b) \cos(\theta_{12}) \sin(\theta_y) - \Delta Y \sin(\theta_x) \cos(\theta_y) \end{aligned} \quad (2.24)$$

where

$$\Delta Y = (a+b)(\sin(\theta_{12}) + r \cos(\lambda_2) - r \cos(\lambda_1))$$

While the first few terms of Equation 2.24 are relatively easy to see from Figure 2.12, the last term in each expression might not be. The last term in each expression is the result of the change in height between the contacts and the roll and yaw as is illustrated in Figure 2.13.

Front view of rocker in local frame Top view of rocker in global frame

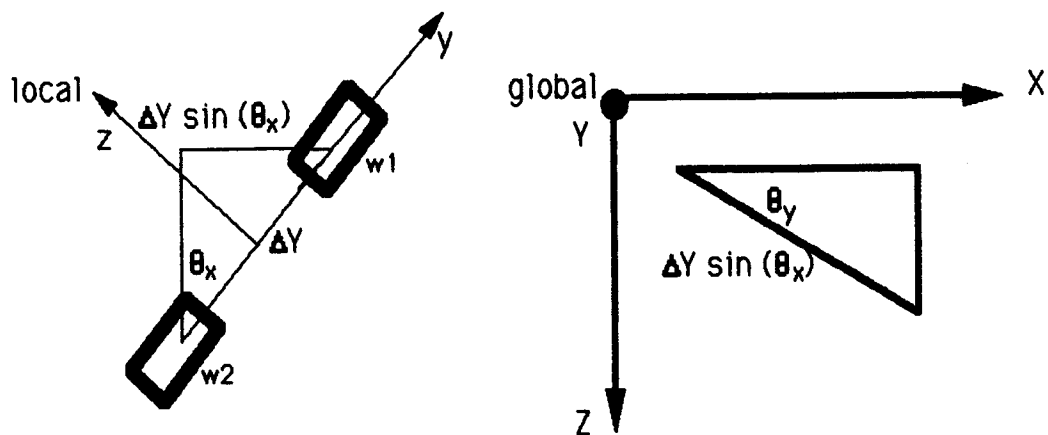


Figure 2.13 – Illustration of last terms in Eqn 2.24

Once X_2 and Z_2 have been solved using Equation 2.24, λ_2 is calculated at point g by the methods of Section 2.1 and shown on Figure 2.12. Since the position of X_2 and Z_2 were found in the first place with an assumed value of λ_2 , the process is iterated. In other words, it was initially assumed that wheel two would contact at point g with zero contact angle, but after determining the actual slope, or contact angle, at point g and iterating back with Equation 2.24, it is found that wheel two would contact at g' . This iterative loop converges within a couple of iterations to a contact angle, particularly for terrains which are not rough. For Figure 2.12 only two iterative loops are necessary: the first time the contact angle at point g is found, then the contact angle at g' is found. Since they have the same contact angle, the loop is terminated.

Now that the contact angle has been found for this orientation, θ_{12} is adjusted to bring wheel two into contact with the ground. Notice, that as θ_{12} is adjusted, the contact angle can change. Perhaps wheel two will actually contact at point g'' which will give it a different contact angle as

is seen in Figure 2.12. Thus finding the position of wheel two requires two nested iterative loops. The outside loop is for adjusting θ_{12} and the inside loop is for finding the contact angle λ_2 since every time θ_{12} is adjusted, λ_2 can change.

In order to speed the convergence of θ_{12} , an educated guess can be made of the correct rocker angle. In order to do this, the angle θ_g of the triangle as shown in the side view of Figure 2.14 is calculated to make the tire contact at point g'. The triangle's hypotenuse is formed by connecting the center of wheels one and two as is shown in Figure 2.14.

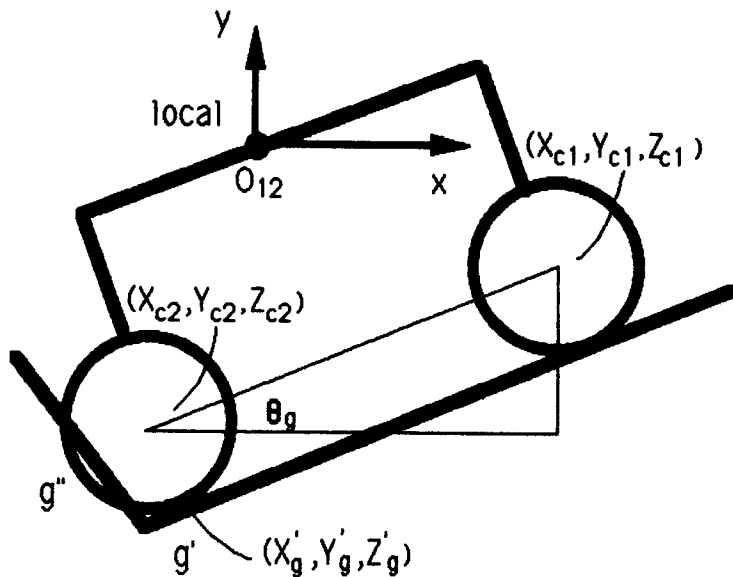


Figure 2.14 - Guessing θ_{12}

The wheel center points can be found as seen in Equation 2.25.

$$\begin{aligned} X_{c1} &= X_1 - r \sin(\lambda_1) \cos(\Phi_1) - r \cos(\lambda_1) \sin(\theta_x) \cos(\Phi_1) \\ Y_{c1} &= Y_1 + r \cos(\lambda_1) \cos(\theta_x) \end{aligned} \quad (2.25)$$

$$Z_{c1} = Z_1 + r \sin(\lambda_1) \sin(\Phi_1) - r \cos(\lambda_1) \sin(\theta_x) \sin(\Phi_1)$$

$$X_{c2} = X_g - r \sin(\lambda_2) \cos(\Phi_2) - r \cos(\lambda_2) \sin(\theta_x) \cos(\Phi_2)$$

$$Y_{c2} = Y_g + r \cos(\lambda_2) \cos(\theta_x)$$

$$Z_{c2} = Z_g + r \sin(\lambda_2) \sin(\Phi_2) - r \cos(\lambda_2) \sin(\theta_x) \sin(\Phi_2)$$

where the last terms of the X and Z components have similar meaning to those of Equation 2.24. θ_g will equal the 'actual' θ_{12} if the contact angle is correct. If instead the tire is found to contact at point g" first as would be the case in Figure 2.14, than it is necessary to iterate again with the new contact angle. θ_{12} is iterated until it is within 0.01 radians of the previous answer and the resulting wheel two contact is named (X_2, Y_2, Z_2). Once the two nested iterative loops have converged, the actual λ_2 and θ_{12} might still not be known since the vehicle roll was assumed to be zero. Since there is no information on the other side of the vehicle yet, the roll cannot be solved. Hence, the next step is to find the position of wheel three and to iterate back on the roll when more information is known.

In order to find the position of wheel three, the pivot point (X_p, Y_p, Z_p) as is shown in Figure 2.12 is first solved for using Equation 2.26.

$$\begin{aligned}
 X_p = & X_2 + (b \cos(\theta_{12}) - e \sin(\theta_{12})) \cos(\theta_y) - r \sin(\lambda_2) \cos(\Phi_2) + \\
 & \Delta Y \sin(\theta_x) \sin(\theta_y)
 \end{aligned} \tag{2.26}$$

$$\begin{aligned}
 Y_p = & Y_2 + \Delta Y \cos(\theta_x) \\
 Z_p = & Z_2 - (b \cos(\theta_{12}) - e \sin(\theta_{12})) \sin(\theta_y) + r \sin(\lambda_2) \sin(\Phi_2) + \\
 & \Delta Y \sin(\theta_x) \cos(\theta_y)
 \end{aligned}$$

where

$$\Delta Y = b \sin(\theta_{12}) + e \cos(\theta_{12}) + r \cos(\lambda_2)$$

Now that the pivot point of the rocker has been found, the position of wheel three can be found by a method similar to that used to find wheel two.

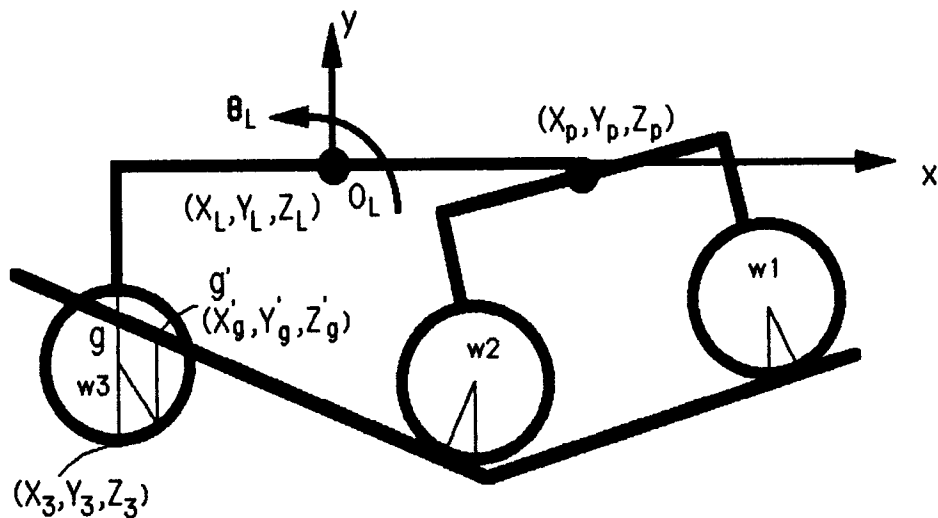


Figure 2.15 - Finding position of wheel three

Assuming that θ_L , λ_3 , and θ_x are all zero, the position of wheel three (X_3, Z_3) is found using Equation 2.27.

$$X_3 = X_p - (d_1 + d_2) \cos(\theta_L) - e \sin(\theta_L) \cos(\theta_y) + \\ r \sin(\lambda_3) \cos(\Phi_3) - \Delta Y \sin(\theta_x) \sin(\theta_y)$$

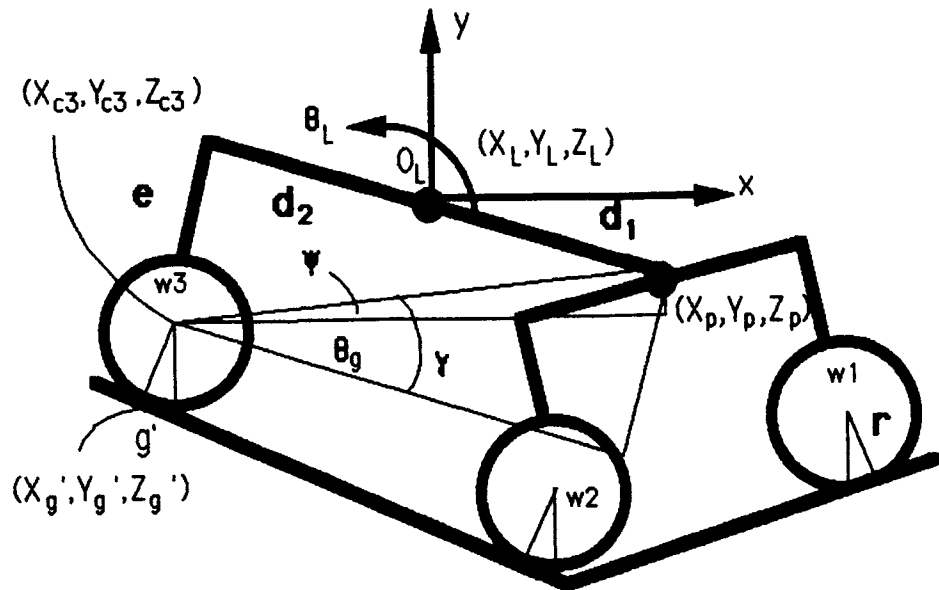
$$Z_3 = Z_p + (d_1 + d_2) \cos(\theta_L) - e \sin(\theta_L) \sin(\theta_y) - \\ r \sin(\lambda_3) \sin(\Phi_3) - \Delta Y \sin(\theta_x) \cos(\theta_y) \quad (2.27)$$

where

$$\Delta Y = r \cos(\lambda_3) + e \cos(\theta_L) + (d_1 + d_2) \sin(\theta_L)$$

The contact angle at the redefined point g is found by the methods of Section 2.1 and then substituted back into Equation 2.27 to find a new point, g'. If the contact angle from this new point is the same as the previous one, the contact angle has converged and θ_L is ready to be adjusted. For Figure 2.15, the contact angle at g is the same as g' so θ_L can now be adjusted. As in the case of the rocker angle, a good guess for θ_L can be obtained as is illustrated in Figure 2.16. First the center of wheel three is solved as if it contacted at g'. This is shown in Equation 2.28.

$$X_{c3} = X_g - r \sin(\lambda_3) \cos(\Phi_3) - r \cos(\lambda_3) \sin(\theta_x) \cos(\Phi_3) \\ Y_{c3} = Y_g + r \cos(\lambda_3) \cos(\theta_x) \quad (2.28) \\ Z_{c3} = Z_g + r \sin(\lambda_3) \sin(\Phi_3) - r \cos(\lambda_3) \sin(\theta_x) \sin(\Phi_3)$$

Figure 2.16 - Guessing θ_L

From Figure 2.16, θ_g can be determined as is shown in Equation 2.29.

$$\gamma = \text{ATAN} \left(\frac{e}{d_1 + d_2} \right)$$

$$\psi = \text{ATAN} \left(\frac{Y_p - Y_{c3}}{\sqrt{(X_p - X_{c3})^2 + (Z_p - Z_{c3})^2}} \right) \quad (2.29)$$

$$\theta_g = \gamma - \psi$$

θ_g will equal the 'actual' θ_L if the correct contact angle was used. If not, the process is repeated. If both θ_L and λ_3 have converged (to within an error tolerance of 0.01 radians of the previous result), wheel three's

contact is named (X_3, Y_3, Z_3) and the program moves on to find the position of wheel four. Keep in mind that the roll has still not been taken into account.

The angle $\theta_L - \theta_{12}$ may be less than the minimum relative angle (θ_{\min}) allowed, or more than the maximum relative angle (θ_{\max}) allowed, due to the mechanical stops. Rather than solve this more difficult kinematics problem in which one tire would not contact the ground, the program advances the vehicle one unit mesh size. It does this until all three wheels contact the terrain and satisfy the relative angle criteria.

The next step is to find the location of wheel four. As is shown in the top view of Figure 2.17, wheel four is assumed to be directly across from wheel one. This can be expressed as is shown in Equation 2.30.

$$X_4 = X_1 - W \cos(\theta_x) \sin(\theta_y) \quad (2.30)$$

$$Z_4 = Z_1 - W \cos(\theta_x) \cos(\theta_y)$$

Y_4 , or the height of wheel four's tire to ground contact, can be found using the methods of Section 2.1. From the assumed position of wheel four, the positions of wheel five and six are found in exactly the same manner that those of wheels two and three were found from wheel one. That is, both wheels five and six require two nested iterative loops.

Due to the assumed value of wheel four, it may be found, as illustrated in Figure 2.17, that the beam does not want to connect up with the body at the same place the body wants to connect up with the beam. This is shown as a Δx in Figure 2.17.

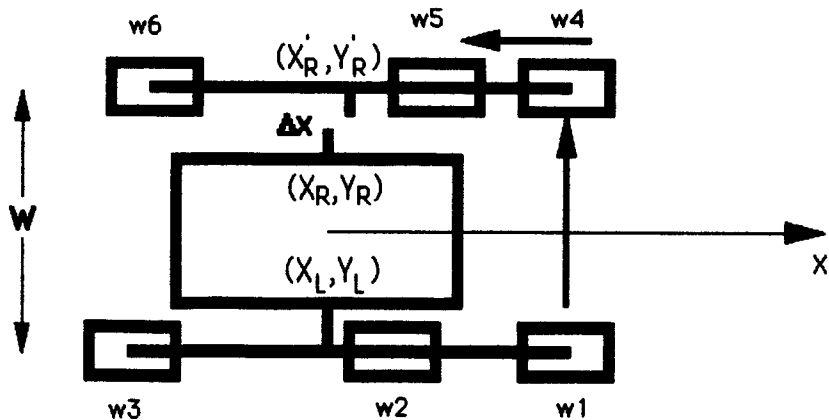


Figure 2.17 - Beam to body joint offset

In order to find out where the body wants to connect to the right beam, first the position of the beam pivot on the left side is solved for. The position of wheel three is used to find the beam's pivot as is shown in Equation 2.31.

$$X_L = X_3 - r \sin(\lambda_3) \cos(\Phi_3) + (d_2 \cos(\theta_L) - e \sin(\theta_L)) \cos(\theta_y) + \Delta Y_L \sin(\theta_x) \sin(\theta_y) \quad (2.31)$$

where

$$\Delta Y_L = r \cos(\lambda_3) + e \cos(\theta_L) + d_2 \sin(\theta_L)$$

Moving across the body to the right side and solving for X_R ,

$$X_R = X_L - W \cos(\theta_x) \sin(\theta_y) \quad (2.32)$$

If the assumed position of wheel four is correct, then X'_R as is shown on Figure 2.17 should be the same as X_R , or Δx should be zero. The position of

wheel six is used to find the beam pivot's X coordinate X'_R as is shown in Equation 2.33.

$$X'_R = X_6 - r \sin(\lambda_6) \cos(\Phi_6) + (d_2 \cos(\theta_R) - e \sin(\theta_R)) \cos(\theta_y) + \Delta Y_R \sin(\theta_x) \sin(\theta_y) \quad (2.33)$$

where

$$\Delta Y_R = r \cos(\lambda_6) + e \cos(\theta_R) + d_2 \sin(\theta_R)$$

If it is found that $X'_R - X_R$ is greater than 0.015 meters (the error tolerance), wheel four is moved back in the X direction by 0.005 meters and the Z coordinate is adjusted accordingly. This is shown in Equation 2.34.

$$X_4 = X_4 - .005$$

$$Z_4 = Z_4 + .005 \tan(\theta_y) \quad (2.34)$$

If it is found that $X_R - X'_R$ is greater than 0.015 meters, wheel four is moved up by 0.005 meters. Each time wheel four is moved, the position of wheels five and six are recalculated with two nested iterative loops required for each tire. This process is repeated until the error tolerance is satisfied.

Once the right beam and body have been aligned, a side view of the right side is analyzed. As seen in Figure 2.18, the beam still does not want to connect to the body where the body wants to connect to the beam. This time the misalignment is in the y-direction instead of the xz plane. In order

to rectify this problem, the body must roll. The approach to align the y-direction is analogous to aligning in the xz plane.

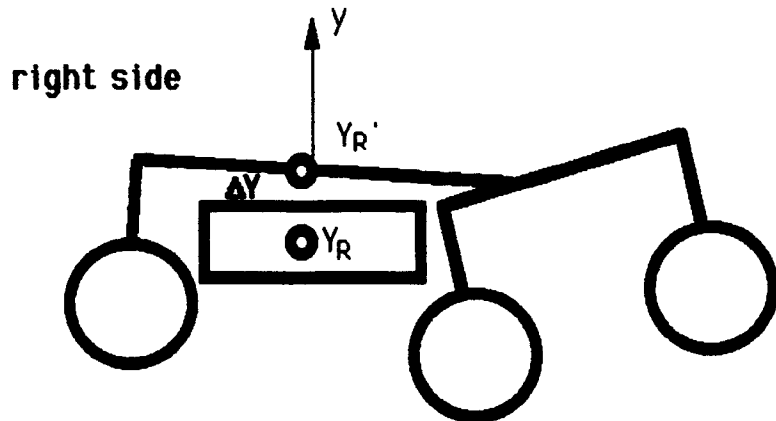


Figure 2.18 - Beam to body joint offset

In order to find out where the body wants to connect to the right beam in the y-direction, first the beam pivot on the left side is found.

$$Y_L = Y_3 + \Delta Y_L \cos(\theta_x) \quad (2.35)$$

where ΔY_L is defined in Equation 2.31

Moving across the body to the right side and solving for Y_R ,

$$Y_R = Y_L + W \sin(\theta_x) \quad (2.36)$$

If the assumed roll angle is correct, than Y'_R as shown on Figure 2.18 should be the same as Y_R or ΔY should be zero. The position of wheel six is used to find the beam pivot's Y coordinate Y'_R as is shown in Equation 2.37.

$$Y_R = Y_6 + \Delta Y_R \cos(\theta_x) \quad (2.37)$$

where ΔY_R is defined in Equation 2.33

If it is found that Y'_R and Y_R are not aligned within an error tolerance of 0.01 meters, the vehicle is rolled. An estimate of what this roll angle should be is shown in Equation 2.38.

$$\theta_x = \theta_x + \frac{Y_R - Y'_R}{W} \quad (2.38)$$

On the second iteration, θ_x is incremented up or down by half a degree.

Of course, since all the wheel positions are roll dependent, all the wheel positions need to be recalculated every time the vehicle is rolled. That is to say, it is necessary to go right back to Equation 2.24 and iterate. Once all the wheel positions are found, the steering routine is executed a second time. Since adjusting the steering affects the wheel positions, the whole routine is repeated again. Figure 2.19 provides a summary of how the wheel positions are found from the known position of wheel one.

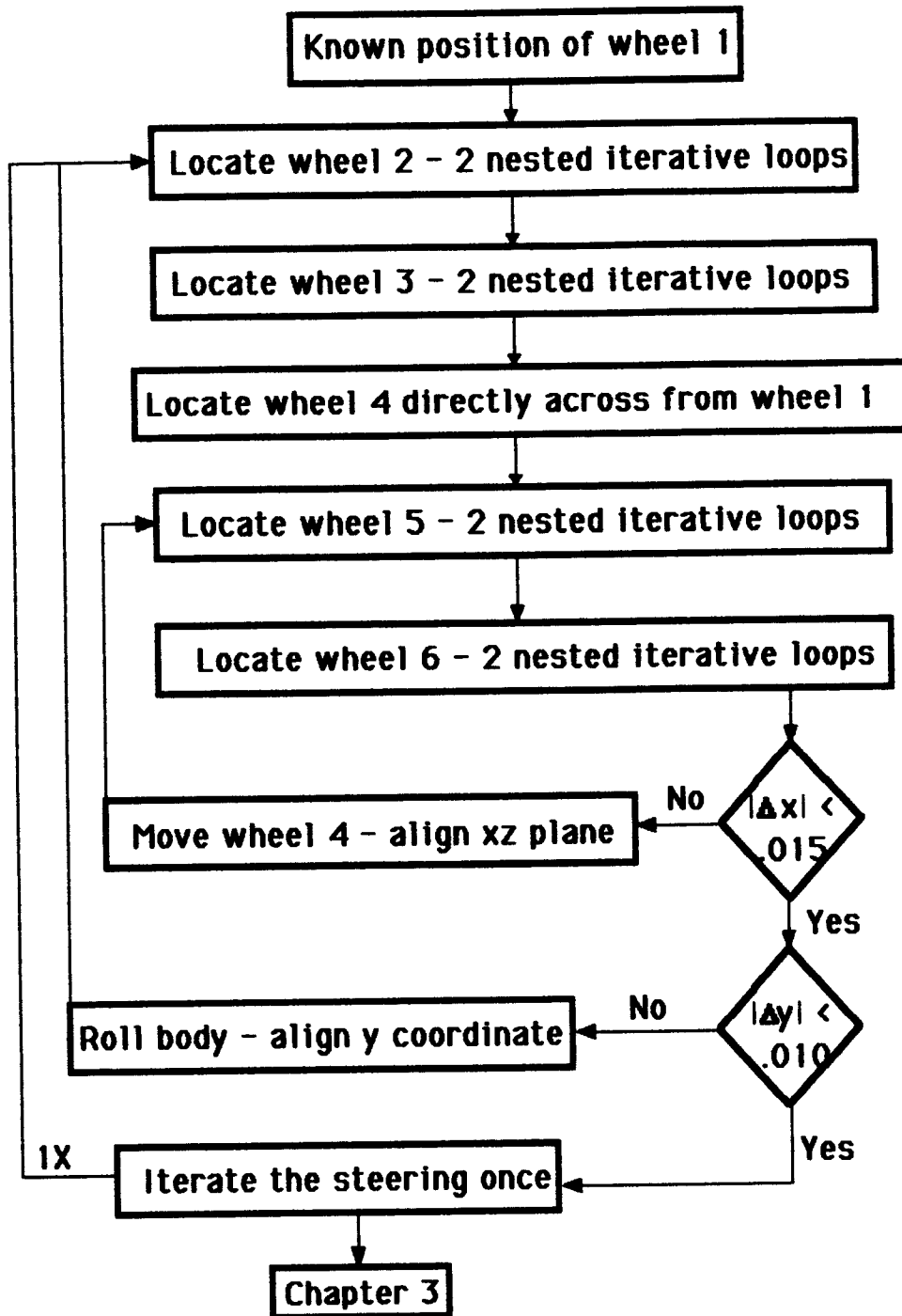


Figure 2.19 – Finding initial positions of wheels

Since at one point there are five nested iterative loops, it takes the computer some time to converge all the values, particularly on rough terrain. There are positions in which the program simply oscillates about the error tolerance. This oscillation typically shows up at the beam pivot on the right side. This can be rectified by decreasing the increment size for moving wheel four and for the roll. Whereas this usually rectifies the problem, it slows down the computer. Another method would be to increase the error tolerances on aligning the right beam pivot.

For the most part, this section allows the user to start 'anywhere' on the terrain map. Since it does take quite some time for the vehicle to transverse an appreciable distance in the program, this feature is handy. If someone was interested in how the vehicle climbed a hill in the center of the terrain map, the program can be started with the vehicle near the center of the terrain map since its initial position can be found as shown in this section. This saves the time of waiting for the vehicle to transverse from the flat terrain at the origin of the global axis (3 by 3 meter flat section) to the desired point. In addition, certain tracks of terrain can be easily rerun by positioning wheel one at the desired point.

CHAPTER III

DYNAMICS

Section 3.1 – Initial Parameters

Before the dynamics can be analyzed, all the masses, centers of gravity, and moments of inertia must be determined for each freebody diagram. Through the input file, the user specifies all the geometrical dimensions seen in Figure 2.8 in meters. The beam and rocker are assumed to be made of hollow square stock as seen in section c-c of Figure 3.1 where the side length (s), the thickness (t_s), and the density of the material (ρ) in kg/m^3 are specified. The user also inputs the mass of the wheel assembly. It is assumed that this mass, composed of the tire, the wheel's concentric motor, and the steering motor, is homogeneously spread through the tire geometry. The tire width is given in the input file as well. Although the tire width was neglected for kinematic purposes, it is included for the purpose of determining the soil sinkage and resistive force. The body, whose length, width, and height are assigned in the input file, is also assumed to be homogeneous.

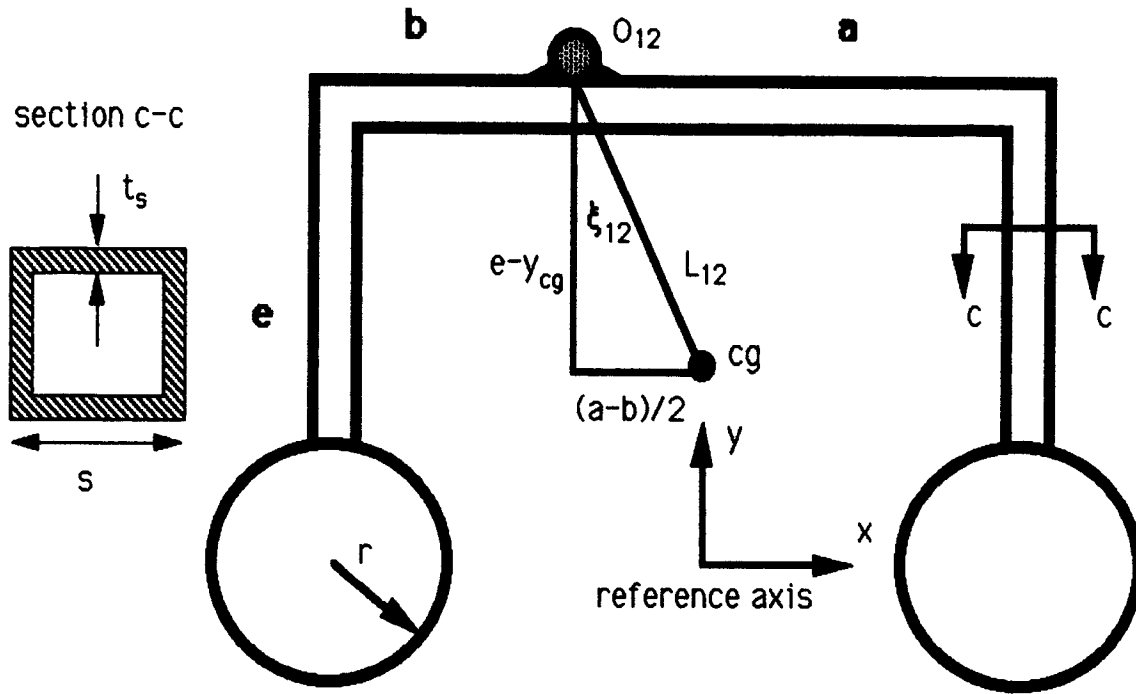


Figure 3.1 – Rocker parameters

First, the parameters of the rocker, as seen in Figure 3.1, are determined. The cross sectional area of the rocker (A_s) is found below.

$$A_s = s^2 - (s - 2t_s)^2 \quad (3.1)$$

Therefore, the mass of the rocker (m_{12}) is as shown in Equation 3.2.

$$m_{12} = 2m_w + 2m_e + m_{ab}$$

where

$$m_w = \text{mass of wheel assembly} \quad (3.2)$$

$$m_e = \rho e A_s$$

$$m_{ab} = \rho (a+b-2s) A_s$$

Since the rocker is symmetric, its center of gravity (x_{cg} , y_{cg}) lies on the y-axis of the reference frame, or x_{cg} is zero. The y value of the center of gravity or y_{cg} as well as its distance and angle from the pivot are shown in Equation 3.3.

$$y_{cg} = \frac{e m_e + (e - s/2) m_{ab}}{m_{12}} \quad (3.3)$$

$$L_{12} = \sqrt{\left(\frac{a-b}{2}\right)^2 + (e - y_{cg})^2} \quad \xi_{12} = \sin^{-1}\left(\frac{(a-b)/2}{L_{12}}\right)$$

In a similar manner, the parameters of the beam as seen in Figure 3.2 are determined.

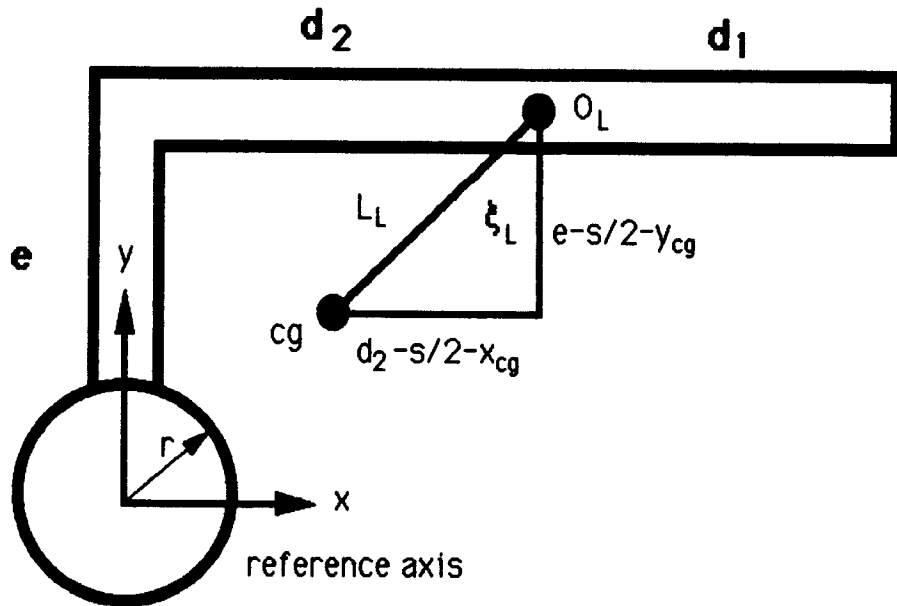


Figure 3.2 - Beam parameters

The mass of the beam is shown in Equation 3.4.

$$m_L = m_w + m_e + m_d$$

$$\text{where } m_d = \rho(d_1 + d_2 - s) A_s \quad (3.4)$$

The center of gravity as well as its distance and angle from the beam pivot are shown in Equation 3.5.

$$\begin{aligned} x_{cg} &= \frac{(d_1 + d_2 - s/2) m_d}{2 m_L} & y_{cg} &= \frac{(e/2) m_e + (e - s/2) m_d}{m_L} \\ L_L &= \sqrt{(d_2 - s/2 - x_{cg})^2 + (e - s/2 - y_{cg})^2} & \theta_L &= \sin^{-1} \left(\frac{d_2 - s/2 - y_{cg}}{L_L} \right) \end{aligned} \quad (3.5)$$

Using the parallel axis theorem, the moment of inertia of the rocker about its pivot (I_{12}) and the beam about its pivot (I_L) are found in Equation 3.6.

$$\begin{aligned} I_{12} &= (2 I_w + m_w (2e^2 + a^2 + b^2)) + (I_{ab} + m_{ab} (a - b)^2) + \\ &\quad (2 I_e + m_e (2(e/2)^2 + a^2 + b^2)) \end{aligned} \quad (3.6)$$

$$I_L = (I_w + m_w (e^2 + d_2^2)) + (I_e + m_e ((e/2)^2 + d_2^2)) + (I_d + m_d (d_1 - d_2)^2)$$

$$\text{where } I_w = 1/2 m_w r^2 \quad I_e = 1/12 m_e (e^2 + s^2)$$

$$I_{ab} = 1/12 m_{ab} ((a + b - 2s)^2 + s^2)$$

$$I_d = 1/12 m_d ((d_1 + d_2 - s)^2 + s^2)$$

The body has a mass specified in the input file (m_B), and, since it is assumed to be homogeneous, its moments of inertia can be readily found using Equations 3.7.

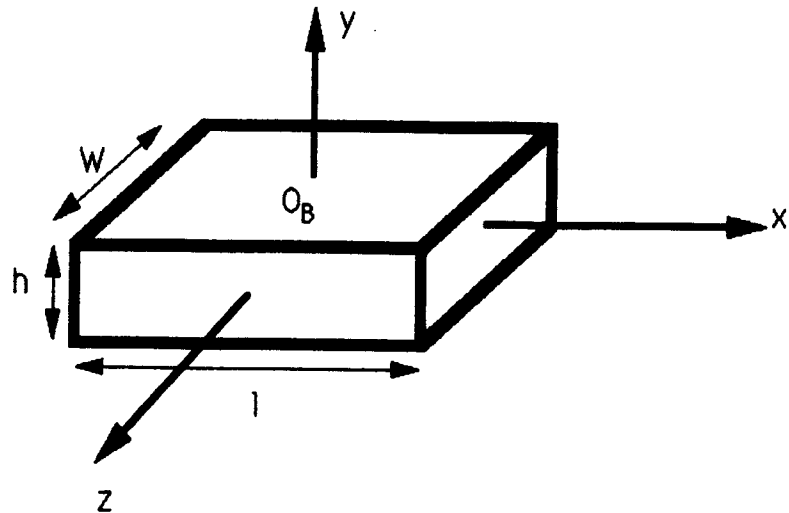


Figure 3.3 – Moments of inertia of the body

$$I_x = \frac{1}{12} m_B (w^2 + h^2) \quad I_y = \frac{1}{12} m_B (w^2 + l^2) \quad I_z = \frac{1}{12} m_B (h^2 + l^2) \quad (3.7)$$

Since the vehicle is rigid in the z , or lateral direction, while it is not in the xy -plane, it is advantageous to separate the analysis into two steps. First, the lateral direction is analyzed and then the xy plane. Afterwards, the two are superimposed on the assumption that it is a linear process. For the z -direction dynamics, where the entire vehicle is treated as one freebody diagram, the moment of inertia of the vehicle as a whole is analyzed. Since the joint angles of the vehicle vary from step to step, it is necessary to recalculate the entire vehicle's moments of inertia at each step. The process to do this is shown in Appendix B.

Before the vehicle can be put in motion, the contact forces at the tires need to be solved. It is assumed that the vehicle starts at the desired position with the brakes on and that it is not slipping. In this manner, the contact forces are solved statically.

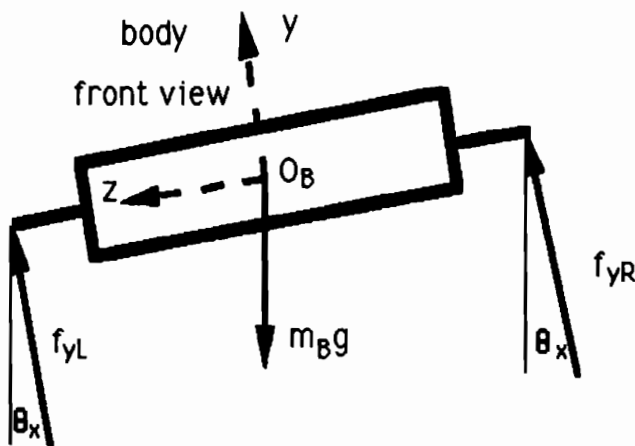


Figure 3.4 - Determining static beam pivot forces

As seen in Figure 3.4, the static beam pivot force can be expressed as seen below.

$$f_{yL} = f_{yR} = \frac{m_B g}{2 \cos \theta_x} \quad (3.8)$$

Moving to the beam's freebody diagram as is shown in Figure 3.5, the contact force of wheel three (f_{c3}) and the rocker pivot force (f_{y12}) can be solved. Since wheel three is locked, the beam frame can only rotate about the tire axle. Hence, the rocker pivot force f_{x12} is zero. After eliminating f_{x12} , there are three unknowns f_{b3} , f_{c3} , and f_{y12} where f_{b3} is wheel three's braking force and f_{c3} is its contact force. The forces f_{y12} and f_{c3} can be solved statically with the results shown in Equation 3.9.

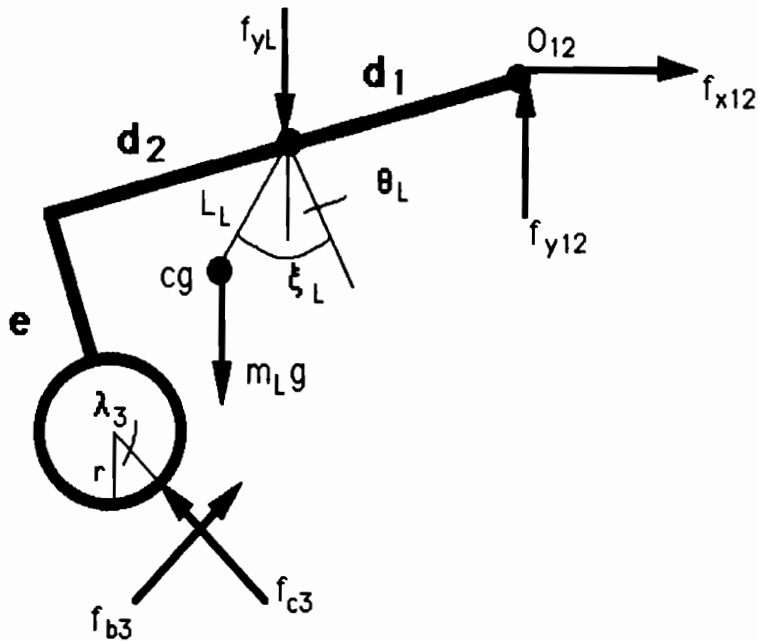


Figure 3.5 – Determining initial contact force

$$f_{y12} = \frac{f_{yL} \Delta x' + m_L g (\Delta x' - L_L \sin(\lambda_L - \theta_L))}{\Delta x}$$

$$f_{c3} = (m_L g + f_{yL} - f_{y12}) \cos(\lambda_3)$$

where (3.9)

$$\Delta x = (d_1 + d_2) \cos(\theta_L) - e \sin(\theta_L) - r \sin(\lambda_3) \cos(\delta_3)$$

$$\Delta x' = \Delta x - d_1 \cos(\theta_L)$$

Analyzing the rocker in Figure 3.6, there are unfortunately four unknowns f_{b2} , f_{c2} , f_{b1} , and f_{c1} . Therefore, this problem is statically indeterminant. In order to avoid this problem, it is assumed that the horizontal components of the contact force cancel the braking force. In other words, the forces represented by the solid arrows at the wheel contacts in Figure 3.6 are

replaced by the forces represented by the dashed arrows. With this assumption, the rocker wheels' contact forces are determined as is shown in Equation 3.10. The same analysis is done for the right side of the vehicle.

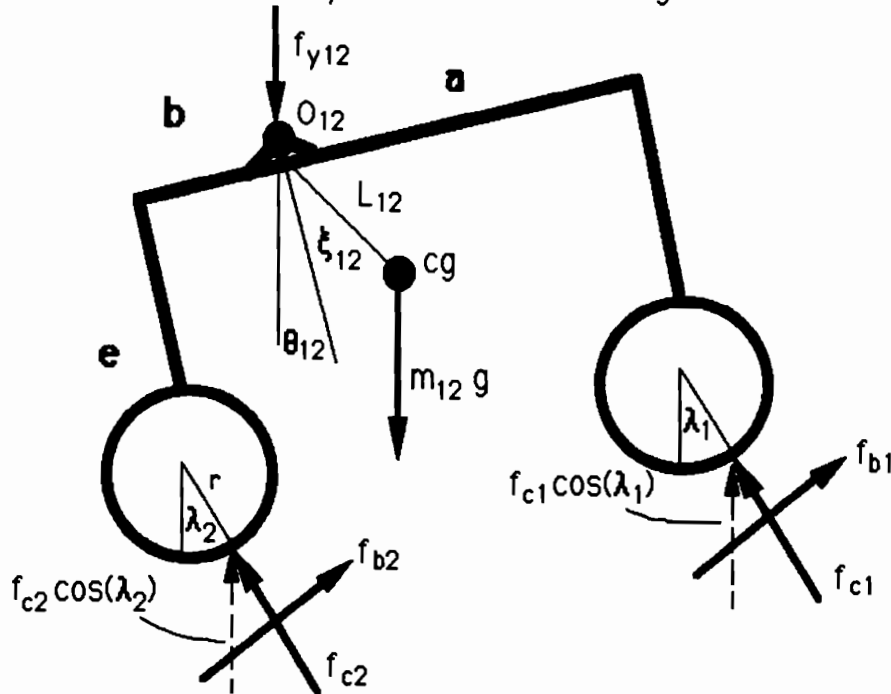


Figure 3.6 - Determining initial contact forces

Summing forces in the y direction the contact forces are found.

$$f_{c1} = \frac{f_{y12}\Delta x' + m_{12}g(\Delta x' + L_{12} \sin(\theta_{12} + \xi_{12}))}{\Delta x \cos(\lambda_1)}$$

$$f_{c2} = \frac{f_{y12} + m_{12}g - f_{c1} \cos(\lambda_1)}{\cos(\lambda_2)}$$

where

(3.10)

$$\Delta x = r \sin(\lambda_1) \cos(\delta_1) + (a+b) \cos(\theta_{12}) - r \sin(\lambda_2) \cos(\delta_2)$$

$$\Delta x' = b \cos(\theta_{12}) - e \sin(\theta_{12}) - r \sin(\lambda_2) \cos(\delta_2)$$

The assumption illustrated in Figure 3.6 can be avoided if the user starts on flat terrain. On flat terrain, the problem is statically determinate since no braking force is necessary. Nonetheless, since this static analysis is only performed for the initial conditions, it really is not a significant part of the problem. The contact forces at all subsequent steps are found dynamically as will be explained later. Therefore, an approximation should be adequate.

Now that the contact forces are known, the brakes are released and a torque is applied. The desired torque is found by first determining a static component of the tractive force (f_s) to hold the wheel stationary. A dynamic component (f_d) is then added to get the total tractive force (f_t) which produces the desired acceleration. The static component can be approximated as having a horizontal magnitude which cancels the horizontal component of the contact force.

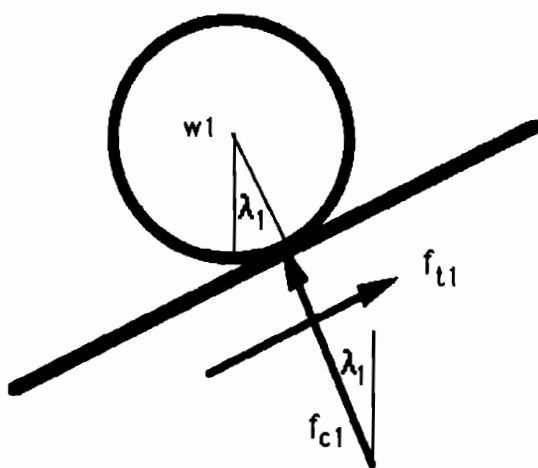


Figure 3.7 - Determining tractive force

The static component of wheel one (f_{s1}) is shown in Equation 3.11.

$$f_{s1} = f_{c1} \frac{\sin(\lambda_1)}{\cos(\lambda_1)} = f_{c1} \tan(\lambda_1) \quad (3.11)$$

Equation 3.11 is calculated for each tire and summed to get the total static tractive force (f_s) for the vehicle.

In order to determine the necessary dynamic component of the tractive force (f_d), a certain acceleration has to be chosen first. It was chosen to have the vehicle reach a forward, or x-direction velocity of .05 m/s in 1.0 seconds from a stand still. Thus, the acceleration (assuming it is uniform) is $.05 \text{ m/s}^2$, and the dynamic component of the tractive force for the entire vehicle becomes Equation 3.12.

$$f_d = m_t 0.05 \quad (3.12)$$

where m_t is the total vehicle mass. If the dynamic component is not harnessed is some way after the first one second of acceleration, the vehicle will continue to increase in speed. In order to avoid this, the dynamic component of the tractive force is made sensitive to the desired velocity (.05 m/s) after the initial second. This is shown in Figure 3.8.

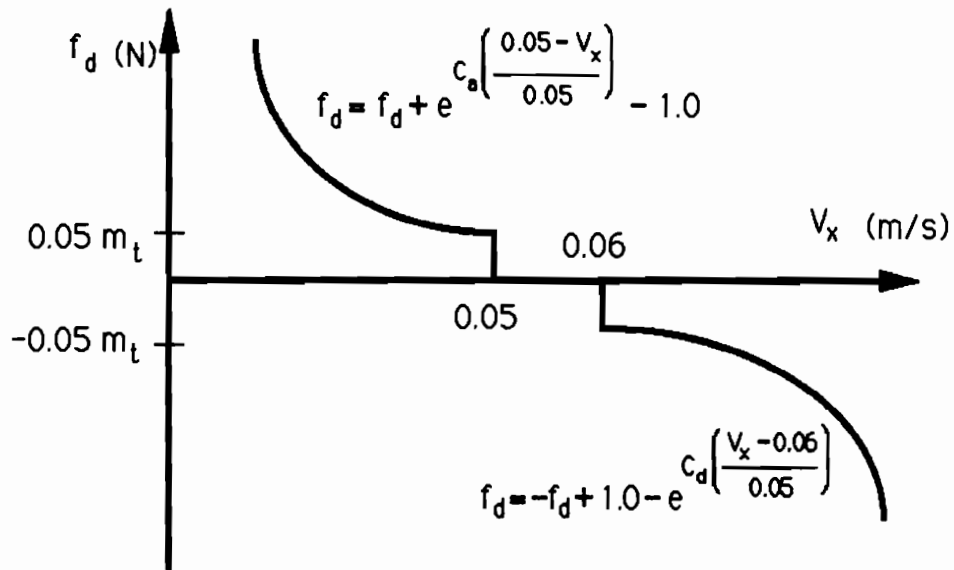


Figure 3.8 - Controlling tractive force

As seen in Figure 3.8, the dynamic component of the tractive force is set to zero if the vehicle has a forward velocity between 0.05 m/s and 0.06 m/s. As the vehicle speeds up past 0.06 m/s, the dynamic component of the tractive force (f_d) decreases in a exponential fashion with a constant of deceleration (C_d) to offset it (see the formula in Figure 3.8). In other words, the wheel torques are reduced or the brakes are applied to bring the vehicle back to the 0.05 m/s to 0.06 m/s velocity range. This typically happens when the vehicle goes downhill. In a similar manner, as the vehicle slows down below 0.05 m/s, the dynamic component of the tractive force increases in a exponential fashion with a constant of acceleration (C_a) to bring the vehicle back to the desired velocity range.

The sensitivity of the dynamic component of the tractive force to the forward velocity is determined by the constants C_a and C_d . These constants can be varied by the user in the input file. The larger C_a is, the more the wheel torques will increase when the velocity is below 0.05 m/s. Likewise,

the larger C_d is, the more the wheel torques will decrease when the velocity is above 0.06 m/s. Setting C_a too large will cause the vehicle to accelerate too fast. As a result, the vehicle races forward and the brakes have to be applied. If C_d is also too large, this braking causes the vehicle to go too slow and the cycle is repeated. Obviously, this oscillation wastes energy. It also causes an instability of the rocker since under hard acceleration, the rocker wants to lift the front tires and under hard deceleration, the front tires come crashing back down.

In order to prevent this, the constants C_a and C_d should be chosen wisely. These constants will have different values for different types of terrain. Values of $C_a = 1.0$ and $C_d = 1.0$ worked fairly well with most terrains, but C_a needs to be increased for steeper hills. The braking constant might also need to be increased for steeper terrains since the vehicle often hops and bounds down large slopes due to the low Martian gravity. Thus, not all tires are in contact with the ground at a given time. Those that are in contact, therefore, have to brake harder. In addition, braking with wheel one and four causes an instability in the rocker. That is to say the middle wheels lift off the ground as the front wheels brake hard. Hence, the front wheels are prevented from braking which means the remaining wheels need to brake harder.

Now that both the static and dynamic components of the tractive force have been found, they are added together to get the total tractive force.

$$f_t = f_s + f_d \quad (3.13)$$

This tractive force is distributed through the wheels according to the user specified constant C_p . The constant C_p is the percentage of the wheel torque seen by the rear wheels. Hence the tractive force of the rear tires is found using Equation 3.14.

$$f_{t3} = f_{t6} = \left(\frac{C_p}{2} \right) f_t \quad (3.14)$$

The rest of the tractive force is split evenly between the remaining four front wheels.

$$f_{t1} = f_{t2} = f_{t4} = f_{t5} = \left(\frac{1 - C_p}{4} \right) f_t \quad (3.15)$$

These wheel torques, however, might not be realizable. It is assumed that the wheel motor can apply any desired tractive force, and that the limiting criterion is the tire-ground contact friction. In other words, although the motor can apply the desired tractive force found in Equations 3.14 and 3.15, the ground to tire interface may not be able to sustain it. This ground to tire contact is modeled with simple coulomb friction, where the coefficient of friction depends on whether the wheel is on sand or rock. Therefore, the maximum tractive force that can be applied is shown in Equation 3.16 where μ is the coefficient of friction under the tire as determined in Section 2.1.

$$(f_{t1})_{\max} = \mu_1 f_{c1} \quad \dots \quad (f_{t6})_{\max} = \mu_6 f_{c6} \quad (3.16)$$

Another thing to consider is the resistive force (f_r) or rolling friction seen by the tire. It is assumed that the resistive force is zero when the tire is on rock. However, as is readily apparent to those who have tried to ride their bikes on the beach, it is far from zero when the tire is on sand. This resistive force is a product of soil work and is heavily dependent on the tire width (w_t) as specified in the input file.

In Bekker's book Introduction to Terrain Vehicle Systems [9], equations for wheel sinkage and resistive force can be found. Using the sand as defined in set 12 on page 240 of Bekker's book, the wheel sinkage (y_s) and resistive force for wheel one (f_{r1}) is found as shown in Equation 3.17.

$$y_s = \left(\frac{3 f_{c1}}{1.9 \sqrt{2r} (0.1 + 3.9 w_t)} \right)$$

$$f_{r1} = \frac{(3 f_{c1})^{1.313}}{4.877 (2r)^{.656} (0.1 + 3.9 w_t)^{.3125}} \quad (3.17)$$

In Equation 3.17, all units are in pounds and inches.

The tractive force as defined in Equations 3.14 and 3.15 are not actually the tractive force applied by the motor. The motor must also overcome the resistive force estimated by Equation 3.17. Thus, the wheel motor torque (Γ) for a given tire is,

$$\Gamma_1 = (f_{t1} + f_{r1}) r \quad \dots \quad \Gamma_6 = (f_{t6} + f_{r6}) r \quad (3.18)$$

And its power consumption (E) is defined as,

$$E_1 = \Gamma_1 \omega_1 \quad \dots \quad E_6 = \Gamma_6 \omega_6 \quad (3.19)$$

where the angular speed of each tire was found in Section 2.2 assuming there was no tangential slip.

If it is found that the sum of the tractive force plus the force to overcome the resistance is greater than the maximum tractive force allowed (Equation 3.16), then the tractive force has exceeded that which the tire ground contact will allow. In other words, any added torque will simply spin the tires. In this case, the tractive force is assigned the maximum tractive force minus the resistance. This is shown in Equation 3.20 for wheel one. All other wheels have similar expressions.

If $(f_{t1} + f_{r1}) > (f_{t1})_{\max}$ then

$$f_{t1} = (f_{t1})_{\max} - f_{r1} \quad (3.20)$$

The other limiting case occurs when braking. The vehicle cannot stop immediately. It is assumed that the brakes can apply any braking force desired, and, thus, can lock the wheels. Nonetheless, the tire ground contact can only sustain a finite braking force. This time, however, the resistive force is an aid rather than a hindrance, as shown in Equation 3.21 for wheel one.

If $f_{t1} < -((f_{t1})_{\max} + f_{r1})$ then

$$f_{t1} = -((f_{t1})_{\max} + f_{r1}) \quad (3.21)$$

In summary, Equations 3.14 and 3.15 are bounded above by Equation 3.20 and below by Equation 3.21. In both limiting cases, no distinction is made between the dynamic and static coefficient of friction.

From Equation 3.19, the power becomes negative as the tractive force becomes more negative than the magnitude of the resistance or when the brakes are applied. Since it is obvious that braking does not add energy to a system, another method of determining the power absorption during braking is applied. The power absorption when the brakes are applied is the force times distance over the time period as shown in Equation 3.22. This is based on the idea that the motors are used for braking which is a worst case scenario from an energy standpoint. Alternatively, regenerative brakes, which would not require very much energy to operate, could be used.

if $(f_{t1} + f_{r1}) < 0.0$ then

$$E_1 = \frac{(|f_{t1}| - f_{r1}) S_t}{t} \quad (3.22)$$

In Equation 3.22, t is the time step and S_t is the total distance traveled by the vehicle's center of gravity in that time step. The time step is specified by the user while the distance traveled is determined later.

The deformation of the tire and the terrain are included to determine the effective stiffness of the contact. It is assumed that the rock terrain has infinite stiffness as compared to that of the tire. Hence, the effective stiffness (k_e) of the tire-ground contact when it is on rock is simply the stiffness of the tire (k_w). If instead the tire is on sand, the soil stiffness (k_s) can be approximated as is shown in Equation 3.23 for wheel one.

$$k_s = \frac{f_{c1}}{y_s} \quad (3.23)$$

The variable y_s , or the wheel sinkage, was found earlier in Equation 3.17. Equation 3.23 is not totally accurate since the soil stiffness is actually a nonlinear phenomenon with somewhat unpredictable characteristics. Nonetheless, it will serve as an approximation. The tire stiffness (k_w) is specified by the user in the input file. Since the soil and tire are in series, the effective stiffness of the tire-ground contact can be determined as is shown in Equation 3.24 for wheel one.

$$k_{e1} = \frac{k_s k_w}{k_s + k_w} \quad (3.24)$$

This stiffness is used to dynamically determine the new contact forces acting on the tires as the vehicle advances. This will be discussed in Section 3.4. Before this can be done, the new position of the vehicle must be determined.

SECTION 3.2 - Z-DIRECTION DYNAMICS

It is expedient to deal with the lateral or z-direction dynamics separately from the xy plane dynamics. This is simply because the vehicle is rigid in the z-direction, while it is not in the xy plane. Hence, whereas the xy plane dynamics requires several freebody diagrams, the z-direction dynamics only requires one, encompassing the entire vehicle. The only drawback is that the entire vehicle's moment of inertia must be calculated at each step. This analysis is carried out in Appendix B to give I_{xt} , I_{yt} , I_{zt} . Notice that the cross terms of the total vehicle moment of inertia are assumed to be negligible. This assumption is based on the idea that the body is significantly heavier than the beam and rocker. In addition, the beam and rocker on both sides are nearly symmetric particularly for nearly flat terrain.

Initially, it was hoped to use a tire map to determine the lateral force on the tires. A tire map plots the lateral force versus the slip angle as seen in Figure 3.9. This map is a result of experimental testing.

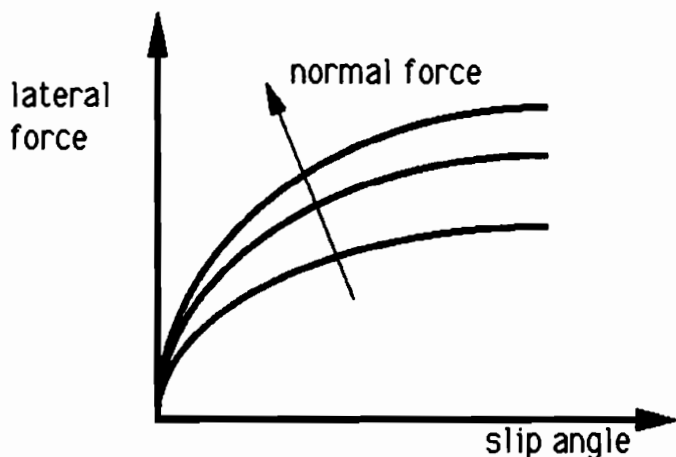


Figure 3.9 – Tire map

If the slip angle is known, the tire's lateral force can be readily determined from Figure 3.9. Although many of these tire maps exist for an elastomer tire on asphalt, none could be found for a spring steel tire on sand. The main problem, however, is not the tire map itself since one could be fabricated, but in the determination of the slip angles.

The slip angle (ψ) is the angle made by the plane of a tire and the tire's direction of travel as is shown in Figure 3.10 for wheel six.

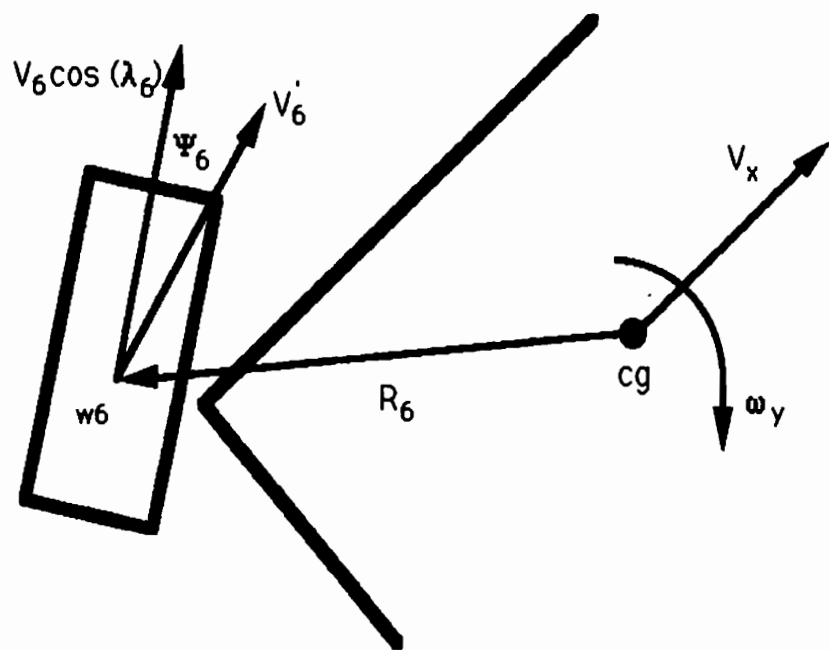


Figure 3.10 - Determining slip angle for wheel six

The slip angle can be extracted by using Equation 3.25.

$$\vec{V}_6 = \vec{V}_x + \omega_y \times \vec{R}_6 \quad (3.25)$$

This will give the direction of travel of wheel six which can be compared with the steering angle to give the slip angle ψ . In comparing Equation 3.25 with Equation 2.23, it is seen that the steering angle is chosen to make the slip angle zero. Nonetheless, slip results if the tire ground contact cannot sustain the lateral force the tire applies. Once the slip angle has been determined, the tire's lateral force can be found from a tire map similar to Figure 3.9 and the z-direction dynamics can be determined.

Unfortunately, the problem is that causality has been violated. In order to use Equation 3.25, the motion of the center of gravity must be known. However, this can not be known until the lateral forces are known. Thus, in the above method, the lateral forces are determined by an equation which assumes they are already known. Since this is obviously impossible, it leads one to question the usefulness of a tire map in the first place. A tire map can be used when the vehicle's path is known. This is called inverse dynamics. For example, a car company may wish to determine what the lateral forces on the tires are as the vehicle follows a specific arc. Since the arc or path is known, the slip angles can be determined and hence, the lateral forces can be found with a tire map. A simulation, as done in this thesis, does not follow a predetermined path. The simulation knows the steering angles and wheel torques and tries to determine from that information where the vehicle is headed. This is called forward dynamics. For forward dynamics, a different approach must be used.

The first step is to break the tractive and contact forces into components which are parallel to, and perpendicular or lateral to the vehicle. There is also a lateral force due to the vehicle roll. In computing the lateral force, at each tire, it is assumed that the component due to the

vehicle roll is equally shared amongst the wheels, as is shown in Figure 3.11

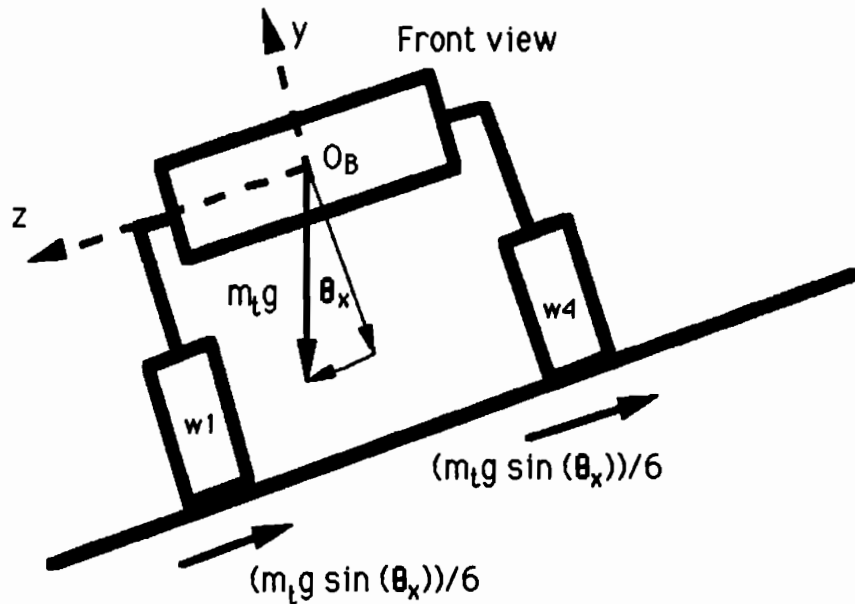


Figure 3.11 - Lateral force due to roll

In other words, if all steering angles were zero, each tire would have a lateral force as shown in Equation 3.26 where f_L is the lateral force.

$$f_{L1} = \frac{m_t g \sin(\theta_x)}{6} \quad \dots \quad f_{L6} = \frac{m_t g \sin(\theta_x)}{6} \quad (3.26)$$

If there is some steering angle, then the force at each tire lateral to the vehicle is as shown in Equation 3.27 for wheel one. All other wheels have the same equation with the appropriate contact angle and steering angle.

$$\mathbf{f}_{L1} = (-f_{t1} \cos(\lambda_1) \sin(\delta_1) + f_{c1} \sin(\lambda_1) \sin(\delta_1) + m_t g \sin(\theta_x)/6) \hat{\mathbf{k}} \quad (3.27)$$

It is of interest to determine what type of torque these forces cause about the vehicle's local y-axis (τ_y). In order to do this, it is necessary to determine the vector \mathbf{R} from the center of gravity to each individual tire's contact point in terms of the vehicle's local frame (O_B). This is shown in Equation 3.28 for the left side of the vehicle. The right side has the same equations with θ_L and θ_{12} replaced with θ_R and θ_{45} and the appropriate contact and steering angles used.

$$\begin{aligned} \mathbf{R}_1 &= (d_1 \cos(\theta_L) + a \cos(\theta_{12}) + e \sin(\theta_{12}) + r \sin(\lambda_1) \cos(\delta_1)) \hat{\mathbf{i}} + \\ &\quad (d_1 \sin(\theta_L) + a \sin(\theta_{12}) - e \cos(\theta_{12}) - r \cos(\lambda_1)) \hat{\mathbf{j}} + \\ &\quad (W/2 - r \sin(\lambda_1) \sin(\delta_1)) \hat{\mathbf{k}} \\ \mathbf{R}_2 &= (d_1 \cos(\theta_L) - b \cos(\theta_{12}) + e \sin(\theta_{12}) + r \sin(\lambda_2) \cos(\delta_2)) \hat{\mathbf{i}} + \\ &\quad (d_1 \sin(\theta_L) + b \sin(\theta_{12}) - e \cos(\theta_{12}) - r \cos(\lambda_2)) \hat{\mathbf{j}} + \\ &\quad (W/2 - r \sin(\lambda_2) \sin(\delta_2)) \hat{\mathbf{k}} \\ \mathbf{R}_3 &= (-d_2 \cos(\theta_L) + e \sin(\theta_L) + r \sin(\lambda_3) \cos(\delta_3)) \hat{\mathbf{i}} + \\ &\quad (-d_2 \sin(\theta_L) - e \cos(\theta_L) - r \cos(\lambda_3)) \hat{\mathbf{j}} + \\ &\quad (W/2 - r \sin(\lambda_3) \sin(\delta_3)) \hat{\mathbf{k}} \end{aligned} \quad (3.28)$$

It is assumed in Equation 3.28 that the beam's pivot runs through the center of gravity of the body. By cross multiplying the appropriate vector in

Equation 3.28 with the z-direction force of Equation 3.27, the moments due to the z-direction forces about the center of gravity are obtained. The resulting \dot{J} term is the torque about the local y-axis and is labeled τ_y^* . This torque is labeled with a prime since the forces at the tires parallel to the vehicle or in the xy plane also contribute to the moment about the vehicle's local y-axis. However, this moment cannot be directly determined. Several freebody diagrams must be used to determine how the xy plane forces affect the center of gravity, since the vehicle is not rigid in this plane. This effect is shown in Section 3.3 to get $\ddot{\tau}_y$. By superimposing these two effects, the total torque about the vehicle's local y-axis is found (τ_y).

$$\tau_y = \tau_y^* + \ddot{\tau}_y \quad (3.29)$$

Since it is assumed that the cross terms of the vehicle's inertia matrix as well as the coriolis effects are negligible, the angular acceleration about the local y-axis is as shown in Equation 3.30.

$$\alpha_y = \frac{\tau_y}{I_{yt}} \quad (3.30)$$

Equation 3.30 would give the angular acceleration if there was no soil resistance. Alternatively, the solution given is as if the vehicle was suspended by a string at the center of gravity when the forces are applied. Clearly, this is not the case. If there is no lateral slip, the vehicle will follow the quasi-Ackerman steering pattern previously presented. If there is slip, the vehicle will follow a different course from the planned course.

To analyze this phenomena, first a technique must be devised to determine if there will be lateral slip or not. In order to do this, the total lateral (z-direction) force at each tire must be found. From Equation 3.27, the z-direction force for each tire contact point is found. However, this is not the only lateral force that the tire will see. Each tire must also resist the torque about the local y-axis as found in Equation 3.29. That is, using wheel one as an example, it will not only see the lateral force it creates, but, because the vehicle is rigid in the z-direction, it will also see the moment created by the other wheels. In order to determine how much of this torque (τ_y) is seen by each wheel, it is necessary to replace τ_y with a force couple system as illustrated in Figure 3.12. The force couple system chosen is linear and increases the farther the wheel is from the center of gravity. Thus, the lateral forces due to the force couple (f_{τ}) at each tire is as seen in Equation 3.31 where the variable q is the slope of the distribution as is shown in Figure 3.12.

$$\begin{aligned} f_{\tau 1} &= q d_{L3} & f_{\tau 2} &= q d_{L2} & f_{\tau 3} &= -q d_{L1} \\ f_{\tau 4} &= q d_{R3} & f_{\tau 5} &= q d_{R2} & f_{\tau 6} &= -q d_{R1} \end{aligned} \quad (3.31)$$

The torque these forces create must be equal to τ_y as is shown in Equation 3.32.

$$\begin{aligned} \tau_y &= f_{\tau 1} d_{L3} + f_{\tau 2} d_{L2} - f_{\tau 3} d_{L1} + \\ &\quad f_{\tau 4} d_{R3} + f_{\tau 5} d_{R2} - f_{\tau 6} d_{R1} \end{aligned} \quad (3.32)$$

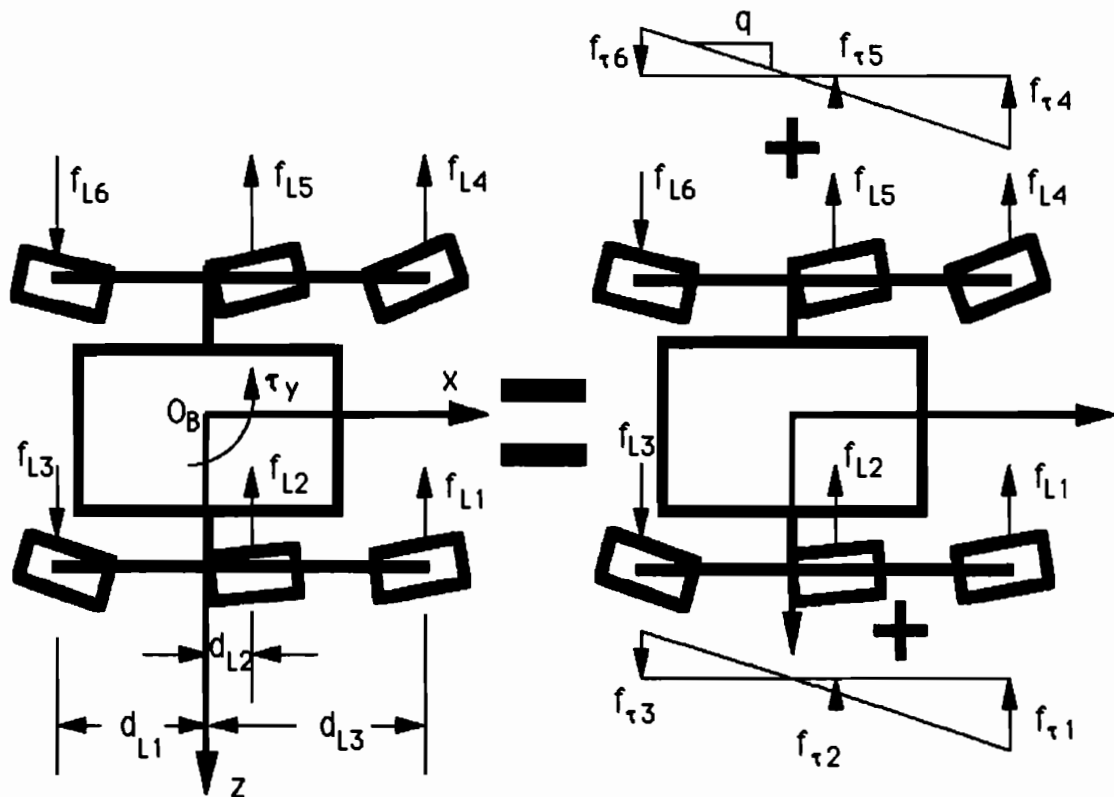


Figure 3.12 – Force couple system

Substituting from Equation 3.31 into Equation 3.32 and solving for the slope results in Equation 3.33.

$$q = \frac{\tau_y}{d_{R1}^2 + d_{R2}^2 + d_{R3}^2 + d_{L1}^2 + d_{L2}^2 + d_{L3}^2} \quad (3.33)$$

Now that the slope is known, the forces due to the force couple at each tire can be found by using Equation 3.31. Finally, by summing the forces seen by each tire in the \$z\$-direction, an approximation to the total \$z\$-direction force (\$f_z\$) seen by each tire is found in Equation 3.34.

$$f_{z1} = f_{t1} + f_{L1} \quad \dots \quad f_{z6} = f_{t6} + f_{L6} \quad (3.34)$$

If the tire-ground contact can sustain this force at each tire, there will be no slip and the vehicle will follow quasi-Ackerman steering. In order to determine if the tire-ground contact can sustain the load, Equation 3.34 is compared with the maximum allowable force as seen in Equation 3.16. The only difference is that Equation 3.16 was used for tangential slip instead of lateral. Lateral slip tends to be associated with a lower coefficient of friction and it is heavily dependent on the velocity of the vehicle. For example, as Don Bickler at JPL pointed out, if someone were to push a parked car along the rear axle, it would not move. If, however, the rear wheels are spinning in place, the vehicle can easily be moved.

For simplicity, this analysis assumes that the maximum lateral force that can be sustained is 75% of the maximum tangential force and is independent of velocity. As is shown in Equation 3.35 for wheel one, the amount of lateral force greater than the maximum lateral force the tire-ground contact can sustain is termed the free force (f_f). In other words, it is the force that is free of friction. If the z-direction force does not overcome friction, the free force is set to zero.

if $|f_{z1}| > .75(f_{t1})_{\max}$ then

$$f_{f1} = |f_{z1}| - .75(f_{t1})_{\max}$$

else $f_{f1} = 0.0$ (3.35)

If some of the wheels overcome the friction force in the lateral direction, or the free force is greater than zero, it does not mean the vehicle will slip. The wheels that do not slip may be able to hold the vehicle on course. In order to determine whether this is possible, the remaining force before slip, or the sticking force (f_{st}), for each tire is calculated. If a certain wheel has started to slip, its sticking force is obviously zero. In other words, only the wheels with a zero free force (Equation 3.35) will have a sticking force. This is shown in Equation 3.36 for wheel one.

If $f_{f1} = 0.0$ then

$$f_{st1} = .75(f_{t1})_{max} - |f_{z1}| \quad (3.36)$$

Next, the torque about the local y-axis is determined using the lateral free forces (τ_f) of Equation 3.35 and then using the sticking force (τ_{st}) of Equation 3.36. If τ_f is greater than τ_{st} , the vehicle will begin to slip with the angular acceleration as seen in Equation 3.37.

$$\alpha_y = \frac{\tau_f - \tau_{st}}{I_{yt}} \quad (3.37)$$

Summing up all the so coined free forces and sticking forces will give the linear acceleration in the z-direction (A_z) when the vehicle is slipping. This is shown in Equation 3.38.

$$f_f = f_{f1} + \dots + f_{f6} \quad f_{st} = f_{st1} + \dots + f_{st6}$$

$$A_z = \frac{f_f - f_{st}}{m_l} \quad (3.38)$$

If τ_{st} can counter τ_f and f_{st} can counter f_f as is usually the case, the vehicle follows the quasi-Ackerman steer principles previously discussed.

The cases when the vehicle does slip laterally in the program is when the vehicle sees a large side slope or when one side of the vehicle sees a steep slope while the other side does not. In the latter case, the vehicle slips in yaw until both sides contact the slope despite the steering angles. These cases will be discussed in the results of Chapter V.

SECTION 3.3 - xy PLANE DYNAMICS

The goal in the xy plane dynamics is to solve for the body centered accelerations. In order to accomplish this, first the rocker is analyzed, then the beam, and finally the body. From the previous work, all the contact forces and tractive forces are known. The next step is to find the internal forces at the pivots for each freebody diagram, which will in turn give the body centered accelerations. The rocker's freebody diagram is shown below.

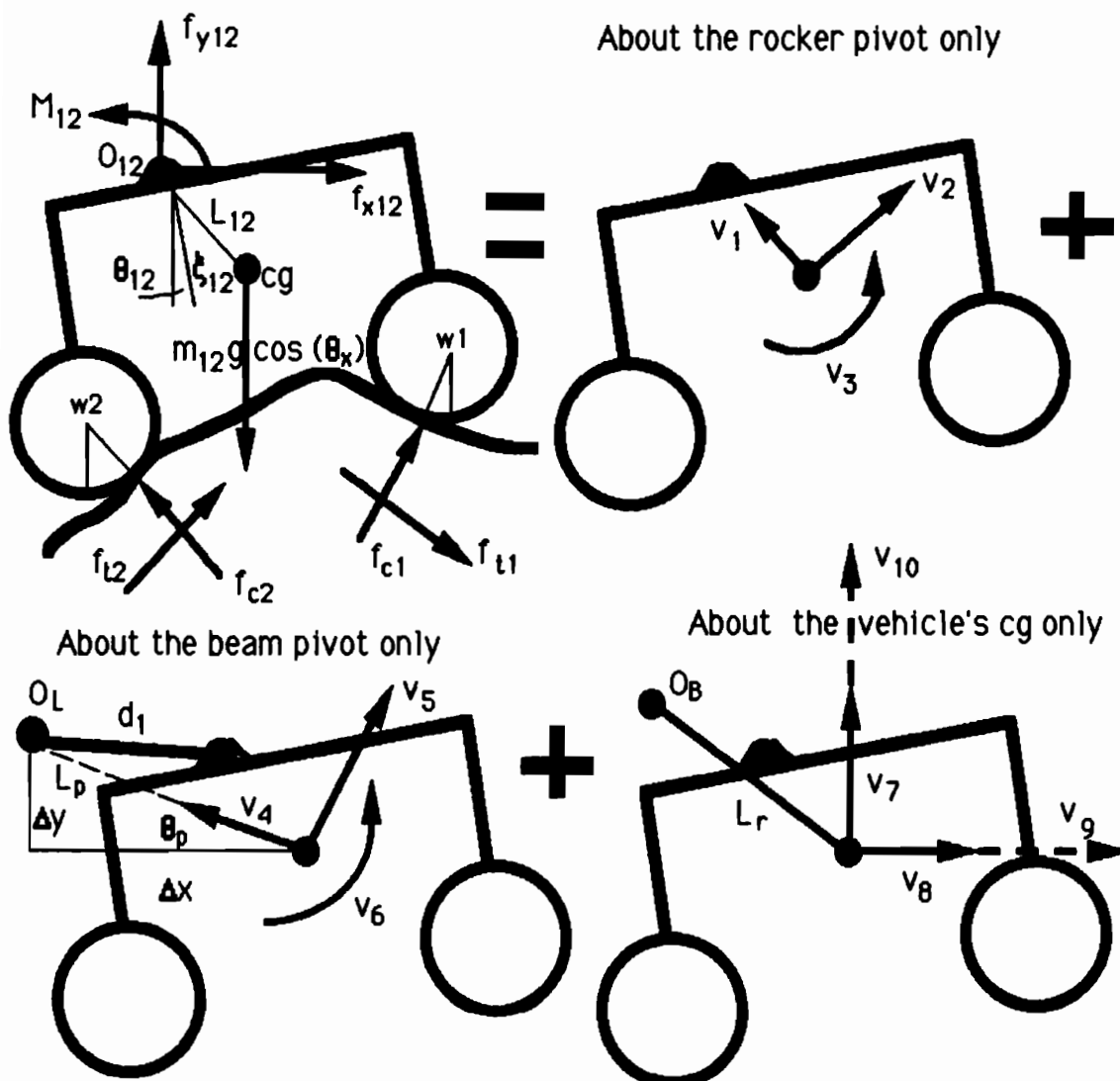


Figure 3.13- Freebody diagram of the left rocker

The symbols used in Figure 3.13 are defined below.

$$v_1 = m_{12} \omega_{12}^2 L_{12} \quad v_2 = m_{12} \alpha_{12} L_{12} \quad v_3 = l_1 \alpha_{12}$$

$$v_4 = m_{12} \omega_L^2 L_p \quad v_5 = m_{12} \alpha_L L_p \quad v_6 = l_1 \alpha_L$$

$$v_7 = m_{12} A_y \quad v_8 = m_{12} A_x \quad v_9 \approx m_{12} \alpha_y L_r$$

$$v_{10} \approx m_{12} \alpha_x W/2$$

where L_r, L_p are lengths between cg's as defined in Figure 3.13

l_1 is defined in Equation 3.47

v_9, v_{10} will be found more accurately using Figure 3.14

The acceleration that the rocker sees is not only that about its own pivot, but also includes the acceleration about the beam pivot as if the rocker pivot is locked. In addition, it includes the acceleration about the vehicle's center of gravity, as if both the rocker and beam pivots were to be locked. An intuitive method of realizing this is to imagine pulling on a string connected to the center of gravity of the vehicle. Even if all the joints are stationary, the internal force at the joints will be nonzero and will increase as the upward acceleration is increased. Hence, the acceleration seen by the rocker includes the acceleration seen by both the beam and the body.

In actuality, the dynamics of the wheels turning about their respective steering axes can also be included. This would create a counter torque about the local y-axis. For simplicity, this is neglected. It would, however, become a significant part of the problem if the wheels were heavy

with respect to the rest of the vehicle and/or the tires were rotated about their steering axes at a high angular velocity. Alternatively, if one wheel is wedged in a rock and the steering motor is activated, a significant counter torque can develop. These are all assumed not to be significant for this analysis.

The x and y components of the acceleration due to the rocker's rotation about its own pivot are found from Equation 3.39.

$$\begin{aligned} \ddot{a}_{x12} &= \alpha_{12} L_{12} \cos(\theta_{12} + \xi_{12}) - \omega_{12}^2 L_{12} \sin(\theta_{12} + \xi_{12}) \\ \ddot{a}_{y12} &= \alpha_{12} L_{12} \sin(\theta_{12} + \xi_{12}) + \omega_{12}^2 L_{12} \cos(\theta_{12} + \xi_{12}) \end{aligned} \quad (3.39)$$

Before finding the x and y components of the rocker's acceleration about the beam pivot as if the rocker joint is fixed, it is necessary to first find θ_p and L_p as seen in Figure 3.13. This can be determined by using Equation 3.40.

$$L_p = \sqrt{(\Delta x)^2 + (\Delta y)^2} \quad \theta_p = \text{ATAN}\left(\frac{\Delta y}{\Delta x}\right)$$

where

$$\Delta x = d_1 \cos(\theta_L) + L_{12} \sin(\theta_{12} + \xi_{12}) \quad (3.40)$$

$$\Delta y = d_1 \sin(\theta_L) - L_{12} \cos(\theta_{12} + \xi_{12})$$

Thus, the x and y components of the rocker's acceleration about the beam pivot alone is calculated in Equation 3.41.

$$\begin{aligned}\ddot{a}_{x12} &= -\alpha_L L_p \sin(\theta_p) - \omega_L^2 L_p \cos(\theta_p) \\ \ddot{a}_{y12} &= \alpha_L L_p \cos(\theta_p) - \omega_L^2 L_p \sin(\theta_p)\end{aligned}\quad (3.41)$$

Next, acceleration of the left rocker due to the vehicle's center of gravity motion is analyzed with all joints locked. The vehicle's center of gravity will vary in position with the joint angles. However, as already mentioned, it is assumed in this analysis that the vehicle's center of gravity remains at the centroid of the body. This is a reasonable approximation if the body is significantly heavier than the rest of the vehicle. As seen in Figure 3.13, vectors v_7 and v_8 contain the accelerations A_y and A_x . The variables A_y and A_x are the linear components of acceleration seen at the vehicle's center of

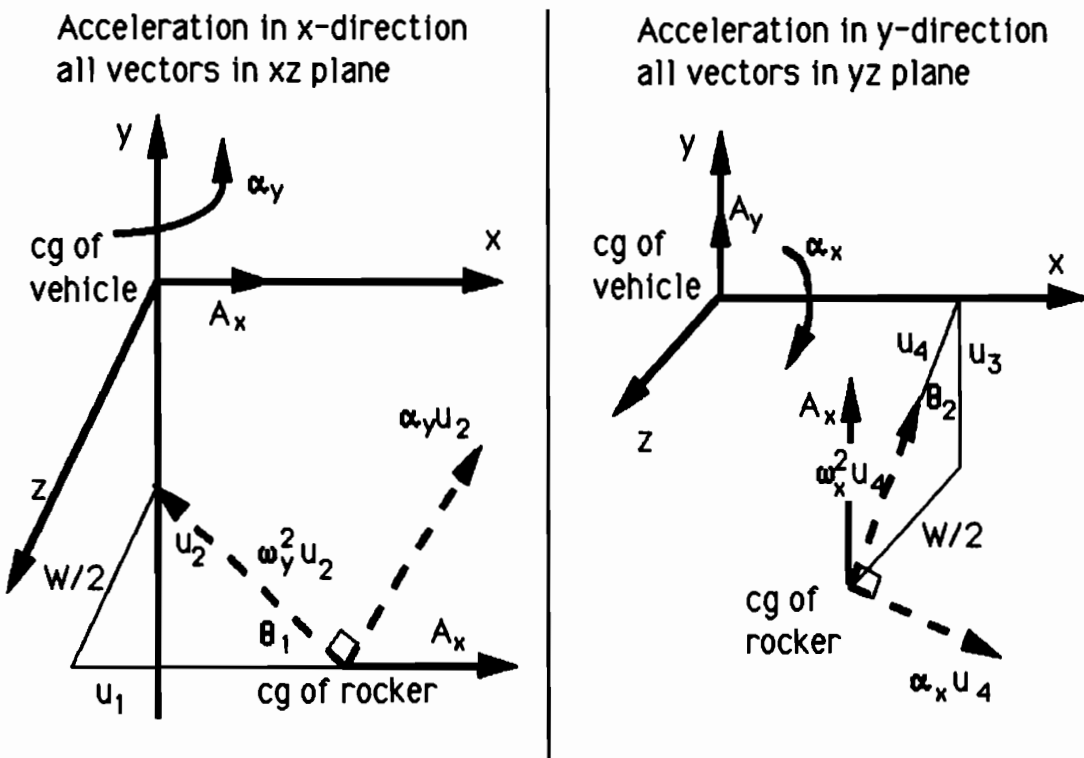


Figure 3.14 - Rocker's acceleration due to vehicle's cg motion

gravity. The dashed vectors v_9 and v_{10} of Figure 3.13 are due to the roll and yaw angular accelerations of the vehicle. This is shown with more detail in the three dimensional views of Figure 3.14.

Since only the xy plane dynamics are of interest (z-direction dynamics are discussed in Section 3.2), it is necessary to find the xy plane components of the accelerations due to roll (α_x) and yaw (α_y). Thus, the x and y components of acceleration due to the body's motion are determined using Figure 3.14 and shown in Equation 3.42.

$$\ddot{a}_{x12} = A_x + \alpha_y u_2 \cos(\theta_1) - \omega_y^2 u_2 \sin(\theta_1)$$

$$\ddot{a}_{y12} = A_y - \alpha_x u_4 \sin(\theta_2) + \omega_x^2 u_4 \cos(\theta_2)$$

where

(3.42)

$$u_1 = d_1 \cos(\theta_L) + L_{12} \sin(\theta_{12} + \zeta_{12})$$

$$u_2 = \sqrt{u_1^2 + (W/2)^2} \quad \theta_1 = \text{ATAN}\left(\frac{u_1}{W/2}\right)$$

$$u_3 = -d_1 \sin(\theta_L) + L_{12} \cos(\zeta_{12} + \theta_{12})$$

$$u_4 = \sqrt{u_3^2 + (W/2)^2} \quad \theta_2 = \text{ATAN}\left(\frac{W/2}{u_2}\right)$$

Summing all the linear accelerations results in Equation 3.43.

$$\dot{a}_{x12} = \dot{a}_{x12} + \ddot{a}_{x12} + \ddot{a}_{x12}$$

$$\dot{a}_{y12} = \dot{a}_{y12} + \ddot{a}_{y12} + \ddot{a}_{y12}$$

(3.43)

Thus, Equation 3.44 can be written for the internal forces at the left rocker's pivot as seen in Figure 3.13 with the coriolis terms neglected.

$$f_{x12} = m_{12} a_{x12} - f_{t2} \cos(\lambda_2) \cos(\delta_2) - f_{t1} \cos(\lambda_1) \cos(\delta_1) + \\ f_{c2} \sin(\lambda_2) \cos(\delta_2) + f_{c1} \sin(\lambda_1) \cos(\delta_1) \quad (3.44)$$

$$f_{y12} = m_{12} a_{y12} - f_{t2} \sin(\lambda_2) - f_{t1} \sin(\lambda_1) - f_{c2} \cos(\lambda_2) - \\ f_{c1} \cos(\lambda_1) + m_{12} g \cos(\theta_x)$$

Similar equations can be written for the right side rocker. Care must be taken in applying Equation 3.42 or the accelerations of Figure 3.14 to the right side since the direction of acceleration due to roll and yaw changes. Looking back at the equations, it is found that there are too many unknowns. The unknowns are buried in the two acceleration terms of Equation 3.43 and are α_{12} , ω_{12} , α_L , ω_L , A_x , A_y , α_x , α_y in addition to the unknowns that are being solved for f_{x12} and f_{y12} . In actuality, ω_{12} and ω_L are dependent on α_{12} and α_L and can be determined if the time history is known. For example, if uniform acceleration is assumed, ω_{12} can be solved as shown in Equation 3.45.

$$\omega_{12} = \dot{\omega}_{12} + \alpha_{12} t \quad (3.45)$$

where

$\dot{\omega}_{12}$ is the angular velocity of the previous step

t is the time period of the step

By summing moments about the rocker's pivot (O_{12}) as shown in Figure 3.13, an additional equation can be found using the general form of Equation 3.46.

$$\Sigma M_{O_{12}} = f L + M = mAL + I\alpha \quad (3.46)$$

First, the right side of Equation 3.46 is found as shown in Equation 3.47 where M stands for moment.

$$\begin{aligned} \Sigma M &= \{ [(L_{12} \sin(\theta_{12} + \zeta_{12})) \dot{i} + (-L_{12} \cos(\theta_{12} + \zeta_{12})) \dot{j}] \times \\ &\quad m_{12} [(a_{x12}) \dot{i} + (a_{y12}) \dot{j}] \} + (I_1 \alpha_{12} + I_1 \alpha_L) \dot{k} \end{aligned} \quad (3.47)$$

where

$$I_1 = I_{12} + m_{12} L_{12}^2$$

The cross products of the left side of the moment Equation 3.46 are shown in Equation 3.48. The terms in successive order in Equation 3.48 are due to the forces at wheel one, due to the forces at wheel two, due to the rocker's weight, and due to the moment at the hinge (M_{12}).

$$\begin{aligned}
 \Sigma M = & \{ [(a \cos(\theta_{12}) + e \sin(\theta_{12}) + r \sin(\lambda_1) \cos(\delta_1)) \dot{i} + \\
 & (a \sin(\theta_{12}) - e \cos(\theta_{12}) - r \cos(\lambda_1)) \dot{j}] \times \\
 & [(f_{t1} \cos(\lambda_1) \cos(\delta_1) - f_{c1} \sin(\lambda_1) \cos(\delta_1)) \dot{i} + \\
 & (f_{c1} \cos(\lambda_1) + f_{t1} \sin(\lambda_1)) \dot{j}] \} + \\
 & \{ [(-b \cos(\theta_{12}) + e \sin(\theta_{12}) + r \sin(\lambda_2) \cos(\delta_2)) \dot{i} + \\
 & (-b \sin(\theta_{12}) - e \cos(\theta_{12}) - r \cos(\lambda_2)) \dot{j}] \times \\
 & [(f_{t2} \cos(\lambda_2) \cos(\delta_2) - f_{c2} \sin(\lambda_2) \cos(\delta_2)) \dot{i} + \\
 & (f_{c2} \cos(\lambda_2) + f_{t2} \sin(\lambda_2)) \dot{j}] \} + \\
 & \{ [(L_{12} \sin(\theta_{12} + \xi_{12})) \dot{i} + (-L_{12} \cos(\theta_{12} + \xi_{12})) \dot{j}] \times \\
 & [(-m_{12} g \cos(\theta_x)) \dot{j}] \} + M_{12}
 \end{aligned} \tag{3.48}$$

By equating Equation 3.47 with 3.48, the third equation for the rocker is found. Hence, there are eight unknowns (α_{12} , α_L , A_x , A_y , α_x , α_y , f_{x12} , f_{y12}) and only three equations. This situation improves as the beam's freebody diagram is considered next as seen in Figure 3.15.

Before proceeding to the beam, it is assumed that no moment is transmitted at the rocker hinge. That is M_{12} in Equation 3.48 is zero. In other words, there is no friction in the joint. If, however, the rocker hits the mechanical stop, it will transmit this moment to the beam. To check if the rocker has hit the stop, the relative angle $\theta_L - \theta_{12}$ is monitored. If indeed, the rocker hits the mechanical stop, then α_{12} and ω_{12} are set to zero.

This simplifies Equation 3.47 since \dot{a}_{x12} and \dot{a}_{y12} are both zero for this case as can be seen by analysing Equation 3.39. The moment term $l_1 \alpha_{12}$ also goes to zero. Notice that the resulting impact of the rocker hitting the stop is neglected. Only the moment to stop the motion (M_{12}) is solved in Equation 3.48 and applied to the beams freebody diagram. This should be an adequate approximation for the low speeds which the vehicle is operating under.

In addition, due to the steering angle of the wheels and the contact angle, the contact forces will cause a moment about the rocker's local x-axis of the freebody diagram. Any z-direction offset in the hinges will have the same effect. For simplicity, and since it is of secondary importance, this effect is neglected. The moment about the rocker's local y-axis is significant and was handled in Section 3.2 for the z-direction dynamics. The freebody diagram of the beam is as shown in Figure 3.15.

As already mentioned, the moment M_{12} is zero unless the mechanical stop is hit. It does not add another unknown to the Equation since α_{12} is zero when M_{12} is not zero. The beam's pivot, on the other hand, is not entirely passive. It does have a resistive moment (M_L) as seen in Figure 3.15 due to the inertia of the body. This moment does not add to the unknowns either since it is dependent on the beams' angular accelerations (α_L and α_R) for the left and right side. Recall that the body attitude is maintained at an angle halfway between the beam angles by the differential. This can be expressed, as is shown in Equation 3.49, where θ_B is the body angle with respect to the vehicle's local x-axis.

$$\theta_B = (\theta_L + \theta_R)/2 \quad (3.49)$$

Differentiating twice, the angular acceleration of the body is found. If this angular acceleration is multiplied by the moment of inertia of the body about the vehicle's local z-axis (I_z), the result is the moment at the beam pivot. It is assumed that the moment required to cause the body's angular acceleration about the z-axis is split evenly between the two beams. This is shown in Equation 3.50 by the 0.5 coefficient.

$$\alpha_B = (\alpha_L + \alpha_R)/2 \quad M_L = 0.5 I_z \alpha_B \quad (3.50)$$

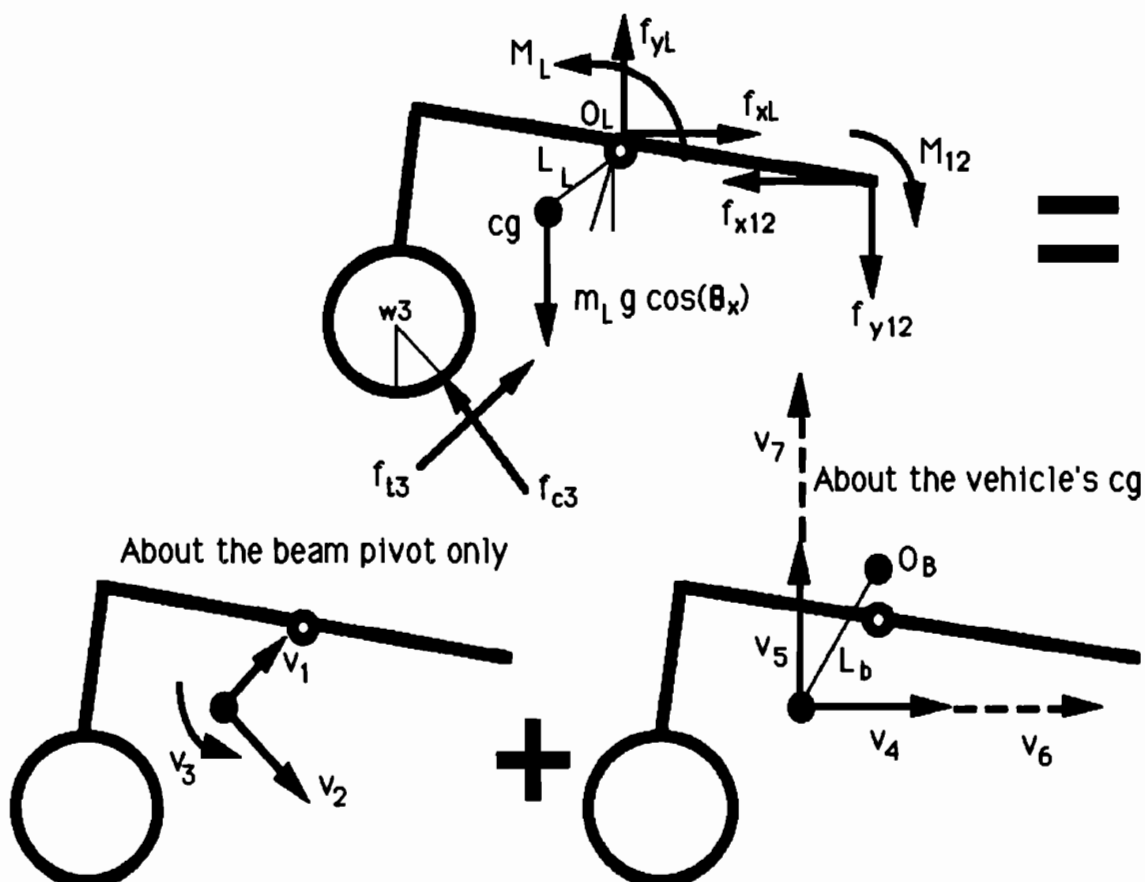


Figure 3.15 - Beam freebody diagram

$$v_1 = m_L \omega_L^2 L_L \quad v_2 = m_L \alpha_L L_L \quad v_3 = l_2 \alpha_L \quad v_4 = m_L A_x$$

$$v_5 = m_L A_y \quad v_6 \approx m_L \alpha_y L_b \quad v_7 \approx m_L \alpha_x W/2$$

where L_b is the length defined in Figure 3.15

l_2 is defined in Equation 3.55

v_6 and v_7 will be found more accurately using Figure 3.16

The acceleration that the beam sees is not only the acceleration about its own pivot, but also includes the acceleration about the vehicle's center of gravity as if the beam pivot is locked. This is, however, less complicated than the rocker's dynamics since the beam is closer in the chain of events to the center of gravity of the vehicle.

The x and y components of acceleration due to the beam's rotation about its own pivot are found from Equation 3.51.

$$\begin{aligned} \dot{a}_{xL} &= \alpha_L L_L \cos(\xi_L - \theta_L) + \omega_L^2 L_L \sin(\xi_L + \theta_L) \\ \dot{a}_{yL} &= -\alpha_L L_L \sin(\xi_L - \theta_L) + \omega_L^2 L_L \cos(\xi_L + \theta_L) \end{aligned} \quad (3.51)$$

Next, acceleration of the left beam due to the vehicle's center of gravity motion is analyzed with the beams' pivots locked. As was done for the rocker, this acceleration is shown with more detail in the three dimensional views of Figure 3.16.

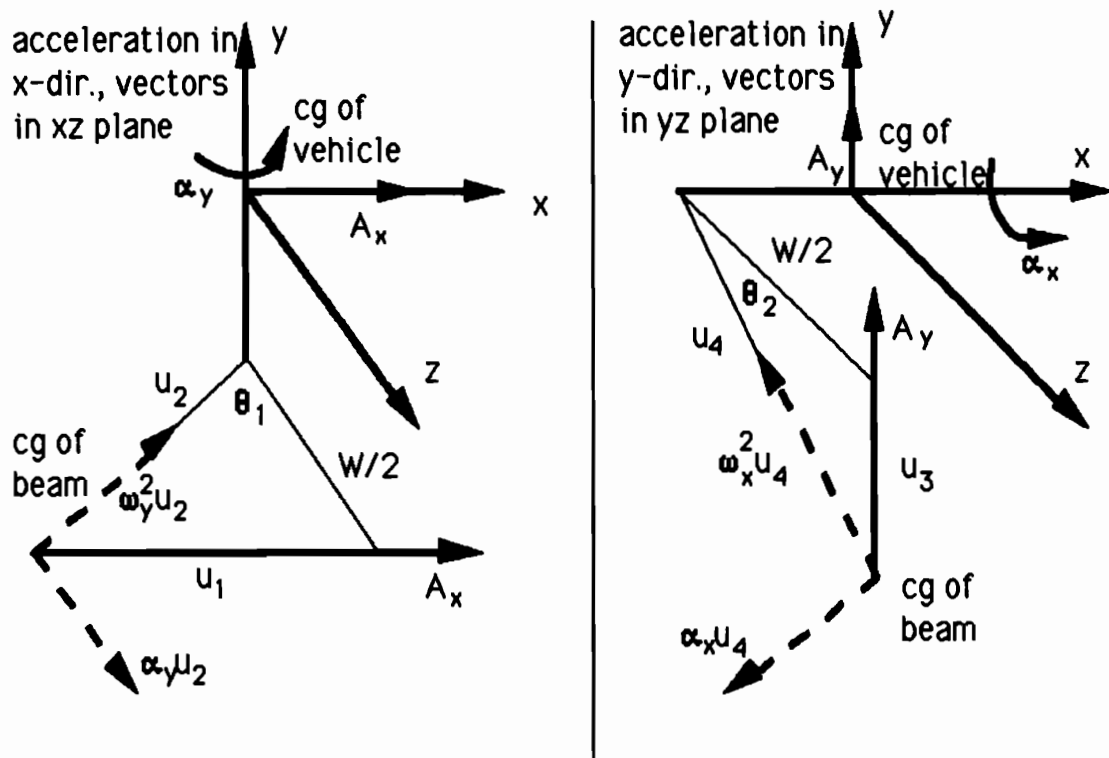


Figure 3.16 – Beam's acceleration due to vehicle's cg motion

Again, since only the xy plane dynamics are of interest here, it is necessary to find the xy plane components of the acceleration.

$$\dot{a}_{xL} = A_x + \alpha_y u_2 \cos(\theta_1) + \omega_y^2 u_2 \sin(\theta_1)$$

$$\dot{a}_{yL} = A_y - \alpha_x u_4 \cos(\theta_2) + \omega_x^2 u_4 \sin(\theta_2)$$

where

(3.52)

$$u_1 = L \sin(\zeta_L - \theta_L) \quad u_2 = \sqrt{u_1^2 + (W/2)^2} \quad u_3 = L \cos(\zeta_L - \theta_L)$$

$$u_4 = \sqrt{u_3^2 + (W/2)^2} \quad \theta_1 = \text{ATAN}\left(\frac{u_1}{W/2}\right) \quad \theta_2 = \text{ATAN}\left(\frac{u_3}{W/2}\right)$$

Care must be taken in finding the right side accelerations due to the body's motion. This happens because the accelerations due to the roll and yaw change sign. Summing all the linear accelerations results in Equation 3.53.

$$\ddot{a}_{xL} = \ddot{a}_{xL}^* + \ddot{a}_{xL}^{\circ} \quad \ddot{a}_{yL} = \ddot{a}_{yL}^* + \ddot{a}_{yL}^{\circ} \quad (3.53)$$

Thus, Equation 3.54 can be written for the internal forces at the pivot of the left beam, with the coriolis terms neglected.

$$\begin{aligned} f_{xL} &= m_L \ddot{a}_{xL} + f_{x12} - f_{t3} \cos(\lambda_3) \cos(\delta_3) + f_{c3} \sin(\lambda_3) \cos(\delta_3) \\ f_{yL} &= m_L \ddot{a}_{yL} + f_{y12} - f_{t3} \sin(\lambda_3) - f_{c3} \cos(\lambda_3) + m_L g \cos(\theta_x) \end{aligned} \quad (3.54)$$

The third equation for the beam can be found by summing the moments created in Figure 3.15 about the beam's pivot using the general form of Equation 3.46. Equation 3.55 is the right side of Equation 3.46.

$$\Sigma M = \{ [(-L_L \sin(\zeta_L - \theta_L)) \dot{i} + (-L_L \cos(\zeta_L - \theta_L)) \dot{j}] \times m_L [(a_{xL}) \dot{i} + (a_{yL}) \dot{j}] \} + (I_2 \alpha_L) \dot{k} \quad (3.55)$$

$$\text{where } I_2 = I_L + m_L L_L^2$$

The terms, in successive order for the left side of Equation 3.46 for the beam's freebody diagram, are due to the forces on wheel three, the pivot forces acting on the rocker, and the beam's weight and moments acting on it. This is shown in Equation 3.56.

$$\begin{aligned}
 \Sigma M = & \{ [(-d_2 \cos(\theta_L) + e \sin(\theta_L) + r \sin(\lambda_3)) \dot{i} + \\
 & (-d_2 \sin(\theta_L) - e \cos(\theta_L) - r \cos(\lambda_3)) \dot{j}] \times \\
 & [(-f_{c3} \sin(\lambda_3) \cos(\delta_3) + f_{t3} \cos(\lambda_3) \cos(\delta_3)) \dot{i} + \\
 & (f_{c3} \cos(\lambda_3) + f_{t3} \sin(\lambda_3)) \dot{j}] \} + \\
 & \{ [(d_1 \cos(\theta_L)) \dot{i} + (d_1 \sin(\theta_L)) \dot{j}] \times \\
 & [(-f_{x12}) \dot{i} + (-f_{y12}) \dot{j}] \} + \\
 & \{ [(-L_L \sin(\zeta_L - \theta_L)) \dot{i} + (-L_L \cos(\zeta_L - \theta_L)) \dot{j}] \times \\
 & [-m_L g \cos(\theta_x) \dot{j}] \} - M_{12} + M_L
 \end{aligned} \tag{3.56}$$

By equating the expression of Equation 3.55 with that of Equation 3.56, the moment equation of the beam is derived. Finally, moving to the last freebody diagram, the body's acceleration is analyzed.

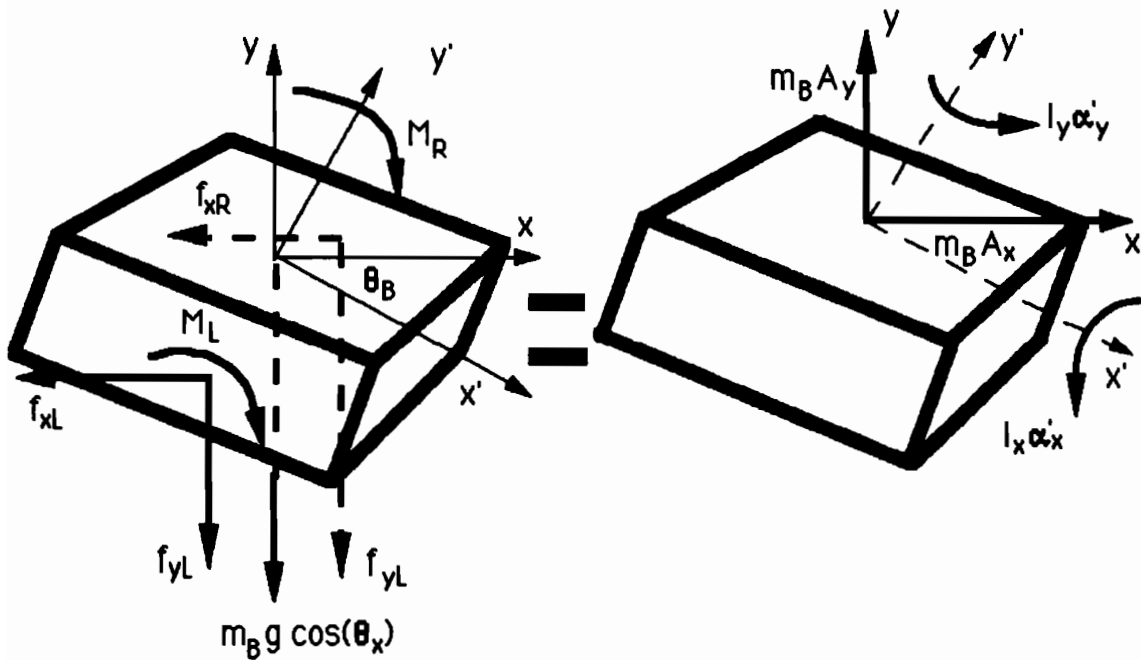


Figure 3.17 - Freebody diagram of the body

The linear accelerations of the body are solved for in the straight forward manner of Equation 3.57.

$$A_x = \frac{-f_{xL} - f_{xR}}{m_B} \quad A_y = \frac{-f_{yL} - f_{yR}}{m_B} - g \cos(\theta_x) \quad (3.57)$$

The moments about the vehicle's local x and y-axis are found in Equation 3.58.

$$M_x = f_{yL} \frac{W}{2} - f_{yR} \frac{W}{2} \quad M_y = f_{xR} \frac{W}{2} - f_{xL} \frac{W}{2}$$

$$M_z = -M_L - M_R \quad (3.58)$$

It is convenient to rotate these moments about the local z axis through angle θ_B to the primed coordinate system as is shown in Figure 3.17. In this manner, the moments of inertia terms for the body need not be reevaluated as θ_B varies. The moments about the primed axes are as shown in Equation 3.59.

$$\dot{M}_x = M_x \cos(\theta_B) + M_y \sin(\theta_B) \quad (3.59)$$

$$\dot{M}_y = -M_x \sin(\theta_B) + M_y \cos(\theta_B) \quad \dot{M}_z = M_z$$

The angular acceleration about the primed axes can be found using Euler's equations shown in Equation 3.60 since the body is assumed to be homogeneous and symmetric about these axes [12].

$$\begin{aligned}\ddot{\alpha}_x - \ddot{\omega}_x &= \frac{l_y - l_z}{l_x} \dot{\omega}_y \dot{\omega}_z + \frac{\dot{M}_x}{l_x} \\ \ddot{\alpha}_y - \ddot{\omega}_y &= \frac{l_z - l_x}{l_y} \dot{\omega}_z \dot{\omega}_x + \frac{\dot{M}_y}{l_y} \\ \ddot{\alpha}_z - \ddot{\omega}_z &= \frac{l_x - l_y}{l_z} \dot{\omega}_x \dot{\omega}_y + \frac{\dot{M}_z}{l_z} = \frac{\alpha_R + \alpha_L}{2}\end{aligned}\quad (3.60)$$

The moments of inertia are found in Equation 3.7. Notice that α_B can be found alternatively using α_R and α_L . These three simultaneous differential equations were solved using a second order Runge-Kutta algorithm. In actually programming this method, it was found that the first term in each of the equations in 3.60 was negligible. This is because the moment of inertia about each axis is similar and the angular velocities about these axes are relatively small compared to the angular accelerations. In order to save computer time, Equation 3.60 was simplified to Equation 3.61 as a close approximation.

$$\ddot{\alpha}_x = \frac{\dot{M}_x}{l_x} \quad \ddot{\alpha}_y = \frac{\dot{M}_y}{l_y} \quad \ddot{\alpha}_B = \frac{\dot{M}_z}{l_z} = \frac{\alpha_R + \alpha_L}{l_z} \quad (3.61)$$

The angular accelerations are then converted back to the local frame by performing a rotation through angle $-\theta_B$ about the z-axis. This results in Equation 3.62.

$$\alpha_x = \alpha_x \cos(\theta_B) - \alpha_y \sin(\theta_B)$$

$$\alpha_y = \alpha_y \sin(\theta_B) - \alpha_x \cos(\theta_B) \quad (3.62)$$

$$\alpha_B = \alpha_B$$

If α_y is multiplied by the total moment of inertia of the vehicle about the y-axis (I_{yt}) as seen in Equation 3.63, the resulting torque due to the xy plane forces (τ_y) is found. This torque is necessary for the z-direction dynamics of Section 3.2.

$$\tau_y = I_{yt} \alpha_y \quad (3.63)$$

All the unknowns can indeed be solved for by means of this analysis. The unknowns are listed below as previously defined. They include the right side of the vehicle.

α_{12}	α_L	f_{x12}	f_{y12}	f_{xL}	f_{yL}	α_{45}	α_R
f_{x45}	f_{y45}	f_{xR}	f_{yR}	A_x	A_y	α_x	α_y

All other variables can be solved in terms of the above list. There are, in all, 16 unknowns. As for the number of equations, there are three for each of the two rockers, three for each of the two beams, and four independent equations for the body. Thus, there are 16 equations which can be used to solve for the 16 unknowns. This method can be used to determine the instantaneous accelerations and forces.

Unfortunately, as it turns out, these accelerations and forces are not what the vehicle will actually experience a very small time instant after

the forces are applied. Just as in the z-direction dynamics, these equations are valid for a reasonable time period only if there is no terrain interface. In other words, if the vehicle is hung above the ground at the center of gravity by a piece of string and the contact forces are applied at the tires by some means, it will experience the acceleration that can be found by the 16 equations in this section. One must also superimpose the z-direction dynamics to get this result. To intuitively realize this, imagine that the equations predict a positive angular acceleration (counterclockwise) of the left rocker. As a result of this acceleration, wheel two sinks into the terrain and retards or reverses the predicted angular acceleration. How much this affects the predicted value depends on the incoming terrain as well as the effective stiffness at the tire-ground contact. If a downward slope is reached, the angular acceleration will actually be negative not positive. Therefore a different approach must be devised. However, many of the previous ideas in this section are still used.

The approach used in the program is to use the linear and angular accelerations of the previous step and try to converge the linear accelerations in an iterative manner. Using the previous a_{x12} and a_{y12} , Equation 3.44 is evaluated. For the initial step, all accelerations are assumed to be zero. The resulting internal rocker pivot forces will not be the same as in the previous step since the current position will have different contact forces. These contact forces will be determined in Section 4.1. Once f_{x12} and f_{y12} have been determined, Equation 3.54 is evaluated again using the acceleration of the previous step. In this manner, f_{xL} and f_{yL} are found. The beam pivot forces on the right side of the vehicle are found in a similar manner. The linear accelerations are then evaluated,

with the above assumptions, using Equation 3.57. If the resulting linear acceleration is the same as that assumed, or is equal to the previous step's acceleration within an error tolerance of 0.01 m/s^2 , then the program proceeds. If not, the assumed linear acceleration is incorrect. The program then takes the average of the assumed linear acceleration and that found from the assumed value. The process is then repeated. This iterative method converges within a few steps to a 'correct' linear acceleration based on the assumed angular accelerations.

In a preview of what will be covered in the next chapter, the vehicle is then advanced by the amount dictated by the linear accelerations (x and y -direction in this section and z -direction in Section 3.2). The vehicle joints are then adjusted in a dynamic manner, the new contact forces are found, and its new position is determined. With the knowledge of the new position and the previous one, the actual angular acceleration of all the joints and the body can be found. If the resulting angular accelerations are not the same as those assumed, the process is iterated. That is, the vehicle is moved back to its previous position and the new assumed angular accelerations become the average of the previously assumed values and those found when the vehicle is advanced based on the previously assumed values. Each time the process is iterated, the new linear accelerations are determined by the iterative method already discussed. When the assumed angular accelerations are the same as those found when the vehicle is advanced based on the assumed values within the error tolerance, the iterative process is terminated and the vehicle is ready for its next step.

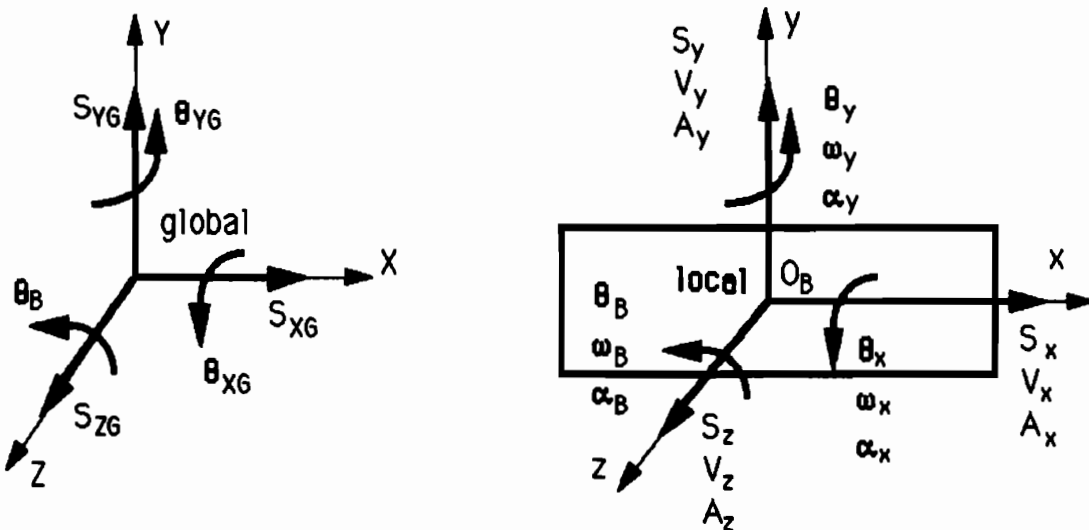
CHAPTER IV

MOVING FORWARD

SECTION 4.1 - NEW CONTACT FORCES

Using the three linear acceleration terms, as well as the angular accelerations about the local y and x-axes found in Sections 3.2 and 3.3, the vehicle is advanced with all joints locked. The roll angular acceleration, that about the local x-axis, is assumed to be the same as in the previous step for the first iteration. Later, the joint positions are adjusted, and the vehicle is rolled based on how much each tire is compressed. The angular accelerations found by comparing the current and previous positions are compared to the assumed values. If they are different the process is iterated.

The position of the vehicle's center of gravity, which is again assumed to be synonymous with the body's centroid for this analysis, is found by successively multiplying the homogeneous transformation matrix at each step. For clarity, the nomenclature between the vehicle's local frame centered at the vehicle's center of gravity and the global coordinate system is illustrated in Figure 4.1.



θ terms - angular displacement

ω terms - angular velocity

α terms - angular acceleration

S terms - linear displacement

V terms - linear velocity

A terms - linear acceleration

Figure 4.1 - Nomenclature

$$S_{xG} = X_3 + \Delta X \cos(\theta_y) + \Delta Y \sin(\theta_x) \sin(\theta_y) - 0.5 W \cos(\theta_x) \sin(\theta_y)$$

$$S_{yG} = Y_3 + \Delta Y \cos(\theta_x) + 0.5 W \sin(\theta_x) \quad (4.1)$$

$$S_{zG} = Z_3 - \Delta X \sin(\theta_y) + \Delta Y \sin(\theta_x) \cos(\theta_y) - 0.5 W \cos(\theta_x) \cos(\theta_y)$$

where

$$\Delta Y = r \cos(\lambda_2) + e \cos(\theta_L) + d_2 \sin(\theta_L)$$

$$\Delta X = d_2 \cos(\theta_L) - e \sin(\theta_L) - r \sin(\lambda_3) \cos(\delta_3)$$

The variables on the global frame of Figure 4.1 are the components of the position of the vehicle's center of gravity. The vehicle's center of gravity in global coordinates for the initial position is found using the known position of wheel three as is shown in Equation 4.1.

For the initial position, θ_{x_0} and θ_x as well θ_{y_0} and θ_y are the same. The initial yaw angle was specified by the user, and the initial roll was solved for as in Chapter 2 to put all the wheels on the ground. For the first time step, the variables in the local frame of Figure 4.1 are measured with respect to the initial local frame. Hence, since the orientation of the local frame and the global frame are not, in general, the same at the first time step, unless the initial roll and yaw are zero, the roll and yaw measured relative to the local frame and global frame are different. As was mentioned in Chapter 2, the vehicle is assumed to first yaw about the local y-axis and then roll about the local x-axis.

Since the time step being used is very small (depends on the users input, but usually around 0.05 seconds) and the forward velocity or V_x is slow (about 0.05 m/s), uniform acceleration can be assumed to be a good approximation. This is shown graphically in Figure 4.2.

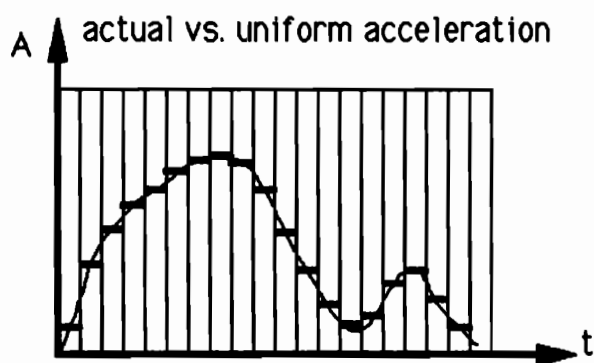


Figure 4.2 - Uniform acceleration assumption

Based on the assumption that the angular acceleration of the joints are the same as in the previous step (zero for initial conditions) as explained in Section 3.3, the vehicle is advanced. In other words, the center of gravity is moved linearly and rotated about the y-axis and x-axis as is shown in Equation 4.2. The primed linear and angular velocity terms in Equation 4.2 are the initial velocities at the step and they vary linearly throughout the step. The distances and rotation variables of Equation 4.2 are measured with respect to the local frame.

$$\begin{aligned} S_x &= 0.5 A_x t^2 + V_x' t & S_y &= 0.5 A_y t^2 + V_y' t \\ S_z &= 0.5 A_z t^2 + V_z' t & \theta_x &= 0.5 \alpha_x t^2 + \omega_x' t \\ \theta_y &= 0.5 \alpha_y t^2 + \omega_y' t \end{aligned} \quad (4.2)$$

The new velocities at the end of the step can also be found using the uniform acceleration concept as is shown in Equation 4.3.

$$\begin{aligned} V_x &= A_x t + V_x' & V_y &= A_y t + V_y' & V_z &= A_z t + V_z' \\ \omega_x &= \alpha_x t + \omega_x' & \omega_y &= \alpha_y t + \omega_y' \end{aligned} \quad (4.3)$$

The velocities of Equation 4.3 become the initial velocities for Equation 4.2 for the next step once all the angular acceleration terms have converged.

The initial transformation matrix, before the vehicle moves, is found in Equation 4.4. Alternatively, this is the transformation (${}^G T_L$) relating the initial local frame to the global frame in global coordinates [13].

$${}^6T_L = \begin{vmatrix} \cos(\theta_{Y6}) & \sin(\theta_{Y6})\sin(\theta_{X6}) & \sin(\theta_{Y6})\cos(\theta_{X6}) & S_{X6} \\ 0.0 & \cos(\theta_{X6}) & -\sin(\theta_{X6}) & S_{Y6} \\ -\sin(\theta_{Y6}) & \cos(\theta_{Y6})\sin(\theta_{X6}) & \cos(\theta_{Y6})\cos(\theta_{X6}) & S_{Z6} \\ 0.0 & 0.0 & 0.0 & 1.0 \end{vmatrix} \quad (4.4)$$

If it is assumed that the vehicle rolls first and then yaws, a different transformation matrix from Equation 4.4 will result.

Since the terrain map is in the global coordinate system, it is necessary to find the vehicle's center of gravity in global coordinates. Later the global wheel positions will be found. The distances and rotations of the first step with respect to the initial local frame are as shown in Equation 4.2. This can be written in the homogeneous transformation matrix form (${}^L T_1$) as is shown in Equation 4.5.

$${}^L T_1 = \begin{vmatrix} \cos(\theta_y) & \sin(\theta_y)\sin(\theta_x) & \sin(\theta_y)\cos(\theta_x) & S_x \\ 0.0 & \cos(\theta_x) & -\sin(\theta_x) & S_y \\ -\sin(\theta_y) & \cos(\theta_y)\sin(\theta_x) & \cos(\theta_y)\cos(\theta_x) & S_z \\ 0.0 & 0.0 & 0.0 & 1.0 \end{vmatrix} \quad (4.5)$$

By multiplying the matrix of Equation 4.4 by that of Equation 4.5, the orientation and position of the vehicle's center of gravity can be found in global coordinates. That is, the homogeneous transformation matrix relating the position after the first step to the global frame can be found by using Equation 4.6.

$${}^G T_1 = {}^G T_L {}^L T_1 \quad (4.6)$$

The position, with respect to the global frame, of the vehicle's center of gravity after the first step is the last column of matrix (${}^G T_1$) found in Equation 4.6. The roll and yaw with respect to the global frame can also be determined by inverse kinematics. The transformation matrix (${}^G T_1$) will have the same general form as Equation 4.4. Thus, by comparing elements (1,1) with (1,3) of ${}^G T_1$, the yaw can be determined. It cannot be determined by simply taking the inverse cosine of term (1,1) since there are two possible quadrants in which it could lie in. By looking at the sign of the sine term at position (1,3), the correct quadrant can be found. Similarly, the roll with respect to the global frame can be found by comparing the element (2,2) with element (2,3) of ${}^G T_1$. Notice again that a different roll and yaw would be found if it was assumed that roll occurred first. Subsequent positions of the vehicle's center of gravity with respect to the global frame can be found by multiplying the previous global to local transformation matrix by the current local transformation. This is shown in Equation 4.7 for position N.

$${}^G T_N = {}^G T_L {}^L T_1 {}^1 T_2 \dots {}^{N-1} T_N \quad (4.7)$$

Now that the position and orientation of the vehicle's center of gravity are known in global coordinates, the wheel positions can be found in the global frame. First, the positions of the wheels are found in the local frame for a given contact and steering angle using Equation 3.28 in Section 3.2. The joints are not adjusted as the vehicle advances from the previous

position. In other words, the R vectors of Equation 3.28 are based on the previous $(N-1)$ joint angles. Later, these joints will be adjusted based on the tires' compression into the terrain. The global positions of the wheels are found by multiplying the transformation matrix 6T_N for the Nth step by the wheels' local positions in the local $N-1$ th frame. This is shown for wheel one in Equation 4.8.

$$\begin{vmatrix} x_1 \\ y_1 \\ z_1 \\ 1.0 \end{vmatrix} = {}^6T_N \begin{vmatrix} R_1 \mathbf{i} \\ R_1 \mathbf{j} \\ R_1 \mathbf{k} \\ 1.0 \end{vmatrix} \quad (4.8)$$

In order to determine the radial position of the maximum compression of each tire in the new position, the global Y coordinate is compared with the terrain height around each tires' circumference at the given X and Z coordinate. The program starts with a contact angle of -90° and increments this by 3° to 0° for each tire (remember that the contact angle is measured with respect to the bottom of the tire). In other words, the lower back half of the tires' circumference is scanned. Equation 3.28 is used to find the position of the tire's circumference for a given contact angle with respect to the vehicle's local frame. This position determined in Equation 3.28 is then multiplied by 6T_N as is shown in Equation 4.8. This transforms the tire's circumference for a given contact angle into global coordinates. By comparing the height or global Y-coordinate of the tire for a given contact angle with that of the terrain, a contact angle can be found at which the tire

is most compressed. In other words, a contact angle for wheel one can be found in which Equation 4.9 is a maximum.

$$\Delta Y_{\max} = Y_g - Y_1 \quad (4.9)$$

The variable Y_1 is the global Y position on the circumference of wheel one for a given contact angle, and the variable Y_g is the terrain height directly above or below Y_1 . The terrain height is found by using the methods of Chapter II. This concept is illustrated in Figure 4.3 for wheel one. The same analysis is done for each tire.

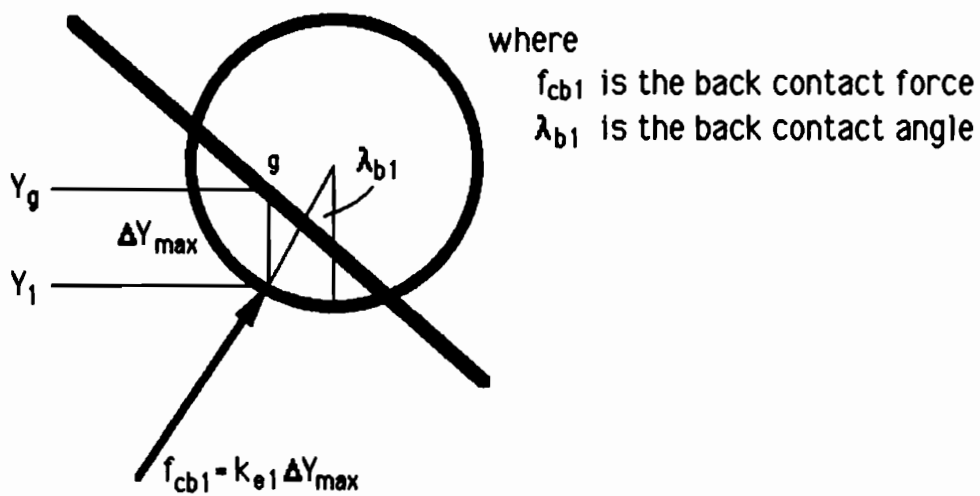


Figure 4.3 - Determining contact force

The contact angle that maximizes Equation 4.9 is the contact angle used for the back side of the tire (λ_b). The contact force is determined by how much the tire is compressed or ΔY_{\max} multiplied by the effective

stiffness K_e of the tire-ground contact. The variable k_e was found in Equation 3.24. Equation 4.10 illustrates finding the back contact force for wheel one.

$$f_{cb1} = k_{e1} \Delta Y_{\max} \quad (4.10)$$

If there is no point where Equation 4.9 is greater than zero on the lower back circumference of the tire, the tire does not contact in this section.

Next, the program starts with a contact angle of 0° and increments it by 3° to 90° for each tire. In other words, the lower front half of the tire's circumference is scanned. The reason the tire circumference is scanned in two steps is that it might contact at two places (due to the polygonal terrain). This is illustrated in Figure 4.4.

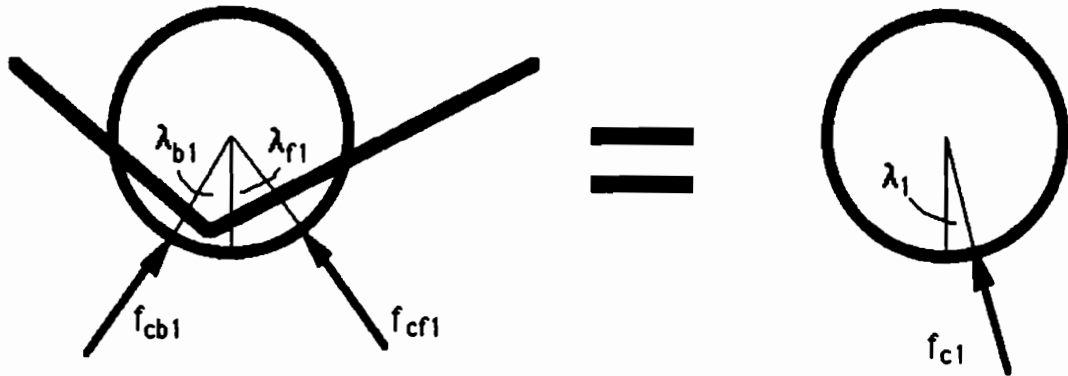


Figure 4.4 - Finding equivalent contact force

If only one scan was used, the larger of the two contact forces of f_{cb1} and f_{cf1} would be found and the other ignored. Therefore, by scanning in the two steps outlined, a more accurate representation of the tire-ground interface

is found. As is illustrated in Figure 4.4, the two contact forces are combined into one equivalent force. The method used to do this is shown in Equation 4.11 for wheel one.

$$f_y = f_{cb1} \cos(\lambda_{b1}) + f_{cf1} \cos(\lambda_{f1})$$

$$f_x = -f_{cb1} \sin(\lambda_{b1}) - f_{cf1} \cos(\lambda_{f1}) \quad (4.11)$$

$$f_{c1} = \sqrt{f_x^2 + f_y^2} \quad \lambda_1 = \text{ATAN}\left(\frac{-f_x}{f_y}\right)$$

In this manner, all the new contact forces are found with the vehicle joint angles in the same position as in the previous step.

SECTION 4.2 – THE VEHICLE'S NEW POSITION

Once all the contact forces and contact angles are found in the new position, the joints are adjusted in a dynamic manner. First, the rocker is adjusted so that the moment about the hinge (M_{12a}) is as shown in Equation 4.12. The passive hinge of the rocker does not transmit a moment (M_{12} is zero) unless a mechanical stop is contacted. The moment M_{12a} is simply the moment to cause an angular acceleration of the rocker about its z-axis.

$$M_{12a} = I_{12}(\alpha_{12} - \alpha_{12nt}) \quad (4.12)$$

where

α_{12nt} = angular acceleration without terrain (previous step)

α_{12} = actual angular acceleration

To intuitively explain Equation 4.12, suppose that the moment about the rocker's hinge caused by the contact force of wheel two is greater than the counter torque created by wheel one and the tractive forces. This is illustrated in Figure 4.5 for step N-1.

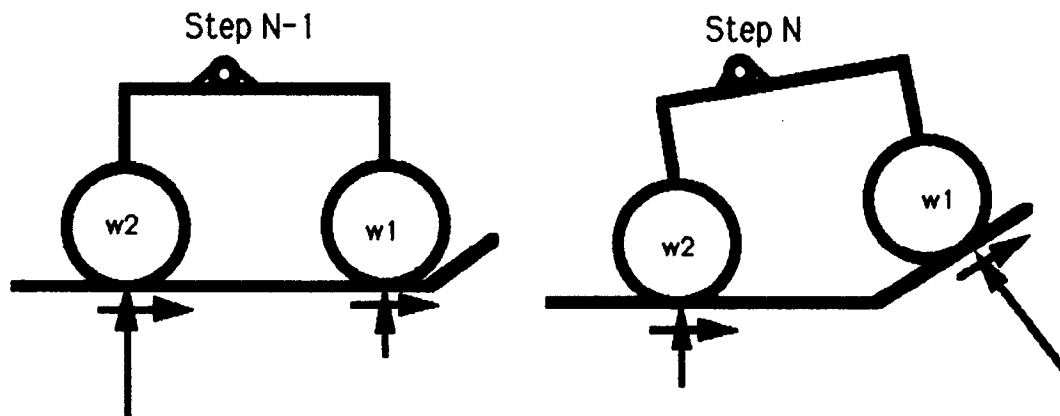


Figure 4.5 – Rocker moving forward

Thus, the rocker wants to rotate clockwise due to the large contact force at wheel two. If there was no terrain, the angular acceleration of the rocker can be found using the Equation 3.48 in Section 3.2. The contact forces used are those of step N-1, and ΣM is equated to $I_{12} \alpha_{12nt}$. In this manner, α_{12nt} , or the angular acceleration of the left rocker about its local z-axis can be solved as if there was no terrain in the previous step. As is shown in Figure 4.5, the rocker actually rotates counterclockwise in the next step. Therefore, not only do the new contact forces have to create the actual counterclockwise angular acceleration (α_{12}) from step N-1 to step N, but they have to overcome the tendency for the vehicle to rotate in the clockwise direction at step N-1.

This is the reason why in Equation 4.12, the actual angular acceleration is subtracted from the angular acceleration as if there was no terrain in step N-1. If in step N-1, the rocker wanted to rotate counterclockwise, the new contact force at wheel one in step N would not be as large. This is since the required moment, shown in Equation 4.12, would be smaller. Intuitive, this makes sense since the vehicle already has the tendency to rotate in a counterclockwise manner and, hence, does not require as large of a counterclockwise moment.

The flaw in this reasoning is that the actual angular acceleration is unknown. As was previously mentioned, the actual angular acceleration is assumed to be the same as in the previous step (N-1) for the first iteration. Later, it is corrected by iterative methods.

In order to obtain the desired moment about the rocker's hinge (M_{12a}), the rocker angle is adjusted in its new position. Since the desired moment is known (based on previous assumptions) from Equation 4.12, and the

effective stiffness of the tire-ground contact is known, a good approximation to how much the pivot joint of the rocker should be adjusted ($\Delta\theta_{12}$) is found as follows.

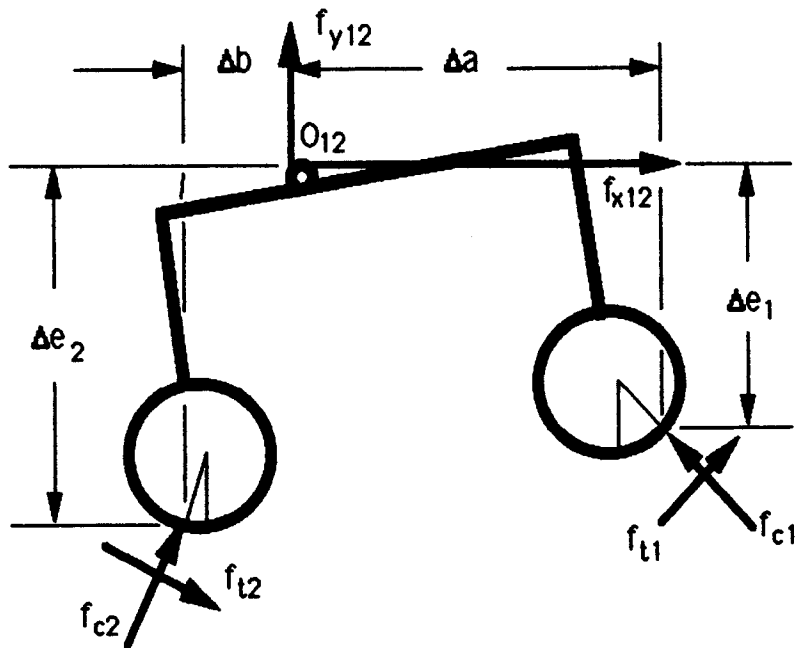


Figure 4.6 - Adjusting rocker angle

The lengths as shown in Figure 4.6 can be determined using Equation 4.13.

$$\Delta a = a \cos(\theta_{12}) + e \sin(\theta_{12}) + r \sin(\lambda_1) \cos(\delta_1)$$

$$\Delta e_1 = a \sin(\theta_{12}) - e \cos(\theta_{12}) - r \cos(\lambda_1) \quad (4.13)$$

$$\Delta b = -b \cos(\theta_{12}) + e \sin(\theta_{12}) + r \sin(\lambda_2) \cos(\delta_2)$$

$$\Delta e_2 = -b \sin(\theta_{12}) - e \cos(\theta_{12}) - r \cos(\lambda_2)$$

By adjusting the angle θ_{12} by $\Delta\theta_{12}$, the contact forces will change approximately by the amount shown in Equation 4.14.

$$\begin{aligned}\Delta f_{c1} &\approx -k_{e1} \Delta a \sin(\Delta\theta_{12}) \\ \Delta f_{c2} &\approx -k_{e2} \Delta b \sin(\Delta\theta_{12})\end{aligned}\quad (4.14)$$

where the Δf_c terms are the change in contact forces

The current moment about the hinge (termed M_{12c}) is calculated using Equation 3.48 with the new contact forces and the joint angles from the previous step. Again, the rocker hinge does not actually sustain this moment, but it is the moment that goes into accelerating the rocker about its hinge. In other words, this moment does not add to M_{12} in any way unless the mechanical stop is contacting the rocker. The moment M_{12c} is compared to the desired moment M_{12a} of Equation 4.12. The difference between these two moments is termed ΔM_{12} in Equation 4.15.

$$\Delta M_{12} = M_{12c} - M_{12a} \quad (4.15)$$

Summing moments about the pivot O_{12} in Figure 4.6, the change in moment about the pivot can be approximated as shown below.

$$\begin{aligned}\Delta M_{12} &= \Delta f_{c1} \Delta a \cos(\lambda_1) + \Delta f_{c1} \Delta e_1 \sin(\lambda_1) + \\ &\quad \Delta f_{c2} \Delta b \cos(\lambda_2) + \Delta f_{c2} \Delta e_2 \sin(\lambda_2)\end{aligned}\quad (4.16)$$

The tractive forces f_{t1} and f_{t2} are assumed to remain the same as the rocker angle is varied. Hence, they do not contribute to ΔM_{12} in Equation 4.16. This is normally a good assumption since the change in the contact forces are not large enough to necessitate a reevaluation of the allowable

tractive forces. If the contact forces did change significantly, the tire-ground contact might not be able to sustain the same tractive forces as before the rocker angle adjustment. This would make Equation 4.16 inaccurate. However, the velocity of the vehicle and the time step are small enough to usually prevent this situation. Nonetheless, the maximum allowable tractive force for each wheel is monitored and adjusted if necessary as the rocker pivot is adjusted. With the above assumptions, Equation 4.14 is substituted into Eqution 4.16.

$$\begin{aligned}\Delta M_{12} = & -k_{e1} \Delta a^2 \cos(\lambda_1) \sin(\Delta\theta_{12}) + \\ & -k_{e1} \Delta a \Delta e_1 \sin(\lambda_1) \sin(\Delta\theta_{12}) + \quad (4.17) \\ & -k_{e2} \Delta b^2 \cos(\lambda_2) \sin(\Delta\theta_{12}) + \\ & -k_{e2} \Delta b \Delta e_2 \sin(\lambda_2) \sin(\Delta\theta_{12})\end{aligned}$$

Finally, $\Delta\theta_{12}$ can be solved from Equation 4.17 as is shown in Equation 4.18.

$$\Delta\theta_{12} = \sin^{-1} \left| \frac{\Delta M_{12}}{k_{e1} \Delta a [\Delta a \cos(\lambda_1) + \Delta e_1 \sin(\lambda_1)] + k_{e2} \Delta b [\Delta b \cos(\lambda_2) + \Delta e_2 \sin(\lambda_2)]} \right| \quad (4.18)$$

If ΔM_{12} is larger than zero, then the rocker joint is adjusted positively by $\Delta\theta_{12}$. Otherwise, it is adjusted negatively.

Since there are approximations in the guess of Equation 4.18, particularly at Equations 4.14 and 4.16, the process is iterated. That is, the rocker joint is adjusted by $\Delta\theta_{12}$ and then the resulting new contact forces and contact angles are found more rigorously by scanning the circumference

of the tire in the same manner as was previously discussed. This process is iterated until the moment M_{12c} converges to within 0.1 N-m of the desired value of M_{12a} ($\Delta M_{12} < 0.1$ N-m in Equation 4.15). It was discovered that the angle found in Equation 4.18 overshoots its mark. By taking half the angle predicted in 4.18, convergence to the correct rocker angle is much quicker.

If the rocker does not converge within 10 iterations using the adjustment of the hinge found in Equation 4.18, θ_{12} is adjusted by 0.001 radians. There are times, although not often, when even this small adjustment to the rocker will not converge the desired moment to within 0.1 N-m, and will instead oscillate about the desired result. For example, $\Delta M_{12} = 0.12, -0.13, 0.12, -0.13 \dots$ might happen. The computer checks for this oscillation and picks the closest value or the value which minimizes Equation 4.15 (0.12 N-m for this example). This oscillation problem is heavily dependent on wheel stiffness, the link lengths, and the terrain the vehicle is on. An example where this oscillation might occur is shown in Figure 4.7.



Figure 4.7 – Possible oscillation problem

A small adjustment of the rocker angle in either direction will have a large effect on the tire forces.

If the rocker hits the mechanical stop in adjusting the rocker pivot, then M_{12} simply becomes M_{12a} as found in Equation 4.12. Since α_{12} is zero in

Equation 4.12 after the rocker contacts the mechanical stop, M_{12} is the moment found in Equation 3.48.

Once the rocker angle has converged, the pivot forces are found using Equation 4.19. If the rocker did contact the mechanical stop, the moment M_{12} is also found, as was explained above.

$$\begin{aligned} f_{y12} = & -f_{c2} \cos(\lambda_2) - f_{c1} \cos(\lambda_1) + m_{12} g \cos(\theta_{xG}) - \\ & f_{t1} \sin(\lambda_1) - f_{t2} \sin(\lambda_2) \end{aligned} \quad (4.19)$$

$$f_{x12} = f_{c2} \sin(\lambda_2) + f_{c1} \sin(\lambda_1) - f_{t1} \cos(\lambda_1) - f_{t2} \cos(\lambda_2)$$

The beam joints can now be adjusted in an analogous manner to that of the rocker joints. The beam is adjusted so that the moment about the hinge (M_{La}) is as shown in Equation 4.20.

$$M_{La} = I_L (\alpha_L - \alpha_{Lnt}) \quad (4.20)$$

where

α_{Lnt} = angular acceleration without terrain (previous step)

α_L = actual angular acceleration

The term α_{Lnt} is found using Equation 3.56 of Section 3.3 with the contact forces set to those of the previous step, and the M_L term neglected. Notice that the rocker pivot forces and the moment M_{12} are employed here. By dividing Equation 3.56, with the above stipulations, by the moment of inertia of the beam I_L , α_{Lnt} , or the angular acceleration as if there was no terrain, is obtained. Again, the actual angular acceleration of the beam (α_L)

is assumed to be the same as in the previous (N-1) step for the first iteration. Later, by iterative methods, it is corrected.

The beam's angle can be adjusted similar to the rocker using an iterative procedure. Since wheel one is farther from the beam pivot than is wheel two, when the beam pivot is adjusted, the contact force at wheel one will probably increase or decrease more than wheel two. As a result, every time the position at the beam pivot is adjusted, the rocker pivot position has also to be adjusted. This results in two nested iterative loops. The inside loop is for the rocker angle adjustment and the outside loop is for the beam angle adjustment. The distances shown in Figure 4.8 are used for a good estimate of the correct beam angle and are found in Equation 4.21.

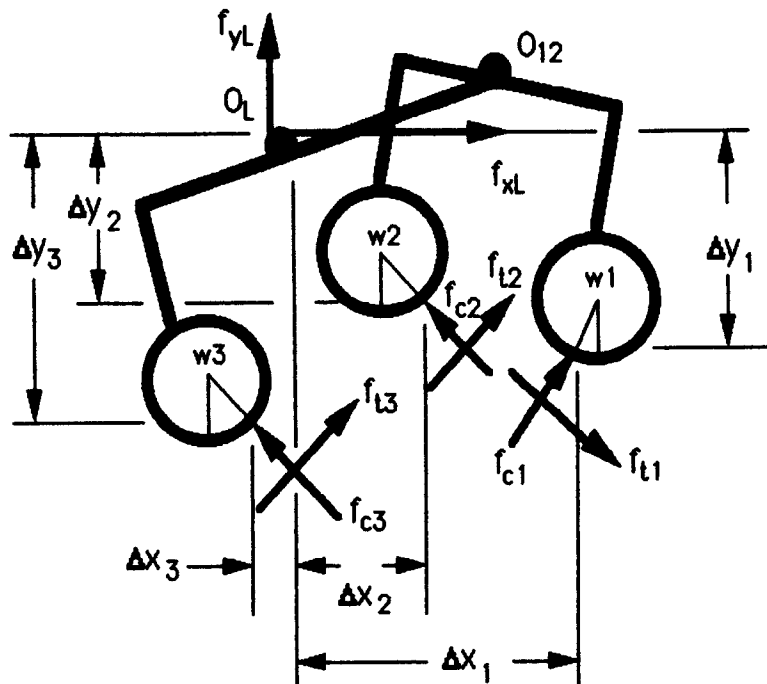


Figure 4.8 - Adjusting beam angle

$$\begin{aligned}
 \Delta x_1 &= d_1 \cos(\theta_L) + a \cos(\theta_{12}) + e \sin(\theta_{12}) + r \sin(\lambda_1) \cos(\delta_1) \\
 \Delta x_2 &= d_1 \cos(\theta_L) - b \cos(\theta_{12}) + e \sin(\theta_{12}) + r \sin(\lambda_2) \cos(\delta_2) \\
 \Delta x_3 &= -d_2 \cos(\theta_L) + e \sin(\theta_L) + r \sin(\lambda_3) \cos(\delta_3) \\
 \Delta y_1 &= d_1 \sin(\theta_L) + a \sin(\theta_{12}) - e \cos(\theta_{12}) - r \cos(\lambda_1) \\
 \Delta y_2 &= d_1 \sin(\theta_L) - b \sin(\theta_{12}) - e \cos(\theta_{12}) - r \cos(\lambda_2) \\
 \Delta y_3 &= -d_2 \sin(\theta_L) - e \cos(\theta_{12}) - r \cos(\lambda_2)
 \end{aligned} \tag{4.21}$$

The change in the contact forces due to a small beam pivot rotation ($\Delta\theta_L$) can be approximated by means of Equation 4.22.

$$\begin{aligned}
 \Delta f_{c1} &\approx -k_{e1} \Delta x_1 \sin(\Delta\theta_L) \\
 \Delta f_{c2} &\approx -k_{e2} \Delta x_2 \sin(\Delta\theta_L) \\
 \Delta f_{c3} &\approx -k_{e3} \Delta x_3 \sin(\Delta\theta_L)
 \end{aligned} \tag{4.22}$$

where Δf_c terms are the change in contact forces

The current moment about the left beam hinge (termed M_{Lc}) is calculated using Equation 3.56 with the new contact forces and the joint angles from the previous step. This is the moment that goes into accelerating the beam about its pivot. The moment M_{Lc} is compared to the desired moment M_{La} of Equation 4.20. The difference between the two moments is termed ΔM_L as is shown in Equation 4.23.

$$\Delta M_L = M_{Lc} - M_{La} \tag{4.23}$$

Summing moments about the hinge of the beam in Figure 4.8, the change in moment about the hinge can be found as shown below.

$$\Delta M_L = \Delta f_{c1} \Delta x_1 \cos(\lambda_1) + (\Delta f_{c1}) \Delta y_1 \sin(\lambda_1) + \\ \Delta f_{c2} \Delta x_2 \cos(\lambda_2) + (\Delta f_{c2}) \Delta y_2 \sin(\lambda_2) + \quad (4.24) \\ \Delta f_{c3} \Delta x_3 \cos(\lambda_3) + (\Delta f_{c3}) \Delta y_3 \sin(\lambda_3)$$

As with the rocker, the tractive forces f_{t1} , f_{t2} , and f_{t3} are assumed to remain the same as the beam pivot is adjusted. Hence, they do not contribute to the change in moment of Equation 4.24. As explained before, this is normally a good assumption. Nonetheless, the maximum allowable tractive force for each wheel is monitored and adjusted if necessary as the beam pivot is adjusted. With this in mind, Equation 4.22 is substituted into Equation 4.24. Solving for $\Delta\theta_L$ then results in Equation 4.25.

$$\Delta\theta_L = \sin^{-1} \left| \frac{\Delta M_L}{[k_{e1} \Delta x_1 (\Delta x_1 \cos(\lambda_1) + \Delta y_1 \sin(\lambda_1)) + k_{e2} \Delta x_2 (\Delta x_2 \cos(\lambda_2) + \Delta y_2 \sin(\lambda_2)) + k_{e3} \Delta x_3 (\Delta x_3 \cos(\lambda_3) + \Delta y_3 \sin(\lambda_3))]} \right| \quad (4.25)$$

If ΔM_L is larger than zero, then the beam joint is adjusted positively by $\Delta\theta_L$. Otherwise, it is adjusted negatively. Once the beam is adjusted, the program scans the tire circumference to come up with the actual tire contact force and the process is iterated if necessary.

Again, it was found that taking half the estimated change in angle of Equation 4.25 helped the beam angle converge faster. Convergence of the

beam angle implies that M_{Lc} approaches M_{La} or ΔM_L becomes small (0.01 N-m is the error tolerance on ΔM_L). Like the rocker, if the beam does not converge within 10 iterations using the beam hinge adjustment of Equation 4.25, θ_L is adjusted by 0.001 radians. In the event that it still does not converge and oscillates about the tolerance, the closest value, or the value of θ_L which minimizes ΔM_L is chosen. Since every time the beam is adjusted, the rocker must also be readjusted, the check for contacting the mechanical stop is done solely in the rocker angle adjustment routine. Once the beam has been adjusted, the beam pivot forces are determined using Equation 4.26.

$$\begin{aligned} f_{yL} &= f_{y12} - f_{c3} \cos(\lambda_3) + m_L g \cos(\theta_{x6}) \\ f_{xL} &= f_{x12} + f_{c3} \sin(\lambda_3) \end{aligned} \quad (4.26)$$

Finally, the roll is adjusted in a similar manner to that by which both the rocker and beam angles were adjusted. Hence, it is desired to have a moment about the body's x-axis which satisfies Equation 4.27.

$$M_{Bxa} = I_x (\alpha_x - \alpha_{xnt}) \quad (4.27)$$

where

α_{xnt} = angular roll acceleration without terrain (previous step)

α_x = actual angular acceleration

$$I_x = I_x \cos^2(\theta_B) + I_y \sin^2(\theta_B)$$

The term α_{xnt} is found by Equation 4.28.

$$\alpha_{xnt} = \frac{f'_{yL} W/2 - f'_{yR} W/2}{I_x} \quad (4.28)$$

The primed forces are the forces of the previous step. Alternatively, Equation 3.62 can be used and superimposed with the z-direction dynamics from the previous step to find α_{xnt} .

The moment in Equation 4.27 is compared with the current moment M_{Bxc} as shown in Equation 4.29.

$$M_{Bxc} = f_{yL} W/2 - f_{yR} W/2 \quad (4.29)$$

The difference between the two moments is termed ΔM_{Bx} , as is shown in Equation 4.30.

$$\Delta M_{Bx} = M_{Bxc} - M_{Bxa} \quad (4.30)$$

As a rough approximation to how the contact forces will vary with the change in roll, Equation 4.31 was developed.

$$\Delta f_{c1} \approx -k_{e1} W/2 \sin(\Delta\theta_x) \quad (4.31)$$

⋮

$$\Delta f_{c6} \approx -k_{e6} W/2 \sin(\Delta\theta_x)$$

where the Δf_c terms are the change in contact forces

$\Delta\theta_x$ is the change in roll

Summing moments about the body's x-axis results in the approximation of Equation 4.32. The cosine terms are used since only the vertical components of the contact force cause any moment about the x-axis.

$$\Delta M_{Bx} \approx (\Delta f_{c1} \cos(\lambda_1) + \dots + \Delta f_{c6} \cos(\lambda_6)) W/2 \quad (4.32)$$

As for both the beam and the rocker, the tractive forces are assumed to be held constant in Equation 4.32. Nonetheless, the maximum allowable force for each wheel is still monitored and adjusted if necessary as the roll is adjusted. Substituting from Equation 4.31 into Equation 4.32, and solving for $\Delta\theta_x$ results in Equation 4.33.

$$\Delta\theta_x = \sin^{-1} \left[\frac{\Delta M_{Bx}}{[k_{e1} \cos(\lambda_1) \dots k_{e6} \cos(\lambda_6)] (W/2)^2} \right] \quad (4.33)$$

Like the rocker and beam pivot adjustments, the roll adjustment estimate of $\Delta\theta_x$ from Equation 4.33 overshoots its mark. Hence, half the estimate is used and oscillation about the error tolerance of 0.1 N-m is checked similar to both the rocker and beam.

Once the estimated roll is applied, the program scans all the tires for the actual contact forces and iterates if necessary. The roll changes the contact forces on every tire by different magnitudes due to the different contact angle of each tire and its actual distance from the local x-axis. Each tire is a distance $W/2$ along the local z-axis away from the local x-axis. However, the distance from the local x-axis for each tire in the global frame, or the frame the terrain is in, is different. As a result, Equation 4.33

is an approximation and the contact force of each tire will vary in a different manner as the vehicle is rolled. Therefore, every time the vehicle is rolled, the beam and rocker pivot angles must be adjusted. This results in three nested iterative loops as is illustrated in Figure 4.9.

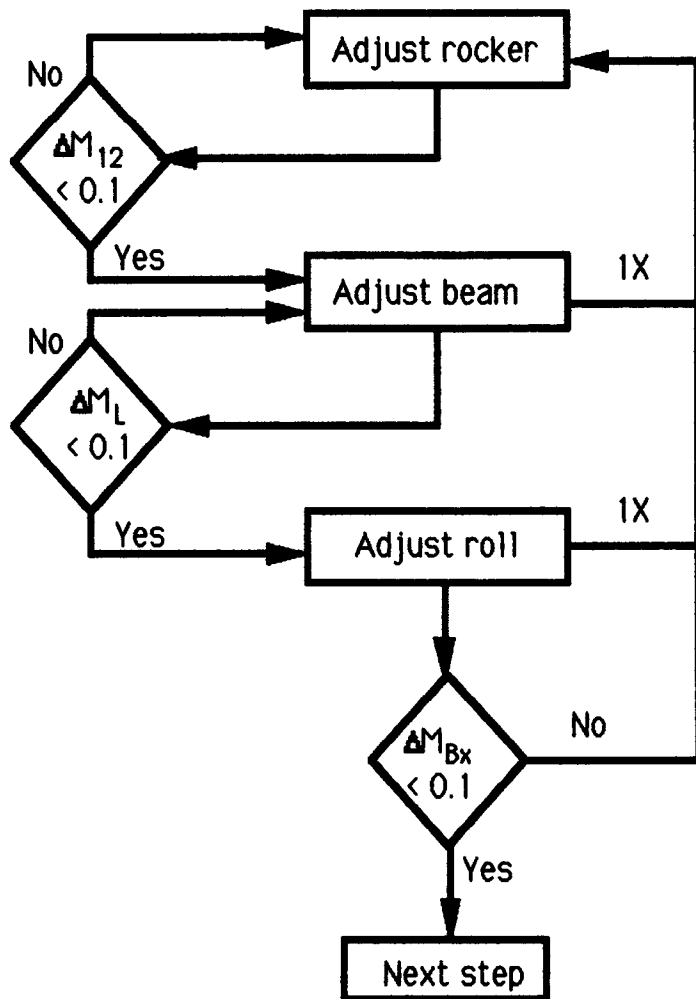


Figure 4.9 - Flowchart for adjusting joints

Now that all the joints have been adjusted to satisfy the error tolerance, the joint angular accelerations can be found for the current step as is shown in Equation 4.34. This is done based on the assumption of uniform acceleration. Uniform acceleration is justified based on the idea that the vehicle is moving slowly and the time increment is very small. Since the angular positions of all the joints are now known for the current, as well as the previous position, and the previous joint speeds are also known, the current angular accelerations can be found from Equation 4.34.

$$\begin{aligned}\alpha_{12} &= \frac{2(\theta_{12} - \dot{\theta}_{12} - \ddot{\omega}_{12})}{t^2} & \alpha_{45} &= \frac{2(\theta_{45} - \dot{\theta}_{45} - \ddot{\omega}_{45})}{t^2} \\ \alpha_L &= \frac{2(\theta_L - \dot{\theta}_L - \ddot{\omega}_L)}{t^2} & \alpha_R &= \frac{2(\theta_R - \dot{\theta}_R - \ddot{\omega}_R)}{t^2} \\ \alpha_x &= \frac{2(\theta_x - \dot{\theta}_x - \ddot{\omega}_x)}{t^2} & (4.34)\end{aligned}$$

where the prime denotes the previous step

For the initial iteration it was assumed, in order to solve the xy plane dynamics, that the current angular accelerations of the joints and about the roll axis are the same as the previous ones. By solving Equation 4.34, the above statement is in general found not to be true. In other words, incorrect angular accelerations were used in order to solve the xy plane dynamics. Therefore, the vehicle is not in the correct current position.

In order to rectify this situation, the vehicle is moved back to its previous position, and new angular accelerations are assumed for the time

step. The xy plane dynamics and z -direction dynamics are reevaluated and, hence, a new vehicle position is determined based on these new assumed angular accelerations. This new set of assumed angular accelerations are found by taking the average of the previously assumed angular accelerations with those found in Equation 4.34. This is shown for the left rocker joint in Equation 4.35.

$$\alpha_{12} = \frac{\alpha_{12} + \alpha'_{12}}{2} \quad (4.35)$$

where the prime denotes the previously assumed value

The program then goes back to the beginning of the dynamics. This process is repeated until all the previously and currently assumed angular accelerations are within 5% of one another. In this manner, the correct vehicle position is found for the current position. Before preceding to the next step, the angular velocity at the end of the previous step, or the beginning of the current step, is found. This is shown for the left rocker joint in Equation 4.36. The current angular velocities (ω terms) become the

$$\omega_{12} = \alpha_{12} t + \omega'_{12} \quad (4.36)$$

previous angular velocities (ω' terms) for the next step in Equation 4.34 and the vehicle's steering angles are then adjusted. Finally, the vehicle is ready for its next step. The basic ideas up to this point are summed up in the flow diagram of Figure 4.10.

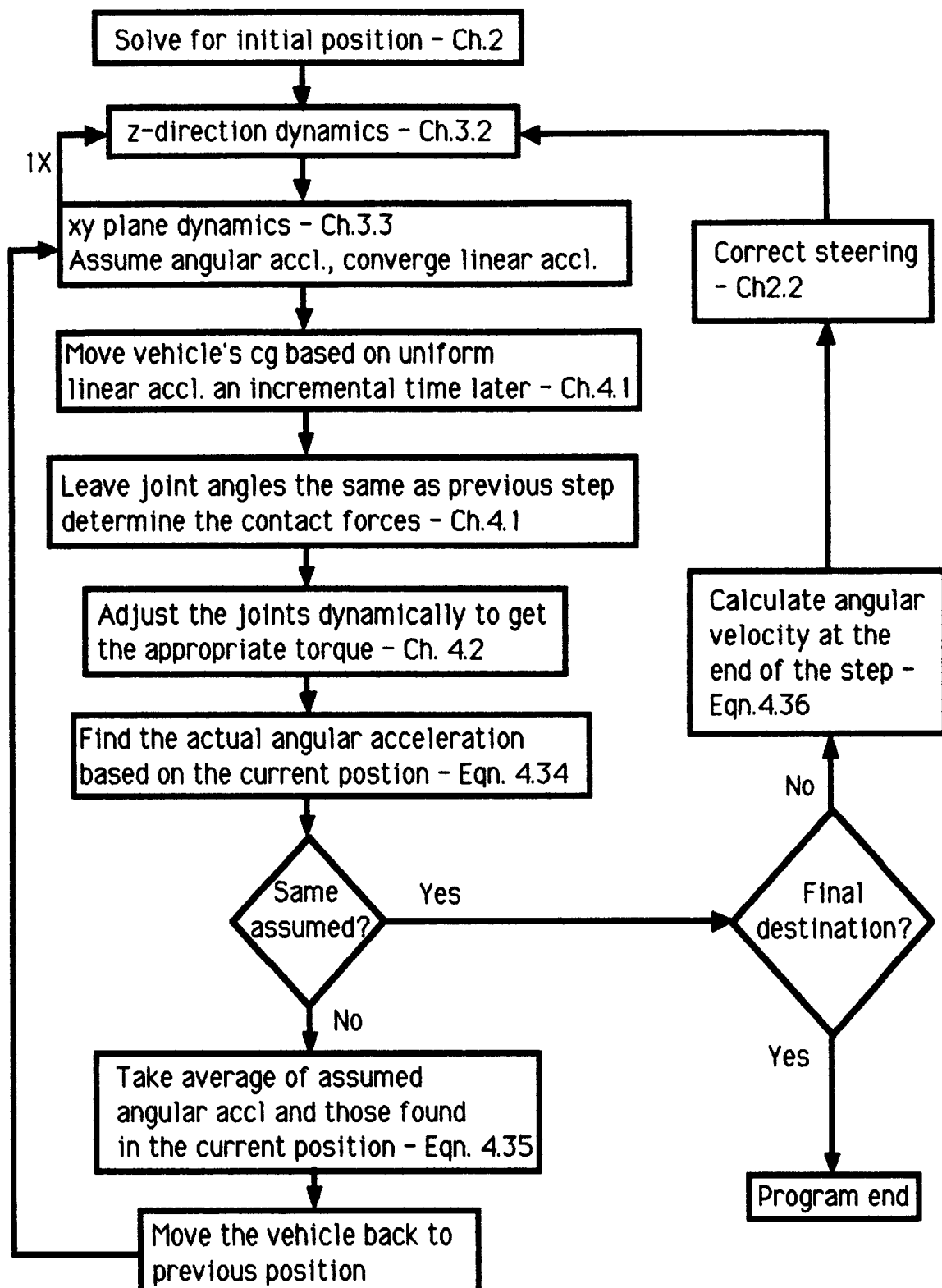


Figure 4.10 - Program Flowchart

SECTION 4.3 – PROGRAM SIMPLIFICATIONS

The method programmed up to this point, requires a lot of computer time. In particular, converging the five angular accelerations (α_{12} , α_{45} , α_L , α_R , and α_x) takes several iterations. Different techniques were tried to get the angular acceleration terms to converge faster. For example, instead of taking the average of the assumed angular accelerations and those actually found based on the assumed values (Equation 4.35), those that were actually found in Equation 4.34 were iterated back. This increased the rate of convergence for some positions, but not for others. Overall, it was found that one method was not advantageous over the other.

Another method is to give the iterative loop for the joint and roll angular accelerations a better set of seed values. Instead of using the previous step's angular accelerations, a method that looks ahead of the vehicle and predicts what the joint angular accelerations are going to be can be devised. This method was not actually programmed, but was simulated by using angular accelerations within 50% of those actually found in a particular position. As a result, the program converged to within three or four iterations. This is still very taxing on the computer considering this would have to be done for every 0.05 second interval. Nonetheless, it is a great improvement over just using the angular accelerations of the previous step. That is dependent, however, on being able to predict the actual angular acceleration to within 50% or so.

The main problem with this iterative method was that it did not always converge to the 5% tolerance desired. Although, for most of the 10 positions evaluated, it did converge, obviously this is not good enough. The vehicle will need to successfully take about 400 of these steps before going

1 meter. The steps that did not converge to the 5% tolerance did not immediately diverge however. They began to converge and approach the desired tolerance. Then, before all five of the angular accelerations converged, one or more of the five began to diverge. Eventually, the diverging angular acceleration terms caused the algorithm to crash.

Perhaps, the closest values or the least discrepancy between the assumed angular accelerations and those found based on the assumptions, can be used for the actual angular accelerations. In other words, an intelligent error tolerance can be devised such that the angular accelerations of least discrepancy and before divergence are used. This is an acceptable solution if larger than 5% errors in angular acceleration terms can be tolerated at those steps that do not converge.

In an attempt to obtain the 5% error tolerance or better for every step, it was decided to move from the purely dynamic realm into the 'quasi-dynamic' domain. This was done by adjusting all the joints statically. In other words, M_{12a} of Equation 4.12 is set to zero, M_{La} of Equation 4.20 is set to zero, and M_{Bxa} of Equation 4.27 is set to zero. The angular acceleration terms, however, are still important in determining the forward dynamics. The only difference in this new method is that when the vehicle reaches the new position, all the joints and roll are adjusted so there is no moment about the passive hinges and local x-axis within the 0.1 N-m error tolerance. The exception to this is when the mechanical stop is contacted. Using this method, the angular accelerations of the joints and the roll, which are necessary to obtain the new position, always converge for the trials tested. Nonetheless, it still takes a significant amount of time for the angular accelerations to converge. Since one of the objectives of this

thesis is to come up with a software package that works closer to real time than ADAMS or DADS, it is necessary to make further simplifications.

These simplifications are obtained by moving farther into the 'quasi-static' realm. This is done by neglecting all the angular accelerations terms in the rocker and beam freebody diagrams. By neglecting the angular acceleration terms in these two freebody diagrams, the analysis is greatly simplified. At the same time, this assumption need not significantly hamper the accuracy if the body is significantly heavier than the frame (rocker and beam) and the wheels. If the body is not significantly heavier than the rest of the vehicle and/or the dimensions of the rocker and beam are such that they have a relatively high moment of inertia about their local z-axes, neglecting the joint angular accelerations would not be a good assumption. Some examples of how this assumption affects the accuracy of the results will be analyzed soon. First, the way in which this assumption simplifies the previous work will be explained.

The rocker's freebody diagram of Figure 3.13 is greatly simplified to that of Figure 4.11. Notice that the right side of Figure 4.11 is dependent only on the linear accelerations of the vehicle's center of gravity based on the previous assumption. As before, the linear accelerations are unknown, and hence they must be iterated. The acceleration terms of Equation 3.44 are simply the body centered accelerations, as is shown in Equation 4.37.

$$a_{x12} = A_x \quad a_{y12} = A_y \quad (4.37)$$

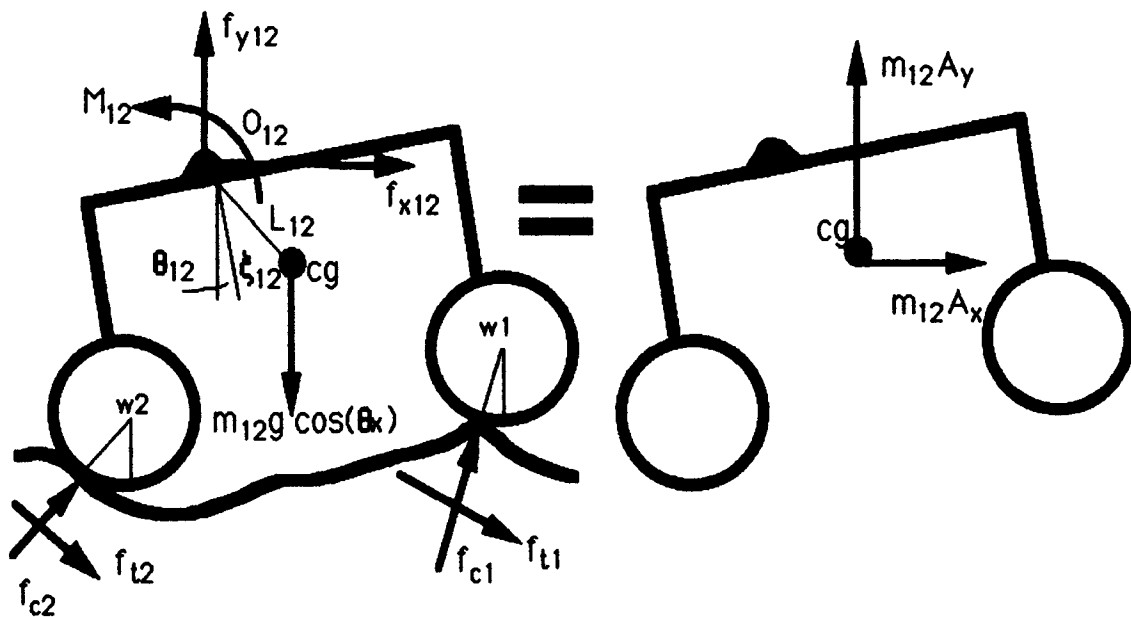


Figure 4.11 - Freebody diagram of rocker

In a similar manner, the beam freebody diagram of Figure 3.15 is greatly simplified to that of Figure 4.12.

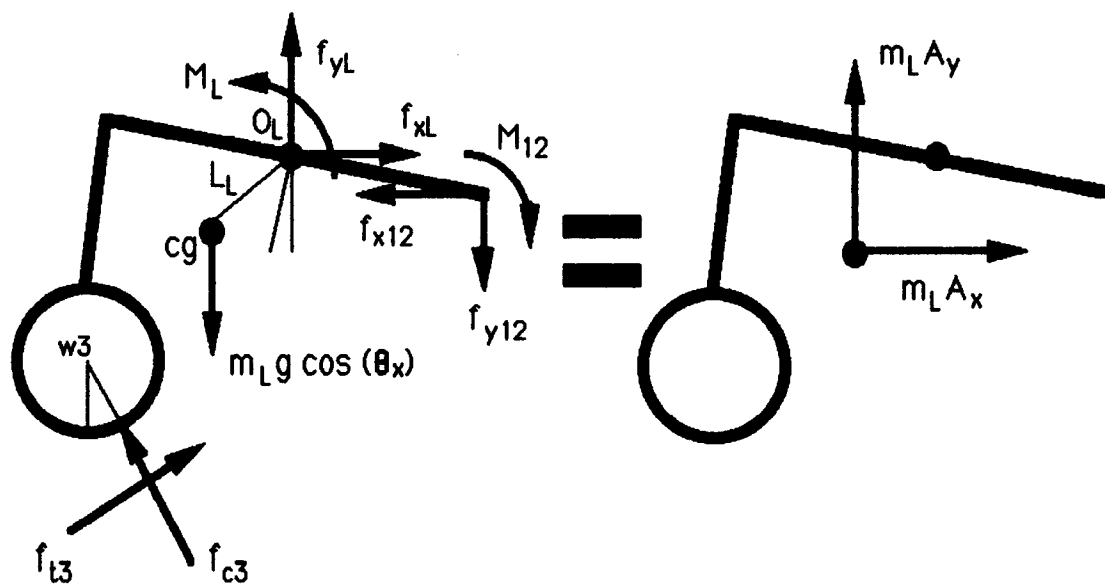


Figure 4.12 - Freebody diagram of beam

As in the case of the rocker, the acceleration terms of Equation 3.54 are the body centered accelerations, as is shown in Equation 4.38. Again, this is due to the aforementioned assumption.

$$a_{xL} = A_x \quad a_{yL} = A_y \quad (4.38)$$

In the same manner as was discussed in Chapter 3, the body's dynamics are analyzed. The linear accelerations are then found using an iterative, but fast converging method previously discussed. This time, however, there is no need to converge the angular accelerations since they are being neglected. Therefore, when the vehicle is moved forward there is no need to iterate back to the previous position based on erroneously assumed angular accelerations. As a result, the program's speed is significantly increased. Perhaps the affect of this simplification can best be seen by comparing the flow diagrams of Figure 4.10 with the new flow diagram of Figure 4.13. Notice that the time consuming iterative loop to the beginning of the dynamics solution has been eliminated.

Again, if the body is much heavier than the rest of the vehicle, a severely hampered accuracy will not be a consequence of this added computer speed. These two methods (dynamic and quasi-static) were compared with the vehicle parameters shown in Table 4.1. These are the approximate values of what those of the actual vehicle could be. The links are assumed to be made of a very low weight composite.

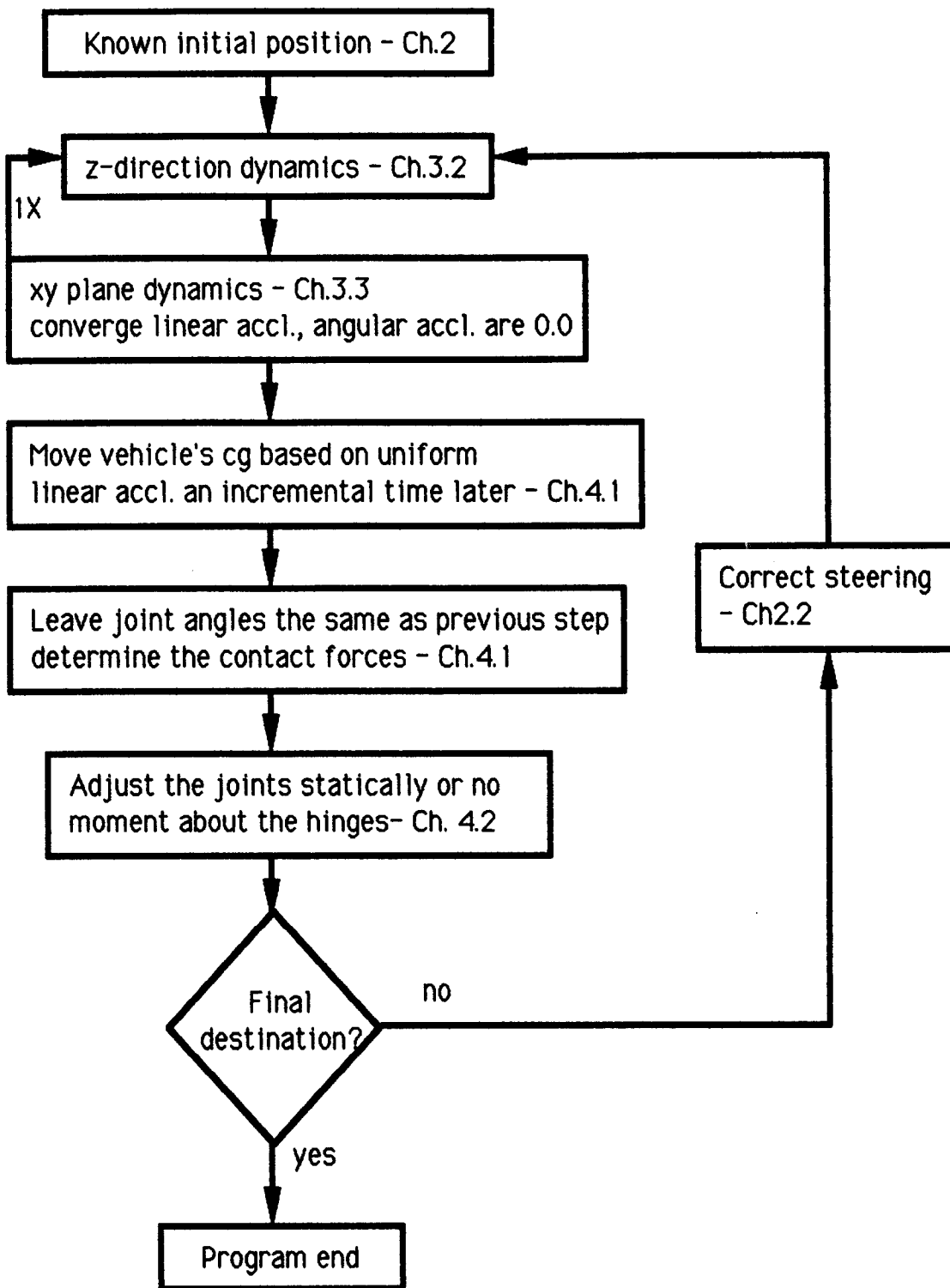


Figure 4.13 - Program Flowchart - 'quasi-static'

Table 4.1 - Vehicle parameters

$a = 0.159 \text{ m}$	$b = 0.0953 \text{ m}$	$e = .0937 \text{ m}$	$d_1 = 0.124 \text{ m}$
$d_2 = 0.200 \text{ m}$	$w = .250 \text{ m}$	$l = .200 \text{ m}$	$h = .05 \text{ m}$
$r = .0587 \text{ m}$	$m_B = 2.0 \text{ kg}$	$\rho = 470 \text{ kg/m}^3$	$s = 0.0254 \text{ m}$
$t_s = .00317 \text{ m}$	$m_w = 0.3 \text{ kg}$		

Using Equations 3.1, 3.2, and 3.4, the mass of the vehicle's frame and wheels is approximately 2 kg. Notice that the frame and wheels have about the same mass as the body ($m_B = 2 \text{ kg}$ also). This is due to the relatively heavy wheel assembly. Hence, the assumption that the body is much heavier than the frame and wheels has been violated. The reason behind this approach is that, if neglecting the angular accelerations with this example does not severely hamper the program's accuracy, it will be a good approximation when the body is much heavier than the rest of the vehicle. The data in Table 4.1 was measured directly from the prototype in Plate I. The only difference is that the mass of the body was deflated for this example to be the same mass as the rest of the vehicle. In Table 4.2, the angular accelerations, displacement during the step, and contact forces are compared for the dynamic and quasi-static methods for two specific positions. The so called dynamic case, displayed in Table 4.2 is actually 'quasi-dynamic' since the joint angles and roll angle are adjusted in the new position in a static manner. Nonetheless, the angular accelerations are used in the dynamics, unlike the 'quasi-static' case.

Table 4.2 - Comparing dynamic and 'quasi-static'

parm.	POSITION 1			POSITION 2		
	dynamic	quasi-st.	%Δ	dynamic	quasi-st.	%Δ
α_{12}	35.18	42.90	21.94	50.57	58.44	15.56
α_{45}	-0.897	-2.38	165.33	-42.81	-52.48	22.59
α_L	1.72	0.01	99.42	-29.30	-39.22	33.86
α_R	8.73	9.30	6.53	48.47	52.60	8.52
α_x	-18.16	-29.13	60.41	12.86	23.37	81.53
S_x	2.12E-3	3.00E-3	41.51	4.95E-3	5.57E-3	12.53
S_y	-1.31E-2	-1.31E-2	0.0	-1.45E-2	-1.43E-2	1.38
f_{c1}	7.95	7.76	2.39	7.99	6.84	14.39
f_{c2}	6.88	6.93	0.73	11.88	10.61	10.69
f_{c3}	7.17	7.37	2.79	11.89	10.45	12.11
f_{c4}	8.16	8.25	1.10	7.83	6.97	10.98
f_{c5}	6.90	6.82	1.16	10.29	8.98	12.73
f_{c6}	7.49	7.35	1.87	9.96	8.66	13.05

By analyzing Table 4.2, it is seen that the angular accelerations differ considerably between the two methods as expected. In some cases, the difference is near to or over 100%. Nevertheless, the more important parameters of the vehicle, such as the displacement and the new contact forces, fare better. The displacement of the vehicle is similar for both cases. The exception is the displacement in the x-direction (S_x) for position 1 of Table 4.2. The new contact forces in position 1 have, at most, a 3%

difference between the two methods. In position 2, the displacement and contact forces for both methods are within 15% of one another. This leads one to conclude that the angular accelerations are of secondary importance relative to the linear accelerations.

In reality, the angular acceleration will even be less significant in the dynamics for the actual vehicle. This is because the actual vehicle will probably have a significantly heavier body than the rest of the vehicle instead of the evenly split weight distribution compared in Table 4.2. If the prototype is to serve as an example, the above statement is definitely true. The mass of the prototype's body is closer to 20 kg due to the computer, and battery pack. Hence for the prototype, since the body mass is about 10 times heavier than the rest of the vehicle, the quasi-static approach would be a very good approximation. The mass of the actual rover is supposed to be only 5 kg. Nonetheless, since the body carries all the computers, scientific equipment, and RTG's, it is expected it will still be significantly heavier than the rest of the vehicle. On these grounds, and in order to obtain a faster running simulation, a 'quasi-static' approach will be used.

In running the program, it was noticed that the vehicle tended to bounce up and down. This was rectified by neglecting the initial velocity term in the y-direction of Equation 4.2. Hence, the displacement in the vertical or y-direction is now determined as is shown in Equation 4.39. In other words, the initial velocity in the y-direction at each step is zero. In this manner, the vehicle does not bounce up and down and runs smoothly on flat terrain. It still however accurately retains the tendency to bounce on rough terrain due to the low Martian gravity. Similarly, it was necessary to neglect the initial velocity term in the z-direction as is also

shown in Equation 4.39. Without neglecting this term the vehicle slipped laterally as if it was on ice. It makes intuitive sense to neglect this initial z-direction velocity term since, unlike in the local x-direction, the tires resist lateral motion. The x-direction retains the initial velocity or the final velocity from the previous step as shown earlier in Equation 4.2.

$$S_y = 0.5 A_y t^2 \quad S_z = 0.5 A_z t^2 \quad (4.39)$$

Another problem with the program was that the nonlinear soil stiffness (found in Equations 3.17 and 3.23) caused the rocker and beam to oscillate back and forth as it transitioned from a sand terrain to a rock terrain or visa versa. When the vehicle's joints are adjusted, it is assumed that the effective tire to ground stiffness for each individual tire is the same as that of the previous step. In actuality, the effective stiffness should be recalculated each time the rocker and beam are adjusted since the soil stiffness is dependent on the sinkage of the tire. This is a result of the soil's nonlinear stiffness. However, taking into account this variable stiffness, would dramatically slow down the program. This is not only due to the fact that the soil stiffness would have to be recalculated each time any joint is adjusted, but adjusting the joints statically becomes a much harder task. The angle adujustment approximations of Section 4.2 do not take the variable stiffness into account. Doing so would be a tedious task since the empirical formula for soil sinkage in Equation 3.17 is not easy to work with.

Therefore, the effective soil stiffness for each tire is recalculated once the vehicle is already adjusted using the previous effective soil

stiffness for each individual tire. This, however, creates an oscillation problem as the vehicle transitions from sand to rock. This is shown in Figure 4.14.

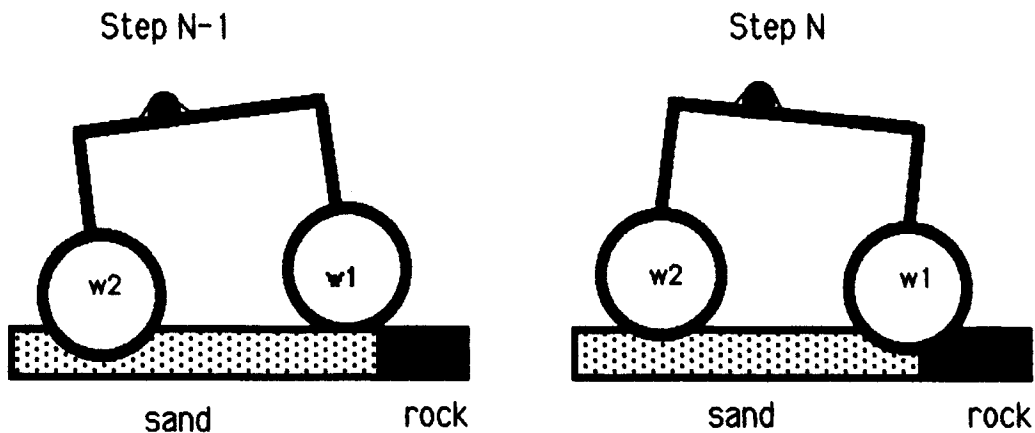


Figure 4.14 - Oscillation problem

At step N-1 in Figure 4.14, the effective stiffness at wheel two is a lot larger than that for wheel one. Again, this is a result of the nonlinear nature of Equation 3.17. The farther the tire sinks, the larger the effective soil stiffness. Thus, at step N the rocker is adjusted so wheel two does not penetrate the soil as much since its effective stiffness determined in step N-1 is larger. Now, however, not only does wheel one penetrate farther into the soil, but it is contacting a rock. Thus, it will be calculated to have a larger effective stiffness. The process then repeats itself and the rocker and beam oscillate back and forth.

In order to rectify this, the average of all the tire to ground effective stiffnesses at the initial position is used and held constant throughout the program. In other words, for the initial step, the effective

stiffness for each tire to ground contact is determined in the same way outlined in Chapter 3.1. The average of the six stiffnesses is then used for all the tires throughout the rest of the program. This average stiffness is calculated as if all six wheels are on sand. Later, if the vehicle runs over a rock terrain, the stiffness of the tire ground contact is still assumed to be the average values determined in the initial step. In actuality, it should be higher and probably just equal to the stiffness of the tire.

Nonetheless, this should not be detectable in the vehicle's performance since the main features of the rock terrain are intact. That is the resistive force or rolling friction on rock is still set to zero, and the coefficient of friction is still 0.8. The only time the higher rock stiffness would affect the vehicle's performance is when the vehicle is moving over the terrain at a fast rate. This could result in the vehicle bouncing off rocks while sand would damp out the impacts. The vehicle's speed is slow enough that these affects are not of much concern. Therefore, keeping the effective stiffness between the tire and ground constant should not hamper the accuracy of the analysis in a significant way. This assumption seems to be justified by the results obtained in Chapter V.

SECTION 4.4 - PATH PLANNING

The user has the option of implementing a path planning scheme. This is an alternative to steering the vehicle directly toward the final destination as previously discussed in Sections 2.1 and 2.2. In order to use the path planning algorithm, the camera's view angle (θ_a), the maximum viewing distance or horizon (C_h), and the camera resolution (C_r) must be specified. An additional parameter, termed the central tendency factor (C_t), is set to make the vehicle favor the straighter path to the final destination. The larger this factor is, the more the vehicle will opt for the direct route.

The maximum viewing distance for a Structured Light Vision System (SLV) is typically about 10 meters. Nonetheless, the horizon is not only limited by the equipment, but by the terrain itself. Since a minirover can not mount the vision system at any significant height (less than 0.5 meters), a boulder can easily obstruct its vision. Clearly, this is a large drawback of the minirover and perhaps of wheeled vehicles in general. Only configurations like the Walking Beam can mount the camera at higher altitudes. Since the camera on the body of the Rocker Bogie cannot be maintained level without an active mount, unlike the Walking Beam, it is assumed the camera rests on a platform which can vary its pitch.

Since there is no attempt to take the obstruction problem into consideration in the program, the user can clearly specify a horizon which is unreasonable in some situations. This limitation should be kept in mind when using the program.

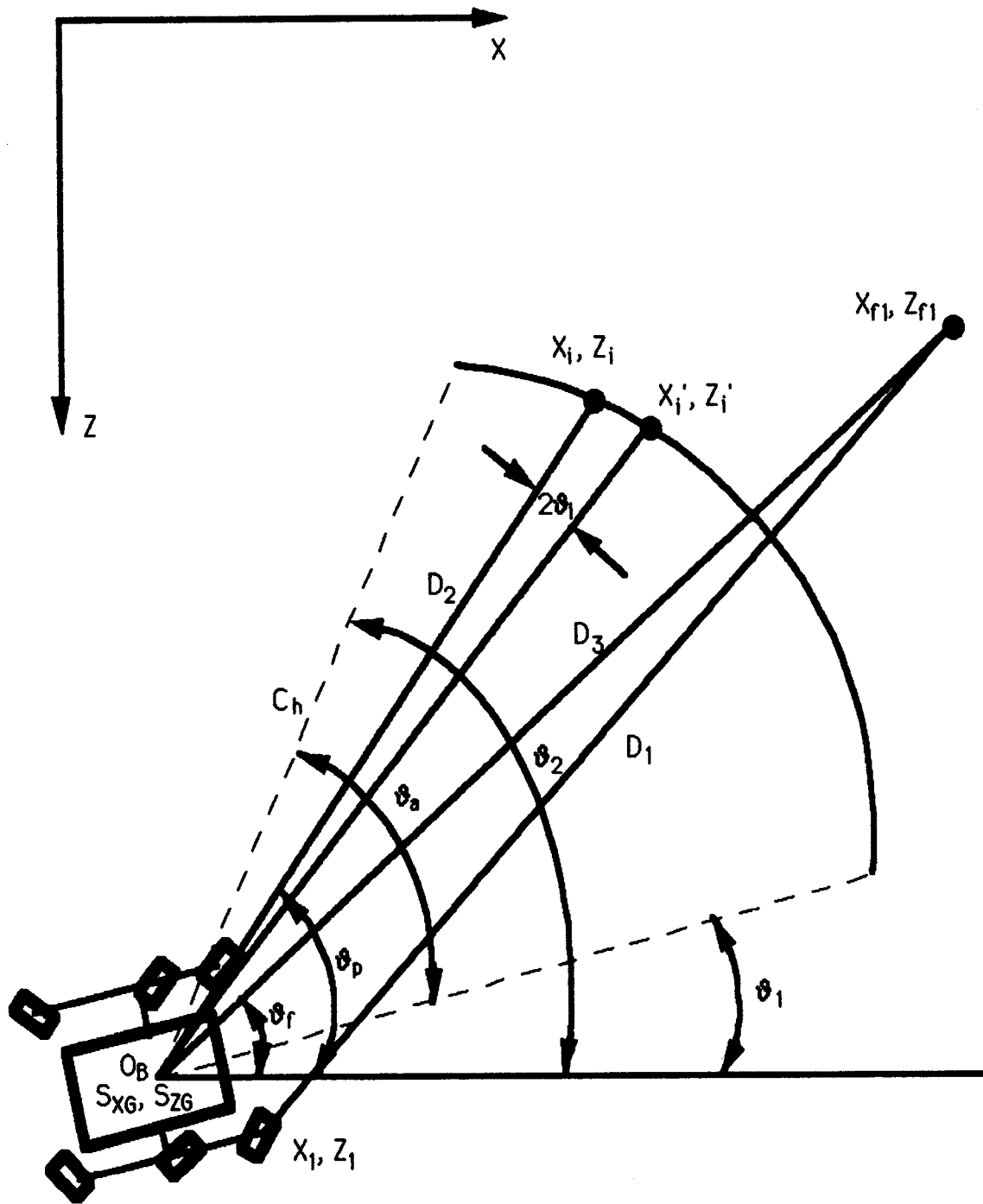


Figure 4.15 - Path Planning

It is desired to make wheel one go from the initially specified position (X_1, Z_1) to the final position (X_{f1}, Z_{f1}) as is shown in Figure 4.15. If the camera's view angle (θ_a) is set at less than 5^0 , wheel one will be simply pointed toward the final destination and the other wheels will follow using the quasi-Ackerman steering principles. If, however, the view angle is greater than 5^0 , the path planning algorithm is activated.

The path planning algorithm chooses an intermediate point (X_l, Z_l) as shown in Figure 4.15 within the view angle and at the horizon. This is the vehicle's immediate destination. Before this point is chosen, the distance D_3 is evaluated from the known position of the vehicle's center of gravity and the final destination. If this distance is less than 0.5 meters, the path planning algorithm is turned off and wheel one is allowed to home in on its final destination. When wheel one is within 0.1 meters of this final destination, the program is terminated.

If D_3 is more than 0.5 meters, the point (X_l, Z_l) is determined by first finding the angle θ_f as shown in Figure 4.15 and determined in Equation 4.40.

$$\theta_f = \text{ATAN} \left(\frac{Z_{f1} - S_{ZG}}{X_{f1} - S_{XG}} \right) \quad (4.40)$$

The camera's view angle (θ_a) is bisected by the line which connects the center of gravity of the vehicle with the final destination of wheel one (or the line of length D_3). With respect to the global frame, the maximum and minimum view angles are then found (θ_2 and θ_1 respectively) as is shown in Equation 4.41.

$$\theta_1 = \theta_f - \frac{\theta_a}{2} \quad \theta_2 = \theta_f + \frac{\theta_a}{2} \quad (4.41)$$

Notice that it is not desired to move the vehicle's center of gravity to the point (X_{f1}, Z_{f1}) , but to move wheel one to this point. This is why the path planning algorithm is turned off when D_3 is less than 0.5 meters or about one vehicle length.

The roughness of the terrain is first evaluated along the line from the known point (S_{x6}, S_{z6}) to the horizon at angle θ_1 or the minimum view angle. The roughness along a given line is defined as the average absolute slope. The slope for the first segment of this line is found by comparing the height of the terrain under the vehicle's center of gravity to that of the point (X_{r1}, Z_{r1}) one camera resolution distance away.

$$X_{r1} = S_{x6} + C_r \cos(\theta_1) \quad Z_{r1} = S_{z6} - C_r \sin(\theta_1) \quad (4.42)$$

where C_r is the camera resolution

Technically, if the camera resolution is less than about 0.3 meters, as it should be, this first point (X_{r1}, Z_{r1}) is still under the vehicle and not visible to the camera. It could, however, be evaluated from a previous position vantage point. By interacting with the terrain map, the terrain height (Y_{r1}) at the point (X_{r1}, Z_{r1}) is found and compared to the height of the terrain directly under the vehicle's center of gravity (Y_{r0}). The absolute value of the slope of this segment (q_1) is simply found as seen in Equation 4.43.

$$q_1 = \frac{|Y_{r0} - Y_{r1}|}{C_r} \quad (4.43)$$

The program then evaluates the next segment of the line and continues until the horizon has been reached. The average of all these segments is then evaluated and termed the roughness along the line. Notice that, if the camera resolution is not small enough, aliasing can result. In other words, if the slope changes every 0.1 meters and the camera's resolution is set at 0.3 meters, an erroneous average slope will be found. It is recommended to use a camera resolution of about three times smaller than the terrain unit mesh size. Anything smaller than this will probably just manage to slow down the computer.

Next, the camera's yaw is incremented by 5° counterclockwise, or positively. The roughness along this line to the horizon is then evaluated. This process is continued until the angle θ_2 has been reached. In case the angle θ_f was missed as the camera is yawed by the 5° increments, the roughness is evaluated at θ_f . This ensures that the straightest route to the point (X_f, Z_f) is considered. The intermediate point (X_i, Z_i) is then chosen to be a point on the horizon whose line from the vehicle's center of gravity has the least average absolute slope.

The vehicle will opt to travel along the line of least average absolute slope only if the central tendency factor (C_t) is set to zero. If C_t is larger than zero, the vehicle will be more likely to take a straighter route even if it might not have the smallest average absolute slope. The larger C_t is, the more it will tend to take the direct path. Now, with a nonzero central tendency factor, the slope of each segment is calculated in a manner similar

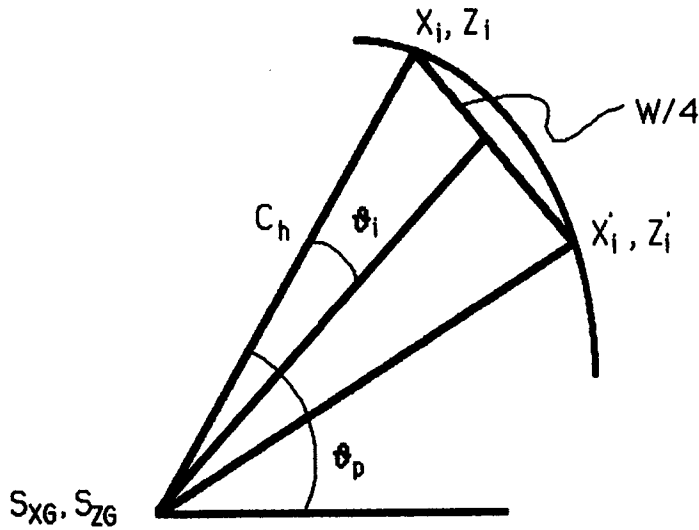
to Equation 4.43 except there is the additional term which includes C_t . This is shown in Equation 4.44 for the first line segment of a particular view angle.

$$q_1 = \frac{|Y_{r0} - Y_{r1}|}{C_r} + C_t |\theta_f - \xi| \quad (4.44)$$

where ξ is a particular angle being evaluated

From Equation 4.44, it can be seen that the farther the path strays from the straight route (at angle θ_f), the more it is affected by C_t . In order to determine an appropriate C_t factor, the user has to make a judgement call on whether it is most important to take the straightest possible route, the least rough route, or somewhere between. For the example shown in Figure 4.17, C_t had to be less than 0.15 to circumvent the obstacle. Anything larger resulted in the vehicle going straight over the hill.

Since the roughness was evaluated from a line emanating from the center of the vehicle, wheel one needs to be directed slightly below the point (X_i, Z_i) . In other words, a point (X'_i, Z'_i) as shown in Figure 4.16, must be found to direct wheel one and allow the vehicle's center of gravity to approach the point (X_i, Z_i) .

Figure 4.16 - Finding X'_i, Z'_i

The point (X'_i, Z'_i) can be approximated as shown in Equation 4.45.

$$\begin{aligned} \theta_p &= \text{ATAN}\left(\frac{Z_i - S_{ZG}}{X_i - S_{XG}}\right) & \theta_i &= \sin^{-1}\left(\frac{W}{4C_h}\right) \\ Z'_i &= S_{ZG} + C_h \sin(\theta_p - 2\theta_i) & (4.45) \\ X'_i &= S_{XG} + C_h \sin(\theta_p - 2\theta_i) \end{aligned}$$

Finally, wheel one is directed towards point (X'_i, Z'_i) and all the other wheels follow using the quasi-Ackerman steering principle previously discussed. At each step, the steering angle of wheel one is updated in a simple proportional controller scheme until D_2 defined in Figure 4.15, is less than 0.3 meters. At this point, the path planning algorithm is executed again and another point (X_i, Z_i) is chosen a distance C_h away. This is repeated until the vehicle reaches its final destination. If, at any time, the

path planner picks a point off the terrain map, a warning message is flashed and the program is terminated. To prevent this, the view angle can be reduced, the horizon reduced, the central tendency factor increased, the final destination point can be moved closer to the center of the terrain, or the terrain can be made larger.

To give a simple example of how the path planning scheme works, consider the obstacle course of Figure 4.17. If, for example, the camera's horizon is set for 0.9 meters and C_t is larger than zero, the vehicle will move in a straight line. The central tendency factor should always be kept larger than zero so that the vehicle will take the straightest route when it is on flat terrain. When it comes time to execute the path planning algorithm the second time, the vehicle will be too close to the hill to circumvent it, unless a camera view angle of almost 180° is used. If, however, the horizon is set at 2.0 meters, the vehicle can easily circumvent the slope providing the view angle is larger than 60° and C_t is smaller than 0.15 as already mentioned. Nonetheless, a longer horizon would not have helped if the vehicle was originally placed 2.1 meters from the hill.

Perhaps, it would be better to set the horizon to about 2 meters, but evaluate the path planning algorithm every 0.5 meters. This would effectively prevent the vehicle from getting too close to a large obstacle. Since the focus of this thesis is not on path planning, and since reevaluating the path more often slows the program down, this approach was not actually attempted. However, the actual vehicle should have this ability since it will improve the effectiveness of the path planner.

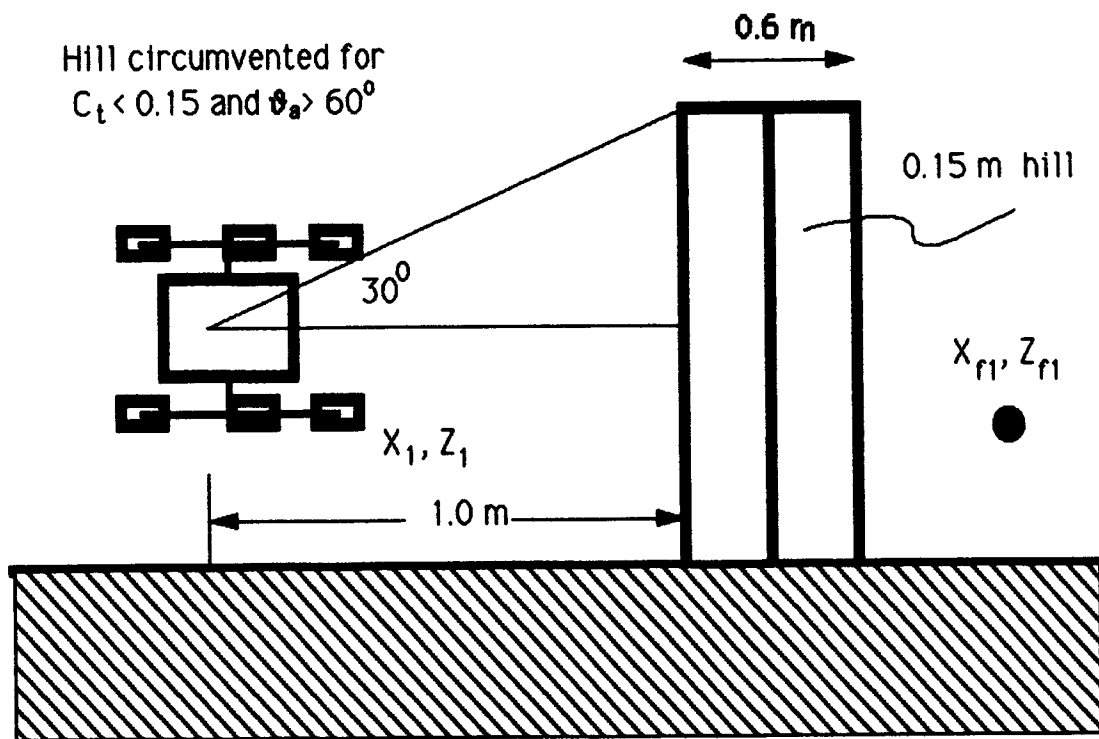


Figure 4.17 - Example of path planner

CHAPTER V

RESULTS

SECTION 5.1 - INPUT AND OUTPUT

As explained in Appendix C, the input is varied using the input file Mars.dat. Through this file, the user assigns the following variables using

Table 5.1 - Input file Mars.dat

a	b	e	d ₁	d ₂		
w	l	h	r	w _t	g	
m _B	p	s	t _s	m _w	k _w	
U	P _{max}	L	S _d	C _a	C _d	C _p
θ _{max}	θ _{min}	θ _{YG}	t	t _i	d _p	
Z ₁	X ₁	Z _{f1}	X _{f1}			
T	T _{SL}	p ₁	p ₂	p ₃	p ₄	p ₅
p ₆	p ₇	p ₈	p ₉			
θ _a	C _h	C _r	C _t			

standard metric units (meters, kilograms, seconds, radians). The first part of this section is about the meaning of the variables shown in Table 5.1. Alongside the variables to follow are typical numerical values used in the program. It is important to pay attention to the decimal points since fortran reads real and integer values differently.

a, b, e, d₁, d₂ : 0.159, 0.0953, 0.0937, 0.124, 0.2

These are some of the variables that define the geometry of the vehicle. They are defined in Figures 2.8 and 2.9 of Section 2.2. The numerical values above define the geometry of JPL's third prototype Rocky III. It should be noted that the dimension e starts at the center of the wheel.

w, l, h : 0.25, 0.2, 0.05

These variables define the width, length and height of the body respectively. They are labeled in Figure 3.3 of Section 3.1. These values were not measured from the prototype and unlike the prototype, it is assumed the body's weight is evenly distributed throughout its geometry.

r, w_t : 0.0587, 0.025

These variables define the radius and thickness of the tires respectively. Whereas the numerical value for the radius of the tire was taken from the prototype, the thickness of the tires was not. For this particular example, the tires are relatively thin which causes significant wheel sinkage.

g : 3.68

This is the approximate value of gravity on Mars.

m_B : 2.0

This is the mass of the body. The prototype's body is actually much more massive than this, but ultimately, this is about where NASA wants the body mass to be.

ρ, s, t_s : 2710.0, 0.0254, 0.00317

The variable ρ stands for the density of the material the beam and rocker are made of. The value shown above is the density for a standard Aluminum. The variables s and t_s are defined in Figure 3.1 of Section 3.1. They are the side length and thickness of the hollow square stock which the beam and rocker are assumed to be composed of. These were taken from the prototype.

m_w, k_w : 0.3, 600.0

The variable m_w is the mass of the wheel assembly (driving motor, steering motor, and tire). Currently, the tire of the prototype alone has a mass of about 0.3 kg. The actual mass of the entire wheel assembly, however, will actually have to be 0.3 kg or less for the vehicle to reach its 5.0 kg 'weight' limit. The variable k_w is the tire stiffness. It was chosen here to give the tire a natural time period of about 0.5 seconds.

U, P_{max}, L, S_d : 0.5, 0.2, 10.0, 36563

The variable U is the unit mesh size or the distance between the terrain mesh points as seen in Figure 2.1 of Section 2.1. The smaller this value is, the more jagged the terrain. Making this value too small significantly slows the program. For a random terrain, a value of 0.3 meters or higher for U is

recommended. The programs functionality for a lower unit mesh size depends on the variable P_{\max} or the maximum relative peak size. The higher P_{\max} is set, the larger the slopes or the more rugged the terrain is. The variable L is the length of the terrain plot as is shown in Figure 2.1. Finally, the variable S_d is the seed value for the random number generator. Leaving the seed the same will give the same terrain for every run as long as the variables U , P_{\max} , and L are also not changed.

C_a , C_d , C_p : 3.0, 1.0, 0.5

These variables are used to control the torque of the wheels. The larger C_a and C_d are, the more sensitive the wheel torques are to forward velocity (V_x). In other words, if the vehicle begins to slow down, the wheel torques will rise to offset it. The rise in torque is controlled by the variable C_a as is shown in Figure 3.8 in Section 3.1. If C_a is too large, the wheel torques rise sharply and the vehicle begins to go too fast. If the variable C_d , which controls the reduction in torque or braking, is also too large, then the vehicle brakes hard. An oscillation between accelerating and braking results. Since this is obviously a waste of energy, it is important to make sure C_a and C_d are not too large. The variable C_p is the percentage of the tractive force used by the rear two tires. The rest of the tractive force is split evenly between the front four wheels if possible.

θ_{\max} , θ_{\min} : 0.4, -0.8

These are the maximum and minimum rotations of the rocker with respect to the beam as illustrated in Figure 1.17 of Section 1.4. θ_{\min} is set to have

an absolute value larger than θ_{\max} for stability reasons. This will be explained later in this section.

$\theta_{v6} : 0.1$

This is the initial vehicle yaw in radians.

$t, t_l : 0.05, 30.0$

The variable t is the time interval between steps. In other words, the vehicle moves forward with its joints locked for t seconds before the new contact forces and joint angles are found. The value 0.05 seconds seems to work well for the program. If a very rugged terrain is used, a smaller value may be appropriate. As the variable t is increased past 0.05 seconds, the program has trouble adjusting the joints properly. The same effect is noticed if the vehicle is going too fast. This often happens when the vehicle is sliding or bouncing down a steep slope. In order to allow the program to function properly when the forward velocity increases, the time step is automatically slowed down according to the function graphed in Figure 5.1. As the forward velocity increases past .07 m/sec, the time step decreases with a slope of -1.0 until it reaches 10% of its original value.

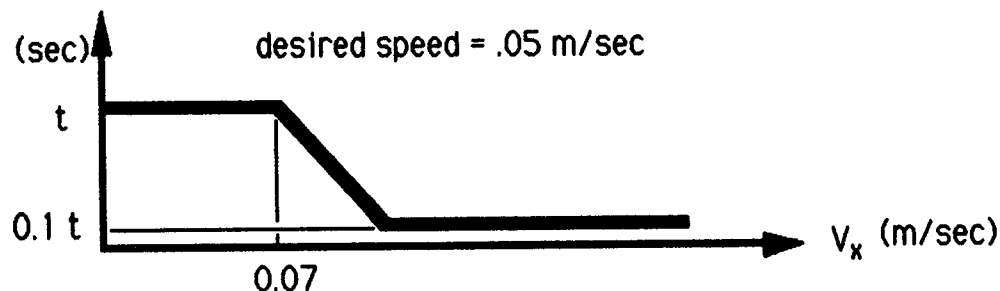


Figure 5.1 – Variation of time step with speed

The variable t_i is the number of time steps before the graphics display is updated. For this example, it would be about every $0.05 \times 30.0 = 1.5$ seconds of real time.

d_p : 0.001

This is the damping factor on the beam pivot. When the beam rotates, the differential and the body also rotate. Since the body has a significant mass, the body's inertia causes a damping moment. The damping factor is used to create a restoring torque on the beam pivot to slow its oscillation. This restoring torque for the left beam is $d_p \omega_L$ and is applied in the direction of rotation of the previous step. It should be noted that d_p is not the damping coefficient, but that it has the same effect.

Z₁, X₁, Z_{r1}, Z_{f1} : 2.0, 1.9, 3.5, 4.9

The first two variables locate the initial position of wheel one in global coordinates. The last two variables defines the destination point for wheel one in global coordinates. A warning message will be flashed if the user selects a point outside the terrain map.

T, T_{SL}, P₁, P₂, P₃, P₄, P₅ : 1, 1, 0.3, 0.2, 0.2, 0.3, -0.2,

P₆, P₇, P₈, P₉ : 3.0, 3.0, 0.1, 0.3

These variables are used to specify a simple terrain if a random terrain is not desired. If the integer variable T is set to the integer 0, all the other variables on this input line and the next one will be ignored and a random terrain will be made according to the variables U, P_{max}, L, and S_d as

previously discussed. If T is the integer 1, on the other hand, the random terrain is ignored and the following ten parameters specify a desired terrain. This terrain is set to have a 5 by 5 meter plot with a unit mesh size of 0.1 meters. If the variable T_{SL} is the integer 1, the specified terrain is rock. For any other value of T_{SL} , the terrain is sand. The remaining nine parameters orient the two hills or crevasses and determine their size. This is best illustrated by means of the top and side view of Figure 5.2.

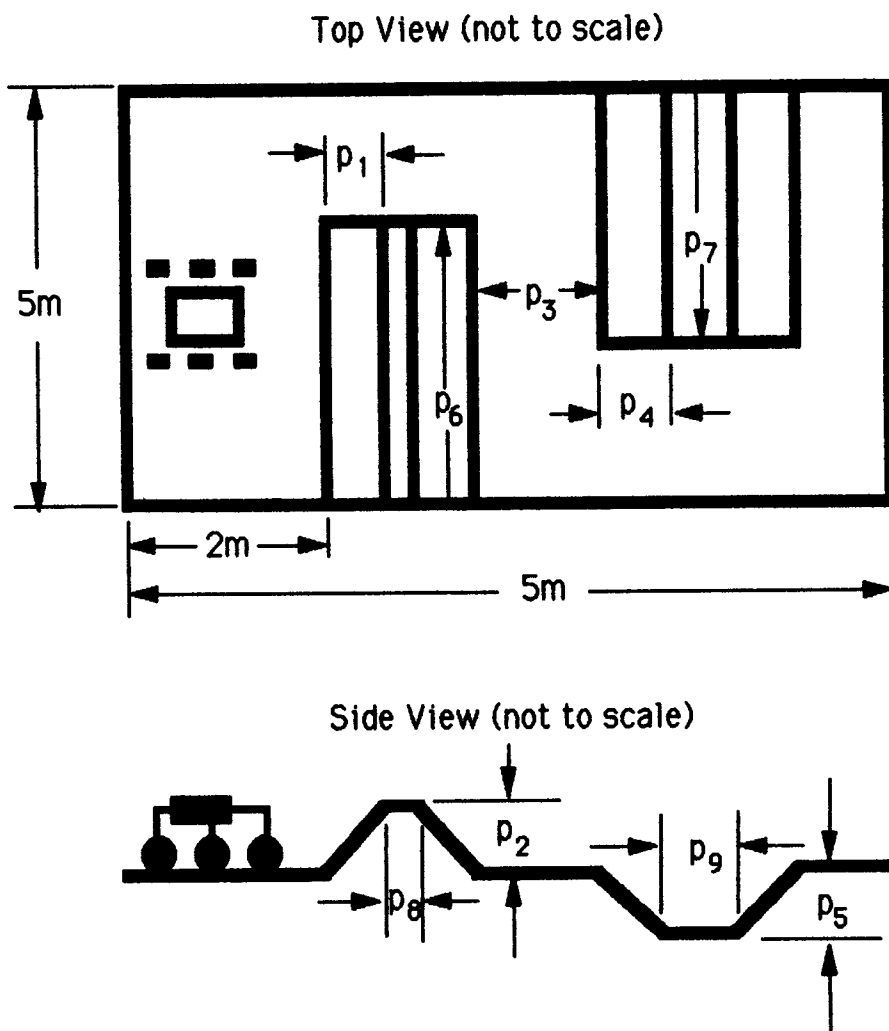


Figure 5.2 – Specified Terrain

Since the step size is automatically set to 0.1 meters, the program will round down the users input to the nearest decimeter with the exception of p_2 and p_5 . The variables p_2 and p_5 define the height of the hill (positive number) or the depth of the crevasse (negative number). These two terrain parameters may be any height or depth desired without the program rounding it off. The initial and final position of wheel one are used here in the same way as for the random terrain, however, one should keep in mind the 5 by 5 meter size of the terrain.

$\theta_a, C_h, C_r, C_t : 120.0, 2.0, 0.1, 0.15$

These four variables specify the type of path planning used. The first variable θ_a is the camera's view angle measured in degrees (note: all other angles are in radians except this one). If a path planner is not desired, set θ_a equal to zero. This will result in the vehicle aiming straight for its final destination. If θ_a is larger than 5.0° , the path planning algorithm is executed. The other camera parameters are specified by the next two variables C_h and C_r . The variable C_h is the maximum distance the camera can see or the horizon (see Figure 4.15 of Section 4.4). Remember this is unrealistically kept constant even if a hill obstructs its vision. The variable C_r defines the camera's resolution. It is recommended to make it about three times smaller than the step size of the terrain. Finally, the variable C_t is the central tendency factor. The larger C_t is, the more the vehicle will tend to opt for the straight path. From the example in Section 4.4, C_t equal to about 0.15 proved reasonable.

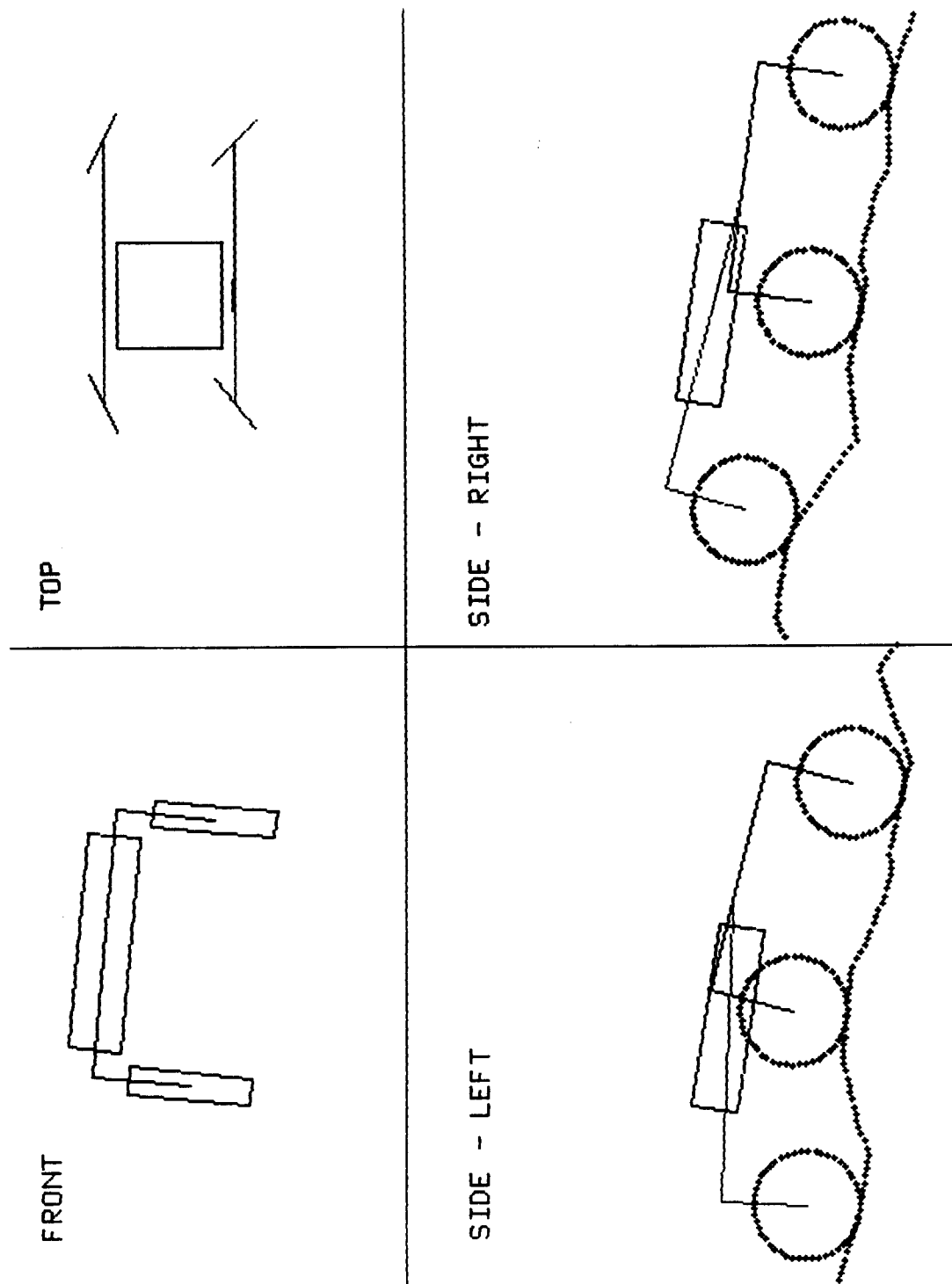


Figure 5.3 – Program Output

After the input has been specified, the program can be run as outlined in Appendix C. The output will be in terms of two side views, a top view, and a front view as seen in Figure 5.3.

The terrain shown in the side views is yellow if it is sand and white if it is rock. It is drawn in the two side views by slicing the terrain with a plane whose normal is perpendicular to gravity and contains the contact points of the front and rear tires. The middle wheel does not, in general, lie in this plane particularly if the vehicle is rolled, the joint angles are nonzero, and the wheels are turned. As a result, the middle wheel is actually into or out of the screen, and it may appear that it does not contact the terrain. This effect is small enough not to be too discernable unless the terrain is very rough and the vehicle has a large roll angle.

The two side views (named right and left when facing the front of the vehicle) are drawn looking down the vehicle's local z-axis. In other words, the vehicle does not increase or decrease in size in the side views as it undergoes yaw or roll. There is, however, no attempt to show that the wheels are turned in the side views. This information can be found in the top view. In reality, a side view of the vehicle would show the turned tires as ellipses.

The first time the side views are drawn, the vehicle is 'kinematically' placed on the terrain. Subsequent graphical displays (depending on the users selection of the variable t_i in the input file) will show the tires embedded into the terrain. How far each tire is embedded will depend on the tire stiffness k_w chosen as well as the terrain on which the vehicle is initially placed. The embedding of the tire into the terrain is due to soil sinkage as well as tire deformation. There is, however, no attempt to show the tire

deformation. Therefore, if a low tire stiffness is chosen, the tire will appear to sink into the soil farther than it would in reality. Despite this fallacy, the embedding of the tire into the terrain is a useful tool in order to determine which tires are seeing the larger contact forces.

The front view of Figure 5.3 simply shows the vehicle's roll angle. It is also the only view to show how thick the tires are. All the joint angles, however, are neglected in this view. In other words, if the front right tire was lower than the front left tire in the local frame, this would not show in the front view. This information can be found in the side views.

The top view of Figure 5.3 shows the vehicle's yaw angle with respect to the global frame and the wheels steering angles. For this particular Rocker Bogie configuration, since the middle tires are very close to the vehicle's local z-axis, they display very little steering angle. Figure 5.4 shows how the top view looks 1.5 seconds later. This shows the vehicle

TOP

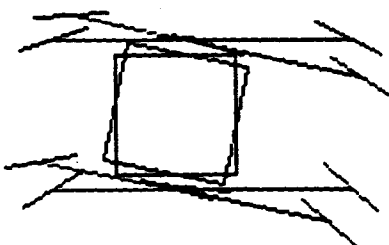
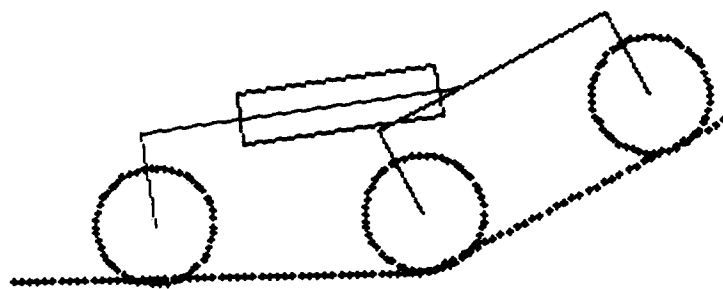


Figure 5.4 - Top view 1.5 seconds later

SIDE - RIGHT



SIDE - RIGHT

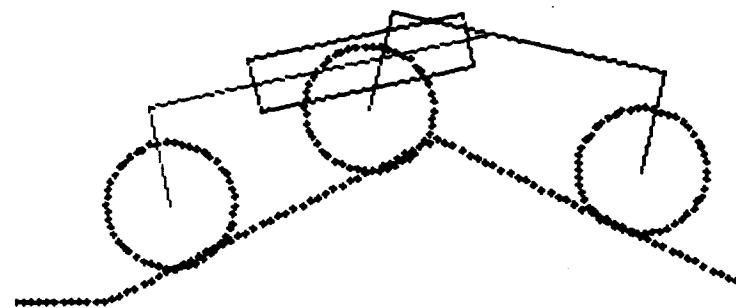
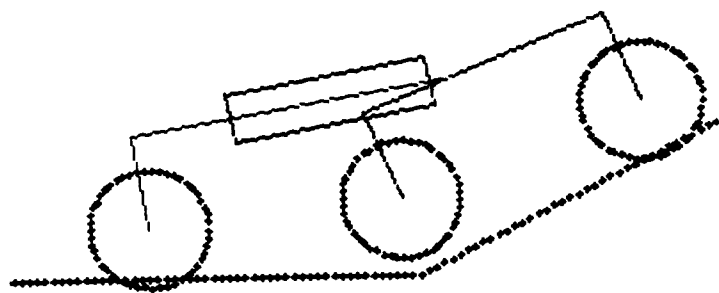


Figure 5.5 - Surmounting hill, stops not contacted

SIDE - RIGHT



SIDE - RIGHT

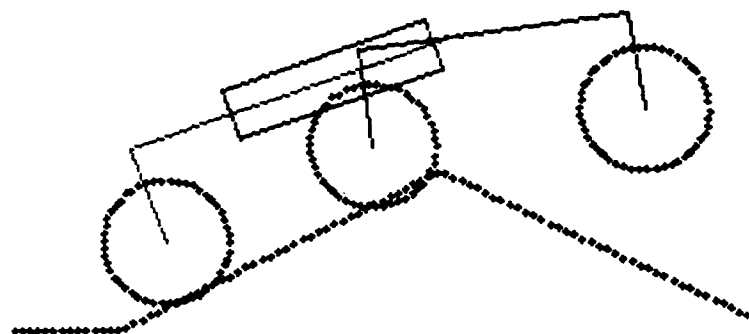


Figure 5.6 - Surmounting hill, stops are contacted

yawed and the steering angles adjusted. By not erasing the screen between displays, the progress of the vehicle can be seen. It is necessary, however, to follow the instructions in Appendix C to clear the screen every once in a while before it gets too cluttered.

Figure 5.5 shows the vehicle going up a 23° slope. First this was done by placing a large θ_{\max} and small θ_{\min} so that the rocker does not contact the mechanical stop. Then, as is shown in Figure 5.6, the same obstacle was transversed with θ_{\max} set at 0.2 radians and θ_{\min} set at -0.2 radians. By comparing Figure 5.5 and 5.6, it can be seen that the rear wheels of Figure 5.6 initially carry a heavier load. Then, as the vehicle reaches the peak, the middle wheels carry most of the load. The front wheel of Figure 5.6 will come crashing down once the middle wheel is close to the peak. As a result, the vehicle wants to hop and bound down the hill at a dangerous and perhaps

SIDE - RIGHT

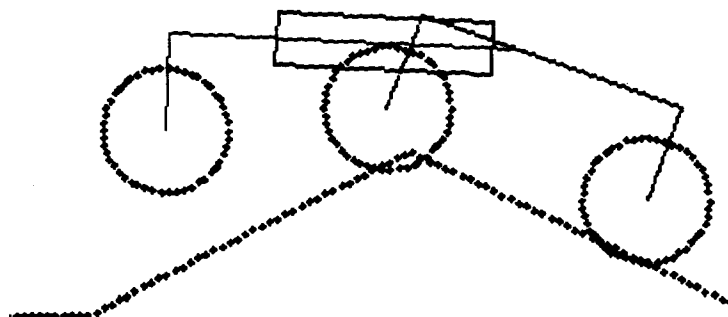


Figure 5.7 - Recovery from instability

fatal rate. For this reason, although a small θ_{\max} seems to not cause many problems, a large θ_{\min} (close to 0.0) causes an instability. Hence, it is recommended not to chose a large θ_{\min} . For θ_{\min} of -0.3 radians, the vehicle was able to recover and precede down the hill as shown in Figure 5.7.

At each step (t seconds), vital statistics will be displayed on the screen. The information displayed is the real time, the local x, y, and z velocities, the global X, Y, and Z distances with respect to the initial position, the joint angles, the roll and yaw with respect to the global frame, the power, and the work. In addition, a warning that the vehicle is unstable will be displayed if the wheels on one side of the vehicle are not contacting the terrain. If the path planning algorithm is selected, then the distance to the final point, the distance to the intermediate point, and the steering angle of wheel one are also listed. Refer to Appendix C about how to control the display on the screen.

SECTION 5.2 - PERFORMANCE

This section is concerned with finding the performance of JPL's rover Rocky III and finding ways to improve it. Although a prototype for Rocky III is available for testing, it can only be tested in Earth gravity. In addition, the prototype is much more massive than the actual vehicle should be. This is due mainly to the heavy battery packs. For these reasons, the performance of a less massive Rocky III on Mars is not known from experiments.

First, it is desired to determine how high Rocky III can climb on a rocky terrain. The input data base, as is shown in Table 5.2 and explained in Section 5.1, will be used to determine this information. The rover geometry defined in Table 5.2 is close to that of JPL's rover Rocky III.

Table 5.2 - Input

0.159	0.0953	0.0937	0.124	0.2		
0.25	0.2	0.05	0.0587	0.025	3.68	
2.0	2710.0	0.0254	0.00317	0.3	600.0	
0.1	0.05	10.0	36563	1.0	1.0	0.5
1.0	-1.0	0.0	0.05	30.0	0.001	
2.625	1.9	2.625	4.9			
1	1	0.2	0.1	0.6	0.2	-0.1
3.0	3.0	0.6	0.0			
0.0	2.0	0.1	0.1			

The specified terrain of Table 5.2 is shown in Figure 5.8. The variable p_2 , which is 0.1 meters in Table 5.2, is varied until the vehicle can no longer surmount the hill. It should be noted that θ_{\max} and θ_{\min} are set so that the

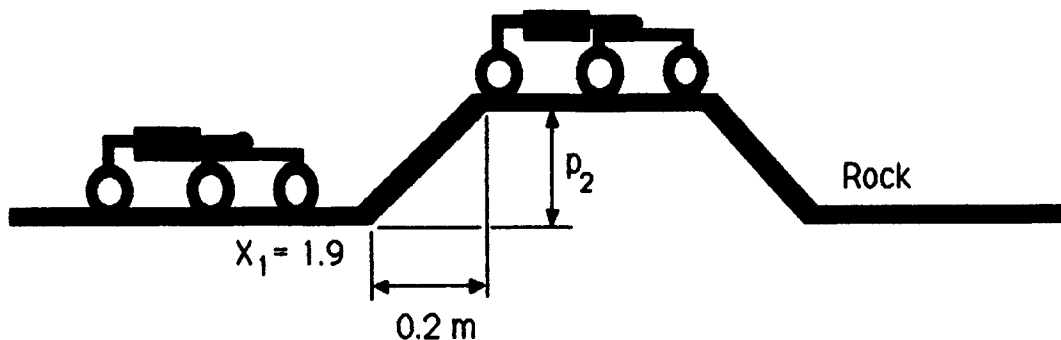


Figure 5.8 – Specified terrain I

mechanical stops are not contacted. They will be varied later. In addition, for now, both sides of the vehicle transverse the same terrain. By gradually increasing p_2 , it was determined that the maximum value of p_2 that Rocky III can surmount is 0.24 meters. For p_2 equal to 0.25 meters, the vehicle did

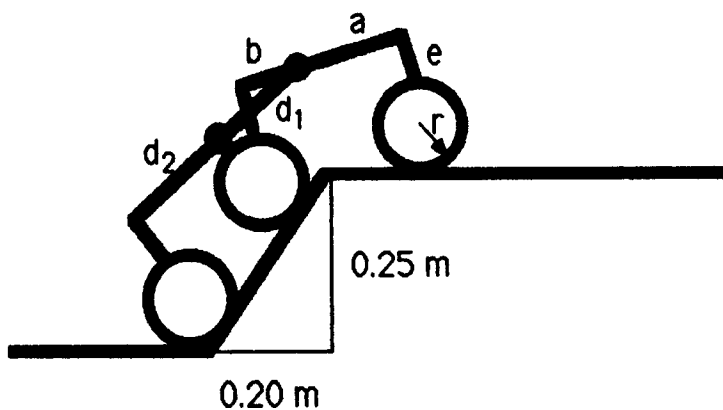


Figure 5.9 – Rocky III unable to proceed

not advance once the rear wheels contacted the slope as is shown in Figure 5.9.

As p_2 increased, the vehicle had trouble maintaining its speed since the wheels began to slip. This is reflected in the decreasing efficiency of the vehicle as is seen in Figure 5.10. The coefficient of acceleration C_a was increased to ensure that the wheels were putting out as much torque as possible as the slope increased. The percentage of torque going to the rear tires (C_p) is not important at this point. This is since C_a is high enough, and the terrain is steep enough, that all the wheels are slipping or are putting out the maximum tractive force independent of C_p .

The work required to surmount the hill is just the potential energy or $m_t g p_2$. This is since the kinetic energy term is negligible and since, unlike

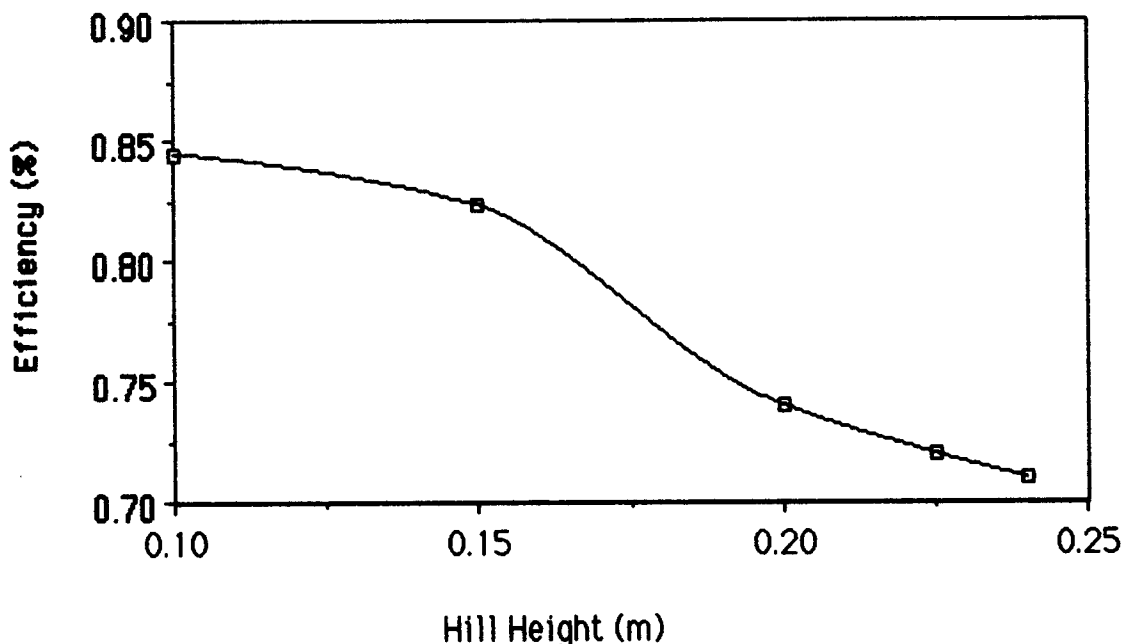


Figure 5.10 - Efficiency vs. Hill Height of Rocky III

the sand terrain, rock is assumed not to cause rolling resistance. The actual work is found from the wheel torques as explained earlier in Section 3.1. The efficiency of the vehicle going up the hill is graphed versus p_2 in Figure 5.10. The large drop in efficiency when p_2 is about 0.175 meters coincides to when the vehicle begins to slip and has trouble maintaining its speed.

As the vehicle moved down the slope of Figure 5.8, an instability of the rocker resulted when braking. This phenomenon, shown in Figure 5.11, was particularly noticeable on steep declines. The rocker is prevented from

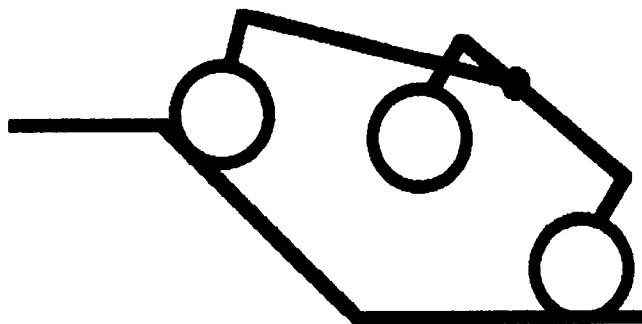


Figure 5.11 - Instability case one

rotating farther by means of the mechanical stops. This instability renders the middle wheels ineffective until they come crashing back down to the ground as soon as the brakes are released and a tractive force at the front wheels are applied. In order to avoid this instability, the front wheels are prevented from braking. The required braking force is then applied equally to the back four wheel.

Another problem in the simulation was that the beam oscillated about the beam pivot. This was particularly noticeable once the rear tires contacted flat ground at the bottom of the decline. To prevent this, a

damping factor, variable d_p as explained in Section 5.1, was added to damp out this oscillation. It was found that d_p , which is not the same as a damping coefficient, of 0.0005 was adequate to avoid this phenomena. This is actually a realistic modification since the beam has resistance to angular acceleration due to its inertia, as well as that of the differential and the body.

In an attempt to improve the vehicle's rock climbing characteristics, the vehicle's geometry was varied one parameter at a time from the JPL design. For convenience, the geometric parameters are shown again in Figure 5.9.

Dimension a was first increased from 0.159 to 0.2 meters. This did not significantly aid the vehicle's rock climbing ability. The vehicle still could not surmount the hill of Figure 5.9. When dimension a was reduced to the same value as dimension b, or 0.0953 meters, a rocker instability again resulted. As illustrated in Figure 5.12, this time the rocker instability occurred when the front wheels contacted the upward slope. Hence, it is important to ensure that dimension a is not made smaller than its current size.

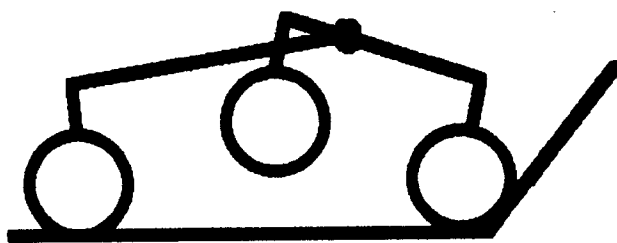


Figure 5.12 - Instability case two

Another way to help avoid this rocker instability is to move the rocker's center of gravity backwards by increasing dimension b. In addition, increasing dimension b did increase the rock climbing ability of the vehicle for this type of hill. It is better able to overcome the sticking point, as seen in Figure 5.9. This is since the larger lever arms of the middle wheels put more force on the front wheels. The front wheels can best be used to accelerate the vehicle forward since they are on the upper plateau. The maximum height of the hill (p_2) that the vehicle can navigate is graphed versus dimension b in Figure 5.13. The maximum value dimension b can assume without changing the length of JPL's design, and before the middle and rear wheels contact, is 0.19 meters. When dimension b is 0.19 meters the rock climbing ability is increased by 21% ($p_2 = 0.29$ meters) for this type of hill.

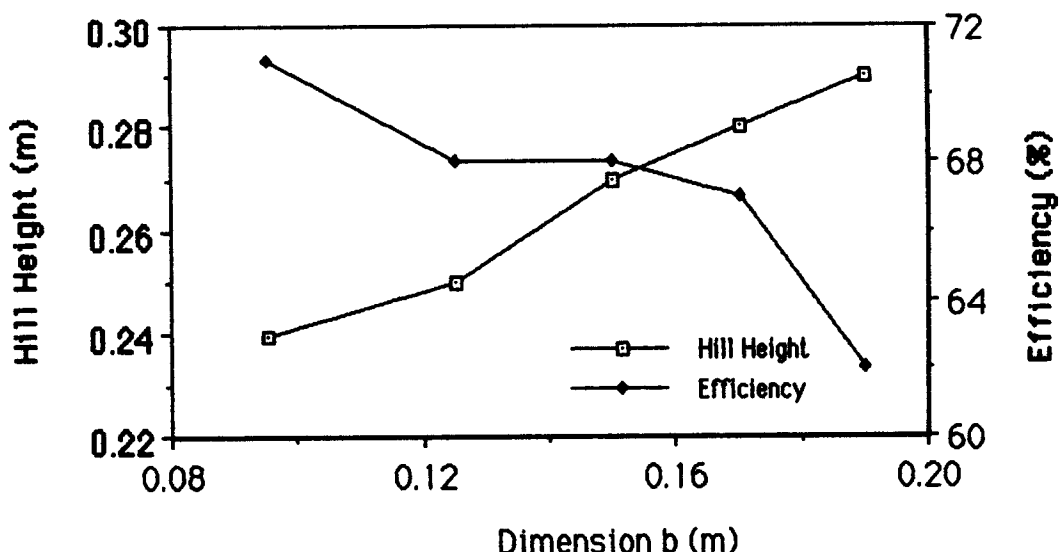


Figure 5.13 – Hill Height and Efficiency vs. b

Since the rocker's frame is relatively light, it only adds 140 grams of mass to the design. This increases the total vehicle mass from 5.0 kg to 5.14 kg. Therefore, increasing dimension b should not require a large increase in power. The efficiency of the vehicle when dimension b is equal to 0.19 meters, when compared with JPL's design appears to be almost the same for the hills both can surmount. The modified vehicle is only one percentage point lower in efficiency.

The disadvantage of increasing dimension b is that the middle wheels could drive the front wheels into a soft soil, since the front wheels will have a larger contact force. At the same time, however, as dimension b is increased, the angular displacement seen by the front wheels due to the middle wheels will be decreased. This could offset the above problem. In addition, as already mentioned, increasing dimension b can help offset the instability problem of Figure 5.12. Overall, increasing dimension b appears to help improve the performance of the vehicle for this type of hill. Unfortunately, as will be seen later in this section, increasing dimension b hinders the rock climbing ability on other types of hills.

In an attempt to further increase the contact forces on the front wheels with dimension b still set at 0.19 meters, dimension a was reduced to 0.13 meters from 0.159 meters. This resulted in a slight improvement in the vehicle's rock climbing ability. The vehicle almost made it up a slope with p_2 set at 0.3 meters. The rear wheels made it halfway up the slope before the vehicle slipped back down. Since this does not constitute a significant increase in the rock climbing ability, while it does increase the chance of a rocker instability, it is recommended not to modify dimension a.

In varying dimension e in JPL's design, it was found that it is essential to keep dimension e small, but large enough for ground clearance. If e is above 0.11 meters for JPL's design, the rocker instability of Figure 5.12 reoccurs when p_2 is 0.25 meters. Increasing dimension b helps to mitigate this problem. Nonetheless, it is recommended not to increase dimension e past 0.10 meters.

Next, the dimension d_1 (Figure 5.9) was varied from the 0.124 meters of JPL's design. Shortening d_1 did not improve the vehicle's rock climbing ability in this situation. Increasing d_1 did, however, increase the rock climbing ability. Roughly, a 20% increase in dimension d_1 results in a corresponding 8% increase in the rock climbing ability (8% increase of p_2) for this type of hill. It should be noted that this is adding to the length of the vehicle which might not be acceptable.

Dimension d_2 was varied next. By increasing dimension d_2 of JPL's design from 0.2 to 0.25 meters (a 25% increase), the vehicle struggled up the hill of Figure 5.8 with p_2 set at 0.25 meters, or 4% above that which JPL's design can climb. It did this with a greatly reduced efficiency of 64% due to slippage. Thus, increasing dimension d_2 causes a corresponding increase in rock climbing ability which is under half that of increasing dimension d_1 by the same amount. In addition, increasing dimension d_2 degrades the efficiency of the vehicle faster than increasing dimension d_1 . Therefore, if it is acceptable to increase the length of the vehicle, dimension d_1 should be increased from JPL's design and not dimension d_2 .

Since it might not be acceptable to increase the length of the vehicle, dimensions d_1 and d_2 were then varied in such a way as to keep their sum constant and equal to 0.324 meters. The results are shown in Figure 5.14.

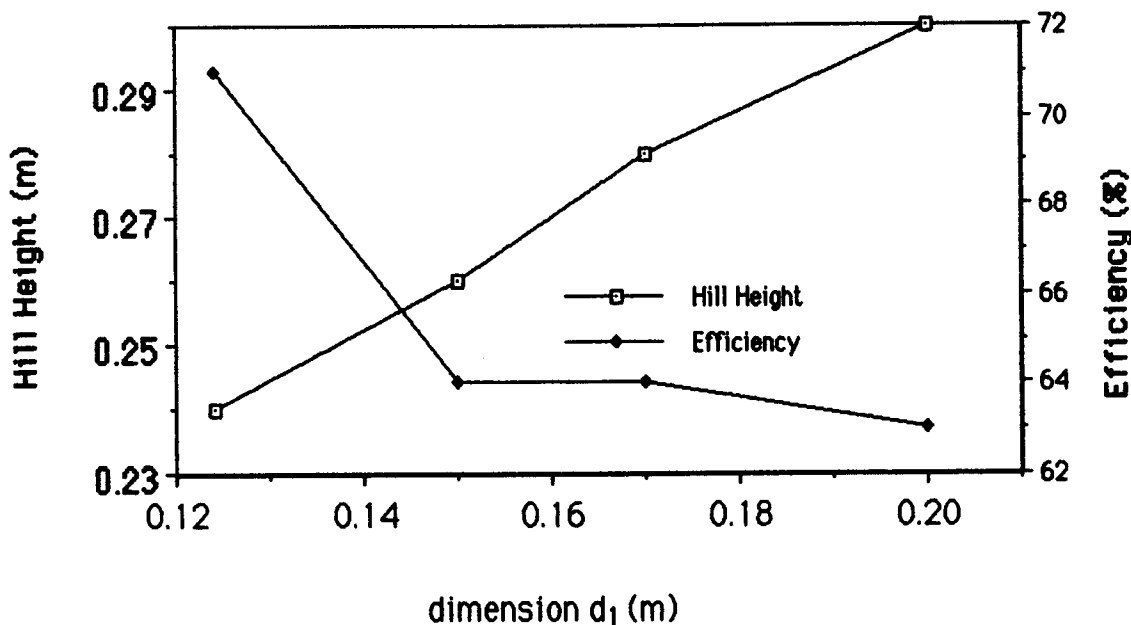


Figure 5.14 – Hill Height and Efficiency vs. d_1

As is seen in Figure 5.14, increasing dimension d_1 while decreasing dimension d_2 , or moving the body towards the back, greatly helps the vehicle's rock climbing ability for this type of hill. When d_1 is 0.2 meters, the rock climbing ability of the vehicle increases by 25% over JPL's design (maximum $p_2 = 0.3$ m). It was hoped to farther increase the rock climbing ability of the vehicle by increasing dimension b again to 0.19 meters. Unfortunately, the vehicle would still not climb a hill with p_2 set to 0.31 meters with this modification. When dimension b was set to 0.953 meters, as in JPL's design, and p_2 was set to 0.31 meters, the instability of Figure 5.12 resulted. The vehicle eventually overcame the instability. However, it can be avoided altogether by increasing dimension b . Moving the body back too far may be unfeasible. If the body is long enough, and is moved back far

enough, it could contact the ground when the vehicle traverses large slopes. In addition, as will be explained later, moving the body back too far reduces the vehicle's crevasse crossing ability.

Another disadvantage of moving the body towards the rear is that it also decreases the efficiency. When dimension d_1 was set to 0.2 meters and dimension d_2 was shortened to keep the vehicle length constant, the vehicle's efficiency decreased. It decreased by an average of 17% when compared to the JPL design for slopes both vehicles can surmount. This loss of efficiency was not seen when dimension b was increased. In addition, increasing dimension b resulted in climbing characteristics almost as good as those obtained by moving the body toward the rear (21% increase as opposed to 25% increase). Therefore, increasing dimension b would be a more prudent design for surmounting this type of hill. If efficiency is not as much a concern, perhaps both methods can be employed to a certain extent.

There was some uncertainty as to whether the Martain gravity would help or hurt the vehicle's rock climbing ability. The vehicle's lower weight would help with rock climbing, but its reduction in the maximum allowable tractive force would hurt it. By running the program for various cases for the JPL design, it was found that the Martian gravity improves the vehicle's performance. The Earth's gravity which is 250% of that on Mars, resulted in approximately a 8% decrease in the rock climbing ability and a 12% decrease in efficiency. Using these as a guide, one could roughly convert Earth performance tests to those the vehicle would see on Mars. Increasing the vehicle's mass uniformly has the same effect as increasing gravity. Hence, since a 250% increase in gravity or in weight only caused an 8% decrease in

the rock climbing ability, the vehicle's weight can be increased uniformly without having a large affect on its performance for this type of terrain. This is not the case for a sandy terrain however.

If the weight is not increased uniformly, or the same weight proportions are not maintained, the above statement does not hold. For example, a 50% increase in the weight of the body alone decreased the rock climbing ability of JPL's design by 17%.

Various parameters of the tire were varied next. It did not appear that increasing or decreasing the tire size helped the rock climbing ability for this case. In actuality, increasing the tire radius almost certainly will help, but perhaps it will not help significantly for the small range of allowable tire sizes. The tire size is restricted by the fact that the rocker instability reoccurs as the tire radius gets too large. Increasing the stiffness of the tires by 100% did not seem to make much of a difference in the performance. This seems to help justify the assumption of keeping the tire to ground stiffness constant throughout the program.

As schematically shown in Figure 1.17 of Chapter I, the mechanical stops are designed to allow the middle wheels to drop by one wheel radius in the event of a crevasse, and the front wheels to drop by one wheel radius in the event of a downward step. In order to accomplish this θ_{\max} is set to 0.23 radians and θ_{\min} is set to -0.23 radians in the input file of Table 5.2. Unless otherwise stated, the mechanical stops are set at +/- 0.23 radians throughout this section. Unfortunately, these mechanical stops greatly reduce the vehicle's rock climbing ability by about 33% for this type of hill. One of the reasons for this degraded rock climbing ability is illustrated by the sequence of events shown in Figure 5.15. As the vehicle shifts its

weight to the front and the entire vehicle is supported by the middle wheels, it slips backwards and the process is repeated. The other more obvious problem is that the front wheels are rendered ineffective as seen

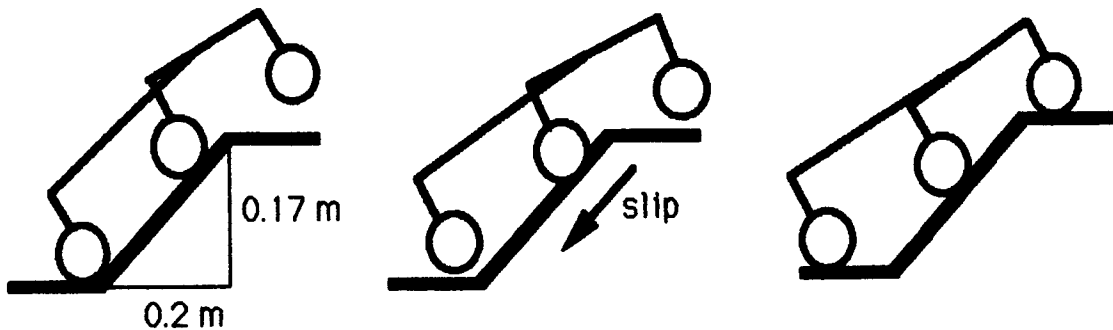


Figure 5.15 – Disadvantage of mechanical stops

in the left most diagram of Figure 5.15. Hence, the one set of wheels that can best propel the vehicle forward are lost. Since the front wheels are out of commission in this situation, increasing dimension b has little affect. Without the mechanical stops, increasing dimension b to 0.19 meters allowed the vehicle to climb a slope with p_2 set at 0.29 meters. Therefore, the vehicle has effectively lost 45% of its climbing ability when the mechanical stops are used. Likewise, moving the body back does not improve the rock climbing ability in this situation. This results in a 47% loss in the vehicle's rock climbing ability when the mechanical stops are used.

To avoid this situation θ_{\max} and θ_{\min} need to have a higher absolute value. If θ_{\max} is set to 0.4 radians and θ_{\min} is set to -0.4 radians, no rock climbing ability will be lost for the case when dimension b is 0.19 meters (still a 26% decrease in rock climbing for JPL's design). Nonetheless, this

would degrade the vehicle's crevasse crossing ability as will be investigated later. Most likely a compromise will have to be made.

The performance of the vehicle on sand is also very important. In order to determine this, the terrain of Figure 5.8 was changed to sand. The maximum height (p_2) of this type of hill that Rocky III can surmount is only 0.05 meters. For p_2 set at 0.06 meters, the vehicle stops advancing once the middle wheels contacted the upper slope as opposed to the rear wheels in the rock terrain. This is shown in Figure 5.16.

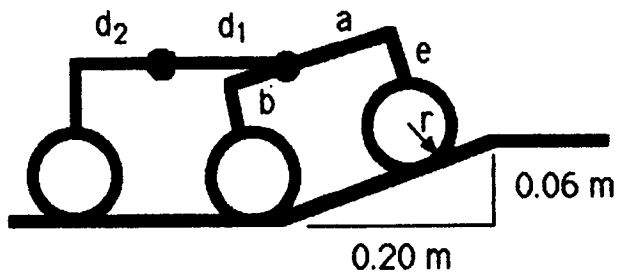


Figure 5.16 - Rocky III unable to proceed

The sand climbing ability is a dramatic 380% lower than the rock climbing ability. One of the reasons for this large reduction is that, unlike rock, sand creates a large resistive force to forward motion. This is particularly acute for the small tire width applied here (0.025 meters). The significance of this resistive force is reflected in the large drop in efficiency. This is since the work required to surmount the hill does not take into account the resistive force of the sand. The efficiency for Rocky III is only 23% when climbing the sand dune with p_2 set at 0.05 meters.

The much lower coefficient of friction used for sand over that used for rock ($\mu_{\text{sand}} = 0.3$, $\mu_{\text{rock}} = 0.8$), is the other culprit for the degraded climbing ability. In actuality, the vehicle will perform better on sand than predicted here since the wheels will have grousers. The effects of grousers are not modeled in the program. The program essentially assumes that the wheels are smooth cylinders. This inaccuracy should be kept in mind when analyzing the results or using the program. A more accurate representation of the vehicle's performance on this soil might be obtained by increasing the coefficient of friction on sand.

In order to reduce the effect of the resistive forces, the tire width was increased. By doubling the width of the tires to 0.05 meters, Rocky III was able to surmount a sand dune 40% higher ($p_2 = 0.7$ meters) with a 16% increase in efficiency. The tire width was then increased by 150% to 0.075 meters, but it still could not climb any higher. This is since the tractive force governed by the coefficient of friction is ruling, and the resistive force is no longer significant. When the tire width was decreased to 0.0375 meters it was still able to climb the sand dune with p_2 set to 0.07 meters. Nonetheless, it did so with a decreased efficiency. Hence, the tire width should be kept to around 0.05 meters. Increasing the radius of the tire would also help, but would increase the chance of a rocker instability and vehicle rollover.

In an attempt to farther increase the climbing ability of the vehicle on sand, dimension b was increased to 0.19 meters. Unexpectedly, this hindered its climbing ability. As will be seen throughout this section, what helps the vehicle's climbing ability in one situation hinders it in another. Generally, if the length of the upward slope is greater than half the vehicle

length or larger, increasing dimension b aides the climbing ability while if the length of the upward slope is about half the vehicle length or less, increasing dimension b hinders the climbing ability. One reason for this is that for a short upward slope, it is advantageous to get the middle wheels on the upper plateau as soon as possible. Moving the middle wheels back prevents this. Actually, decreasing dimension b helps the climbing ability for slopes less than half the vehicle length. Unfortunately, since the Martian terrain is not known in any detail, it is difficult to assess the optimal length for dimension b. The inflexibility of this vehicle illustrated here is one of its downfalls. However, due to the instability shown in Figure 5.12, it is still recommended to increase dimension b, but not to 0.19 meters. Dimension b should be around 0.12 meters for a compromise as opposed to 0.0953 meters of JPL's design.

Varying the position of the body did not help the vehicle climb any higher as it did for the rock terrain. This may be due to the difference in where the vehicle stops advancing as can be seen in comparing Figure 5.9 with Figure 5.16.

When Earth gravity was applied to the vehicle, its climbing ability was reduced by 42% and its efficiency was reduced by 77%. Thus, on sand, changing the vehicle's weight by adding mass or varying the gravitational constant changes the performance of the vehicle significantly. This is mainly due to the increase in sinkage and the resulting resistive force. Varying the vehicle weight uniformly when it was on rock did not significantly affect its performance since the resistive force on rock is assumed to be zero. Increasing the mass of the body from 2 kg to 3 kg resulted in a 40% reduction in climbing ability, but it did not adversely

effect the efficiency. Increasing the mass of each wheel from 0.3 kg to 0.4 kg, on the other hand, did not hamper or help the climbing ability, but resulted in a slight decrease in efficiency. Increasing the mass of the wheels, however, reduces the accuracy of the program while increasing the mass of the body improves it. This is a result of the assumption that the angular accelerations can be neglected.

As in the case of the rock terrain, a 100% increase in the wheel stiffness did not change the vehicle's performance. This further validates the assumption of leaving the terrain stiffness constant throughout the program. Finally, the mechanical stops also did not affect the vehicle's performance on this type of hill since the relative joint rotations are small.

Next, p_1 was changed to be 0.1 meters to allow for a steeper grade. The terrain was changed back to rock and both wheels still see the same conditions. This new terrain (specified terrain II) is shown in Figure 5.17.

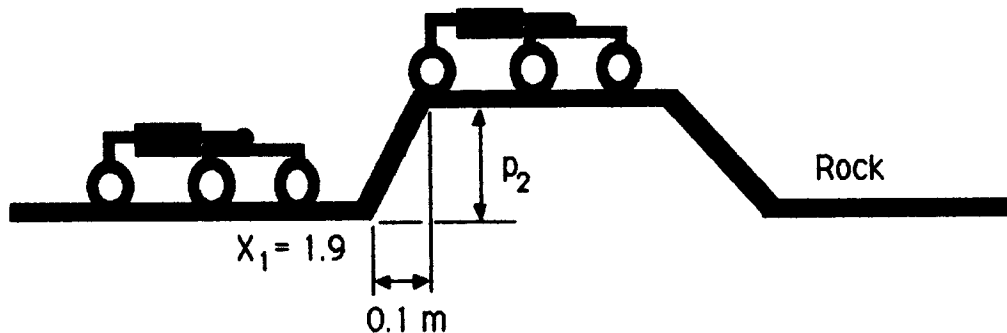


Figure 5.17 – Specified terrain II

By gradually increasing the height (p_2) of the hill, it was determined that the maximum height that Rocky III can surmount without the use of the mechanical stops is 0.21 meters. This is a 14% decrease in height when

compared to the case when p_1 was 0.2 meters (Figure 5.8). The efficiencies, however, are similar. The position where the vehicle can no longer advance is shown in Figure 5.18.

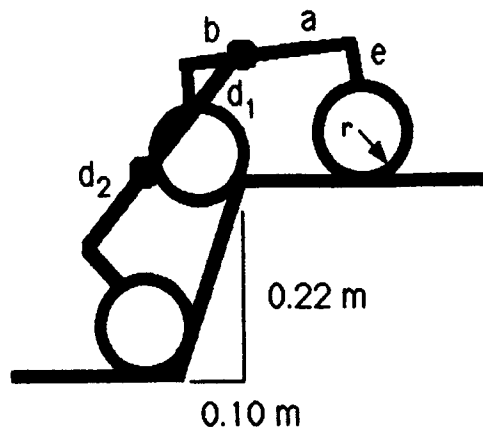


Figure 5.18 - Rocky III unable to proceed

Unlike the position shown in Figure 5.9, in Figure 5.18 it is seen that the middle wheels are almost on the upper plateau. As a result, and in contrast to the previous rock terrain, increasing dimension b decreases the rock climbing ability. The percentage increase and decrease in rock climbing ability as dimension b is varied is shown in Figure 5.19 for a base of 0.1 meters ($p_1 = 0.1$) and a base of 0.2 meters ($p_1 = 0.2$). As seen by this graph, it would be unwise to increase dimension b to 0.19 meters as first advocated. It is still prudent to increase dimension b to 0.12 meters for stability reasons.

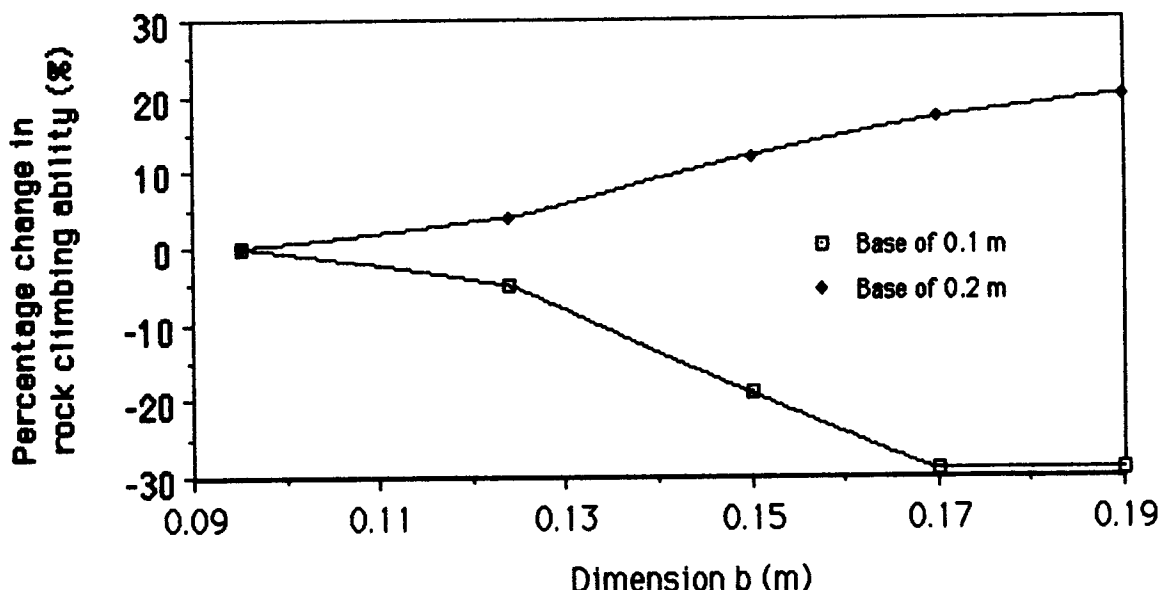


Figure 5.19 – Change in rock climbing vs. b

Decreasing dimension b to 0.09 meters allowed the vehicle to climb a hill one centimeter higher ($p_2 = 0.22$). However, this did increase the instability of the rocker as the front wheels contacted the upward slope (Figure 5.12). Since the objective here is to get the middle wheels on the upper plateau before the vehicle can no longer advance, the same effect as decreasing dimension b can be realized by increasing dimensions d_1 and/or d_2 . The advantage of increasing dimensions d_1 and/or d_2 is that it does not increase the rocker instability. Increasing d_1 from 0.124 meters to 0.15 meters indeed did allow the vehicle to climb the hill of height 0.22 meters. When it climbed a hill one centimeter taller ($p_2 = 0.23$) the rocker instability began to occur. This shows that even though increasing dimension b hinders this type of rock climbing, it is necessary to prevent the instability. The vehicle actually surmounted the hill of height 0.24 meters, or a 14% increase, even without increasing dimension b. The

transition to this hill, however, was not very smooth. The front wheels dug in at the base of the hill, jumped up into the air, hit the stops, crashed back on the terrain, and finally became stable. It could probably have climbed even higher slopes, but was limited by the rocker instability.

Another way to help avoid the rocker instability of Figure 5.12 is to decrease dimension e . In addition, decreasing dimension e would not decrease the rock climbing ability as does increasing dimension b for this terrain. By varying dimension e on Rocky III, it was found that there were varying degrees of instability. For example, when p_2 is set to 0.21 meters the rocker rotated negatively by 0.15 radians before it recovered. When dimension e was increased from 0.0937 meters of JPL's design to 0.1 meters, the rockers rotated negatively by 0.45 radians before they recovered. Finally, when dimension e was increased to 0.11 meters, the vehicle did not recover from the instability. Hence, for this type of hill dimension e needs to be less than 0.09 meters unless dimension b is also increased. Decreasing dimension e too far, however, causes interference problems on other types of hills.

It was postulated that the design where d_1 was 0.15 meters was limited to a hill of height 0.24 meters due to the rocker instability. This was proven to be the case since when dimension e was decreased to 0.08 meters to avoid the rocker instability, the vehicle climbed a hill of height 0.25 meters (19% above JPL's design). Similar results can be obtained by increasing dimension d_2 by the same amount. It is, however, more advantageous to increase dimension d_1 since it appears to provide a little more stability for the rocker and is more helpful on different types of terrain.

The placement of the beam pivot was varied without varying the length of the vehicle. This does not significantly aid the rock climbing ability in this case since it was limited by the rocker instability. By moving the beam pivot back by 2.5 centimeters, the rock climbing ability did not change, but the efficiency of the vehicle dropped from 64% to 50% when p_2 was set to 0.21 meters. When dimension e was reduced to 0.08 meters, the vehicle overcame its instability and climbed one centimeter higher than JPL's design. Hence, if the rocker instability can be overcome, the rock climbing ability of the vehicle can be increased by moving the body back with some sacrifice to the efficiency.

Unlike the dramatic decrease in the rock climbing ability when p_1 was 0.2 meters and the mechanical stops were in place, there is only a 10% decrease in the vehicle's rock climbing ability when p_2 is 0.1 meters with the mechanical stops used. The sticking point of the vehicle on this type of hill is the same as shown in Figure 5.15.

By moving the body back by 2.5 centimeters ($d_1 = 0.15$, $d_2 = 0.174$), and keeping the mechanical stops in place, the vehicle was able to surmount the same hill as when there was no stops. As before, when the body was moved back, however, the efficiency of the vehicle is degraded. It decreases from 64% to 57%. Overall, despite the slightly lower efficiency, it appears that increasing d_1 to 0.15 meters and decreasing d_2 to 0.174 meters is advantageous for most situations and should be implemented on the vehicle. If efficiency is of utmost importance, perhaps d_1 should not be increased. Finally, varying dimension b as well as moving the body forward did not help the vehicle's climbing ability for this type of terrain when the mechanical stops are used.

The terrain of Figure 5.17 was changed to sand to determine its effects on the vehicle's performance. The maximum height (p_2) of this type of hill that Rocky III can surmount is only 0.04 meters with an efficiency of 28%. For p_2 set at 0.05 meters the vehicle stopped advancing in the position shown in Figure 5.16. Moving the middle wheels as far back as possible ($b=0.19$) increased the vehicle's climbing ability by 25%. It was already decided that moving the middle wheels so far back would be impractical however. Fortunately, moving the body back by 2.5 centimeters had a similar result.

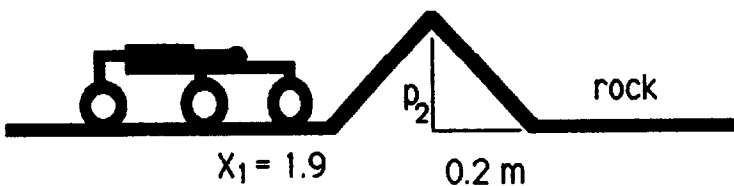


Figure 5.20 - Specified terrain III

Figure 5.20 illustrates the next type of hill investigated. Unlike the other hills analyzed, the vehicle is limited in how high it can climb by interference between the vehicle and the hill. If the interference problem is ignored, the vehicle is capable of climbing this hill for p_2 as high as 0.3 meters without using the mechanical stops. In actuality, however, the interference between the hill and the vehicle make it impossible to climb a hill of height any higher than 0.2 meters. The interference shown in Figure 5.21 can be mitigated by increasing dimension e (height of vehicle) or increasing the radius of the wheels. This is however unacceptable from a stability point of view. Keeping the middle wheels halfway between the front and rear wheels also helps. Increasing dimension b to 0.12 meters and

dimension d_1 to 0.15 meters as recommended maintains this situation to a certain extent.

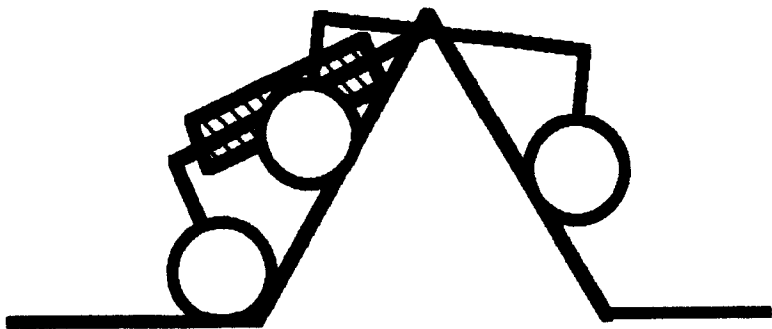


Figure 5.21 - Interference

Another way to avoid interference is to set the mechanical stops. The vehicle is illustrated going over this type of hill with the mechanical stops in Figures 5.6 and 5.7 of Section 5.1. As already explained, this creates another type of instability since the vehicle wants to come crashing down the hill.

When the mechanical stops are used, Rocky III could surmount a hill of height 0.15 meters (25% reduction in height). For a hill of height 0.16 meters, the vehicle could no longer advance once it reached the position shown at the bottom of Figure 5.6 of Section 5.1. When dimension b was increased to the recommended 0.12 meters, the vehicle could climb 7% higher with the mechanical stops in place. This was expected since the larger dimension b allowed more relative rotation between the joints for the same angles on the mechanical stops. In addition, increasing dimension b allowed the vehicle to make the transition from Figure 5.6 to Figure 5.7 of Section 5.1 in a more stable fashion.

Moving the body back by 2.5 centimeters ($d_1 = 0.15$ and $d_2 = 0.174$) from JPL's design with the mechanical stops in place also increased the rock climbing ability of the vehicle by 7%. Combining the increase in dimension b and in d_1 , however, did not further improve the vehicle's performance. Moving the body back more also did not improve the vehicle's rock climbing ability in this situation.

When the terrain of Figure 5.20 was switched to sand, JPL's design without the mechanical stops was able to climb a hill of height 0.06 meters. The vehicle could no longer advance once the rear tires contacted the upward slope. Although both increasing dimension b and moving the body back helped in rock climbing, it did not allow the vehicle to climb a higher sand dune. Increasing, the tire width past 0.05 meters also did not help.

When the mechanical stops were set the vehicle's sand climbing ability reduced by 17%. However, a slight increase in the absolute value of the mechanical stop angle would resolve this decreased performance.

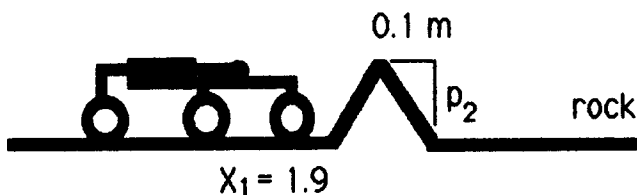


Figure 5.22 – Specified terrain IV

Figure 5.22 shows the last type of hill investigated. Similar to the terrain of Figure 5.20, interference is the main problem with this type of hill. Although the vehicle can climb the hill of height (p_2) 0.2 meters, it is actually impossible when interference is taken into account. The vehicle can navigate a peak of height around 0.15 meters without any interference.

With the mechanical stops in place, the vehicle's rock climbing ability is decreased by 40% (maximum height $p_2 = 0.09$ m) while its efficiency is reduced by 15%. With the mechanical stops set, increasing dimension b to the recommended 0.12 meters did not help the rock climbing ability on this type of hill as it did for the terrain shown in Figure 5.20. Moving the body back ($d_1 = 0.15$ m, $d_2 = 0.174$ m), however, did help increase the rock climbing ability by 22% ($p_2 = 0.11$ m) with the mechanical stops set. Moving the body back even farther ($d_1 = 0.2$ m, $d_2 = 0.124$ m) increased the rock climbing ability by 33%.

When the terrain of Figure 5.22 was changed to sand, Rocky III could only climb the sand dune of height 0.04 meters with or without the mechanical stops. Neither increasing dimensions b or d_1 allowed the vehicle to surmount the hill of height 0.05 meters. Only when the tire width was changed to 0.075 meters from 0.05 meters was the vehicle able to surmount the hill of height 0.05 meters. Hence, it makes sense to make the tires even wider. The minimum width for the tires should be 0.05 meters, and if possible, they should be made even larger.

The crevasse crossing ability of the vehicle was next analyzed using the rock terrain of Figure 5.23.

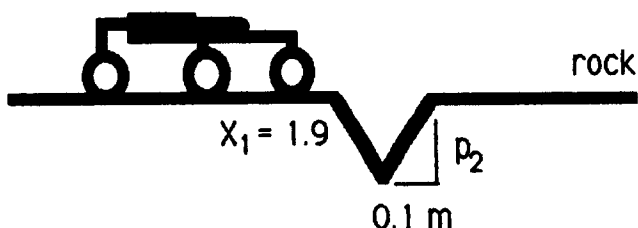


Figure 5.23 - Specified terrain V

Without the mechanical stops, Rocky III was able to cross a crevasse of depth -0.16 meters ($p_2 = -0.16$ m) in 12.82 seconds using 3.72 Joules of work. When the depth of the crevasse was increased to -0.17 meters, the rocker became unstable as is shown in Figure 5.24.

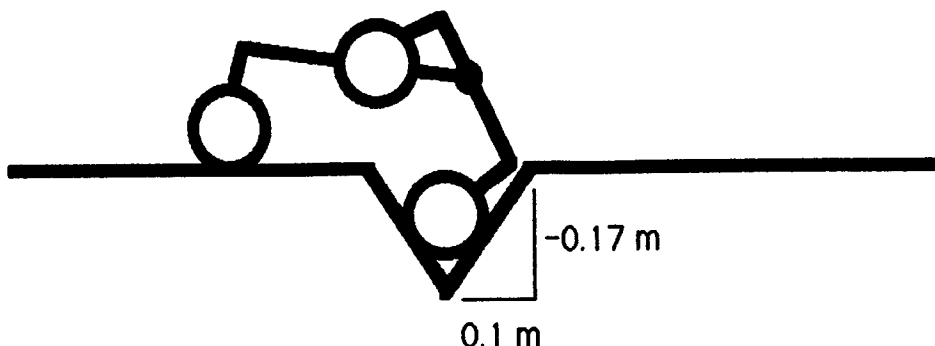


Figure 5.24 – Unable to cross crevasse

Increasing dimension b to 0.12 meters increased the crevasse crossing ability by 6% since the rocker instability was delayed. Increasing dimension b further to 0.19 meters increased the crevasse crossing ability by 13%, however, it was already determined that increasing dimension b to 0.19 meters would not be prudent. Neither increasing dimension a or moving the body towards the back seemed to aid the crevasse crossing ability in this situation.

When the mechanical stops were set on JPL's design, they unexpectedly reduced the crevasse crossing ability by 30%. The reason for this can be seen by analyzing Figure 5.25. Due to the mechanical stops, the rear wheels are lifted as the vehicle pivots about the middle wheels. Moving the body back and reducing the angle on the mechanical stops improves the situation. There is a delicate balance between the position of

the middle wheels and the body. The body has to be farther back than the middle wheels so the vehicle does not pitch forward into the crevasse as is seen in Figure 5.25. At the same time, if the body is too far back, the vehicle will pitch backwards into the crevasse after the first two sets of wheels have cleared and the rear tires are over the crevasse. Thus, in a new design, if dimension b is increased, dimension d_1 must likewise be increased.

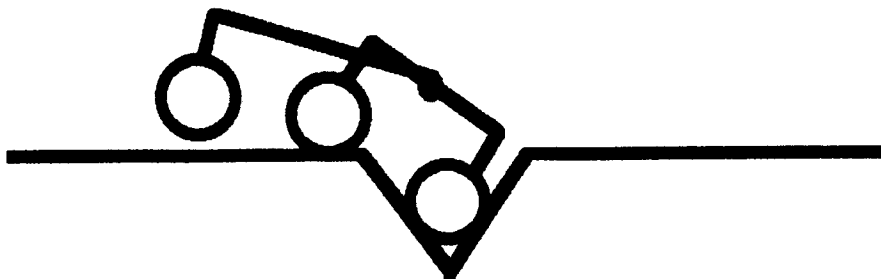


Figure 5.25 - Failure of mechanical stops

When d_1 is 0.2 meters, d_2 is 0.124 meters, and the mechanical stops are set at $+/- 0.1$ radians, the vehicle was able to cross this crevasse for any depth. Nonetheless, such a small allowable relative rotation between the rocker and beam would drastically reduce the rock climbing ability.

Whereas the program seems to work fine for rock climbing with and without the mechanical stops and crevasse crossing without the mechanical stops, there is some question as to the accuracy of this quasi-static analysis for crevasse crossing using the mechanical stops. This has to do with the separation of the dynamics of the body center and the adjustment of the joints. Nonetheless, the general trend seems to accurately show that what appears to help increase the crevasse crossing ability hinders the rock

climbing ability. Making a good rock climber and crevasse crosser is not feasible with this vehicle due to its passive joints.

When the terrain of Figure 5.23 was changed to sand, the JPL design without the mechanical stops would only cross a crevasse of depth -0.04 meters. When the crevasse depth was changed to -0.05 meters, the vehicle could no longer advance once the front wheels reached the bottom. Neither increasing dimension b or moving the body back allowed it to cross a deeper crevasse. The relative angles between the rocker and the beam are too small to be affected by the mechanical stops.

The last type of crevasse analysed is the rock terrain of Figure 5.26.

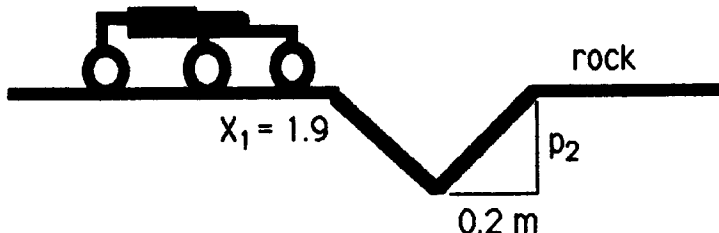


Figure 5.26 – Specified terrain VI

Without the mechanical stops, Rocky III was able to cross this crevasse of at most a depth of -0.15 meters. It did so in 18.4 seconds using 3.54 Joules of work. When the depth increased past -0.15 meters, the same rocker instability as is shown in Figure 5.24 resulted.

Unlike the crevasse of smaller width (specified terrain V of Figure 5.23), however, the mechanical stops did seem to help slightly. With the mechanical stops, the vehicle could cross the crevasse one centimeter deeper with a 37% reduction in the average power. Nonetheless, the

mechanical stops only increase the crevasse crossing ability in this situation by 6%.

In order for the vehicle to cross a deeper crevasse of this type, the rocker instability had to be resolved. As in other situations, this is achieved by moving the middle wheels back or increasing dimension b. When dimension b was set to the recommended 0.12 meters and the mechanical stops were not used, the vehicle's crevasse crossing ability increased by 27% for this type of terrain. Again, the vehicle was only limited in its crevasse crossing ability by the rocker instability (Figure 5.24). By increasing dimension b as far as possible without changing the vehicle length (0.19 meters), the crevasse crossing ability increased by a very significant 67%. Moving the body towards the back, however, neither helped or hurt the vehicle's crevasse crossing ability.

Changing the terrain of Figure 5.26 to sand, it was found that Rocky III could only cross a crevasse of depth -0.07 meters. Due to the small relative angles, the performance was not affected by the mechanical stops. When the depth was increased to -0.08 meters, the vehicle could not longer proceed once the middle wheels reached the bottom of the crevasse. Increasing dimension b did not improve the situation. This time, the vehicle could no longer proceed once the rear wheels reached the bottom of the crevasse. Moving the body back by 2.5 centimeters, however, did increase the crevasse crossing ability in this situation by 14%. Any further increase in the crevasse depth resulted in the vehicle unable to proceed once the front wheels reached the bottom of the crevasse.

The modification which increased the performance of the vehicle the most in this situation was increasing the tire width. By increasing the tire

width from 0.05 meters to 0.1 meters, the crevasse crossing ability increased by 29% since the wheel sinkage and hence resistive force was reduced. Therefore, as was confirmed on other sand terrains, it makes sense to increase the tire width past 5.0 centimeters. Since a 10.0 centimeter width seems unreasonably wide, perhaps a 7.5 centimeter tire width could be used.

Finally, the specified terrain of Figure 5.8 (using rock) was used to determine the track of the vehicle. The vehicle was positioned so that one side would stay on flat terrain while the other side would experience the hill. The criteria used to determine the vehicle's track was that the vehicle should be able to surmount a hill of the same height as when both wheels experience the hill. In order to accomplish this, the vehicle's ability to yaw had to be disabled. This is since the side of the vehicle on the flat terrain yaws towards the slope the other side is contacting. This phenomena is illustrated in Figure 5.27 and seems to accurately reflect what one would

Vehicle yaws

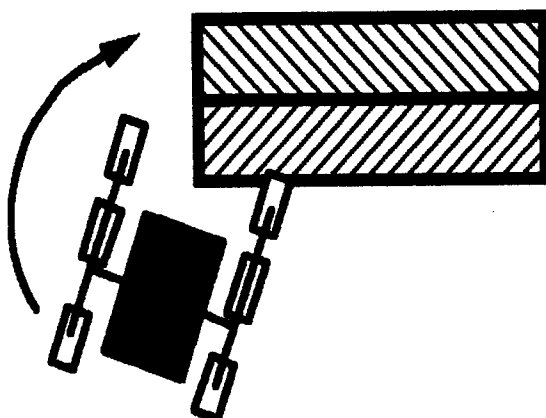


Figure 5.27 - Vehicle yaw

intuitively expect in this situation.

When the track was set to 0.25 meters, the hill height was set to 0.2 meters, and the mechanical stops were not used, Rocky III began to slip laterally before it reached the top. Once the roll angle reached 0.85 radians, the vehicle tipped over. By reducing the hill height to 0.19 meters, however, the vehicle could surmount the hill. Nonetheless, at the top, the vehicle's lateral velocity was greater than the forward velocity.

By increasing the vehicle's track to 0.30 meters, the vehicle's lateral slip was reduced by 60% on the hill of height 0.19 meters. In addition, the hill height could safely be increased to 0.21 meters (an 11% increase). At a hill height of 0.22 meters, however, the vehicle tipped over. It should be noted that as the track size increased, it was assumed that the mass of the vehicle remained the same.

The vehicle's track had to be increased to 0.35 meters to obtain the desired criteria. In addition, JPL's design needed to be modified once the height of the hill reached 0.25 meters due to a rocker instability. In order to avoid this, dimension b was increased to 0.12 meters and dimension e was decreased to 0.085 meters. In this manner, the vehicle did not roll over until the hill height reached 0.28 meters. This is approximately the hill height a new design could reach with both sides climbing the hill and with the recommended changes. Hence, 0.35 meters for the track appears to be reasonable. However, to add a factor of safety, it is recommended to make the track at least 0.4 meters. This is about 0.2 meters less than the vehicle's length. Figure 5.28 shows how the track affects the maximum height of the hill before rollover. The efficiencies are nearly the same for

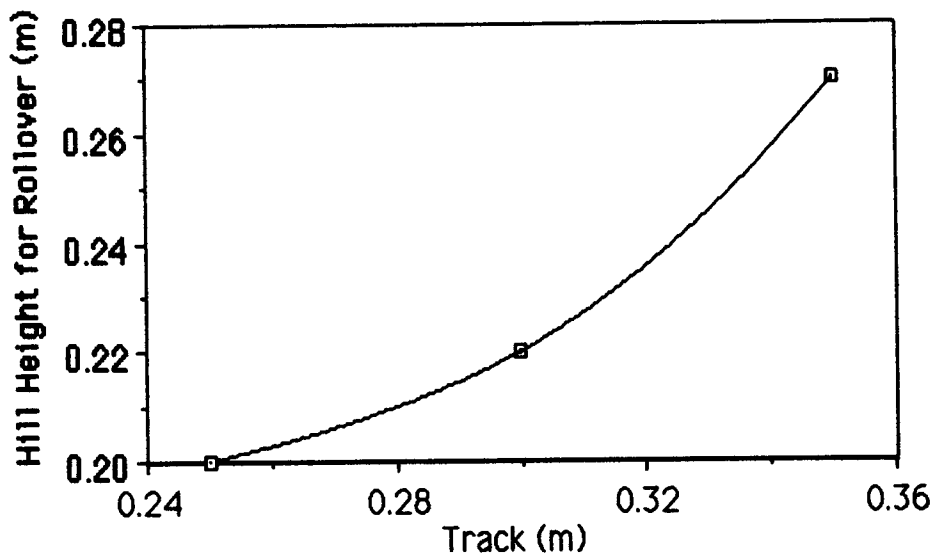


Figure 5.28 - Hill height for rollover vs. track

each case and are around 88%. This is 15 percentage points higher than if both wheels saw the same terrain. The larger slope of the graph between a track size of 0.3 meters and 0.35 meters is a result of lowering the vehicle's center of gravity (dimension e was reduced by about one centimeter to avoid the rocker instability).

Summary of Results

I. Specified terrain I (Figure 5.8)

A. Rock terrain, both sides see the same terrain.

1. JPL's design without mechanical stops can climb at most a hill of height 0.24 meters with an efficiency of 72%. It climbs smaller hills with efficiencies as high as 85%.
2. A rocker instability results during braking. Preventing the front wheels from braking resolves the instability here.
3. Increasing dimension a does not aid the rock climbing ability and decreasing dimension a causes the rocker instability.
4. Increasing dimension b to 0.19 meters increases the rock climbing ability by 21% without changing the efficiency. It also helps to prevent the rocker instability.
5. Dimension e should be less than 0.1 meters.
6. A 20% increase in dimension d_1 results in about an 8% increase in rock climbing.
7. A 25% increase in dimension d_2 results in about a 4% increase in rock climbing and degrades the efficiency faster than increasing dimension d_1 .
8. Moving the body back ($d_1 = 0.2 \text{ m}$, $d_2 = 0.124 \text{ m}$) increases the rock climbing by 25%, but decreases the efficiency by 17%.
9. Earth gravity causes an 8% decrease in rock climbing and a 12% decrease in efficiency.
10. A 50% increase in body weight decreases the rock climbing by 17%
11. The mechanical stops reduce the rock climbing ability of JPL's vehicle by 33% and the modified vehicle's by up to 47%.

B. Sand terrain, both sides see the same terrain.

1. JPL's design without mechanical stops can climb at most a hill of height 0.05 meters with an efficiency of 23%.
2. A 100% increase in the tire width to 0.05 meters resulted in a 40% increase in climbing (height = 0.7m) and a 16% increase in the efficiency.
3. Increasing dimension b hinders the sand climbing ability.
4. In general, for upward slopes larger than half the vehicle length, increasing dimension b aids climbing. If the length of the upward slope is about half the vehicle length or less, increasing dimension b hinders the climbing ability.
5. Moving the body did not aid climbing.
6. Earth gravity reduces the climbing ability by 42% and reduces the efficiency by 77%.
7. A 50% increase in the body mass results in a 40% decrease in climbing.
8. Increasing the mass of the wheels does not help or hinder climbing, but results in a lower efficiency.

C. Rock terrain, only one side sees the hill. This causes roll.

1. When the roll angle reached 0.85 radians, Rocky III tips over.
2. In order for the vehicle to transverse a hill of the same height it can with both sides encountering the hill, the track size needs to be at least 0.35 meters. A track of 0.40 was chosen.
3. The efficiencies are all around 88%. This is 15 percentage points higher than if both sides see the same terrain.

II. Specified terrain II (Figure 5.17)

A. Rock terrain, both sides see the same terrain.

1. JPL's design without mechanical stops can climb at most a hill of height 0.21 meters with similar efficiencies found in terrain I.
2. Increasing dimension b decreases rock climbing and decreasing dimension b improves it. When dimension b is 0.19 meters, the rock climbing ability decreases by 29%.
3. Increasing d_1 to 0.15 meters increases rock climbing by 14%.
4. Dimension e should be kept below 0.09 meters.
5. With dimension e set to 0.08 meters and dimension d_1 set to 0.15 meters, the rock climbing ability increases by 19%.
6. Increasing d_2 had similar results to step 5 above.
7. Moving the body back aids rock climbing slightly and reduces efficiency.
8. With the mechanical stops in place, the rock climbing ability decreases by 10%.
9. With the mechanical stops in place and the body moved back by 2.5 centimeters, the vehicle surmounts the same hill as when there was no stops. The efficiency, however, is degraded.
10. Varying dimension b does not help the vehicle.

B. Sand terrain, both sides see the same terrain.

1. JPL's design can climb at most a hill of height 0.04 meters with a 28% efficiency.
2. Increasing dimension b to 0.19 meters increases the sand climbing ability by 25%.
3. Moving the body back by 2.5 centimeters also increases the sand climbing ability by 25%.

III. Specified terrain III (Figure 5.20)

A. Rock terrain, both sides see the same terrain.

1. JPL's design without mechanical stops can climb at most a hill of height 0.3 meters, but due to interference it can only climb a hill of height about 0.2 meters.
2. With the mechanical stops, JPL's design can surmount a hill of height 0.15 meters (25% decrease).
3. Increasing dimension b to the recommended 0.12 meters allows it to climb 7% higher with the mechanical stops.
4. Moving the body back by 2.5 centimeters allows it to climb 7% higher with the mechanical stops.
5. Combining the two above modifications does not allow it to climb higher.

B. Sand terrain, both sides see the same terrain.

1. JPL's design can climb at most a hill of height 0.06 meters.
2. No modification allowed it to climb higher.
3. When the mechanical stops are set, the vehicle's sand climbing ability reduces by 17%.

IV. Specified terrain IV (Figure 5.22)

A. Rock terrain, both sides see the same terrain.

1. JPL's design without mechanical stops can climb at most a hill of height 0.2 meters, but due to interference it can only climb a hill of height about 0.15 meters.
2. When the mechanical stops are set, the vehicle's rock climbing ability reduces by 40% and its efficiency reduces by 15%.
3. Moving the body back 2.5 centimeters increases the rock climbing ability by 22% with the mechanical stops.

4. Increasing dimension b does not aid the rock climbing ability with the mechanical stops.
- B. Sand terrain, both sides see the same terrain.
1. JPL's design can climb at most a hill of height 0.04 meters.
 2. Increasing the tire width to 0.075 meters allows the vehicle to climb a hill of height 0.05 meters.

V. Specified terrain V (Figure 5.23)

- A. Rock terrain, both sides see the same terrain.
1. JPL's design without mechanical stops can cross at most a crevasse of depth -0.16 meters.
 2. Increasing dimension b to 0.12 meters increases the crevasse crossing ability by 6%.
 3. Increasing dimension d_1 or moving the body backwards does not help its crevasse crossing ability here.
 4. The mechanical stops unexpectedly degrade the crevasse crossing ability by 30% in JPL's design. (See number 6)
 5. When d_1 is set to 0.2 meters and the mechanical stops are set at ± 0.1 radians, the vehicle can cross this crevasse for any depth. (See number 6)
 6. The program's accuracy for crossing crevasses when the mechanical stops are used is questionable.
- A. Sand terrain, both sides see the same terrain.
1. JPL's design without mechanical stops can cross at most a crevasse of depth -0.04 meters.
 2. No change enables it to cross a deeper crevasse with the vehicle length held constant.

3. The mechanical stops do not affect the performance here.

VI. Specified terrain VI (Figure 5.26)

A. Rock terrain, both sides see the same terrain.

1. JPL's design without the mechanical stops can cross at most a crevasse of depth -0.15 meters.
2. With the mechanical stops on Rocky III, the crevasse crossing ability increases 6% and the efficiency improves by 37%.
3. When dimension b was set to 0.12 meters and the stops were not set, the crevasse crossing ability increased by 27%.
4. When dimension b was set to 0.19 meters and the stops were not set, the crevasse crossing ability increased by 67%.
5. Moving the body back did not help or hurt the crevasse crossing.

B. Sand terrain, both sides see the same terrain.

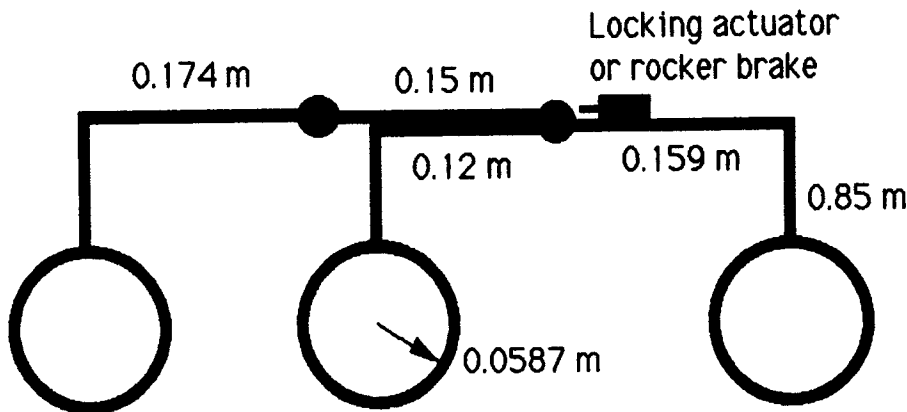
1. Rocky III with or without the stops can cross at most a crevasse of depth 0.07 meters.
2. Increasing dimension b did not help the crevasse crossing here.
3. Moving the body back by 2.5 centimeters increased the rock climbing ability by 14%.
4. Doubling the tire width from 0.05 meters to 0.10 meters improved the crevasse crossing ability by 29%.
5. At least a 0.075 meter width tire for the vehicle should be used.

SECTION 5.3 - CONCLUSIONS

By analyzing the summary of results outlined at the end of Section 5.2, the changes shown in Table 5.3 are recommended. Figure 5.29 shows the new design with the recommended dimensions.

Table 5.3 - New design

Parameter	JPL design	New design	Parameter	JPL design	New design
a	0.159 m	0.159 m	r	0.0587 m	0.0587 m
b	0.0953 m	0.120 m	w _t	-	0.075 ⁺ m
d ₁	0.124 m	0.150 m	θ _{max} , θ _{min}	0.23 rad	0.5 ⁺ rad
d ₂	0.200 m	0.174 m	w	-	0.4 ⁺ m
e	0.0937 m	0.0850 m	k _t	-	600 ⁺ N/m



Vehicle width = 0.4 m

Tire width = 0.075 m

Tire stiffness = 600 N/m

Mechanical stops = +/- 0.5⁺ rad

Figure 5.29 - New design

By relaxing the mechanical stops at the rocker pivots, the vehicle's rock climbing ability is greatly improved. Unfortunately, this is at the expense of a degraded crevasse crossing ability. As already mentioned, making a good rock climber and crevasse crosser is not feasible with this vehicle due to its passive joints.

One way around this might be to avoid crevasses altogether and design for a good rock climber. This could be accomplished by relaxing the mechanical stops to say +/- 0.5 radians as suggested or more. However, since not much is known about the Martian terrain on the small scale, this would not be a very realistic solution. Mars could be riddled with myriads of crevasses.

Another suggestion would be to place small actuators close to the passive joints of the rockers with the purpose of locking them in the event of a crevasse (Figure 5.29). Otherwise, the actuators would allow the passive joints of the rockers to act unimpeded. Alternatively, a brake capable of locking the rocker joint can be used. The locking actuators or rocker brakes could be powered to extend and lock the rocker joints and be automatically retracted away from the passive hinges by springs when the power is cut. In this manner, the actuators or brakes would not interfere with the rocker joints in case they fail. Using this fairly simple and safe modification, the vehicle could become both a good rock climber and crevasse crosser. In addition, many of the rocker instability problems could be prevented.

Finally, the passive hinges of the rockers could be replaced by active or powered hinges which would eliminate the need for the mechanical stops. This would require the vehicle to have a more sophisticated control scheme,

but it should greatly improve the performance of the vehicle. The drawback of this technique is that it could cripple the vehicle if one or both of these actuators failed. In addition, these actuators will require the RTG's to supply more power whereas the locking actuators or rocker brakes would require very little power. For these reasons, it is recommended that either locking actuators or rocker brakes be used on the passive joints of the rockers.

In conclusion, the new recommended design is compared to JPL's design to get an idea of how the performance of the vehicle changes. JPL's design has the mechanical stops set at $+/- 0.23$ radians and the recommended design has the mechanical stops set so they do not contact. Again, this is feasible since the locking actuators or brakes on the rockers are used in the event of a crevasse instead of the mechanical stops. Table 5.4 compares the maximum absolute p_2 values (heights and depths) that the two designs are capable of navigating.

In analyzing Table 5.4, it is seen that the new design performs much better on rocky terrain than Rocky III. Unfortunately, on sandy terrain, this success is not repeated. One of the reasons that JPL's design performs better, or the same as, the new design on sandy soil is that the mechanical stops on Rocky III do not contact. This is a direct result of the small heights and depths that the vehicle can navigate on sandy soil. In addition, the middle wheels of the new design are pushed back which hinders climbing on hills less than half the vehicle length.

Nevertheless, it should be kept in mind that the grousers on the tires are not modeled in the program. If the grousers were modeled, the vehicle probably would not have trouble surmounting sand dunes less than half the

Table 5.4 - Climbing comparison

Terrain	Figure	Soil	JPL p_2 (m)	New p_2 (m)	Change
I	5.8	rock	0.16	0.26	+ 63%
I	5.8	sand	0.07	0.05	- 29%
II	5.17	rock	0.19	0.20*	+ 5%
II	5.17	sand	0.04	0.04	0%
III	5.20	rock	0.15	0.20	+ 33%
III	5.20	sand	0.05	0.05	0%
IV	5.22	rock	0.09	0.13*	+ 44%
IV	5.22	sand	0.04	0.04	0%
V	5.23	either	0.223**	0.204**	- 12%
VI	5.26	rock	-0.16	-0.20	+ 25%
VI	5.26	sand	-0.07	-0.05	- 29%

* Restricted in climbing due to interference only.

** This is the maximum crevasse width and is just the smallest distance between two sets of wheels.

vehicle length. This is particularly true since most sand dunes should not have very steep slopes due to wind erosion. For larger sand dunes (larger than half the vehicle length) the modifications of the new design, namely moving the middle wheels back by 2.5 centimeters, will be helpful. In addition, for these larger sand dunes, the relative rotations between the rocker and beam will be larger. Therefore the mechanical stops on JPL's

design will contact and degrade the sand climbing ability. Hence, in reality, it is felt that the recommended new design will perform better than Rocky III on sandy terrains as well as on rocky terrains.

The main drawback of the recommended new design is the 12% reduction in specified terrain Ψ . The entries of Table 5.4 for specified terrain Ψ are the maximum widths of a crevasse of infinite depth that the vehicle can cross. Rocky III fares better here since the middle wheels are closer to the center of the vehicle. Nonetheless, if it is acceptable to make the vehicle about two centimeters longer by increasing dimension d_2 , then the recommended new design will cross a crevasse of the same width as Rocky III. This is based on the assumption that the locking pivot or brake works effectively to lock the rocker pivot in the new design.

Table 5.5 compares the efficiency of the two designs for specified terrains I and II. For the other terrains, it is more appropriate to compare the average power consumption. This is done in Table 5.6. For both tables, the efficiency and average power are rated at half the maximum height or depth Rocky III can navigate.

Table 5.5 - Efficiency comparison

Terrain	Figure	Soil	JPL η	New η	Change
I	5.8	rock	0.88	0.85	- 3%
I	5.8	sand	0.22	0.24	+ 9%
II	5.17	rock	0.84	0.85	+ 1%
II	5.17	sand	0.16	0.17	+ 6%

Table 5.6 - Average power comparison

Terrain	Figure	Soil	JPL watts	New watts	Change
III	5.20	rock	0.105	0.085	+ 19%
III	5.20	sand	0.158	0.140	+ 11%
IV	5.22	rock	0.130	0.130	0%
IV	5.22	sand	0.154	0.143	+ 7%
VI	5.26	rock	0.084	0.122	- 45%
VI	5.26	sand	0.157	0.144	+ 8%

As for efficiency and power consumption, the new design generally does slightly better than Rocky III. The exception is the large rock crevasses of specified terrain VI. The rocker joints were not locked for this crevasse when the power consumption of the new design was determined. If the rocker joints were locked with the recommended locking actuators or brakes, the new design would have a power consumption for this large crevasse similar to Rocky III.

BIBLIOGRAPHY

1. Encyclopedia Americana. Grolier Inc., Vol. 18, 1991, pg. 355-359.
2. Woodis, William R. et. al. Rover Mobility and Surface Rendezvous Study. Task 2 (FY89) for Martin Marietta Space Systems Company. November 1989. JPL Contract No. 958073 Mars Rover/Sample Return.
3. McTamaney et. al. Studies of Rover Mobility and Surface Rendezvous. Final Report for FMC Corporation. December 1989. JPL Contract No. 958074 Mars Rover/Sample Return.
4. Klein, G. Planetary Spacecraft Systems Technology Final Report 1985. Jet Propulsion Laboratory, Nov. 15, 1985, pg. 9.
5. Bhargava, Samir. Simulation of Motion Planning and Stability Analysis of the Walking Beam. M.S. Thesis. The Ohio State University, 1990.
6. Whittaker et. al. Ambler '90. The Robotics Institute. Carnegie Mellon, 1990.
7. Sreenivasan, Sidlgata V. A Simulation Study of a Baseline, Actively Coordinated Locomotion System for a Mars Rover. M.S. Thesis. The Ohio State University, 1988.
8. Yu, Jyh-Cheng. Design of Wheeled Actively Articulated Vehicle. M.S. Thesis. The Ohio State University, 1990.
9. Bekker, M.G. Introduction to Terrain - Vehicle Systems. Ann Arbor: The University of Michigan Press, 1969, pg. 240, 437-439.

10. Moore, Henry J. Preliminary Mars Surface Models. JPL Report.
11. Guenther. ME654 Land Vehicle Dynamics. Class notes.
12. Beer, Ferdinand P. and E. Russell Johnston, Jr. Vector Mechanics for Engineers. 4th ed. McGraw - Hill Book Co., 1984, pg. 821, 355.
13. Craig, John J. Introduction to Robotics. Addison-Wesley Publishing Company, 1989, pg. 49.

APPENDIX A

ASSUMPTIONS

- 1) For kinematics, both the tire and the terrain are rigid.
- 2) The width of the tire is neglected for most of the analysis. It is included, however, for determining the wheel sinkage.
- 3) The contact point is at the center of the contact patch.
- 4) The horizontal component of wheel velocity causes pure rotation about the Ackerman axis.
- 5) The vehicle first yaws about the local y-axis then rolls about the local x-axis.
- 6) The beam and rocker are made of a hollow square aluminum stock.
- 7) The wheel assembly, which includes the mass of the tire, driving motor, and steering motor, is homogeneously spread through the tire geometry.
- 8) The body is homogeneous.
- 9) The z-direction and xy plane dynamics can be superimposed.
- 10) In finding the initial contact forces, the horizontal components of the contact forces cancels the brake force.
- 11) The wheel motor is capable of applying any tractive force desired, and the brakes can apply any braking force desired.
- 12) The ground to tire contact is modeled with simple coulomb friction with $\mu_{\text{sand}} = 0.3$, $\mu_{\text{rock}} = 0.8$, and $\mu_{\text{static}} = \mu_{\text{dynamic}}$.
- 13) There is no rolling resistance on rock.
- 14) Soil is either sand or rock. The sand is as defined in case 12 of page 240 of Bekker's Introduction to Terrain Vehicle Systems [9].
- 15) Rock has infinite stiffness. For sand, the soil stiffness is determined by using Bekker's nonlinear sinkage formula on page 437 [9]. Once determined, the stiffness is used in the program as if it was linear.

- 16) The vehicle starts at rest with the brakes on and no slip.
- 17) The lateral force due to vehicle roll is equally shared among the six wheels.
- 18) The cross terms of the total vehicle moment of inertia, or the products of inertia, are assumed to be negligible.
- 19) The differential passes through the centroid of the body.
- 20) τ_y is replaced by an 'equivalent' linear force couple system.
- 21) The maximum lateral force before slip is 75% of the maximum tangential force before slip.
- 22) Coriolis effects are neglected.
- 23) The tire contact force is in the plane of the tire.
- 24) The lateral offsets in the joints and in the tires are neglected. This is the case even when the tires are turned.
- 25) The center of gravity of the body is synonymous with the center of gravity of the vehicle and the body's centroid.
- 26) The impact of the rocker hitting the stop is neglected.
- 27) The hinges are frictionless.
- 28) The dynamics of a tire turning about its steering axis is neglected.
- 29) The moment required to cause the angular acceleration of the body about the z-axis is split evenly between the two beams.
- 30) The terms containing the product of two angular velocities in Euler's equation are neglected.
- 31) Uniform acceleration is used.
- 32) The effective stiffness of the previous step is used to adjust the joints in the current step. The new wheel stiffness is calculated once the tires have been adjusted.

FURTHER PROGRAM SIMPLIFICATIONS

- 33) Joints and roll are adjusted statically.
- 34) Angular acceleration terms are neglected in the dynamics.
- 35) The tire to ground effective stiffness is held constant throughout the program.
- 36) Neglect initial velocity terms in the y and z displacement equations.

APPENDIX B

TOTAL VEHICLE MOMENT

OF INERTIA

In this Appendix the moment of inertia of the vehicle as a whole is found (I_{xt} , I_{yt} , I_{zt}). The total moment of inertia terms are used for the z-direction dynamics (particularly I_{yt}), and must be recalculated for each step since they are dependent on the joint angles.

As was previously mentioned, the cross terms of the moment of inertia, or the products of inertia, are neglected. This is justified on the basis that the body accounts for the majority of the vehicle's weight, and that the body is symmetric about the local x-axis (see Figure B.1).

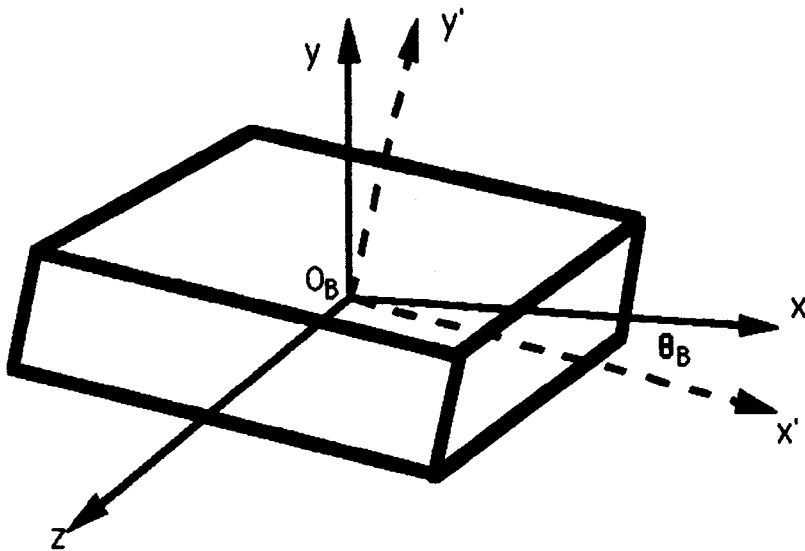


Figure B.1 - Local frame at body center

In actuality, even if the vehicle was totally composed of just the body's weight, not all the product of inertia terms would go to zero. Although I_{xyt} and I_{xzt} would go to zero due to the symmetry about the local x-axis, I_{yzt} would not. This is since the body is not symmetric about either the local y or z-axes unless the body angle (θ_B) is zero. It should, however, be smaller than the principal moment of inertia terms since the body is kept

as level as possible through the differential. For this reason, I_{yzt} will also be neglected.

In Chapter III, Equation 3.6, the moment of inertia of the rocker and beam about their respective pivots were solved. In order to distinguish the axis about which these were determined (the rocker and beam local z-axes), they will be renamed I_{z12} and I_{zL} . The moment of inertia of the left rocker about its z-axis (frame O_{12} as seen in Figure 2.8 of Chapter II), or I_{z12} , is independent of the rocker joint angle. Likewise, the moment of inertia of the beam about its z-axis (frame O_L), or I_{zL} , is independent of the beam joint angle. As a result, the moment of inertia of the right rocker about its local z-axis (frame O_{45}), or I_{z45} , and the moment of inertia of the right beam about its local z-axis (frame O_R), or I_{zR} , are the same as I_{z12} and I_{zL} respectively.

In order to determine the vehicle's total moment of inertia, I_{x12} , I_{y12} , I_{xL} , and I_{yL} must also be found. Unlike the moments of inertia found about the local z-axis of the rocker and beam, the moments of inertia about the x and y-axes are dependent on the joint angles. They are determined first for when all joint angles are zero. The moment of inertia of the rocker about its local x-axis with a zero pivot angle , or I_{x12} , can be found by analyzing the front view of the rocker as is shown in Figure B.2.

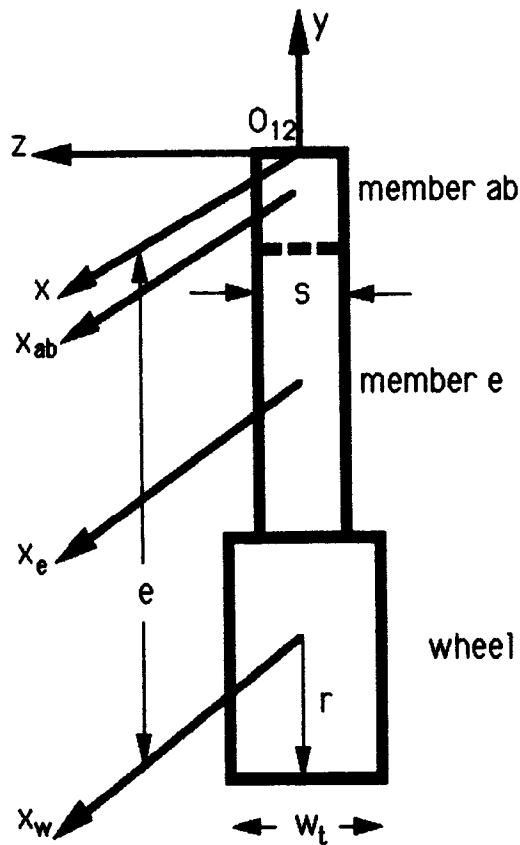


Figure B.2 - Front view of rocker

$$I_{xw} = \frac{1}{12} m_w (3r^2 + w_t^2) \quad I_{xe} = \frac{1}{12} m_e (e^2 + s^2)$$

$$I_{xab} = \frac{1}{6} m_{ab} s^2 \quad (B.1)$$

where all the values on the right side are defined in Section 3.1

Using the parallel axis theorem to move the moments of inertia to the rocker's pivot, the primed moments of inertia in Equation B.2 result.

$$\begin{aligned}
 I_{xw} &= I_{xw} + m_w e^2 & I_{xe} &= I_{xe} + m_e \left(\frac{e}{2} \right)^2 \\
 I_{xab} &= I_{xab} + m_{ab} \left(\frac{s}{2} \right)^2 & & (B.2) \\
 \therefore I_{x12} &= I_{x45} = 2I_{xw} + 2I_{xe} + I_{xab}
 \end{aligned}$$

The moments of inertia for both the wheel and member e are doubled in the final expression for I_{x12} since there are two of these members in each of the rockers.

Now, the top view of the rocker as is shown in Figure B.3 is used to determine I_{y12} for a zero rocker angle.

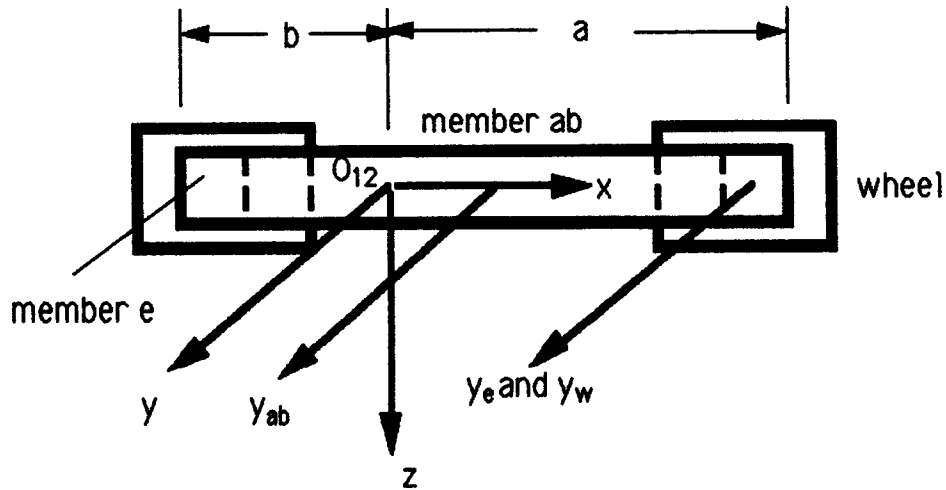


Figure B.3 - Top view of rocker

$$I_{yw} = I_{xw} \quad I_{ye} = \frac{1}{6} m_e s^2$$

$$I_{yab} = \frac{1}{12} m_{ab} (s^2 + (a+b-2s)^2) \quad (B.3)$$

Using the parallel axis theorem to move the y-axis moments of inertia to the rocker's pivot, the primed moments of inertia of Equation B.4 result.

$$\begin{aligned} I_{yw} &= 2 I_{yw} + m_w (b^2 + a^2) \\ I_{ye} &= 2 I_{ye} + m_e ((a-s/2)^2 + (b-s/2)^2) \\ I_{yab} &= I_{yab} + m_{ab} ((a-b)/2)^2 \\ \therefore I_{y12} &= I_{y45} = I_{yw} + I_{ye} + I_{yab} \end{aligned} \quad (B.4)$$

Since the local axis of the rocker, centered at its pivot, has no axis of symmetry with respect to the rocker, or length a does not equal length b (see Figure 3.1 of Section 3.1), a product of inertia I_{xy12} results. Although the product of inertia terms are neglected in the final result, they are not neglected at this point. This is since they contribute to the principal moments of inertia when the inertias are rotated to coincide with the vehicle's local frame. The product of inertia term for the rocker is shown in Equation B.5.

$$I_{xy12} = I_{xy45} = m_w e(b-a) + m_e \frac{e}{2} (b-a) + m_{ab} \left(\frac{b-a}{2} \right) \frac{s}{2} \quad (B.5)$$

Next, a similar analysis is done for the beam. The front view of the beam will look similar to Figure B.2, and its moment of inertia is similar to Equation B.1 and B.2. The difference is that the member of length $a+b$ (member ab) is replaced by the member of length d_1+d_2 (member d).

$$I_{xd} = \frac{1}{6} m_d s^2 \quad I_{xd} = I_{xd} + m_d \left(\frac{s}{2} \right)^2$$

$$\therefore I_{xL} = I_{xR} = I_{xe} + I_{xw} + I_{xd} \quad (B.6)$$

The top view of the beam will look similar to Figure B.3, and its moment of inertia is similar to Equation B.3 and B.4. The difference here is in the distances d_1 and d_2 of the beam rather than the distances a and b of the rocker.

$$I_{yd} = \frac{1}{12} m_d (s^2 + (d_1 + d_2 - s)^2) \quad I_{yw} = I_{yw} + m_w (d_2)^2$$

$$I_{ye} = I_{ye} + m_e (d_2 - s/2)^2 \quad I_{yd} = I_{yd} + m_d \left(\frac{d_1 - d_2}{2} \right)^2 \quad (B.7)$$

$$\therefore I_{yL} = I_{yR} = I_{yw} + I_{ye} + I_{yd}$$

Similar to the rocker, the beam's local axis at its pivot has no axis of symmetry with respect to the beam. Hence, it contains the product of inertia term I_{xyL} as is shown in Equation B.8.

$$I_{xyL} = I_{xyR} = m_w(e) d_2 + m_e \left(\frac{e}{2} \right) d_2 + m_d \left(\frac{s}{2} \right) \frac{d_2 - d_1}{2} \quad (B.8)$$

The next step is to move the moments of inertia of both the rocker and the beam to the vehicle's center of gravity. This makes the moments of inertia dependent on the joint angles. Using Figure 2.9 in Section 2.2 as a guide, the distance from the joint pivot on the rocker (O_{12} and O_{45}) to the vehicle's center of gravity is shown in Equation B.9.

$$\begin{aligned} x_{12} &= d_1 \cos(\theta_L) & y_{12} &= d_1 \sin(\theta_L) & z_{12} &= W/2 \\ x_{45} &= d_1 \cos(\theta_R) & y_{45} &= d_1 \sin(\theta_R) & z_{45} &= -W/2 \end{aligned} \quad (B.9)$$

Now, the moments of inertia of the rocker is translated to the vehicle's local frame using the parallel axis theorem.

$$\begin{aligned} I_{x12} &= I_{x12} + m_{12} (y_{12}^2 + z_{12}^2) & I_{y12} &= I_{y12} + m_{12} (x_{12}^2 + z_{12}^2) \\ I_{z12} &= I_{z12} + m_{12} (x_{12}^2 + y_{12}^2) & I_{xy12} &= I_{xy12} + m_{12} x_{12} y_{12} \\ I_{x45} &= I_{x45} + m_{12} (y_{45}^2 + z_{45}^2) & I_{y45} &= I_{y45} + m_{12} (x_{45}^2 + z_{45}^2) \\ I_{z45} &= I_{z45} + m_{12} (x_{45}^2 + y_{45}^2) & I_{xy45} &= I_{xy45} + m_{12} x_{45} y_{45} \end{aligned} \quad (B.10)$$

Next, the moments of inertia are aligned with the vehicle's local frame by rotating about the z-axis as shown in Figure B.4 [12]. This is necessary since the moments of inertia of the rocker and beam about their local x and y-axes were solved when the joint angles were set to zero. Alternatively,

they were solved as if the local axes centered at O_{12} , O_{45} , O_L , and O_R rotate along with the rocker or beam they are attached to.

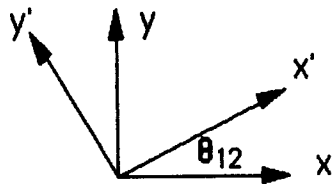


Figure B.4 - Rotation about z-axis

Notice that the product of inertia terms are not rotated in Equation B.11 since they are later neglected. They do, however, contribute to the principal moments of inertia when they are rotated about an angle. This is shown in Equation B.11.

$$\begin{aligned} \dot{I}_{x12} &= \dot{I}_{x12} \cos^2(\theta_{12}) + \dot{I}_{y12} \sin^2(\theta_{12}) - 2 \dot{I}_{xy12} \sin(\theta_{12}) \cos(\theta_{12}) \\ \dot{I}_{y12} &= \dot{I}_{x12} \sin^2(\theta_{12}) + \dot{I}_{y12} \cos^2(\theta_{12}) + 2 \dot{I}_{xy12} \sin(\theta_{12}) \cos(\theta_{12}) \\ \dot{I}_{z12} &= \dot{I}_{z12} \end{aligned} \quad (\text{B.11})$$

$$\begin{aligned} \dot{I}_{x45} &= \dot{I}_{x45} \cos^2(\theta_{45}) + \dot{I}_{y45} \sin^2(\theta_{45}) - 2 \dot{I}_{xy45} \sin(\theta_{45}) \cos(\theta_{45}) \\ \dot{I}_{y45} &= \dot{I}_{x45} \sin^2(\theta_{45}) + \dot{I}_{y45} \cos^2(\theta_{45}) + 2 \dot{I}_{xy45} \sin(\theta_{45}) \cos(\theta_{45}) \\ \dot{I}_{z45} &= \dot{I}_{z45} \end{aligned}$$

An analogous method is used to translate and then rotate the moments of inertia of the beam to the vehicle's local frame. The distances from the

joint pivot on the beam to the vehicle's center of gravity is shown in Equation B.12.

$$z_L = W/2 \quad z_R = -W/2 \quad (B.12)$$

all other distances are zero

Now, the moments of inertia of the beam are translated to the center of gravity using the parallel axis theorem.

$$\begin{aligned} i_{xL} &= i_{xL} + m_L z_L^2 & i_{yL} &= i_{yL} + m_L z_L^2 \\ i_{zL} &= i_{zL} & i_{xyL} &= i_{xyL} \end{aligned} \quad (B.13)$$

i_{xR} , i_{yR} , i_{zR} , and i_{xyR} are the same as above

Next, the moments of inertia of the beams are rotated to the orientation of the vehicle's local frame.

$$\begin{aligned} i_{xL} &= i_{xL} \cos^2(\theta_L) + i_{yL} \sin^2(\theta_L) - 2 i_{xyL} \sin(\theta_L) \cos(\theta_L) \\ i_{yL} &= i_{xL} \sin^2(\theta_L) + i_{yL} \cos^2(\theta_L) + 2 i_{xyL} \sin(\theta_L) \cos(\theta_L) \\ i_{zL} &= i_{zL} \\ i_{xR} &= i_{xR} \cos^2(\theta_R) + i_{yR} \sin^2(\theta_R) - 2 i_{xyR} \sin(\theta_R) \cos(\theta_R) \\ i_{yR} &= i_{xR} \sin^2(\theta_R) + i_{yR} \cos^2(\theta_R) + 2 i_{xyR} \sin(\theta_R) \cos(\theta_R) \\ i_{zR} &= i_{zR} \end{aligned} \quad (B.14)$$

The moments of inertia of the body also have to be rotated to the orientation of the vehicle's local frame, but do not have to be translated (see Figure B.1). The body's moments of inertia were defined in Section 3.1 Equation 3.7. To distinguish about which axis the moments are taken, they will be renamed (\bar{I}_{xB} , \bar{I}_{yB} , \bar{I}_{zB}).

$$\begin{aligned}\bar{I}_{xB} &= I_{xB} \cos^2(\theta_B) + I_{yB} \sin^2(\theta_B) & \bar{I}_{zB} &= I_{zB} \\ \bar{I}_{yB} &= I_{xB} \sin^2(\theta_B) + I_{yB} \cos^2(\theta_B) & \theta_B &= \frac{\theta_R + \theta_L}{2}\end{aligned}\quad (B.15)$$

Finally, all the moments of inertia are summed up to find the total moment of inertia of the vehicle (I_{xt} , I_{yt} , I_{zt}).

$$\begin{aligned}I_{xt} &= \bar{I}_{x12} + \bar{I}_{x45} + \bar{I}_{xL} + \bar{I}_{xR} + \bar{I}_{xB} \\ I_{yt} &= \bar{I}_{y12} + \bar{I}_{y45} + \bar{I}_{yL} + \bar{I}_{yR} + \bar{I}_{yB} \\ I_{zt} &= \bar{I}_{z12} + \bar{I}_{z45} + \bar{I}_{zL} + \bar{I}_{zR} + \bar{I}_{zB}\end{aligned}\quad (B.16)$$

APPENDIX C
RUNNING THE
PROGRAM

This appendix gives step by step instructions on how to run the program. The program should be run on a VAX computer using a Tektronics 4107A or 4110 terminal. Before running the program, first check that the following subprograms are in the directory of the disk or magnetic tape: mars.for, mars.dat, mars.out, grph.for, grph.cmn. If the disk contains all the necessary subprograms, the following should be typed at the \$ sign prompt. Bold is used to show what the user types, and a command within the following brackets <command> is a particular key to be pressed.

```
$ fort77 mars.for      <return>  
$ fort grph.for        <return>  
$ link mars+grph      <return>
```

These commands compile the programs and create the executable files. It only needs to be typed once unless either the main program mars.for or the graphics program grph.for are edited.

The input file may be changed to suit the user's needs by typing:

```
$ ed mars.dat          <return>  
* c                      <return>
```

(change input, see Section 5.1)

```
<cntrl> z - typed simultaneously  
* exit                  <return>
```

Once the input is set, the program is run by typing.

\$ run mars <return>

Again, there is no need to recompile the program when changing the input. As a result, many different parameters can be varied relatively easily and efficiently. This is one advantage of this simplified and specialized analysis over other dynamic software packages.

If one wishes to stop the program before the vehicle reaches its final destination, the following command should be typed.

<cntrl> c - typed simultaneously

When the program is running, the output will be displayed as explained in Section 5.1. If it is desired to pause the program so as to study the numerical values on the screen before they pass, the following should be typed.

<cntrl> s - typed simultaneously

To get the program going again after a pause type:

<cntrl> q - typed simultaneously

If it is wished not to see the character and numerical value display, or it is desired only to see the graphics display, hit the key entitled dialog at the top left position of the keyboard.

<dialog>

Hitting the dialog button again will bring back the character and numerical value display.

The graphics display is purposely not erased between steps. In this manner, the user can see how the vehicle is progressing. After several displays, the screen becomes cluttered. To erase the graphics display while the program is running, hit the G Eras button or type:

<shift> <dialog> - typed simultaneously

Finally, after the program has been run or after it has been interrupted, the following should be typed.

<setup>
*** code ansi <setup>**

This insures that the computer goes from the graphics mode to the editor mode. Even if one wishes just to change the input after a particular run, these commands must be typed. Otherwise, the editor scrambles words and numbers in an unreadable fashion.